Experimental and Numerical Study of Acoustic Streaming in a Standing Wave Tube

By

Yasser Rafat

Doctor of Philosophy

Department of Mechanical Engineering

McGill University

Montreal, Quebec

May 2014

A dissertation submitted to McGill University in partial fulfillment of the

requirements for the degree of Doctor of Philosophy

Dedicated,

To my parents, reason for my being

To my wife, reason for my healthy being

Abstract

Acoustic streaming is a steady recirculated flow produced by interactions between acoustic waves and solid boundaries. Acoustic streaming significantly affects heat transfer between stack and heat exchangers [1]. In thermoacoustic engines, devices that convert acoustical power into heat pumping, or vice versa, heat load is transferred to the heat exchanger due to convection caused by acoustic streaming. The efficiency of the thermoacoustic machines produced to date has been hampered by several types of thermal losses. Acoustic streaming was identified as a significant source of thermal loss. Different types of acoustic streaming occur in a thermoacoustic machine. The objective of the present study was to characterise vortical types of acoustic streaming flows in an idealised thermoacoustic system, consisting of an acoustic standing wave tube with and without spoilers.

Experimental investigations of acoustic streaming were performed in a standing wave acoustic resonator using Particle Image Velocimetry, PIV. The experimental approach was verified by comparing experimental results with predictions from linear acoustic theory, for the well-known Rayleigh streaming problem. The formation of classical and non-classical two-dimensional Rayleigh streaming structures was investigated. The effects of resonator shape on Rayleigh streaming were studied by reconstructing a three-dimensional streaming cell from planar streaming velocity data. The interactions between thermoacoustic core elements; stack and heat exchanger, and acoustic standing waves produces streaming structures which are different from Rayleigh streaming cells. This type of streaming was studied by introducing idealised models of thermoacoustic core elements within the resonator.

A commercial code, PowerFLOW, based on the Lattice Boltzmann Method (LBM) was used to simulate acoustic standing waves inside a rectangular resonator. The results obtained from the LBM model were compared with those from linear acoustic theory. Both two and three-dimensional Rayleigh streaming cells were observed in the simulations. A rectangular spoiler was introduced in the numerical model and its effects on streaming flow were studied. A different type of streaming, named edge streaming, appeared due to interactions between the standing wave field and the spoiler. Comparisons were made between edge streaming and Rayleigh streaming. A parametric study of the effects of key flow and spoiler geometric parameters on edge streaming was then performed. It was observed that a spoiler with greater thickness, rectangular edge shape and shorter length would yield greater edge streaming amplitudes

Experimental and numerical investigations of the instantaneous flow structures, formed by the interactions between the acoustic standing waves and the spoiler were performed. Flow and spoiler shape parameters were varied and their effects on the shear layer and the shed vortices were studied. The effects of these instantaneous flow structures on the heat transfer characteristics of the stack were studied.

The current study is unique in its approach to study different acoustic streaming flows in a standing wave resonator with a spoiler. It was observed that the presence of stack and heat exchangers introduces edge streaming. In most cases, the peak amplitude of the edge streaming velocity was found to be orders of magnitude larger than the peak Rayleigh streaming velocity. It was concluded that among different types of acoustic streaming present in a standing wave thermoacoustic machine, edge streaming is dominant in heat transfer enhancement. This

observation is significant because edge streaming has notably been overlooked in the design of the thermoacoustic systems to date.

Résumé

Les machines thermoacoustiques convertissent l'énergie mécanique présente dans des ondes acoustiques stationnaires en chaleur pompée, ou vice-versa. Le rendement des machines thermoacoustiques produites à ce jour est limité en raison de pertes thermiques associées à différents mécanismes. Entre autre, les écoulements moyens redressés produits par des phénomènes physiques non linéaires résultant des interactions entre l'empilement et les ondes stationnaires produisent des échanges de chaleur importants. Le but de la présente étude était de quantifier ces échanges de chaleur dans des résonateurs acoustiques sans obstacles, et obstrués en partie par des plaques orientées dans la direction de l'écoulement, simulant des plaques d'empilement. Des mesures faites à l'aide d'imagerie particulaire à haute vitesse furent prises, les écoulements moyens redressés dans des tubes sans obstacles ont été observés. Les vitesses ainsi que la forme des structures tourbillonnaires furent en accord avec des résultats précédemment publiés. Les mesures avec obstacles révèlent la présence d'écoulements tourbillonnaires de très haute amplitude, beaucoup plus marqués que les écoulements dits de Rayleigh dans les tubes vides.

Des études de simulation numériques furent alors réalisées à l'aide du logiciel Power Flow. Le logiciel permet de varier la forme des obstacles ainsi que la vitesse acoustique et la fréquence d'excitation. Les résultats confirment l'importance des écoulements moyens redressés induits par les obstacles, des plaques rectangulaires. Ces phénomènes sont induits principalement par la vorticité près des bords des plaques. La vitesse des écoulements redressés augmente avec l'amplitude acoustique, avec la fréquence d'éxitation, et change avec la géométrie du profil des plaques. Les résultats suggèrent que les phénomènes d'écoulements moyens redressés dominent le transfert thermique entre l'empilement et les échangeurs de chaleur dans les machines

thermoacoustiques, ce résultat est étonnant considérant que ces phénomènes ont été largement ignorés dans la modélisation des systèmes thermoacoustiques, ou bien ils ont été modélisés en tant qu'écoulements de Rayleigh, ce qui sous-estime leur contribution.

Acknowledgements

I would like to express deep gratitude to my supervisor, Dr. Luc Mongeau. This work would not have been possible without his patience. He believed in me even when I was doubtful. His guidance, support and advice as an advisor and as a mentor have helped me through the years, leading to this thesis.

I am also grateful to all my colleagues, especially Dr. Jong Beom Park and Dr. Rani Taher, for their help at various stages of the experimental studies and Kaveh Habibi for the guidance he provided for the numerical studies. Sincere thanks also go to Dr. Ida Reyt and Dr. Helene Bailliet of the University of Poitier for their collaboration during their visit to McGill.

Financial support was provided by McGill University, through MIDA, and an NSERC Discovery grant.

I would like to thank Exa corporation for providing PowerFLOW academic licenses and for their continuous technical support. I also thank Calcul Canada for the use of their high performance computational resources. The numerical simulations were performed on clusters supported by the Consortium Laval, Université du Québec, McGill and Eastern Quebec (CLUMEQ).

Abstract iii

Nomenclature xiii

1 Introduction 1

1.1 Background 1

1.2 Literature review 3

1.2.1 Analytical studies 3

1.2.2 Experimental studies 6

1.2.3 Numerical studies 10

1.2.4 Motivation for the present study 13

1.3 Objectives 15

1.4 Organisation of the thesis 16

2 Experimental and numerical methods 18

2.1 Experimental methodology 18

2.1.1 Particle Image Velocimetry 18

2.1.2 Experimental setup 19

2.1.3 Experimental procedures 21

2.1.4 Data acquisition 23

2.1.5 Image processing 25

2.1.6 Velocity vector calculation 26

2.1.7 Acoustic streaming velocity calculation 28

2.1.8 Error and uncertainty analysis 29

2.2 Numerical methods 30

2.2.1 Mathematical background 30

2.2.2 Simulation case setup in PowerFLOW 33

2.2.3 Geometry and variable resolution region 34

2.2.4 Operating conditions and parameters 35

2.2.5 Initial conditions and boundary conditions 37

2.2.6 Measurement window parameters 39

2.2.7 Post processing of simulation data 40

3 Experimental study of acoustic streaming in an empty standing wave resonator 56

3.1 Introduction 56

3.2 Validation of experimental results 56

3.2.1 Acoustic velocity: Phase-locked and Time Resolved 56

3.2.2 Acoustic streaming 59

3.2.3 Time evolution of acoustic instantaneous and streaming velocities 60

3.2.4 Repeatability of results 62

3.3 Influence of peak instantaneous acoustic velocity on Rayleigh streaming 62

3.4 Three-dimensional reconstruction of one streaming cell 65

3.5 Conclusions 67

4 Acoustic streaming due to the introduction of a stack in the resonator 82

4.1 Introduction 82

4.2 Methodology 82

4.3 Results and discussion 83

4.4 Conclusions 87

5 Numerical study of acoustic streaming in a standing wave resonator 96

5.1 Introduction 96

5.2 Validation 96

5.2.1 Acoustic velocity 97

5.2.2 Streaming velocity 97

5.3 Streaming from a rectangular spoiler 99

5.3.1 Acoustic velocity amplitude 102

5.3.2 Effects of spoiler thickness 103

5.3.3 Effects of spoiler length 104

5.3.4 Influences of edge cross-sectional shape 105

5.4 Three-dimensional simulation of acoustic streaming flow 107

5.5 Conclusions 109

6 Transient flow characteristics in a channel with a spoiler 127

6.1 Introduction 127

6.2 Acoustic flow at the stack plate ends 127

6.3 Flow between the stack plates 131

6.4 Parametric study 132

6.4.1 Influence of peak instantaneous acoustic velocity amplitude 133

6.4.2 Effects of spoiler thickness 135

6.4.3 Effects of spoiler length 135

6.4.4 Influence of spoiler edge profile 136

6.4.5 Effects of excitation frequency 137

6.5 Conclusions 138

7 Conclusions and Future work 152

7.1 Summary 152

7.2 Conclusions from experimental studies 153

7.3 Conclusions from numerical studies 155

7.4 Proposed future work 158

Appendix: Comparison between experimental and numerical results 160

References 177

Nomenclature

Roman Symbols

Br	Blockage ratio
c	Speed of sound [m/s]
e_v	Mean error percentage [%]
f_a	Excitation frequency [Hz]
$\hat{f}$	External force per unit mass of a molecule [N/kg]
f^{eq}	Maxwell-Boltzmann distribution function
g	Gap between the stack plates [m]
H	Width of the resonator [m]
k	Boltzmann constant [J/K]
L	Length of the resonator [m]
L_{char}	Characteristic length [m]
L_p	Length of the spoiler [m]
Lv	Dimension of a voxel [m]
L_{s1}	Non-dimensional axial length of the primary streaming cell
L_{s2}	Non-dimensional axial length of the secondary streaming cell

M	Mach number
m	Number of images captured for ensemble averaging
n	Number of sub-phases in which an acoustic cycle is divided
N	Total number of data points
p_a	Peak acoustic pressure amplitude [Pa]
p_{char}	Characteristic pressure [Pa]
p_0	Ambient pressure inside a standing wave resonator [Pa]
Re	Reynolds number
Re_s	Streaming Reynolds number
Re_{nl}	Non-linear streaming Reynolds number
$\hat{r}$	Position vector in LBM [m]
t	Time [s]
ts	Timestep in LBM [s]
t_l	Time lag used in phase-locked method [s]
T	Time period of an acoustic cycle [s]
T	Temperature [K]
T_{char}	Characteristic temperature [K]
t_p	Spoiler thickness [m]

$\hat{u}$	Velocity vector in LBM [m/s]
u_a	Peak instantaneous acoustic velocity amplitude [m/s]
u_R	Peak Rayleigh streaming velocity [m/s]
u_{st}	Axial components of streaming velocity [m/s]
V_{char}	Characteristic velocity [m/s]
V_{st}	Overall streaming velocity [m/s]
V_{ac}	Overall acoustic velocity [m/s]
V_{sp1}	Peak amplitude of first edge streaming cell [m/s]
V_{sp2}	Peak amplitude of second edge streaming cell [m/s]
X,Y,Z	Cartesian coordinates for the global origin
x_a	Peak instantaneous acoustic displacement [m]

Abbreviations

BC	Boundary Condition
CFD	Computational Fluid Dynamics
COP	Coefficient Of Performance
DNS	Direct Numerical Simulation
HWA	Hot Wire Anemometry

IA	Interrogation Area
LBM	Lattice Boltzmann Method
LDV	Laser Doppler Velocimetry
LGA	Lattice Gas Automata
PIV	Particle Image Velocimetry
PSD	Power Spectral Density
TTL	Transistor-Transistor Logic
TR-PIV	Time Resolved PIV
VR	Variable Resolution
2D	Two-Dimensional
3D	Three-Dimensional

Greek Symbols

δ_v	Viscous penetration depth [m]
λ	Acoustic wavelength [m]
ν	Kinematic viscosity [m^2/s]
ν_{char}	Characteristic viscosity [m^2/s]
Ω	Collision operator in LBM
ω	Acoustic excitation frequency [rad/s]

θ	Phase in an acoustic cycle [degrees or radian]
τ	Relaxation time in BGK model [s]
ρ	Density [kg/m^3]
ρ_{char}	Characteristic density [kg/m^3]

1 Introduction

1.1 Background

The issues related to climate change and the decrease of non-renewable energy sources pose important environmental challenges. The reduction of greenhouse effect gas emissions, the development of renewable energy sources and the improvement of energy efficiency are important technological challenges. The Montreal Protocol has banned the production of CFCs (Freon) in 1996 [2], which have been commonly used as refrigerant in air-conditioners and refrigerators, due to their potential to contribute to the depletion of the ozone layer. The CFCs were largely replaced with HFCs, but these refrigerants are also harmful to the environment. Conventional cooling systems release large amounts of carbon dioxide (CO_2) to the environment, increasing the greenhouse effect. This has motivated the development of new cooling technologies that are environmentally benign.

Thermoacoustic systems produce cooling through the utilization of energy in high amplitude acoustic waves. Heat pumping is obtained in a thermoacoustic system from the periodic compression and expansion of the working fluid. Thermoacoustic systems employ environmentally benign working fluid, namely Helium-Argon gas mixtures. Electrical power from a linear mechanical actuator is first transformed into acoustic power, which in turn produces heat pumping within the core, either a stack or a regenerator. Hot and cold heat exchangers located on either side of the core provide a path for heat transfer with the "outside world" through a secondary cooling loop [1].

Thermoacoustic devices do not use greenhouse effect gases, but rare gases such as argon or helium, which can safely be released in the atmosphere. Thermoacoustic engines can use non fossil and renewable energies, such as solar energy [3]. They may also be used to recover wasted heat at low temperatures [4]. Other potential advantages of thermoacoustic systems in addition to their low environment impact, include their simplicity for low temperature applications and continuous cooling capacity control as opposed to on-off control in ordinary vapor compression cycle refrigerators.

The long-term goal of research performed in the field of thermoacoustic refrigeration is to develop an environmentally friendly, highly efficient thermoacoustic cooler that can substitute conventional vapor compression cycle refrigerators in certain niche applications. For most thermoacoustic cooler prototypes developed so far, the thermodynamic second law efficiency (defined as the ratio of the actual coefficient of performance (COP) and that of an ideal reversible cycle) is substantially lower than that of domestic refrigerators using the conventional vapor compression refrigeration cycle [5]. This factor has so far hampered the successful commercialization of thermoacoustic cooling. Losses include additional heat gain in prototypes due to imperfect thermal insulation of the thermoacoustic cooler housing, lower heat pumping due to irregular and deformed stack spacing and plates, and adverse convective heat transfer due to acoustic streaming. The imperfect insulation and the irregular stack geometry can be minimized by proper design and fabrication. The effects of acoustic streaming, however, are not clearly understood.

1.2 Literature review

A general review of the literature available on analytical studies of acoustic streaming was performed by Nyborg [6] and Riley [7]. Boluriaan *et al*. [8] presented a thorough review of analytical and numerical studies of different types of acoustic streaming. In the following section a more specific critical review of the literature on acoustic streaming with applications in thermoacoustic refrigeration is presented. The available literature on acoustic streaming was tentatively categorized into analytical, experimental and numerical studies.

1.2.1 Analytical studies

Acoustic streaming is a second order steady flow that is superimposed on the larger first order time dependent acoustic flow [1]. Different types of acoustic streaming occurring in thermoacoustic refrigerators are shown in Figure 1-1.

In mathematical expressions obtained through substitution of an asymptotic expansion in the relevant equations of motion, acoustic variable (pressure, velocity and temperature) are usually sinusoidal and of first order magnitude in the expanded variable. Streaming quantities arise from time averaged products of two acoustic variables, and they are thus of second order magnitude in the expanded variables. Linear acoustic theory is usually built upon the assumption of a perfectly quiescent medium at rest. This assumption is only approximately correct. It breaks down for large amplitudes of the acoustic variables. The motion of the medium in response to the sound waves constitutes the basic streaming phenomenon.

The phenomenon of streaming was first reported by Faraday [9], who observed unusual sand patterns on vibrating elastic plates. Acoustic streaming is produced by time averaged Reynolds

stresses, defined as the mean value of the acoustic momentum flux. The dissipation of the acoustic energy flux allows gradients in the momentum flux, which in turn forces acoustic streaming [10]. Lord Rayleigh was the first to propose a mathematical model for boundary layer driven acoustic streaming in a wide channel [11]. He assumed the boundary layer thickness to be negligible in comparison to the channel width, and the wavelength to be large compared to the tube radius. He used the method of successive approximations, where the solution of the first order linear problem provides the forcing function for the second order governing equations. Rayleigh streaming, also known as outer streaming, is a steady recirculated fluid flow outside the boundary layer. Rayleigh streaming is characterised by acoustic energy dissipation within the Stokes boundary layer adjacent to the solid boundary [7]. Streaming flows inside the boundary layer were first studied by Schlichting [8]. Schlichting streaming is also known as inner streaming. The thickness of inner streaming cell is approximately equal to $1.9\delta_\nu$, where $\delta_\nu = \sqrt{2\nu/\omega}$ is the viscous penetration depth, ν is the kinematic viscosity and ω is the acoustic excitation frequency.

Early analytical studies on acoustic streaming were limited to incompressible fluids. But compressibility is needed for the propagation of acoustic waves, and therefore compressibility is inherently important [12]. The effect of compressibility can be neglected when the wavelength, λ, is much larger than the characteristic geometric length involved. The incorporation of compressibility effect becomes necessary when the wavelength is comparable to or smaller than the characteristic geometric length. The effect of compressibility was studied by Qi [13]. It was found that the inclusion of compressibility increases streaming velocity amplitudes outside the boundary layer.

Early analytical studies generally assumed that the channel is wide. For example, Rudenko *et al*. [12] studied streaming in a boundary layer assuming an infinite channel width. Hence the proposed solution was not rigorously applicable to narrow channels. Two studies of channels with arbitrary width appeared in 2001; both Waxler [14] and Bailliet *et al*. [15] studied acoustic streaming in thermoacoustic stack pores. Bailliet *et al*. accounted for the thermal conductivity and the temperature dependence of the viscosity. A mean temperature gradient was imposed along the channel walls. The focus was on thermoacoustic engine stacks. Numerical integration was required to calculate the streaming velocity. Their analysis was based on the Eulerian streaming velocity, and proper interpretation requires analysis of the average mass transport velocity. Temperature effects were not considered by Hamilton *et al*. [16] in their derivation of the analytic solution for the average mass transport velocity generated by a standing wave within parallel plates having arbitrary width. For wide channels and away from the solid boundary, their solution was in agreement with classical results for Rayleigh streaming. They found that the size of the inner streaming cell, in relation to that of the outer streaming cell, increased with a decrease in channel width. The outer streaming cells were found to completely disappear for channel widths less than about ten times the boundary layer thickness.

Linear thermoacoustic theory is accurate for low amplitude acoustic pressure [17]. However, potential applications of thermoacoustic refrigeration would require a high acoustic pressure inside the resonator [18]. At high acoustic velocity amplitudes, deviations from linear model predictions are significant. Menguy *et al*. [19] indicated that for large streaming velocities the axial velocity profile in cylindrical waveguides is not parabolic due to fluid inertia effects. They also introduced an appropriate Reynolds number, Re_{nl}, which compares the relative importance of inertia and viscous effects. They introduced the terminology “slow streaming” when $\mathrm{Re}_{nl} \approx 0$

and "non-linear streaming" when $\mathrm{Re}_{nl} > 0$. Where $\mathrm{Re}_{nl} = (u_a/c)^2 (H/\delta_v)^2$, u_a is the peak acoustic velocity amplitude, c is the speed of sound, H is the channel width and δ_v is the viscous penetration depth.

1.2.2 Experimental studies

Minimally invasive fluid flow velocity measurement techniques such as Particle Image Velocimetry (PIV) and Laser Doppler Velocimetry (LDV) have been extensively used for the measurement of acoustic and streaming velocities [20]. The experimental technique of PIV yields two-dimensional (2D) and three-dimensional (3D) velocity fields. High spatial resolution is possible with appropriate lenses and good resolution digital cameras. A high temporal resolution can also be achieved by using Time resolved PIV (TR-PIV) [21]. Arroyo *et al*. [22] were the first to measure both acoustic and streaming velocities inside a square channel using PIV. Hann *et al*. [23, 24] developed methods for the measurement of instantaneous acoustic velocities from the PIV data.

Efforts have been made to measure streaming flows in standing wave devices using either PIV [20, 22, 23, 25] or LDV [26-28]. Thompson *et al*. [26] measured simultaneously both acoustic and streaming velocities using LDV in a resonator with a spatially uniform temperature distribution. They studied the onset of streaming, and observed it to occur five seconds after switching on the acoustic field. They [27] also studied the influence of the axial temperature gradient and observed decrease in acoustic streaming magnitudes with increasing magnitude of temperature gradient. Moreau *et al*. [28] studied both inner and outer streaming vortices using LDV. They performed a thorough study of inner streaming cells at high Re_{nl} and observed deviations in the streaming cell shape from theoretical predictions. Reyt *et al*. [29] used both

experiments and numerical models to investigate acoustic streaming for $1 < \mathrm{Re}_{nl} < 30$. They found that for slow streaming, experimental and theoretical results were in reasonable good agreement. But for fast streaming, $\mathrm{Re}_{nl} > 1$, the experimental results deviated from the theoretical predictions and additional streaming vortices started to appear. Nabavi *et al*. [30] developed a novel technique, which they termed as synchronized PIV, for measuring simultaneously the acoustic and streaming velocities inside an acoustic resonator. The acoustic velocity was obtained from the cross-correlation between two consecutive PIV images. The streaming velocity was obtained from the cross-correlation of two equal phase PIV images separated in time by an integer number of acoustic cycles. This technique enables the measurement of streaming velocities at any location along the standing wave resonator in presence of large amplitude acoustic waves. Any flow phenomenon that is asynchronous with the acoustic field thus gets included in the measured streaming variables. Nabavi *et al*. [31] studied the formation of regular (classical) and irregular streaming structures based on Re_{nl}. The theoretically predicted streaming cells have a dimension of one quarter wavelength, and are symmetric about the channel centerline. Such streaming cell structures were termed "classical" or "regular". Those streaming cell structures where the shape, size and the number of vortices were different from the classical case were termed as "irregular". Their results show that, for a given frequency, classical streaming structures are observed only when the displacement of the acoustic driver is sufficiently large.

Nabavi *et al*. [32] also studied the influence of a temperature gradient along the resonator walls on the shape and the amplitude of the acoustic streaming velocity field. Most of the past studies of acoustic streaming have been focused on Rayleigh streaming. They were not performed in actual thermoacoustic coolers which are usually pressurised to increase gas density. They have

been done, for convenience, in either square or circular resonators filled with air at ambient conditions. Optical, laser based flow measurements require good optical access, which is technically difficult to achieve in thermoacoustic coolers operating at high mean pressure.

Streaming and edge effects are expected to influence strongly the overall efficiency of thermoacoustic systems [33, 34]. Streaming flows [18, 35] contribute significantly to heat transfer. Early studies on the enhancement of heat transfer due to streaming caused by suspended rigid bodies in standing wave were performed by Mozurkewich [36]. He found that acoustic streaming occurring at edges of the suspended rigid body enhances the heat transfer much more than the Rayleigh streaming. He also suggested the presence of vortical streaming flows localised near the rigid body edges. Acoustic streaming was also found to help in cooling microelectronic chips. A prototype miniature cooling system was designed by Wu *et al*. [37]. They found that acoustic streaming enhanced the heat transfer. Moreau *et al*. [38] employed LDA to study the effect of a stack on Rayleigh streaming and found that the magnitude of the streaming velocities in the vicinity of the stack ends is very high when compared with typical Rayleigh streaming velocities. The streaming flow near the edges of one single flat spoiler was studied by Aben *et al*. [39]. They investigated two different methods of quantifying the streaming velocity from the PIV data and concluded that the cyclic average of the phase-locked acoustic velocities yield results that appear to better indicate the strength of streaming vortices around edges.

In thermoacoustic refrigerators, heat pumping occurs within the stack and the heat exchangers. Stacks help in creating a temperature gradient. The two heat exchangers on either side of the stack help in removing the heat from low temperature source to a high temperature sink [1]. The interactions between standing wave at high amplitudes and the stack-heat exchanger couple

create complex flow structures which regulate the heat transfer phenomenon. The formation of vortices at the stack end, and their interaction with the heat exchangers along with acoustic streaming are major flow phenomena which need to be characterised for increasing the performance of thermoacoustic devices [40]. There are several challenges in experimentally characterising such flow interactions. Intrusive techniques such as Hot Wire Anemometry (HWA) or pressure transducers [41] can alter the flow pattern. Non-intrusive techniques such as LDA and PIV do not disturb the flow but are challenging due to the close proximity of stack and heat exchangers and also due to highly pressurized gases being used in realistic thermoacoustic refrigerators. For these reasons, PIV has been used in idealized configurations to study the flow structures behind the stack.

Berson *et al*. [33] studied the flow structures inside a simplified thermoacoustic refrigerator using PIV. They measured the acoustic velocity inside the boundary layer between consecutive stack plates. Symmetric pairs of counter-rotating vortices were observed at the end of the stack for low acoustic pressure amplitude. Detachment of vortices and loss of symmetry was found at high acoustic pressure levels. Mao *et al*. [40] suggested that the characterisation of the fluid motion outside the stack based on ensemble-averaged phase-locked PIV data was relatively simple and addressed the need for understanding turbulence characteristics of oscillatory flows past a stack of parallel plates. Several PIV studies [34, 39, 42, 43] investigated the vortex structures at the stack end. The effects of different geometrical parameters of a parallel plate stack were studied. Zhang *et al*. [44, 45] also performed similar parametric studies employing PIV. They tried to correlate geometrical and flow parameters with the heat transfer within the thermoacoustic core.

1.2.3 Numerical studies

The transport equations of mass, momentum and heat in a gas system can be solved by employing two broad approaches, continuum and discrete. In the continuum approach, the governing equations are obtained in the form of differential equations by using conservation of mass, momentum and energy. The resulting equations are converted to algebraic equations and then solved using different computational methods. Navier-Stokes based numerical solvers follow the continuum approach. In the discrete approach, the properties of a group of particles (atoms, molecules) are described by a particle distribution function. The Lattice Boltzmann Method (LBM) is based on the discrete approach. In LBM the microscopic and mesoscopic processes are modelled using kinetic theory in such a way that the averaged macroscopic properties still obey the macroscopic conservation equations [46]. The Lattice Boltzmann Method is a numerical technique which is simple to implement. The incorporation of complex geometries inside the flow domain is comparatively easier than for codes requiring a mesh generation program. Codes based on LBM can be easily parallelized. Due to its straight forward implementation it is considered as a viable alternative to Navier-Stokes based numerical methods [46].

The analytical models discussed before were tailored to slow or linear streaming in simple geometries and for idealized boundary and operating conditions. Many limitations of the analytical models can be overcome by using numerical methods. Direct numerical simulation (DNS) of fully coupled Navier-Stokes equation is the most accurate approach. Early numerical simulations of acoustic streaming were performed by Kawahashi *et al*. [47]. They applied a fourth order spatial difference method to the 2D analysis of acoustic streaming. They failed to reproduce the classical streaming structures typical of low pressure amplitude inside a simple

standing wave tube. Yano [48] studied turbulent acoustic streaming in the presence of shock waves and concluded that streaming velocity was of the same order of magnitude as the piston velocity. There are many numerical studies on the topic by Aktas *et al*. [35, 49, 50]. They studied Rayleigh acoustic streaming inside a standing wave resonator and investigated the time required for the onset of streaming. Both regular and irregular streaming cells were simulated and the effects of differentially heated walls on the streaming cells were identified. Daru *et al*. [51] studied non-linear acoustic streaming inside a standing wave resonator by solving the compressible Navier-Stokes equations. They compared their numerical results with experimental data for non-linear acoustic streaming and observed the transition from regular acoustic streaming flow towards irregular acoustic streaming flow.

Numerical methods offer an interesting alternative to experiments to study complex flows present in actual stack-heat exchanger couple. The instantaneous flow structures created by the interactions between the standing waves and the stack have been numerically studied. Cao *et al*. [52] performed direct numerical simulations of the compressible Navier-Stokes, continuity and energy equations for an ideal gas to study the energy flow within a distance of one acoustic displacement amplitude from the stack end. They observed the vertical energy flux density near the stack end occurs within a region proportional to acoustic displacement. Ishikawa *et al*. [53] simulated a 2D Navier-Stokes equation to study the flow field and energy transport near the stack. They also studied the effects of plate length, plate spacing and acoustic amplitude and found that heat pumping is effectively localised near the stack edges. Blanc-Benon *et al*. [54] obtained the instantaneous velocity and vorticity fields in the vicinity of stack ends numerically, using a low Mach number model. They compared numerical results with experimental results and obtained a good agreement. In the numerical simulations performed by Besnoin *et al*. [55],

the computational domain consisted of a complete idealised thermoacoustic couple, i.e the domain contained both the heat exchangers and the stack. They employed a vorticity based scheme for low Mach number flow. Parametric studies were performed where the effects of drive ratio, plate thickness, heat exchanger length and location on the performance of the thermoacoustic refrigerator and the fluid flow were studied. They also provided design recommendations for the stack and heat exchanger based on the thermal performance and the fluid flow in and around the thermoacoustic couple. Jaworski *et al*. [56] studied the entrance effects on the channels made by stacks of parallel plate due to oscillatory flow. They solved the 3D Navier-Stokes equation using the SIMPLE scheme [57]. Their numerical model was created using the commercial Computational Fluid Dynamics (CFD) software, FLUENT 6.2. They pointed out the limitations of the numerical method used by Blanc-Benon *et al*. [54], namely the constant dynamic viscosity assumption and low Mach number restriction. They concluded that the entrance length observed in the channels between the stack plates differ from the piston induced oscillatory flow. Therefore, thermoacoustic flows would require different correlations for predicting entrance lengths.

The applicability of the LBM for simulations of acoustic flows with zero mean velocity inside a channel was studied by Cosgrove *et al*. [58]. The accuracy of their scheme was limited to second order in space and first order in time. Wang *et al*. [59] simulated 2D standing waves inside a resonator using a thermal LBM. Habibi *et al*. [60] simulated standing wave acoustic flow inside a 3D resonator using a commercial LBM code called PowerFLOW [61]. They studied the sound absorption characteristics of an orifice plate. There are very few studies of acoustic streaming using LBM. A study of acoustic streaming produced by a standing wave between two parallel plates was reported by Stansell *et al*. [62]. They used the lattice gas approach, a predecessor of

LBM, to simulate full Navier-Stokes equation and streaming appeared as a small correction to the oscillatory flow field. However, lattice Gas Automata (LGA) simulations, are inherently noisy, and streaming was only observed for high amplitudes and viscosities. In order to overcome the noise problems, LBM was developed. Like LGA, LBM also simulates the full Navier-Stokes equation. The first study was reported by Haydock *et al*. They studied acoustic streaming in both standing [63] and travelling [64] waves. They also simulated acoustic streaming around various obstacles. They concluded that acoustic drive ratio, $\left(p_a / p_0 \right)$ defined as the ratio of peak acoustic pressure, p_a and ambient pressure, p_0 determines that after how many acoustic cycles streaming would be established. Meng *et al*. [65] studied high frequency oscillating flow between two plates using thermal LBM. They observed enhancement of heat transfer at high frequency oscillations due to non-linear streaming flows.

1.2.4 Motivation for the present study

Acoustic streaming is recognized as one of the major contributors to thermal losses in thermoacoustic devices [1]. Both its understanding and control are necessary to design more efficient thermoacoustic devices. A strongly nonlinear phenomenon, streaming is not captured by linear classical models [1, 17] or 1D numerical codes such as DeltaEC. Moreover, ideal models of the various types of streaming (as shown in Figure 1-1) [11] are generally valid for elements being "isolated" from the thermoacoustic machines and have not been entirely validated experimentally. On the other hand, acoustic streaming observed recently in several experiments in idealized configurations is not satisfactorily explained by any existing theory [31, 32, 38]. The differences between predictions and experiments are not generally quantified. Finally, the

experimental evaluations of nonlinear second order acoustic phenomena presents a challenge in metrology and signal processing, and requires very precise velocity measurement methods.

From the literature review it was concluded that most analytical models are accurate for slow streaming velocities only. Only few studies considered the effects of inertia on acoustic streaming flows. Although analytical solutions are available for both inner and outer streaming inside a cylindrical resonator, no solutions were available for 3D Rayleigh streaming in square or arbitrary shaped resonators. Many efforts were made to characterise Gedeon streaming [66], which is the averaged mass flow through a looped path in traveling wave thermoacoustic devices, and Rayleigh streaming which is the streaming in a confined region of the resonator driven by viscous and thermal boundary layer effects near the vessel walls [17] . Efforts were made in order to minimize or eliminate the effects of streaming. Gedeon streaming and Rayleigh streaming in pulse-tube refrigerators have been reportedly suppressed by jet pumps [67] , and tapered pulse tubes [68], respectively. Elastic membranes were also employed [69, 70] to suppress Gedeon streaming in travelling wave systems, where the amplitudes of volume flow rate were relatively small. Unlike Gedeon streaming, little is known about the streaming within the stack and the resonator in a standing wave device, often called internal streaming, as mentioned by Backhaus *et al*. [17].

Experimental studies of 2D Rayleigh streaming in empty resonators have been performed. But the effects of resonator shape on the inner and outer streaming cells inside a standing wave resonator have not yet been studied. Few studies have considered the presence of a rigid body inside a standing wave resonator. Thus, there is still a need for characterising the effects of different thermoacoustic core elements on the flow field of 2D acoustic streaming cells and for quantifying the associated heat transfer.

Rayleigh streaming inside 2D empty standing wave resonators has been extensively studied using Navier-Stokes based solvers. The LBM has been used as an alternative numerical approach for performing large scale fluid flow simulations. Very few studies have used LBM based solvers for studying acoustic streaming. Most previous numerical studies of acoustic streaming have been performed for an empty standing wave resonator, and a 2D computational domain. The interaction between standing wave and obstacles inside a standing wave resonator results in a complex acoustic streaming environment, which is very different from Rayleigh streaming. No numerical studies have investigated streaming flows inside standing wave resonators with obstacles.

1.3 Objectives

The overall objective of the work presented in this thesis was to identify and characterise different streaming flows in an idealised standing wave thermoacoustic machine. The resonator of the thermoacoustic machine was idealised by a square cross-section standing wave resonator. The stack was idealised as a flat spoiler. The research objectives included the following specific aims.

The first aim was to quantify Rayleigh streaming in an empty standing wave resonator and to study the effects of the resonator cross section shape on the outer and inner streaming cells. The second aim was to characterise the acoustic streaming due to interactions between standing waves and a spoiler. One of the objectives was to investigate the effects of different flow and spoiler geometric parameters on the resulting acoustic streaming flows. The flow parameters investigated were the peak instantaneous acoustic velocity amplitude and the excitation frequency. The geometric parameters investigated were the spoiler length, the spoiler thickness

and the spoiler edge shape. The third aim was to study the instantaneous vortical flow structures formed by interactions between the standing wave and the spoiler. A parametric study similar to the one performed for acoustic streaming was repeated for studying the instantaneous vortical structures.

The ease with which complex geometries can be incorporated in the computational domain is believed to be a significant advantage of LBM [46]. Actual thermoacoustic machines would include stacks/regenerators with pores of different shapes and heat exchangers with complex geometries. Therefore, the LBM is well suited for studying the flow environment inside an actual thermoacoustic machine. A secondary objective of the study presented in this dissertation was to assess the applicability of the LBM based commercial code called PowerFLOW for simulations of streaming flows in a standing wave resonator with and without the spoiler. Once the validity of the LBM model developed in PowerFLOW was established, more realistic geometries were investigated to study different kinds of streaming flows occurring in a thermoacoustic machine.

1.4 Organisation of the thesis

Chapter 2 describes of the experimental and numerical methodology employed in the study. In chapter 3, the validity of the experimental data is verified and experimental data on streaming in an empty square cross-section resonator are reported. The introduction of stack in the resonator changes the streaming structure and also amplifies streaming velocity amplitudes in the vicinity of the stack end. This phenomenon is studied experimentally in chapter 4. In chapter 5, the phenomenon of acoustic streaming is studied numerically using computational methods. Results are presented for both empty resonator and when a spoiler is present. The interaction between acoustic flow and spoiler and the resulting transient flow structures are studied both

experimentally and numerically in chapter 6. Finally, the conclusions and contributions are summarised in chapter 7.

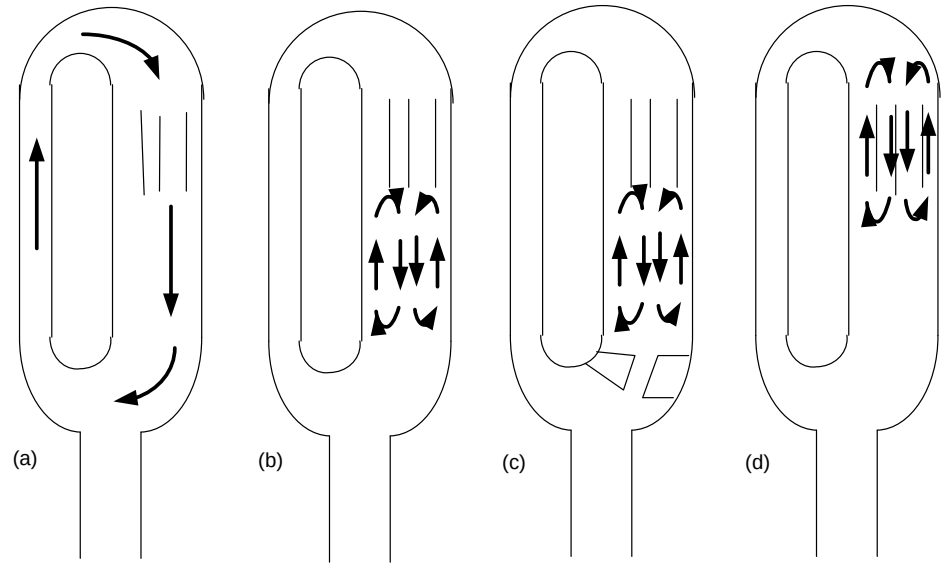

Figure 1-1: Types of streaming encountered in thermoacoustic systems. (a) Rayleigh streaming, (b) Gedeon streaming, (c) jet driven streaming, (d) inside stack/regenerator.[1]

2 Experimental and numerical methods

In this chapter, background on the experimental and the numerical methods employed during this research are presented. The experimental and the numerical techniques used in the research are described. The governing principles and the mathematical equations behind these techniques are explained. The experimental and the numerical procedures followed in the calculation of instantaneous acoustic and streaming velocities are also described in detail.

2.1 Experimental methodology

In the following subsections, details of the experimental setup and the procedures followed in obtaining instantaneous acoustic and streaming velocities using PIV are explained.

2.1.1 Particle Image Velocimetry

Particle Image Velocimetry is an optical technique for the measurement of flow velocity. The principle by which PIV operates is illustrated in Figure 2.1. Tracer or seeding particles are added to the flow. The particles (size and material) are selected to ensure good entrainment and minimal flow disturbance. The flow is illuminated at least twice within a short interval of time. Currently, lasers are widely used for flow illumination. The tracer particles scatter the incident laser light. The scattered light is recorded over one single frame or a sequence of frames using a digital camera. The flow velocity is obtained by analysis of the digital images. Each image is divided into small subareas, known as interrogation areas (IA). A typical interrogation area can range from 8×8 pixel^2 to 128×128 pixel^2. The displacement vector within each pair of interrogation areas is found by using statistical cross-correlation. It is assumed that all particles move homogeneously between the two IAs of an image pair. Finally, the global velocity of the

particles in each pair of IA is found by dividing the displacement vector and the time delay between two successive laser pulses, taking into account the image magnification factor. The magnification factor is defined as the ratio of the actual distance in the physical world and the distance in the image plane.

In fluid velocity measurements using PIV, no probe is required and thus PIV is minimally intrusive. But the flow needs to be seeded with small particles, which may change the flow field in some cases, if the particles are too large. The spatial resolution of PIV is on the order of 1 μm and TR-PIV allows a temporal resolution of up to several kHz [71]. Although the image resolution and temporal resolution are inversely proportional, higher resolution images can be captured by employing multiple cameras. A more detailed overview of PIV is available in the book of Raffel *et al*. [71].

2.1.2 Experimental setup

In the study presented in this dissertation, acoustic streaming was studied in an idealised thermoacoustic resonator. The acoustic streaming inside this standing wave resonator was studied using PIV. The experimental setup used in this study along with the PIV system is shown in Figure 2.2 and Figure 2.3. A schematic of the experimental setup is shown in Figure 2.4. The standing wave acoustic resonator walls were made of Plexiglas sheets of 9 mm thickness. The resonator had a square cross-section of 4×4 cm^2. The length of the resonator was 98 cm. A 100 W RMS loudspeaker (Max, model: Professional) with a DC coil resistance of 8 Ω excited acoustic standing waves within the resonator. A data acquisition system (model: Data Translation) was used, with both input and output channels. A built-in signal generator was used to generate sinusoidal signals which were then fed through the output channel to the power

amplifier. The data acquisition system was controlled using computer software, Measure Foundry (Data Translation). The amplified signal from the power amplifier (Audio Source, Amp 100) drove the loudspeaker. A power analyzer (Valhalla Scientific) was connected in parallel with the loudspeaker to monitor the instantaneous true RMS voltage, current and power fed to the loudspeaker. The acoustic pressure inside the resonator was measured using two pressure transducers (PCB, model: 102A07). These pressure transducers were mounted flush near the two extremities of the resonator, as shown in Figure 2.3.a. The pressure signal was fed to the signal conditioner (PCB, model: 480E09) and then recorded through the input channels of the data acquisition system. The PIV system (Dantec Dynamics) is also shown in Figure 2.2. The light source for the PIV system consisted of a dual cavity time-resolved Nd:YLF laser (Litron lasers, model: LDY 302) with a maximum repetition rate of 10 kHz per cavity. The light coming out of the laser had a wavelength of 528 nm, which is in the green portion of the spectrum. The light sheet optics (Dantec Dynamics) converted the laser beam into a diverging sheet with a diverging angle of 20°. The light sheet optics included a telescopic element through which the focal distance of light sheet was adjusted. The digital camera (NanoSense, model: MkIII) used for capturing PIV images had a CMOS sensor and a resolution of 1280×1024 pixels. The pixel pitch of the camera sensor was 12 μm. The frame rate of the camera was 1000 frames per second at full resolution. It was possible to achieve higher frame rates with reduced resolutions. The digital camera was used in conjunction with a micro lens (Nikon, model: Nikkor) with a focal length of 60 mm and a maximum aperture size of f/2.8. The camera was mounted on a 2D traverse mechanism, which allowed motion of the camera along the axial and the transverse axes of the resonator. A timing electronic circuit (Dantec Dynamics, model: 80N77) shown in Figure 2.3 was used for triggering and synchronising the laser and the camera. The camera and the laser

could be triggered internally using the PIV software, Dynamic Studio (Dantec Dynamics), or externally by providing a trigger signal to the timing circuit. A synchronisation unit, shown in Figure 2.2, was used to convert the pressure signal obtained from the pressure transducer located at the resonator hard end into the transistor-transistor logic, TTL trigger signal. The trigger signal generated by the synchronisation unit was used to synchronise the acoustic flow inside the resonator with the PIV system. A Laskin nozzle seeding generator, using mineral oil, produced 1 μm particles which were used for flow seeding. The temperature inside the resonator was recorded using a K-type thermocouple (Omega), which was attached to the inside wall of the resonator near the acoustic driver. Overall the room temperature was regulated in such a way that between the experiments the resonator temperature did not vary more than ± 1.0 °C. This was done to minimise the natural convection within the resonator.

2.1.3 Experimental procedures

The instantaneous and the cyclic time-averaged acoustic velocities inside a standing wave resonator were obtained using PIV. In this section the experimental procedures involved to obtain the velocity fields inside the standing wave tube are described.

Before starting velocity acquisition using PIV, the lasers were checked for beam overlap and power stability by following the protocol provided by the laser manufacturer. Both near field and far field beam overlap were performed by putting a ceramic plate first a few centimeters away from the laser assembly and then 2-3 m away. A power meter (Coherent, model: Energy Max) was used for making sure that both laser cavities were emitting similar power. A level meter was used to check the alignment of the light sheet, the resonator and the camera. The light sheet was

oriented in the XY plane according to the axis system shown in Figure 2.2. The axes of the resonator, the camera and the laser were along the X-, Y- and Z- axis respectively.

The resonator was excited by sending a sinusoidal signal to the acoustic driver. The acoustic pressure signal obtained from the pressure transducer located at the resonator hard end was recorded. The standing wave resonator system was always excited at one of its resonant modes, such that the pressure antinode occurred at the resonator hard end. The peak instantaneous acoustic velocity, u_a was calculated from the peak acoustic pressure, p_a value using the relation $u_a = p_a / \rho c$, where ρ and c are the density and the speed of sound. The knowledge of the excitation frequency, f_a and u_a provided an estimation of the velocity profile inside the resonator based on linear acoustic theory. Before starting velocity data acquisition, the chiller inside the laser control unit was turned on. The chiller was made to run idle for around 10-15 min until the temperature of the coolant became stable at 23 °C, as recommended by the laser manufacturer. The seeding particles were introduced into the resonator through an orifice located at the hard end of the resonator, as shown in Figure 2.3. A second orifice at the driver end was made in order to facilitate the cross flow of seeding particles inside the resonator. This was done to ensure a uniform seeding density inside the resonator. After closing both openings, the seeding particles were observed to make sure there was no leakage and to verify that, due to static charges, there was no bulk movement of the particles inside the resonator. It was observed that with time the seeding particles tend to deposit on the resonator wall, which reduced the transparency of the Plexiglas. This problem was solved by frequently washing the resonator inside walls with detergent. The water droplets left on the walls after drying the resonator were removed using a cotton towel. After each cleaning, when the seeding was introduced into the

channel, bulk movement of the seeding resulted making the seeding density non uniform inside the channel, even in the absence of any acoustic field. Similar problems were encountered by Thompson *et al*. [27] during their experiments. It was observed that static charge builds up during the drying process causing seeding particles to be attracted towards the resonator wall, which in turn causes bulk seeding movement. This problem of static charge was solved by applying anti-static polish (Novus Plastic Polish, Grade 1) on the inside walls of the resonator. Examples of uniform and non-uniform seeding densities are shown in Figure 2.5. After ensuring proper seeding density, PIV velocity data were recorded. The camera field of view was limited by image resolution and frame rate. The maximum length of the field of view employed in this study was 10 cm. In order to obtain velocities along the complete axial and transverse axes, the resonator was moved along the X and the Z axes while keeping the laser and the camera positions fixed.

2.1.4 Data acquisition

The velocity data acquisition through PIV was controlled by the PIV software Dynamic Studio. In this software different camera and laser parameters were given as input. The PIV data was captured in the single or the double frame mode. In the single frame mode, one image was captured each time a trigger signal was sent to the PIV system. The rate at which the PIV system was triggered, also known as the trigger rate, was entered as input to the software. This trigger rate can also be externally provided. In the case of the phase-locked velocity data acquisition method, the trigger rate was determined from the frequency of the pressure signals obtained from the pressure sensor located at the hard end of the resonator. In the double frame mode, two PIV images were captured for each trigger signal. The image captured during the first laser pulse was labeled as frame 1, and the one captured during the second laser pulse was labeled as frame 2.

The time delay between the two laser pulses was provided as an input. The value of the time delay was selected such that the seeding particles would have enough time to travel over a distance of few pixels within one IA. For example, for an interrogation region of $64 \times 64\,\text{pixel}^2$, the time delay between the two laser pulses was calculated based on the expected theoretical flow velocity in that IA and the required displacement of the seeding particles. The seeding particle displacement was chosen from a minimum of two pixels to a maximum of eight pixels. Generally, the maximum displacement of the seeding particles within an IA should be one quarter of its size [72, 73]. In the double frame mode, the exposure time for frame 1 was set to 20 μs, which was based on the time delay value between the two laser pulses and the combined maximum allowable exposure time of frame 1 and frame 2. The laser time delay cannot be less than the exposure time of frame 1, because then both laser flow illuminations would be captured in frame 1 only. The laser time delay cannot be more than the combined exposure time of the two frames, because then only one of the two laser flow illuminations would be captured. Velocity data was acquired after setting laser and camera parameters in Dynamic studio.

Two methods of velocity acquisition of oscillating flow were used: phase-locked, and time-resolved. The phase-locked system of capturing PIV data is generally employed for finding velocities of time dependent steady flow or pulsatile flow. Examples of such flows are acoustic standing wave [30], or blood flow through the heart [74]. For reconstructing an acoustic standing wave inside a resonator, the phase, $\theta = \omega T$, corresponding to the time period of one acoustic wave, T was divided into a number n of sub-phases as shown in Figure 2.6. At each specific sub-phase value, velocity was computed from the PIV data using ensemble-averaging. In the phase-locked ensemble-average method, a number m of velocity data was acquired at each individual sub-phase. These m velocity vector maps were ensemble-averaged for finding the

final velocity vector map at each individual sub-phase within an acoustic standing wave cycle. In this way a complete time history of the time dependent steady state flow can be retrieved from the individual time instants, known as sub-phases. The unsteady flow can be properly captured by employing TR-PIV. Through TR-PIV, a complete time history of the flow can be saved. Through post processing of the TR data, different frequency components and harmonics of the flow can be resolved. The sampling frequency of the TR data depends on the laser repetition rate, the camera frame rate and the required image resolution.

2.1.5 Image processing

The PIV images captured by the camera were transferred to the computer where they were post processed and analysed for obtaining the velocity vectors. Before starting the experiment, a set of calibration image were acquired. The calibration images stores the information regarding the magnification factor of the lens. Whenever the lens magnification was changed, another set of calibration images was recorded. The calibration images provided a relation between the two points in the actual setup, and on the camera sensor. This relation was used to calculate the correct velocity magnitudes. A sample of the calibration image and the calculation of magnification/scale factor in Dynamic studio are shown in Figure 2.7. After acquiring the calibration images, the PIV images of the flow were acquired. The image pre-processing steps followed are shown in Figure 2.9. The fluid domain shown in the images of Figure 2.9 is also shown in the schematic of Figure 2.8. The raw image acquired by the camera is shown in Figure 2.9.a. In acquiring the images, phase-locked ensemble-average method of data acquisition was used (unless stated otherwise). A total of m PIV images were captured. From these m images, an image consisting of minimum intensity was calculated as shown in Figure 2.9.b. This value of the minimum intensity was then subtracted from each image of the ensemble. The

resulting image with minimum intensity removed is shown in Figure 2.9.c. This process was done in order to remove background noise from the images and to increase the signal-to-noise ratio of the PIV cross-correlation peak. Due to the parallax effect, the motion of the seeding particles was sometimes observed inside the solid boundaries. This problem was solved by applying masks on the solid boundaries in the original raw images. Black masks were applied on solid boundaries. A mask was also applied on the solid objects within the flow domain. This was done to identify the fluid and solid regions. An image with mask applied is shown in Figure 2.9.d.

2.1.6 Velocity vector calculation

The velocities were calculated from the cross-correlation of the processed images. In Dynamic studio, a modified form of cross correlation known as the adaptive correlation was used. It is an iterative multi pass, multi grid interrogation scheme. Velocity vectors are calculated in an initial IA, of size N times larger than the final IA. The results for velocity vectors obtained from larger IA are used as information for the next IA of smaller size, until the final IA is reached. This method increases the dynamic spatial range, defined as the ratio of the largest observable length scale to the smallest observable length scale [75]. A detailed analysis of this velocity calculation scheme and its advantages is available in the literature [71]. Another parameter used in the velocity calculation was IA overlap. The percentage of overlap between the two adjacent IA and the size of the two IAs can be independently specified in both the horizontal and the vertical directions.

The velocities obtained after adaptive cross correlation were then validated in order to remove the outliers. Two velocity vector validation methods were used simultaneously namely, the peak

height validation and the local neighbourhood validation. In the peak validation method, a minimum value was specified for the ratio of the height of the first and the second peak in the correlation plane. For high quality data, the peak height ratio should be higher than unity. A minimum peak height ratio of 1.15 was used as per the guidelines provided in the Dynamic studio user guide. The velocity vectors for which the peak height ratio was less than 1.15 were substituted by zero. The peak height validation method was able to identify invalid vectors. But the local moving average validation method was used for the estimation of the substitute vectors. In this method, a neighbourhood velocity vector area of 3×3 was specified and the outliers or spurious vectors were identified based on an acceptance factor. A typical value of acceptance factor used was 0.12-0.15, as specified in the user manual of Dynamic studio. Each element of the 3×3 velocity matrix was compared with the average of the velocity matrix. In this velocity vector matrix if a spurious velocity vector was identified, it was substituted by averaging the velocities in the 3×3 velocity vector matrix. Following validation, the final velocity vector map was obtained for each pair of PIV image. One such individual velocity vector map obtained in Dynamic studio is shown in Figure 2.10.a. The velocity vector map corresponds to the PIV image of Figure 2.9. In the ensemble-average method, the final velocity vector map was obtained by averaging the individual velocity maps. The result is shown in Figure 2.10.b. Further post processing was done by applying a mask on the velocity vector, (similar to that of Figure 2.9.d) as shown in Figure 2.11.a. It was also possible to perform further analysis of the velocity vector map. The vorticity of the flow field was calculated using Dynamic studio; the results are shown in Figure 2.11.b.

2.1.7 Acoustic streaming velocity calculation

Acoustic streaming is a second order steady flow superimposed over the first order acoustic oscillating flow. Experimentally, streaming flows can be captured by the PIV either by capturing the phase-locked ensemble-averaged velocity data or by averaging the TR data over integer number of acoustic cycle. In the present study, the phase-locked ensemble-averaging was used for the experimental estimation of the streaming velocities. Simultaneous measurements of the instantaneous and the streaming velocities were performed using the synchronised PIV technique [30]. As shown in Figure 2.12, the PIV image pairs were captured at a fixed phase within each acoustic cycle. The instantaneous acoustic velocity was obtained from a cross-correlation between the images at time instants t1 and t2. The images at time instants t2 and t3 correspond to the same phase, but different acoustic cycles. After applying cross-correlation between these images, the resultant was the streaming velocity. As mentioned before, the PIV image pairs were captured at a fixed phase within each acoustic cycle and the time delay between the two images (t2-t1) equals the time delay between the two laser pulses. For performing the cross correlation between the two images separated by a time duration equivalent to acoustic time period (t3-t2), the following steps were taken in Dynamic studio. One single frame was extracted from the double frame images (these image pairs had a time delay of t2-t1 in between them) captured at each acoustic cycle and then again double frames were formed from these extracted single frames. These newly created double frame image pairs had a time delay of t3-t2 in between them. In this way, the streaming velocity was calculated for N number of consecutive acoustic cycles and then finally the average streaming velocity was calculated by finding the average of the ensemble.

2.1.8 Error and uncertainty analysis

In order to make a comparison between the experimental, the numerical and the theoretical results, mean error percentage was calculated. The mean error percentage, e_{v} was calculated using the equation given below

$$e_{\mathrm{v}}(\%) = \frac{1}{N}\sum_{i=1}^{N}\left|\frac{\mathrm{V}_{th} - \mathrm{V}_{ex,num}}{\mathrm{V}_{th}}\right| \times 100,$$

where N denotes total number of data points at which the absolute value of difference was calculated between the theoretical velocity, V_{th} and the experimental or the numerical velocity, $\mathrm{V}_{ex,num}$.

The instantaneous acoustic and the time averaged streaming velocities were obtained experimentally using PIV. The uncertainty in the velocity determination was due to the accuracy of the PIV system. The uncertainty in the velocity as a result of the PIV processing was calculated in a manner similar to [76, 77]. In the calculation of velocity using the PIV, the particle displacement is determined by the cross correlation of image intensity of the two PIV images and the time is determined by the delay between the two laser pulses. The overall uncertainty in velocity determination is the sum of the uncertainties in the particle displacement and the time between the pulses. According to laser manufacturer, the uncertainty in the laser pulse timing even when accounting for delay generator does not exceed 10 ns. A constant pulse delay was used in each experiment. The minimum pulse delay used was 180 μs, therefore the overall uncertainty in pulse delay determination is of the order of 0.005 %, which is negligible. The uncertainty in the estimation of the particle displacement was determined by the ratio of the

correlation peak width and the average displacement of the seeding particle in the interrogation area. The peak position within the correlation plane can be determined within an accuracy of 0.1 pixels, for a particle image of 1-2 pixels. The interrogation area size used in this study was 64×64 pixels with 50% overlap. The maximum allowable particle displacement was one-quarter of the interrogation area. Therefore, the uncertainty in the estimation of the particle displacement was of the order of 0.3%. The overall uncertainty in the estimation of velocity using PIV was of the order of 0.3 %.

2.2 Numerical methods

The Lattice Boltzmann Method (LBM) is a numerical technique which is simple to implement. For low Mach numbers, LBM is faster than Navier-Stokes based Direct Numerical Simulation (DNS). The LBM code is very stable, can be easily parallelized and due to its straight forward implementation it is considered as a successful alternate numerical technique [46]. In LBM, complex geometries can be easily incorporated inside the flow regime.

2.2.1 Mathematical background

The mathematical treatment of the LBM described below follows the work of He *et al.* [78]. To describe a system statistically, the distribution function $f\left(\hat{r},\hat{u},t\right)$ is used, which denotes the probable number of particles at a time t positioned between $\hat{r}$ and $\hat{r}+d\hat{r}$ and have velocities between $\hat{u}$ and $\hat{u}+d\hat{u}$. The space consisting of the coordinates $\left(\hat{r},\hat{u}\right)$ is called the *phase space*.

Consider a particle at a position, $\hat{r}$ with a velocity, $\hat{u}$ and at a time instant, t. If there were no intermolecular collisions, unimolecular reactions, radiative transitions and so on, then this molecule would move in time duration $t+dt$ to a position $\hat{r}+\hat{u}\,dt$ and its velocity would be

$\hat{u} + \hat{\mathrm{f}}dt$, where $\hat{\mathrm{f}}$ is the external force on molecules per unit mass of a molecule. Therefore, in case of no collision, the number of molecules before applying the external force would be equal to the number of molecules after disturbance

$$f\left(\hat{r},\hat{u},t\right)d\hat{r}\,d\hat{u} = f\left(\hat{r}+\hat{u}dt, u+\hat{\mathrm{f}}dt, t+dt\right)d\hat{r}\,d\hat{u}\,. \qquad (1)$$

However, if collision takes place between the molecules, there will be a net difference between the numbers of molecules in the interval $d\hat{r}\,d\hat{u}$. The rate of change between the final and the initial status of the distribution function is called the collision operator, Ω. Now, equation (1) can be written as

$$f\left(\hat{r}+\hat{u}dt, \hat{u}+\hat{\mathrm{f}}dt, t+dt\right)d\hat{r}\,d\hat{u} - f\left(\hat{r},\hat{u},t\right)d\hat{r}\,d\hat{u} = \Omega\left(f\right)d\hat{r}\,d\hat{u}\,dt\,. \qquad (2)$$

Dividing equation (2) by $d\hat{r}\,d\hat{u}\,dt$ and passing to the limit $dt \to 0$, yielded

$$\frac{df}{dt} = \Omega\left(f\right). \qquad (3)$$

The above equation (3) states that the total rate of change of the distribution function is equal to the rate of collision. The above equation is called the Boltzmann transport equation. Since f is a function of $\hat{r}$, $\hat{u}$ and t, the total rate of change can be given by

$$df = \frac{\partial f}{\partial \hat{r}}d\hat{r} + \frac{\partial f}{\partial \hat{u}}d\hat{u} + \frac{\partial f}{\partial t}dt\,. \qquad (4)$$

Dividing the above equation by dt yielded

$$\frac{df}{dt} = \frac{\partial f}{\partial \hat{r}}\hat{u} + \frac{\partial f}{\partial \hat{u}}\hat{a} + \frac{\partial f}{\partial t}, \qquad (5)$$

where, $\hat{u} = \frac{d\hat{r}}{dt}$, $\hat{a} = \frac{d\hat{u}}{dt} = \hat{\mathrm{f}}$, and $\hat{\mathrm{f}}$ is the force per unit mass of the molecule. Finally, the Boltzmann equation was written as,

$$\frac{\partial f}{\partial t} + \hat{u} \cdot \frac{\partial f}{\partial \hat{r}} + \hat{\mathrm{f}} \cdot \frac{\partial f}{\partial \hat{u}} = \Omega . \tag{6}$$

In order to solve the Boltzmann equation (6), the collision operator, Ω needed to be defined. A simple model for the collision operator was given by Bhatnagar *et al*. [79], known as Bhatnagar-Gross-Krook (BGK) model. The collision operator therefore was replaced by

$$\Omega = \frac{1}{\tau}\left(f^{eq} - f \right), \tag{7}$$

where, $\frac{1}{\tau}$ is the collision frequency and τ is the relaxation time. By introducing BGK approximation in the Boltzmann equation, following equation was obtained

$$\frac{\partial f}{\partial t} + \hat{u} \cdot \frac{\partial f}{\partial \hat{r}} + \hat{\mathrm{f}} \cdot \frac{\partial f}{\partial \hat{u}} = \frac{1}{\tau}\left(f^{eq} - f \right). \tag{8}$$

The local equilibrium distribution function, was given by f^{eq}, which was Maxwell-Boltzmann distribution function. The Maxwell-Boltzmann velocity distribution function was given by

$$f^{eq}\left(\hat{u}\right) = \frac{\rho}{\left(2\pi RT\right)^{D/2}} \exp\left(\frac{-\left(\hat{u} - \hat{v}\right)^2}{2RT} \right), \tag{9}$$

where, R is the ideal gas constant and D is the dimension of the space. The relation between the above equation (8) and the macroscopic quantities, such as fluid density ρ, fluid velocity vector v, and internal energy e, was given by

$$\rho\left(\hat{r},t\right) = \int m f\left(\hat{r},\hat{u},t\right) d\hat{u} , \tag{10}$$

$$\rho(\hat{r},t)\hat{v}(\hat{r},t) = \int m\hat{u}f(\hat{r},\hat{u},t)d\hat{u} \text{ , and} \tag{11}$$

$$\rho(\hat{r},t)e(\hat{r},t) = \frac{1}{2}\int m\hat{v}_a^2 f(\hat{r},\hat{u},t)d\hat{u} . \tag{12}$$

In those equations, m was the molecular mass, $\hat{v}_a$ was the particle velocity relative to fluid velocity, $\hat{v}_a = \hat{u} - \hat{v}$ and $e = 3/2mk\mathrm{T}$. Equations (10), (11) and (12) represented the conservation of mass, momentum and energy.

In LBM, equation (8) is discretized and assumed to be valid along specific directions (lattice). Above equation (8) was written in discretized form as follows

$$f_i(r + u_i\Delta t, t + \Delta t) - f_i(r,t) = \frac{\Delta t}{\tau}\left[f_i^{eq}(r,t) - f_i(r,t)\right]. \tag{13}$$

In the above equation (13), the left hand side (L.H.S) represents the propagation, streaming or moving, step where the momentum was transferred between the lattice points. The right hand side (R.H.S) of equation (13) represents the relaxation (collision) process, which determines the viscous properties of the fluid. For an isothermal incompressible fluid flow, f_i^{eq} was obtained by applying low Mach number expansion to Maxwell-Boltzmann distribution function [78]. The Lattice Boltzmann equation resembles Navier-Stokes equations for incompressible flow for low Mach number, M. The lattice used in PowerFLOW for the 2D and 3D simulation cases is shown in Figure 2.13.

2.2.2 Simulation case setup in PowerFLOW

A commercial Lattice Boltzmann solver, PowerFLOW (EXA Corp: version 4.3) was used for the numerical simulations. PowerFLOW consists of many packages. In this study, all the simulation

preparation and case setup was done in PowerCASE. Actual simulations were performed in PowerFLOW and for simulation analysis and for post processing the results, PowerVIZ was used. PowerCASE and PowerVIZ are packages within the PowerFLOW. In the numerical study presented here, acoustic streaming was studied in an empty resonator and in a resonator with spoiler. In the following sections, the numerical setup of these two set of cases in the PowerFLOW would be described.

2.2.3 Geometry and variable resolution region

The acoustic streaming was simulated in a square cross section standing wave resonator. The numerical simulations were performed both in two-dimensional, 2D and three-dimensional, 3D domain. Figure 2.14 shows a 2D schematic for the two set of cases; an empty resonator and a resonator with a spoiler. The origin of the spoiler was located at the symmetry plane. The 3D geometry of the square cross section resonator was created in PowerCASE. The length of the resonator, L was equal to one-half wavelength. For example, when simulating standing wave of 824.25 Hz, the channel length was 0.21 m. The width, H of the resonator was 0.01 m. The computational domain consisted of the entire channel area, $L \times H$.

The entire computational domain was divided into several variable resolution (VR) regions. This was done in order to resolve the flow structures in sufficient detail in regions of high shear along with managing the computational resources. The concept of VR regions in PowerFLOW is similar to grid-stretching techniques used in Navier-Stokes based CFD. Each grid cell is known as voxel in fluid domain and surfel if it lies on the solid surface. Finer resolution voxels were placed in those regions where velocity gradients were higher. Acoustic standing wave in a resonator is an internal flow similar to pipe flow in the sense that higher velocity gradients were

located in the acoustic boundary layer region close to the inner walls of the resonator. Therefore, the finest resolution voxels were located in the acoustic boundary layer and coarser resolution voxels were located away from the wall towards the center of the channel. The voxels were always square for 2D simulations and cubic for 3D simulations. The size of each voxel, Lv in a coarser level was two times the size of each voxel in the previous finer level. Each VR region had voxels of same size. Thus, VR regions close to the wall had finer voxels and VR regions away from the wall had coarser voxels. Three level of VR regions were used, as shown in Figure 2.15. For those cases where simulations were performed in an empty resonator, the finest resolution VR region, located next to the resonator wall had a width equal to the acoustic boundary layer or viscous penetration depth, δ_ν . Throughout this dissertation, acoustic boundary layer and viscous penetration depth were considered equivalent and would be used interchangeably. The second level VR region had a width equal to twice the first level VR region and the third level VR region consisted of rest of the simulation domain. Similarly, for the cases with spoiler, finest resolution VR regions were located in the acoustic boundary layer at the resonator and the spoiler wall and coarser resolution VR regions were away from the solid boundaries.

2.2.4 Operating conditions and parameters

The simulation parameters were provided to PowerFLOW which helped it to decide which solver to use for simulation. The simulation parameters were: the simulation model, if it was 2D or 3D; the flow, if it was internal or external, which in present case was internal; isothermal fluid; ideal gas and compressible fluid. In PowerFLOW, certain parameters were specified as characteristic parameters. Characteristic parameters helped in establishing a dynamic range for

the parameters like velocity, pressure etc. within which flow can be reliably simulated [61]. The characteristic parameters used in the simulations presented here are given in Table 2-1. The atmospheric pressure was selected as the characteristic pressure, p_{char}. It was used in the calculation of the characteristic density, ρ_{char}. The peak instantaneous acoustic velocity amplitude was selected as the characteristic velocity, V_{char}, for each case. The values of the characteristic temperature, T_{char} and the characteristic viscosity, ν_{char} for all the cases was kept same. The characteristic length, L_{char} was equal to the acoustic boundary layer thickness (viscous penetration depth). The Reynolds number and the Mach number for the simulation were calculated based on these characteristic parameters.

The resolution, Res, parameter in PowerFLOW specifies the number of voxels within the characteristic length. In all the simulations the value of resolution was chosen as 12. There were 12 voxels (grid points) in the viscous penetration depth. For simulations with acoustic excitation frequency, f_a of 824.25 Hz, the value of δ_ν was 2.16e-4 m and the size of voxels in viscous penetration depth was 1.8e-5 m. This value of resolution was selected after considering the necessity of resolving the acoustic boundary layer flow and the computation time. Since the flow was laminar, 12 grid points were sufficient in resolving the flow velocity variations in the acoustic boundary layer. The VR region and the resolution parameters determined the overall number of voxels in the simulation domain. The total number of voxels for the cases without spoiler was around 1.2 million and with the spoiler the total number of voxels was around 2.2 million. The simulations were performed at Mach number same as experimental Mach number. In this setting acoustic waves propagated at the same rate relative to the main flow as in experiments [61].

The flow variables were simulated at discrete time intervals, known as timesteps, ts. In PowerFLOW, the value of timestep was calculated using the characteristic parameters and a constant, K (=0.0288 s/m) by the following equation

$$ts = \frac{K}{\sqrt{T_{char}} \times \mathrm{Re}\, s / L_{char}}. \qquad (14)$$

The value of timestep for the excitation frequency of 824.25 Hz was 3.004e-8 s. The simulations were evolved for 300 acoustic cycles, which was found sufficient for the standing wave flow inside the resonator to reach steady state. Initially, a simulation was evolved for the case of empty resonator over 100, 150, 200, 250 and 300 acoustic cycles and the value of peak acoustic velocity was observed. It was observed that after the simulation had evolved for 200 acoustic cycles, the difference between the peak acoustic amplitude of two adjacent acoustic cycles was less than 0.001 m/s and after 250 acoustic cycles it was less than 0.0001 m/s.

2.2.5 Initial conditions and boundary conditions

The initial conditions were used to specify the initial state of the flow variables in the simulation domain. The initial pressure was equal to the characteristic pressure and the fluid was in a quiescent state. Two types of boundary conditions (BC) were used namely, the wall boundary conditions and the driving boundary conditions. The wall boundary conditions were used for those surfaces which were solid and through which fluid cannot pass. All the walls were assigned no slip boundary condition. In PowerFLOW, the bounce back rule was used to model solid walls, obstacles etc. In the bounce back rule the incoming distribution functions at the wall boundary were reflected back in the fluid domain with directions rotated by π radians. In one of the implementation of bounce back rule, the wall fluid interface was moved halfway between the

wall and fluid lattice nodes [80]. The bounce back rule ensures conservation of mass and momentum at the boundary. According to the schematics shown in Figure 2.14, the wall boundary condition was assigned to those faces of the resonator geometry which were parallel to the X-axis and had a dimension of $L \times H$ and the resonator end face which was perpendicular to the X-axis, and had a dimension of $H \times H$ and was away from the origin. The spoiler was also assigned wall boundary conditions.

The driving boundary conditions were prescribed at the inlet face, which was perpendicular to the X-axis and was located at origin as shown in Figure 2.14. The driving BC, forces the flow field to behave in accordance with the constraints put on pressure, velocity, mass flux or mass flow [61]. The mathematical implementation of driving boundary condition in PowerFLOW can be seen in the works of Zou *et al.* [81]. In all the simulations presented in this study, the static pressure was imposed as the driving BC at the inlet face. The static pressure was defined as the sum of the characteristic pressure and the time dependent sinusoidal acoustic pressure, $p_a \sin\left(2\pi f_a t\right)$. The direction of flow at the inlet face was also specified. With respect to the origin system shown in Figure 2.14, the flow direction was towards +X axis when $\sin\left(2\pi f_a t\right)$ was positive and towards -X axis when $\sin\left(2\pi f_a t\right)$ was negative. The velocity of the flow was allowed to take any value as the fluid responded. A pressure antinode occurred at the two ends of the channel, while a pressure node occurred in the center of the channel. The acoustic particle velocity distribution was similar to that of the pressure with the location of nodes and antinodes interchanged. In order to observe the transient nature of the simulation results, virtual probes were located at the node and the antinode locations of the acoustic pressure and acoustic velocity as shown in Figure 2.14.a. Four probes were also located on each side of the flat spoiler edges as

shown in Figure 2.14.b. The distance between each probe was equal to the peak instantaneous acoustic displacement, x_a.

2.2.6 Measurement window parameters

The measurement window setup defines the way in which the data is collected and stored in the PowerFLOW. Only those fluid and surface parameters which were specified in measurement windows were collected. The total number of timesteps in an acoustic cycle can be found by dividing one acoustic cycle time period and the physical time value corresponding to a timestep. For an excitation frequency of 824.25 Hz and a timestep value of 3.004e-8 s, the total number of timesteps within one acoustic cycle was 4.0e5. Although during simulation the flow variables were calculated at each timestep and voxel, only 1000 data points were collected within each acoustic cycle. This meant that each data point was recorded after every 40 timesteps. Data recording was done for 30 acoustic cycles after simulation had already evolved for 270 acoustic cycles.

After setting up a case in PowerCASE, the simulation was performed in three steps namely, discretization, decomposition and simulation. During discretization, the continuous geometry of a case was discretized in voxels (fluid elements) and surfels (surface elements). During decomposition, a case was partitioned for simulation over a cluster of computers. After decomposition, simulation starts. A typical 2D simulation was evolved on 64 cores for 40 hours and a 3D simulation was evolved on 128 cores for 198 hours.

2.2.7 Post processing of simulation data

The instantaneous acoustic velocity data available from the simulations was time averaged over an integer number of acoustic cycles for finding the streaming velocities as shown in the following equation

$$V_{st} = \frac{1}{jT}\int_0^{jT} V_{ac} \cdot dt\,, \quad (15)$$

where V_{st} is the overall streaming velocity, V_{ac} is the overall acoustic velocity, j is the integer number of acoustic cycles and T is the time period of an acoustic cycle. In the results presented in this study, n was 30.

The simulation results were obtained in the form of measurement files. These measurement files were analysed and visualised in PowerVIZ. For example, flow derivatives like vorticity were calculated using PowerVIZ.

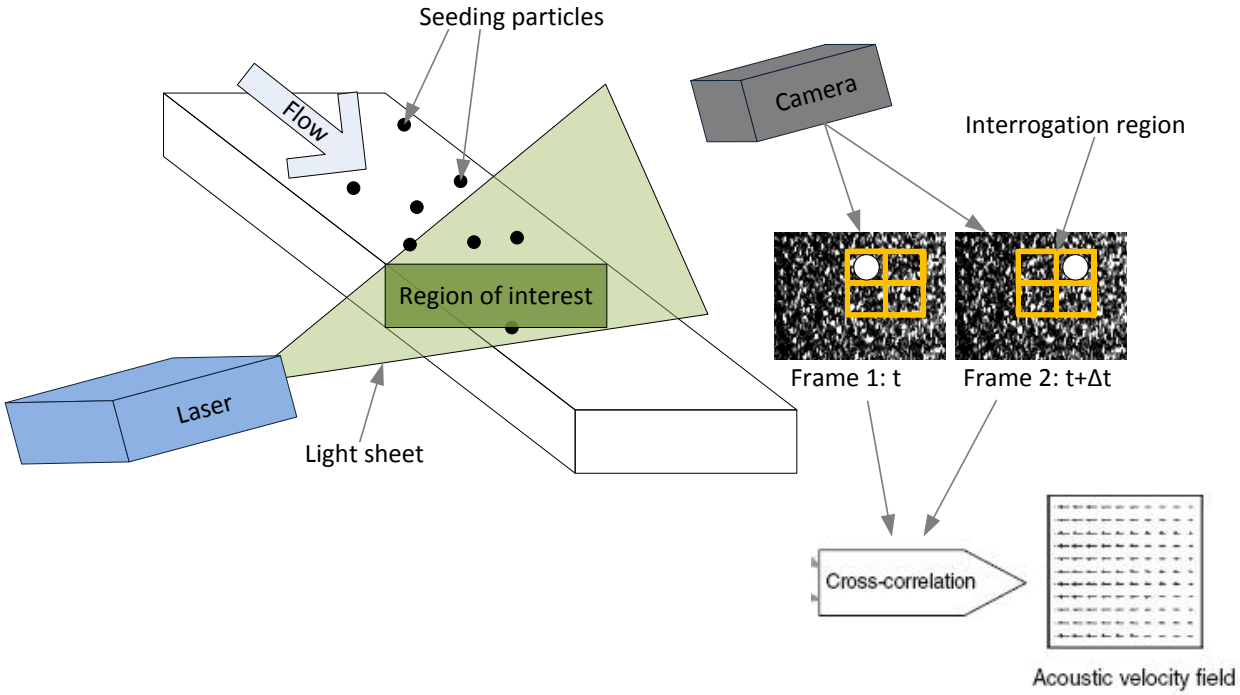

Figure 2.1 Illustration of the basic PIV principles.

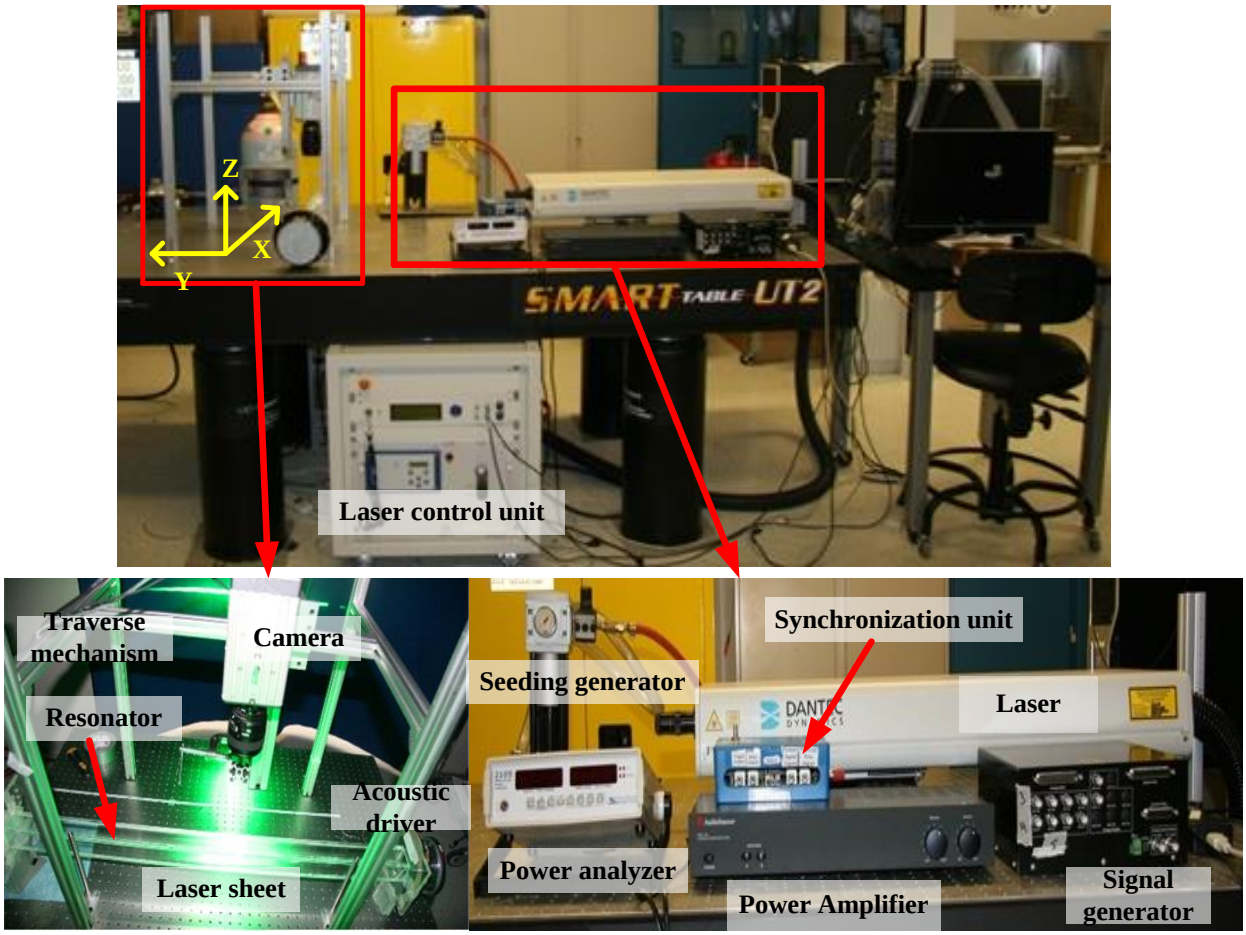

Figure 2.2 Photographs of the experimental apparatus.

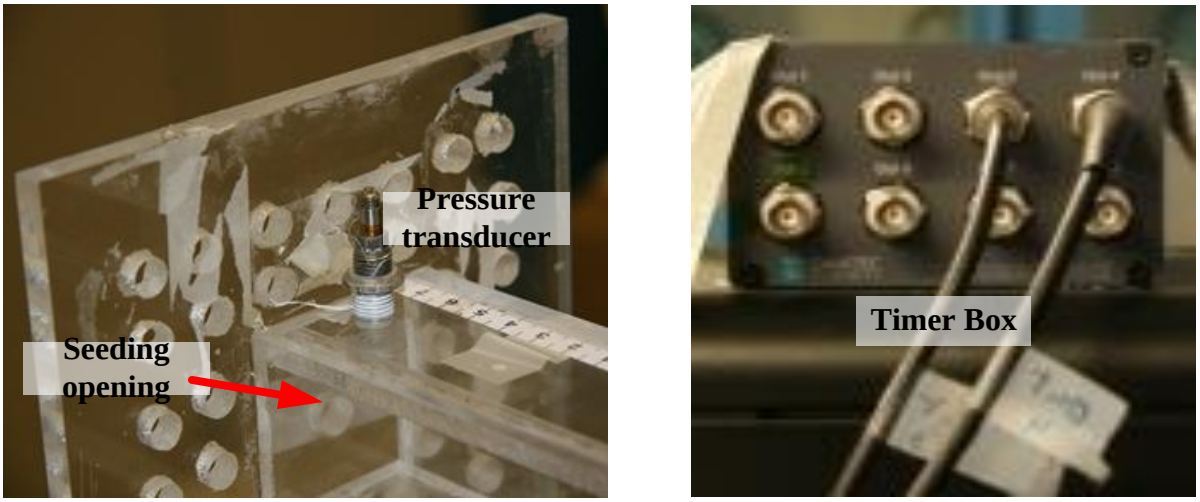

(a) (b)

Figure 2.3 Pressure transducer and timer box used for synchronizing laser and camera.

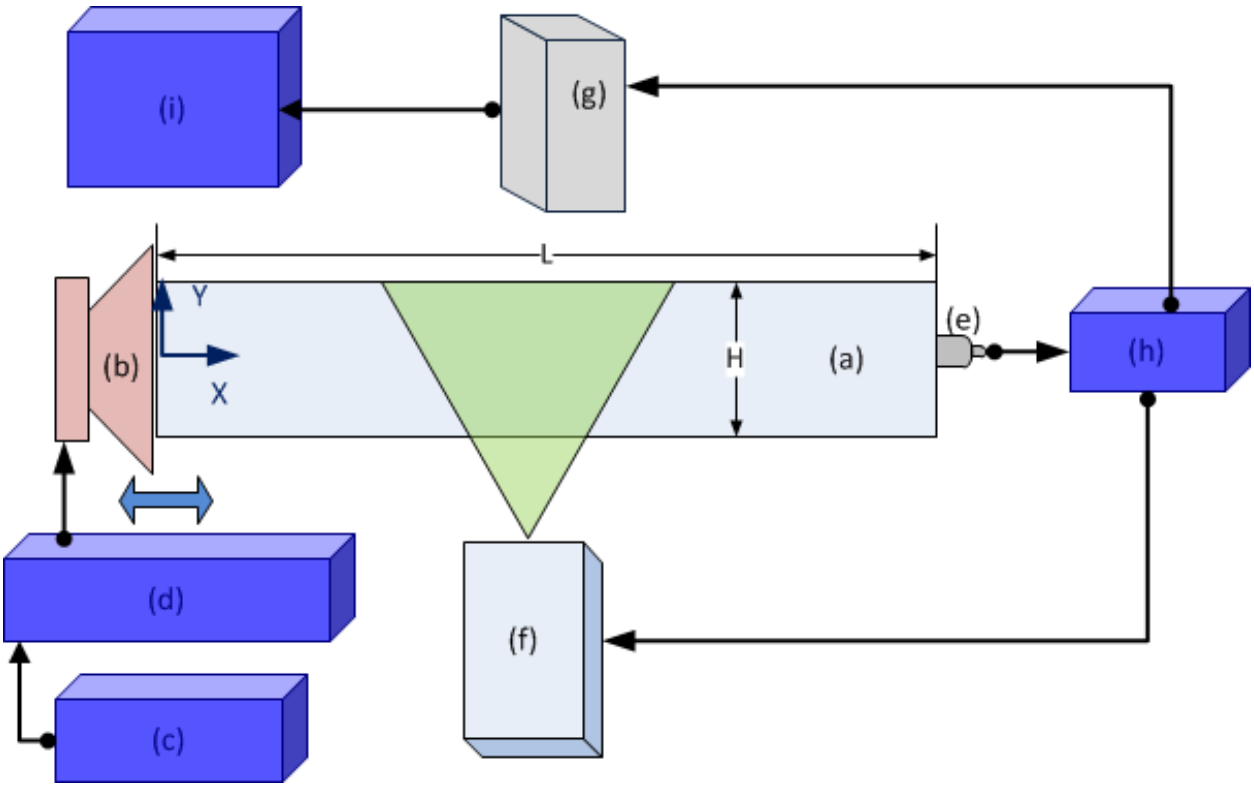

Figure 2.4 Schematic of the experimental setup: (a) resonator tube; (b) acoustic driver; (c) function generator; (d) power amplifier; (e) pressure transducer; (f) laser; (g) CCD camera; (h) synchronization unit; and (i) computer with frame grabber.

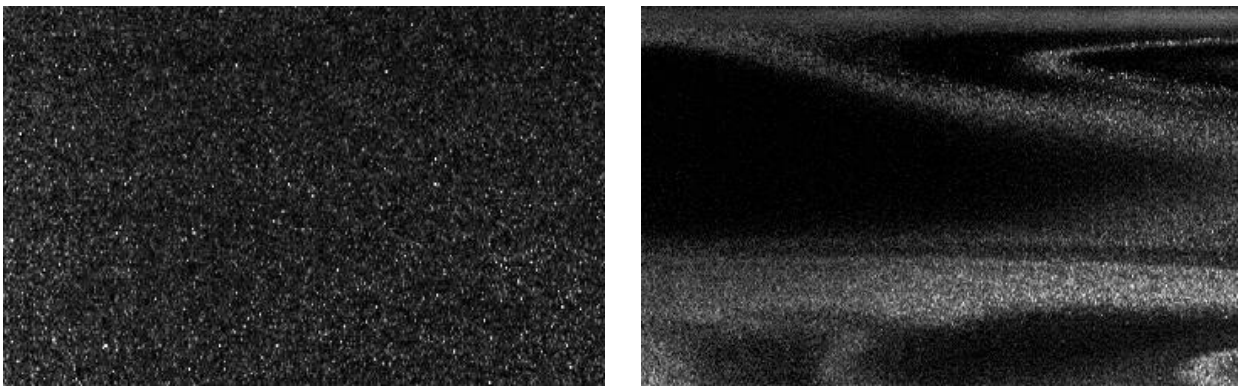

(a) (b)

Figure 2.5 PIV raw image: (a) uniform seeding density, and (b) non uniform seeding density.

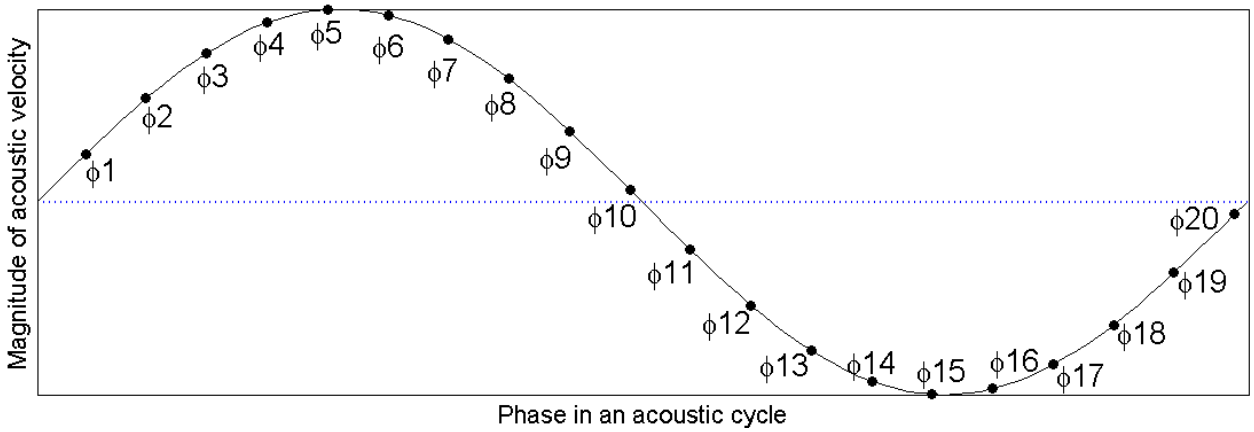

Figure 2.6 Illustration of the 20 phases at which phase-locked velocity data was acquired.

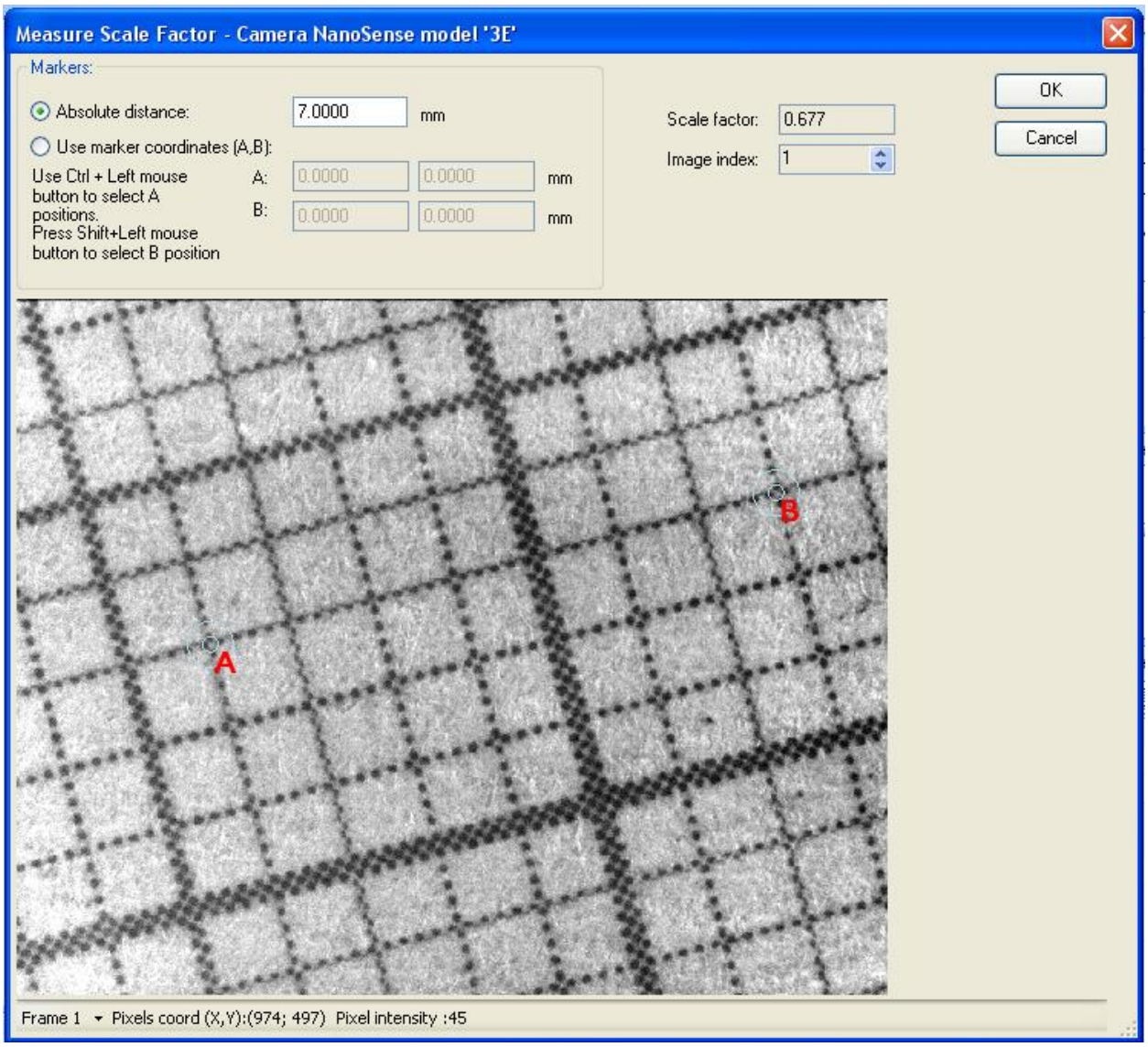

Figure 2.7 Calculation of magnification factor in Dynamic studio.

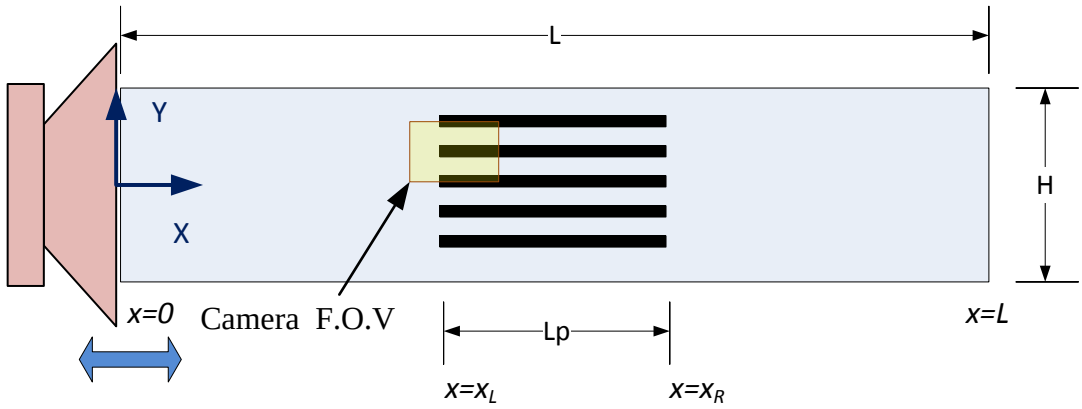

Figure 2.8 Camera field of view for the images shown in Figure 2.9.

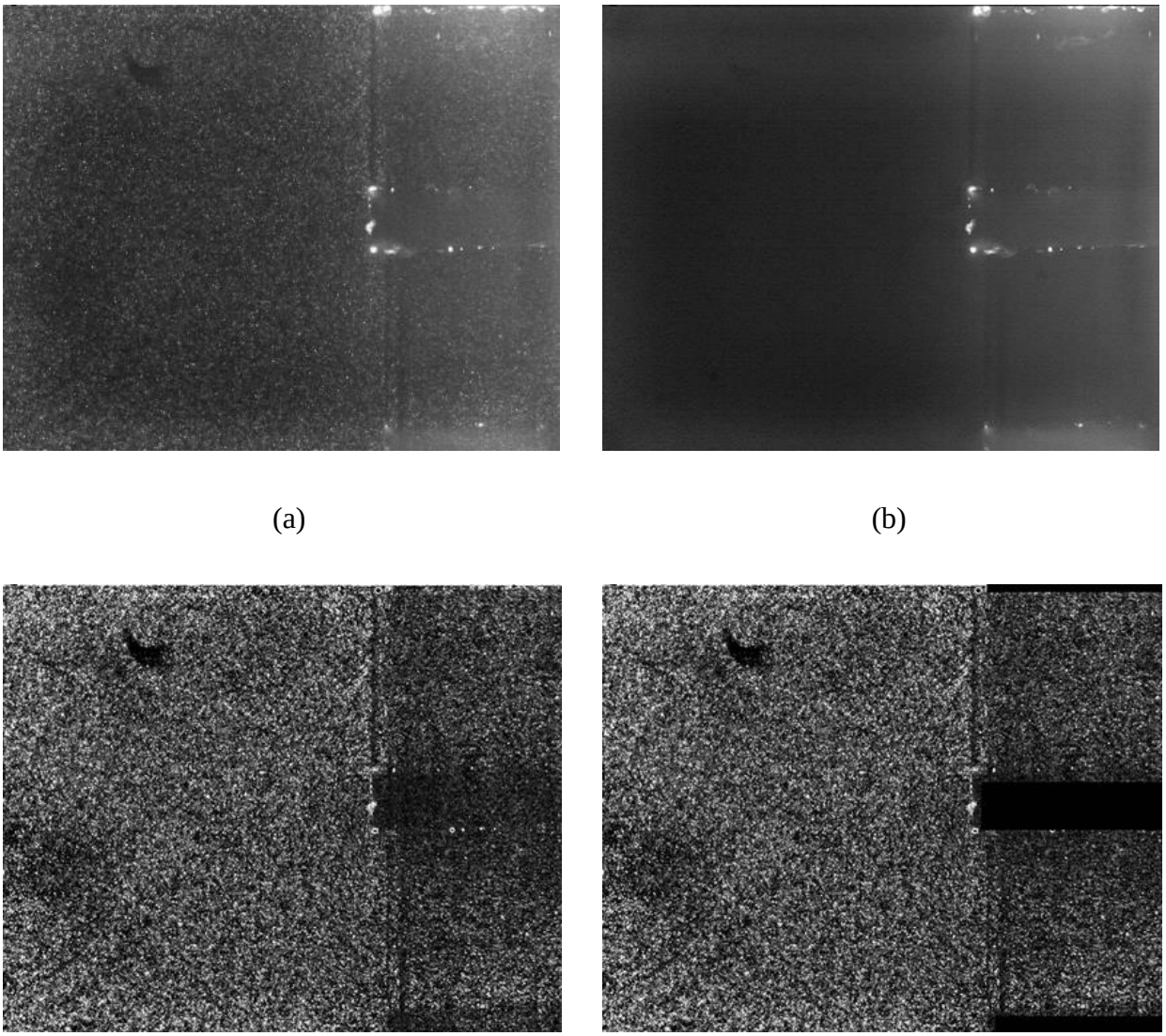

(a) (b)

(c) (d)

Figure 2.9 Image processing steps during the PIV velocity calculation in Dynamic studio. (a) Raw image, (b) Image of minimum intensity, (c) Image with minimum intensity removed, and (d) Mask applied to solid objects.

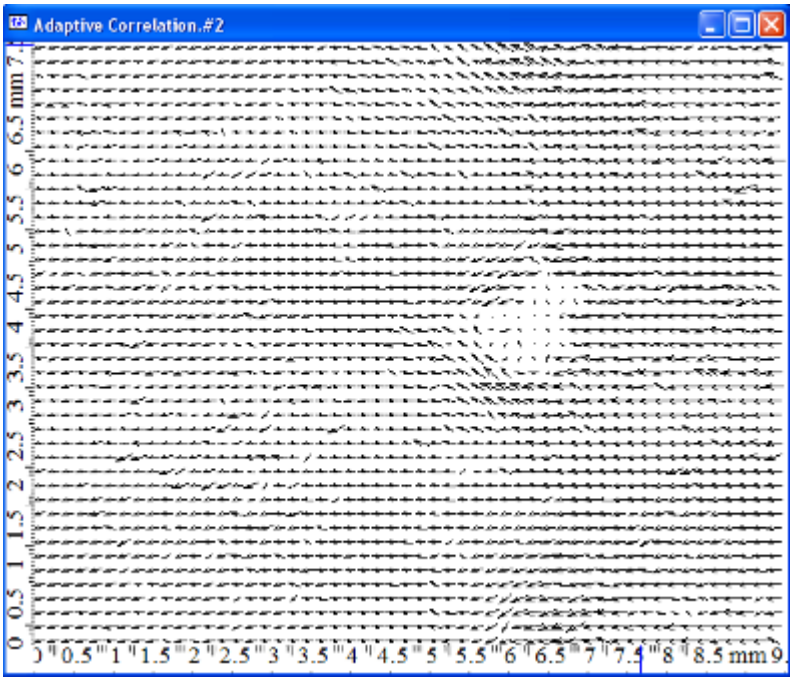

(a)

(b)

Figure 2.10 Instantaneous acoustic velocity vector calculation in Dynamic studio: (a) individual velocity vector map; and (b) ensemble-averaged velocity map.

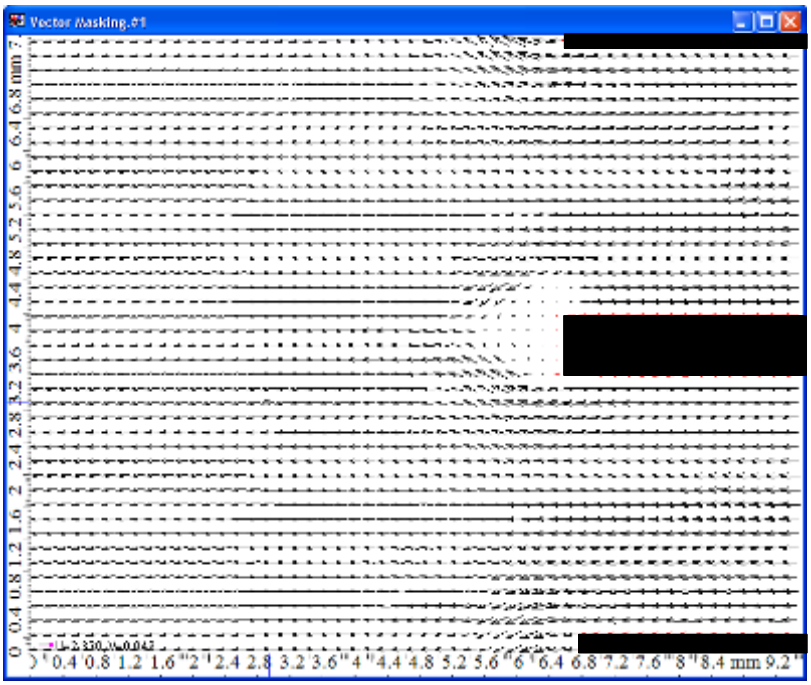

(a)

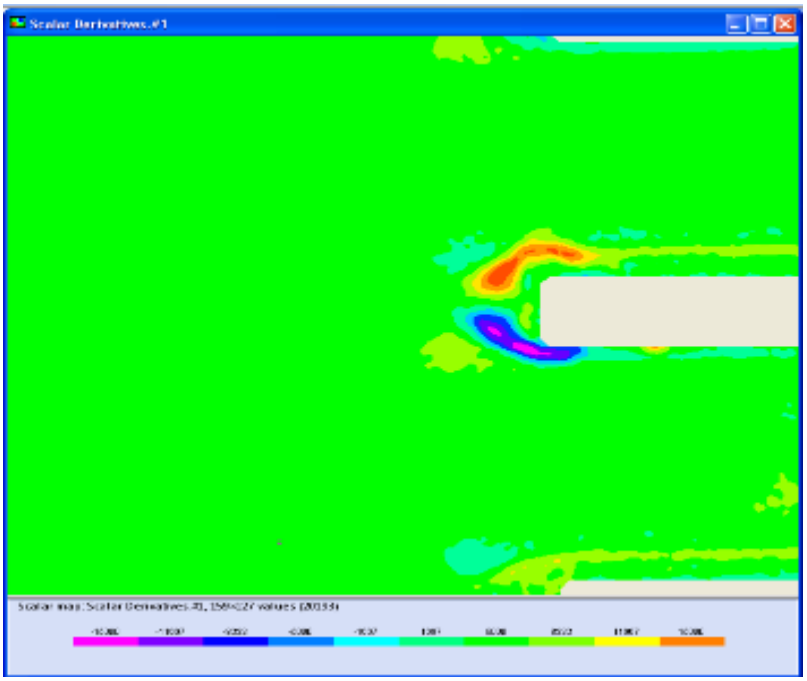

(b)

Figure 2.11 Post processing of the instantaneous acoustic velocity vectors in Dynamic studio. (a) Vector masking. (b) Vorticity calculation.

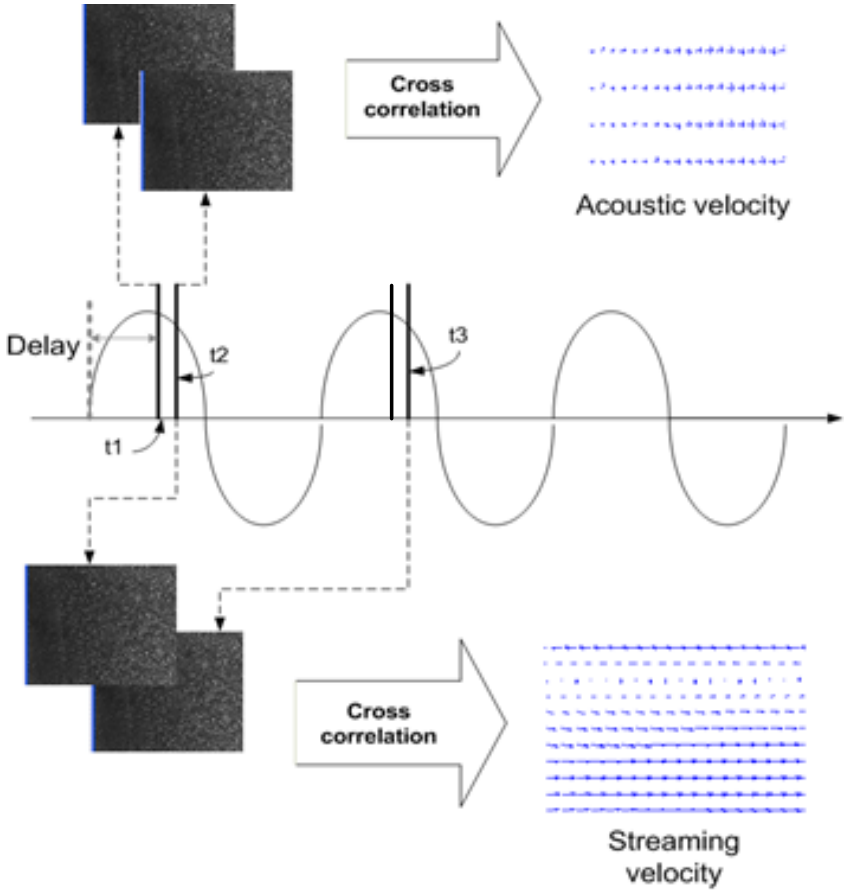

Figure 2.12 Data processing for obtaining the instantaneous acoustic and the streaming velocities.

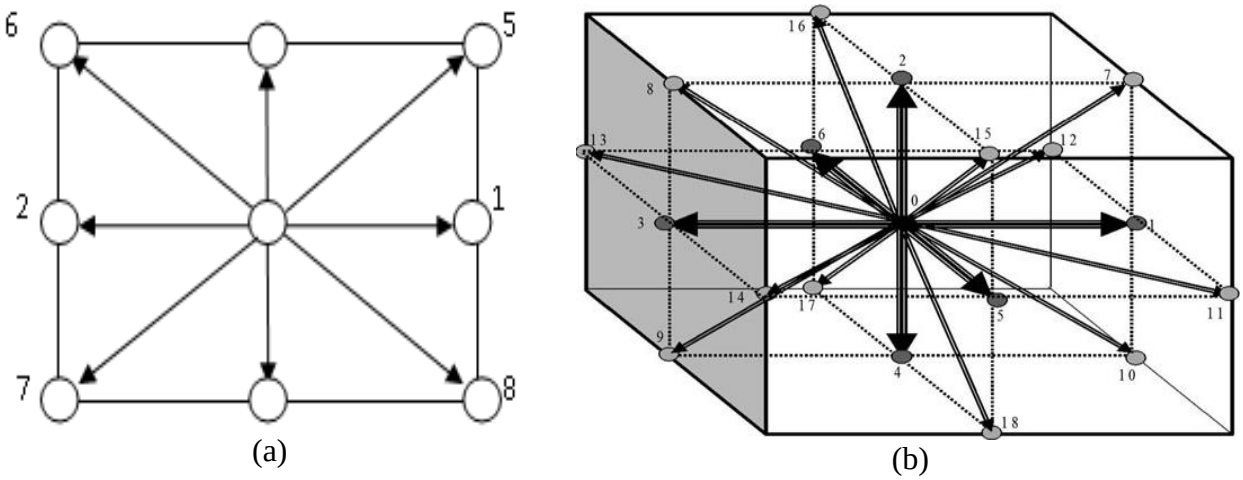

(a) (b)

Figure 2.13 Lattice arrangement in the PowerFLOW. (a) D2Q9, and (b) D3Q19

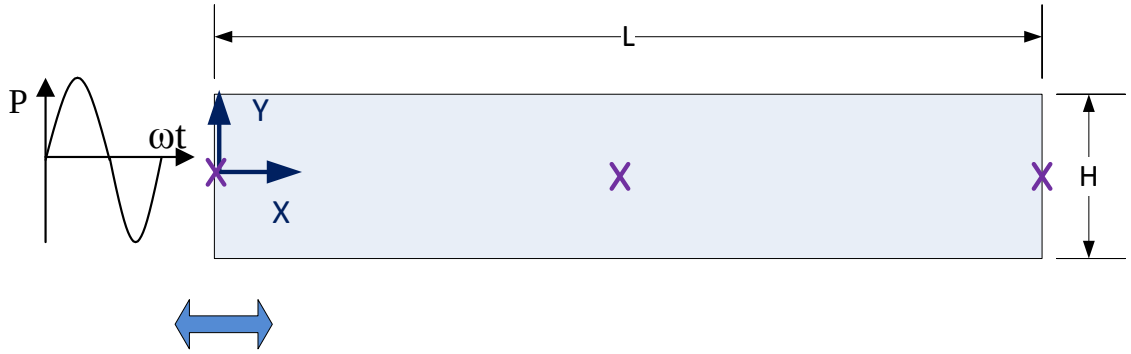

(a)

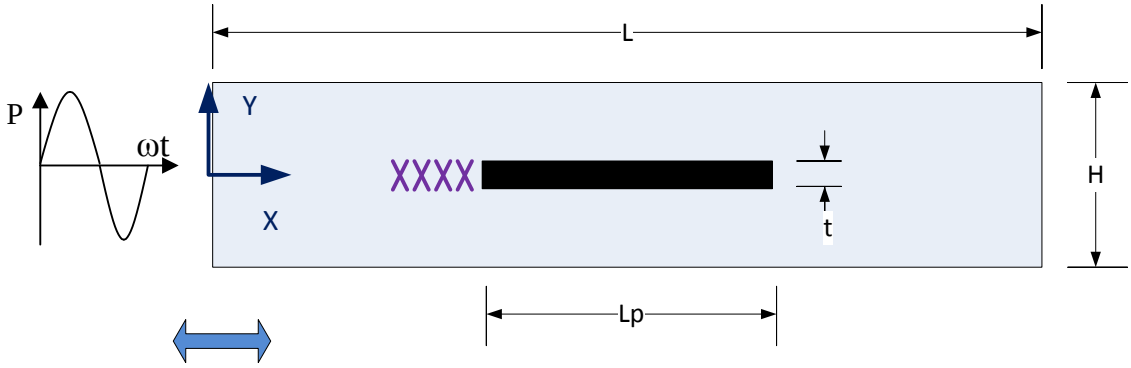

(b)

Figure 2.14 Schematic of a standing wave resonator: (a) empty; and (b) with spoiler. The purple color cross denote the location of virtual probes. Similar to left side virtual probes were located on the right side of the spoiler.

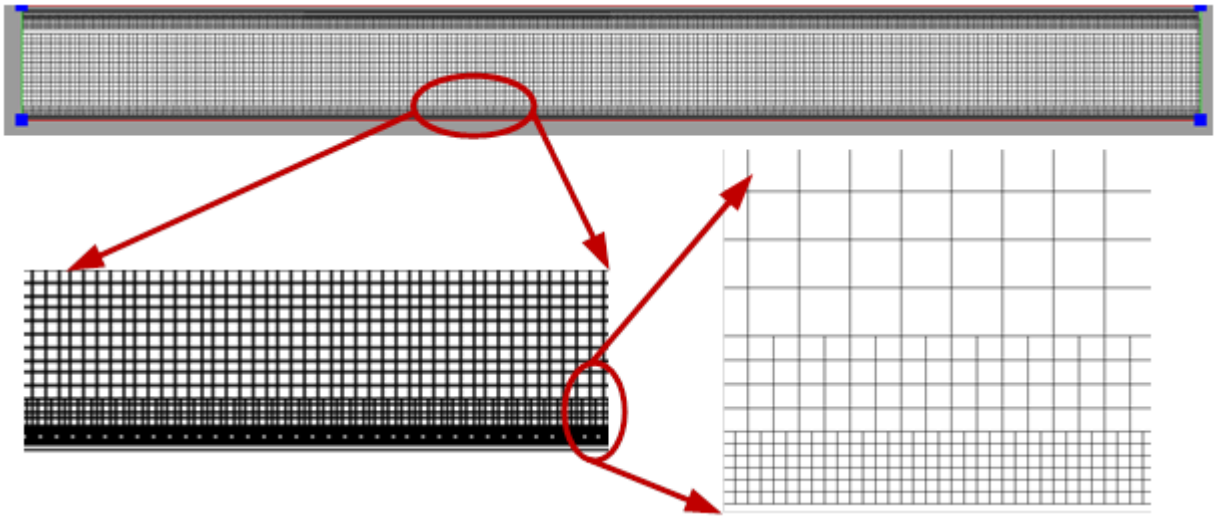

(a)

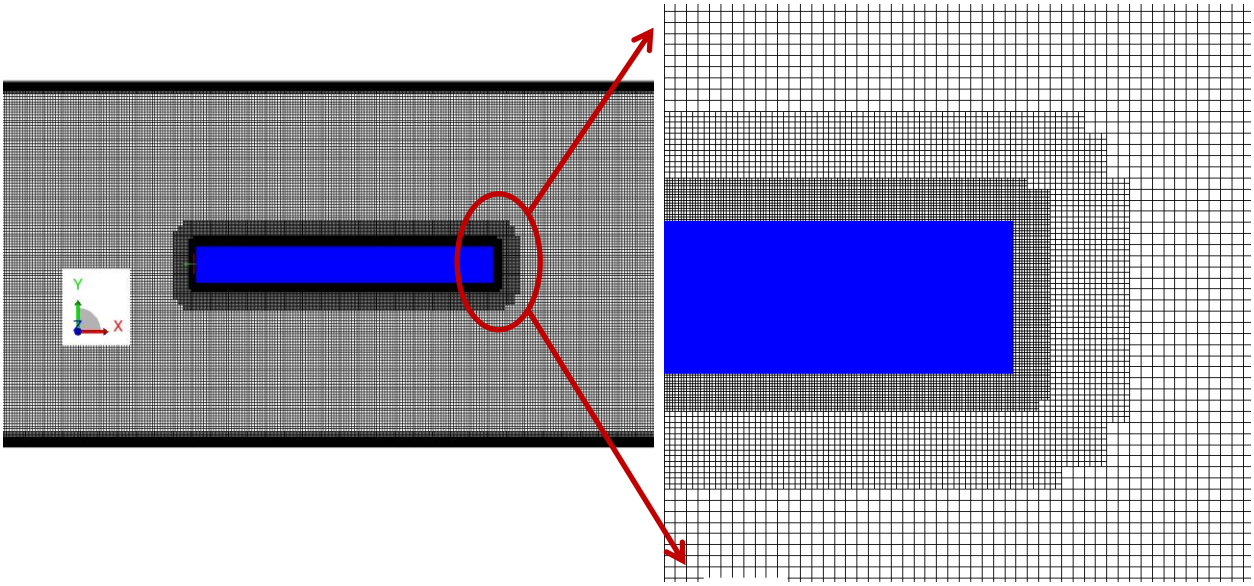

(b)

Figure 2.15 Schematic of the VR region and voxel distribution: (a) empty; (b) with spoiler.

Table 2-1 Simulation characteristic parameters given in PowerFLOW

Parameter	Value
Characteristic pressure (Pa)	101000
Characteristic velocity (m/s)	Peak acoustic velocity
Characteristic temperature (K)	298
Characteristic viscosity (m^2/s)	0.00012088
Characteristic length (m)	Viscous penetration depth
Resolution	12

3 Experimental study of acoustic streaming in an empty standing wave resonator

3.1 Introduction

Experiments were performed to investigate Rayleigh steaming in a rectangular channel. The accuracy of the experimental methods was verified. The acoustic instantaneous and the streaming velocities were measured using PIV. The experimental results were compared with the predictions from the linear acoustic theory. A three-dimensional streaming cell inside a square cross section channel was reconstructed from planar velocity vector maps.

3.2 Validation of experimental results

In order to verify the validity of the experimental results obtained from PIV, comparisons were made with the analytical results available from linear acoustic theory.

3.2.1 Acoustic velocity: Phase-locked and Time Resolved

In order to validate the PIV methodology, instantaneous acoustic particle velocities were measured at different phases, θ, within one acoustic cycle by phase locking the laser and camera with the pressure signal from the transducer at the rigid end of the resonator. The pressure signal obtained from the transducer was converted into a TTL signal. This TTL signal was used by the synchronisation unit for synchronising the laser and the camera with the acoustic flow. Velocity data were obtained for 13 phase values, namely, θ = 0°, 36°, 72°, 90°, 108°, 144°, 180°, 216°, 252°, 270°, 288°, 324° and 360° degrees. A time lag, t_l, was introduced between the TTL signal and the trigger signal for the camera and the laser in the PIV software to obtain instantaneous

acoustic particle velocities at different phase values. In a similar experimental study performed by Mao *et al.* [34], instantaneous acoustic velocities inside a resonator were evaluated using PIV. The number of instantaneous images needed for a reliable determination of the mean flow features was determined. In their results, 100 images were captured at each phase. Velocity fields were processed from these images. In the results presented in this chapter, a total of 300 images were captured in the double frame mode for each phase value. One ensemble-averaged velocity map was then obtained for each individual phase value.

Comparisons were made between the acoustic particle velocities predicted from linear theory and the measured values. The peak dynamic pressure amplitude measured at the driven and the rigid ends of the resonator were 227 Pa and 731 Pa, respectively. The mean pressure inside the resonator was atmospheric and the mean temperature was 395 K. The measured instantaneous acoustic particle velocities were obtained for an excitation frequencies, f_a, of 198, 396 and 1137 Hz, for which the resonator length corresponds approximately to one-half, one and three wavelengths. A rigid, perfectly reflecting termination was assumed at the closed end. The results are shown in the spatial domain and in the time domain in Figure 3.1 and Figure 3.3, respectively. Figure 3.1 shows a comparison between the measured and the predicted axial component of the instantaneous acoustic particle velocity at 1137 Hz in the spatial domain, for two different phases. The horizontal axis depicts the distance from the driven end of the standing wave tube. The mean difference between the theoretical and the experimental results presented in Figure 3.1 was calculated following the formulation described in section 2.1.8 and it was found to be 5.6%.

The measured ensemble-averaged axial instantaneous acoustic particle velocities at different phases for an excitation frequency of 1137 Hz are shown in Figure 3.2. This figure illustrates the standing wave nature of the acoustic field inside the resonator. In order to obtain comparisons between the experimental and the theoretical results in the time domain, the particle velocities were obtained at different locations inside the resonator, as indicated in Figure 3.2. For each location, ensemble-averaged instantaneous acoustic velocities were measured for 13 different phases. Figure 3.3 shows a comparison between the predicted and the measured acoustic velocities in the time domain for four spatial locations identified in Figure 3.2. The mean error for the results presented in Figure 3.3 was found out to be 8.6 %. These results support the accuracy of the PIV method for measuring the instantaneous acoustic flow field inside the resonator.

Most previous PIV studies [30, 33, 34] reported results with good spatial resolution, but with limited temporal resolution. There was a need for time-resolved studies in acoustics in general, and thermoacoustics in particular. This was useful to characterize unsteady flows that are not synchronous with the dominant periodic excitation. In order to obtain data in the time domain, phase-locked data were usually obtained at different phases within an acoustic cycle. The reason for this was the limitation in hardware capacity, namely, the laser repetition rate and the camera frame rate. Transient acoustic phenomena such as the formation of streaming structures or vortex formation behind stack plates, as well as turbulence, could be better understood from time-resolved data. Recent developments in the hardware of PIV systems made it possible to capture time-resolved images. The validation study presented here was one such attempt at obtaining high temporal resolution data for an acoustic flow. The acoustic resonator was excited at 198 Hz, which was near the typical operating frequency of a thermoacoustic refrigerator. PIV images

were captured at 4000 Hz, which meant that for each acoustic cycle, 20 data points were captured. The camera field of view was set in the middle region of the resonator along the transverse axis.

Figure 3.4 shows a comparison between the measured and the predicted axial component of the instantaneous acoustic particle velocities. The linear acoustic model slightly over predicted (9.4% at the peak value) the acoustic velocity, but overall the experimental results agree well with the theoretical results obtained from linear acoustic models. The frequency content of the time-resolved velocity vector map was obtained from the time history of the velocity vectors from the two-dimensional vector maps. The power spectral density (PSD) of the velocity vector time history was calculated and is shown in Figure 3.5. The total time history comprising of 40,000 data points was considered for calculating the PSD, with a record length NFFT=1024. A Hann window was used for each segment with an overlap of 50%. The major component occurred at the excitation frequency of 198 Hz, as expected, with smaller components corresponding to higher harmonics. The frequency spectrum analysis also revealed components at frequencies other than the harmonics of the excitation frequency. As illustrated in Figure 3.5, secondary tonal components (identified by dotted line) are visible adjacent to higher harmonics (identified by dashed line) at 600, 1400 and 1800 Hz. Un-harmonic fluctuations tend to be averaged out in phase-locked ensemble-averaged measurements.

3.2.2 Acoustic streaming

The next step in the validation procedure was to compare measured acoustic streaming velocities with linear acoustic model predictions. For this validation case, the resonator was excited at 245.5 Hz. The results are shown in Figure 3.6. Both the measured and the predicted streaming

velocity amplitudes were non-dimensionalised by the peak Rayleigh streaming amplitude. The horizontal axis is non-dimensionalised by $\lambda/4$, which corresponds to the axial dimension of one Rayleigh streaming cell. Figure 3.6.b is a velocity vector plot wherein one complete streaming cell is revealed. Each arrow line represents the axial component of the streaming velocity at that location. Here the vertical axis represents the non-dimensionalised channel width. For comparison, the velocity vectors along the axial direction corresponding to the channel centreline are shown. Figure 3.6.a compares the measured and the predicted streaming velocities. The comparison reveals a very good agreement both in terms of the amplitude and shape of the streaming cell. The mean error was found to be 3.5%. The measured size of the streaming cell is also in agreement with the predicted one. The streaming velocity is shown in non-dimensional form, being divided by the peak Rayleigh axial streaming velocity, u_R given by $3u_a^2/8c$, where u_a is the peak amplitude of the instantaneous acoustic velocity.

3.2.3 Time evolution of acoustic instantaneous and streaming velocities

The time evolution of the instantaneous and the streaming velocity was studied. Velocity data were collected at different time instants starting from when the driver was initially excited. This initial state was denoted by T0. Three cases were considered, corresponding to the driver excitation frequencies of 240, 825 and 1620 Hz. These frequencies were chosen to excite the resonant modes of the resonator. For each of these excitation frequencies, the resonator was excited for more than 15 minutes. Several PIV recordings were made during this time duration starting from initial time, T0. The results, shown in Figure 3.7, correspond to the driver excitation frequency of 825 Hz, peak acoustic velocity amplitude of 1 m/s and peak Rayleigh streaming velocity amplitude of 0.0013 m/s. The reason for choosing this excitation frequency

was that the field of view of the camera could capture one complete streaming cell which corresponds to an axial dimension of λ/4. Figure 3.7.a shows the time evolution of the axial variation of the axial component of the instantaneous acoustic velocity. Four time instants corresponding to 3, 5, 7 and 9 minutes after the driver was excited are shown. The instantaneous acoustic velocity reached a steady state before T0+3 minutes. From these results it was deduced that the instantaneous acoustic velocity reaches a steady state around three minutes after the initial excitation of the driver.

Figure 3.7.b shows the time evolution of the axial component of the Rayleigh streaming velocity along the transverse direction. The axial location at which the velocity profile was taken corresponds to the peak Rayleigh streaming amplitude. The peak streaming velocity amplitude is two orders of magnitude smaller than the first order peak instantaneous acoustic velocity amplitude. Therefore, the time required for the Rayleigh streaming velocity to reach a steady state is larger than that for the instantaneous acoustic velocity. In Figure 3.7.b, for brevity, Rayleigh streaming velocity is shown only for four time instants namely, T0+3.0, T0+4.7, T0+6.9 and T0+9.1 minutes. The acoustic streaming velocity reached a steady state five minutes after the initial driver excitation. One of the challenges in capturing PIV data for time duration longer than ten minutes was the diminishing concentration of seeding due to settling. This resulted in regions where spurious velocity vectors were observed due to very low seeding concentration. The seeding concentration was reduced faster in regions of high streaming velocity as compared with regions of low streaming velocity amplitude. This may explain the larger differences between the velocity profiles at higher amplitudes, $u_{st}/u_R \approx -1$, after 4.7 min.

3.2.4 Repeatability of results

Repeatability of the experimental data is defined as the ability to get consistent results after starting the experiment afresh. To further verify the accuracy of the PIV data, four tests were performed, with the same driver excitation frequency and the peak acoustic amplitude as explained in the time evolution results of section 3.2.3. For each of these tests, both the PIV system and the driver exciting the resonator were started from rest. Fresh seeding was supplied for each of these tests. The time duration between each of these consecutive tests was of the order of few hours. The results for the data repeatability are shown in Figure 3.8. Both the instantaneous acoustic, Figure 3.8.a, and the streaming velocity, Figure 3.8.b profiles for different tests have similar trend and magnitudes, with the exception of the streaming velocity profile of test 4. Test 4 shows higher streaming velocity magnitudes. Overall, the results for the instantaneous acoustic and streaming velocities indicated repeatability of the experimental setup.

3.3 Influence of peak instantaneous acoustic velocity on Rayleigh streaming

Linear acoustic theory predicts the pattern of acoustic streaming cells within a plane. Such planar pattern is termed classical or regular streaming. A previous study performed by Nabavi *et al*. [31], reported that the Rayleigh streaming pattern changes from the theoretically predicted classical/regular pattern to non-classical/irregular pattern with increasing streaming Reynolds number. They studied the effects of two Reynolds numbers for characterisation of the Rayleigh steaming. The first one, $\mathrm{Re}_{s1} = \left(u_a^2/\nu\omega\right)$, is obtained in terms of the length of the resonator, chosen as the characteristic length, and the peak Rayleigh streaming velocity $\left(\sim u_a^2/c\right)$, chosen as the characteristic velocity. The second one, $\mathrm{Re}_{s2} = 0.5\times\left(u_a^2/c\right)^2\times\left(H/\delta_\nu\right)^2$, includes another non-

dimensional parameter, H/δ_v, in the Reynolds number. The second streaming Reynolds number quantifies nonlinearity in the streaming flows [19]. Aktas *et al*. [49] used Re_{s1} in their numerical study and Re_{s2} was used by Thompson *et al*. [26, 27] in their experimental study. The shape of the 2D Rayleigh streaming cell was experimentally studied using PIV by Nabavi *et al*. [31, 82]. Conflicting results were obtained from these two very similar studies of Nabavi *et al*. The former concluded that Re_{s1} is the non-dimensional number which governs regular or irregular streaming, and Re_{s2} was not a suitable parameter for this characterisation. It was also concluded that for $\mathrm{Re}_{s1} > 7$, the onset of classical/regular streaming cell structure occurs. In their latter study they concluded that Re_{s2} is the governing parameter and for $\mathrm{Re}_{s2} < 50$ regular streaming cell shape occurs and that Re_{s1} is not an appropriate parameter to classify regular and irregular streaming. Therefore, in the study presented here, similar experiments were also performed by varying the excitation frequencies and the peak instantaneous acoustic velocity amplitude. Three excitation frequencies, 818, 1152 and 1658 Hz were chosen. Several values of the drive ratios were considered for each excitation frequency. Four selected cases are shown for each excitation frequency to illustrate the evolution of the 2D Rayleigh streaming cell shape with increasing drive ratios. The flow parameters, along with the resulting streaming Reynolds number, are given in Table 3-1. The drive ratios in Table 3-1 are the ratio between the peak amplitude of the acoustic pressure and the ambient mean pressure. The theoretical peak acoustic velocity was calculated from the peak acoustic pressure value using the relation $u_a = p_a/\rho c$. The ambient mean pressure in this case was taken as the atmospheric pressure. The evolution of the streaming cells in a square cross section standing wave resonator at different drive ratios and excitation frequency are shown in Figure 3.9-Figure 3.11. As shown in a previous study [82], regular

streaming structures were obtained only for $\mathrm{Re}_{s1} > 7$. These results differ from the previous study of Nabavi *et al.* which reported that regular streaming cell shape occurs for $\mathrm{Re}_{s2} < 50$. In the results presented here, except for case 8 where $\mathrm{Re}_{s2} > 50$, for all other cases $\mathrm{Re}_{s2} < 50$, but both regular and irregular streaming shape were observed. The only obvious trend was that the streaming shape changes from non-developed/irregular to regular/classical and then back to irregular when the drive ratio was increased. The results obtained in the present study show that the shape of the streaming cell was dependent on both the excitation frequency and the drive ratio. Linear acoustic theory predicts classical streaming cell for even very low drive ratios, but experimentally, irregular streaming cell shapes were observed at low drive ratios. This may be due to the fact that the streaming velocity amplitude, which is proportional to ($\sim u_a^2/c$), was very small at very low drive ratios, where $u_a < 1$. Therefore, the time required for the streaming cell to completely develop was longer than the duration for which the experimental data was recorded. This was difficult to verify experimentally through PIV as the seeding concentration drops with time and new seeding particles cannot be introduced without disturbing the flow. The analytical results of linear acoustic theory cannot predict the effects of nonlinearity on the shape of streaming cell for high drive ratios. The experimental results reveal irregular streaming cell shapes, which can be attributed to nonlinear effects at high drive ratios. In experiments, conducted at the excitation frequency of 1152 Hz (Figure 3.10), the streaming cell shape was irregular/non-developed at low drive ratios but changed to a classical/regular shape (Figure 3.10.a,b) when the drive ratio was increased. The shape starts to deviate from classical (Figure 3.10.c), and adapted to a complete irregular shape (Figure 3.10.d), when the drive ratio was further increased. Due to the limitations of the acoustic driver, higher drive ratios could not be achieved. The results shown in Table 3-1 further show that the streaming cell shape was

different for the same streaming Reynolds number but different excitation frequencies. This suggests that the streaming Reynolds numbers used in the previous study of Nabavi *et al*. are not the only parameters determining the shape of the Rayleigh streaming cell at various drive ratios.

3.4 Three-dimensional reconstruction of one streaming cell

Most of the available experimental data on the Rayleigh acoustic streaming were collected in only one plane and they focus on the streaming velocity in the symmetry plane where the maximum streaming amplitude occurs. Actual thermoacoustic devices have a complex geometry, where out of plane fluid motion could be significant. To better reveal acoustic streaming in a 3D resonator, one complete Rayleigh acoustic streaming cell was reconstructed in a square cross section channel.

The system was driven at its third resonant mode, corresponding to $L = 3\lambda/4$ at $f_a = 245\,\mathrm{Hz}$. The loudspeaker input voltage was set so that the peak instantaneous acoustic velocity amplitude reached 3.4 m/s to limit nonlinear propagation effects and thus higher harmonics generation in the resonator. For $L = 3\lambda/4$, the length of one streaming cell, $\lambda/4$, is about 0.35 m. In order to obtain sufficient spatial resolution, the studied streaming cell was divided into six equal intervals corresponding to the length of the camera field. The central streaming cell was scanned over six successive axial positions with an overlap of 0.5 cm. The camera field of view was 7 cm x 7 cm, thus the spatial resolution of the PIV image was $\Delta x = \Delta y = 0.47$ mm. The temperature inside the resonator was also recorded using a K-type thermocouple, which was attached to the inside wall of the resonator near the acoustic driver. Overall the room temperature was regulated in such a way that the resonator temperature did not vary more than ± 1.0 °C between the experiments. Figure 3.12.a shows one example of the measurement results for the axial component of the

streaming velocity, for the six camera positions. Measurements were performed at 18 vertical positions, as shown in Figure 3.13 so that 3D streaming cell structure could be reconstructed from the different planar streaming velocity fields. For each of 18 vertical planes, the streaming velocity was obtained by traversing the camera at six locations. The velocity vector data obtained for the six camera positions was then imported into MATLAB. A MATLAB script was written for stitching the planar velocity data in order to construct a streaming velocity vector map in each vertical plane. Figure 3.12.b shows the corresponding reconstructed streaming cell.

Figure 3.14 shows the measured and the predicted axial components of the Rayleigh streaming velocity, u_{st}, along the y- and z- transverse axes. The z-profile was reconstructed from the different scanned velocity fields, as shown in Figure 3.15. Here, the velocity profiles are given for the x-location corresponding to the centre of the streaming cell, i.e. $x = \lambda/8$. The measured streaming velocities are in good agreement with the theoretical predictions for both the inner and outer streaming cells along the y-axis. Considering the difficulty of reconstructing a z-profile from different horizontal velocity fields, the results are very satisfactory. Here again, the experimental and theoretical results are in good agreement.

Figure 3.16 shows isovelocity contours of the measured streaming structure. The isosurface is shown for the streaming velocity value of 0.006 m/s. This first qualitative comparison suggests that, overall; the outer streaming vortices are not greatly influenced by the shape of the resonator section. Although the resonator has a square cross-section, the shape of the outer streaming cell is cylindrical. Rayleigh streaming cell inside a cylindrical resonator was calculated using the equations provided by Bailliet *et al*. [15]. The theoretically obtained 3D Rayleigh streaming cell constructed from the axial component of the streaming velocity is shown

in Figure 3.17. In this figure, isovelocity contours of the axial component of the streaming velocity magnitude for a value of 0.006 m/s is shown. Figure 3.16 and Figure 3.17 show the isovelocity contour at the same value of the streaming velocity. Comparing the outer streaming cell for the two resonator cross sections, it was observed that they have similar shape in square and cylindrical resonators. However, streaming in the near wall region seems to differ significantly in a square resonator compared to the case of a cylindrical resonator. A detailed comparison between the model predictions of the streaming cell shapes for the cylindrical resonators, and the measured streaming cell shapes for the square cross section resonators is available in a collaborative work done by the author of this dissertation [83]. The work which was done by the author was described in this section.

3.5 Conclusions

The instantaneous acoustic and the Rayleigh streaming velocities were simultaneously measured using PIV. The PIV results were compared with the results obtained from the linear acoustic theory. They were found to be in good agreement. Time evolution and repeatability studies were also performed to verify the PIV results. The evolution of the streaming cell shape was observed along the symmetry plane of the resonator for increasing streaming Reynolds number. Finally, one 3D streaming cell was reconstructed in space from collections of planar velocity data. It was found that that the shape of the resonator does not affect the outer streaming shape.

All these results show that Rayleigh steaming velocity is of very low magnitude. The 3D reconstruction of the streaming cell shed light on the fact that the heat transfer effect of Rayleigh streaming even at a fixed axial location is not uniform. Near the wall of the resonator inner streaming occurs which has small area of influence (~2 δ_v). The velocity magnitude in the inner

streaming cell is larger than that in the core of the outer streaming cell. Thus inner streaming cells should cause more efficient heat transfer near the walls of the resonator. The outer streaming cell should cause more efficient heat transfer near the core of the resonator while the inner streaming cell can cause better heat transfer near the resonator wall. In thermoacoustic applications, it is difficult to assess the importance of overall streaming based on Rayleigh streaming model only. The Rayleigh streaming studies performed thus far were mostly for an empty resonator. The influence of the stack and heat exchangers was absent. The next step was to study the streaming environment in a non-empty resonator, as discussed in the next chapter.

Table 3-1 Effects of streaming Reynolds number on streaming pattern.

Case	f (Hz)	Drive ratio (%)	u_a (m/s)	Re_{s1}	Re_{s2}	Streaming pattern
1	818	0.3	1.69	36.8	3.2	Irregular/Non-developed
2	818	0.9	2.87	106.1	9.3	Regular
3	818	1.3	3.64	170.6	15.0	Regular
4	818	1.6	4.70	284.4	25.1	Irregular
5	1152	0.3	0.85	6.6~7	1.1	Regular
6	1152	0.4	1.10	11.1	1.9	Regular
7	1152	0.8	1.95	34.8	6.0	Regular
8	1152	2.1	6.30	362.9	63.5	Irregular
9	1658	0.2	0.63	2.5	0.9	Irregular/Non-developed
10	1658	0.5	1.42	12.8	4.6	Irregular/Non-developed
11	1658	0.8	1.65	17.3	6.2	Regular
12	1658	0.9	2.12	28.6	10.3	Irregular

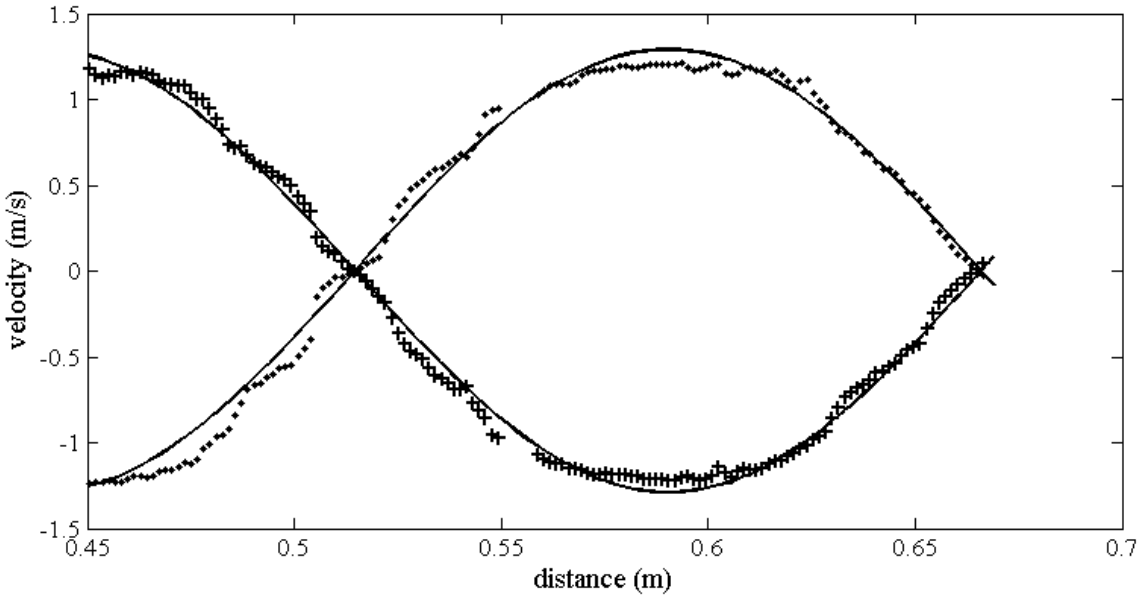

Figure 3.1 Axial component of the ensemble-averaged instantaneous acoustic velocity vs. axial distance at f_a = 1137 Hz. Measured: ···θ=0°, +++θ=180° and predicted: ——.

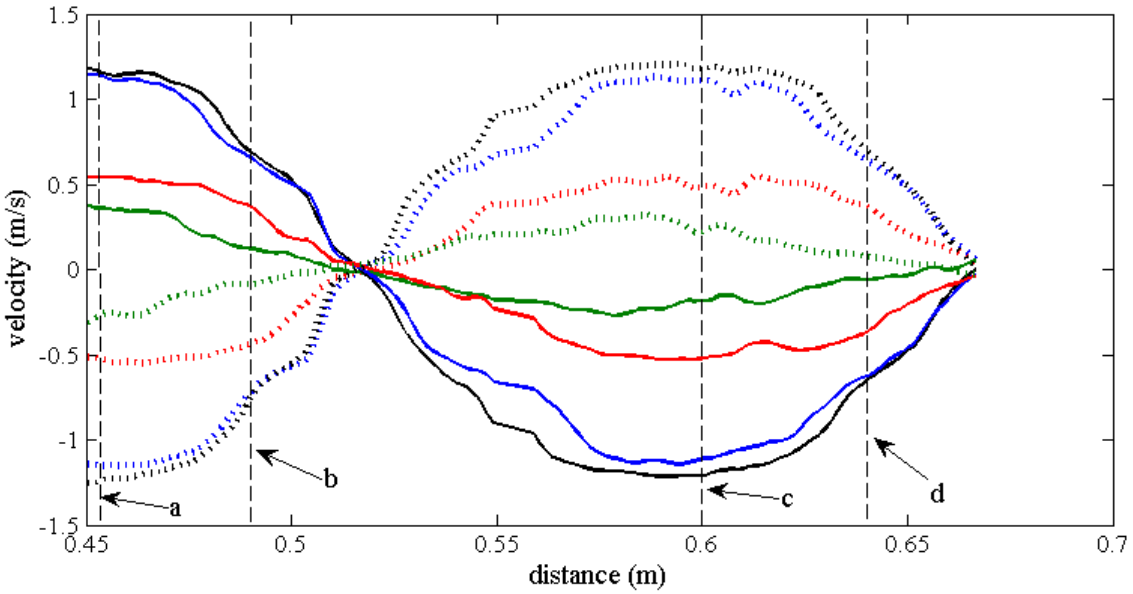

Figure 3.2 Velocity profiles of the axial component of the ensemble-averaged instantaneous acoustic velocity at different phases of an acoustic cycle at f_a=1137 Hz. Dotted black: θ=0°, dotted blue: θ=36°, dotted red: θ=72°, dotted green: θ=90°, solid black: θ=180°, solid blue: θ=216°, solid red: θ= 252°, and solid green: θ=270°. The velocity time history was extracted at the locations a, b, c and d for Figure 3.4.

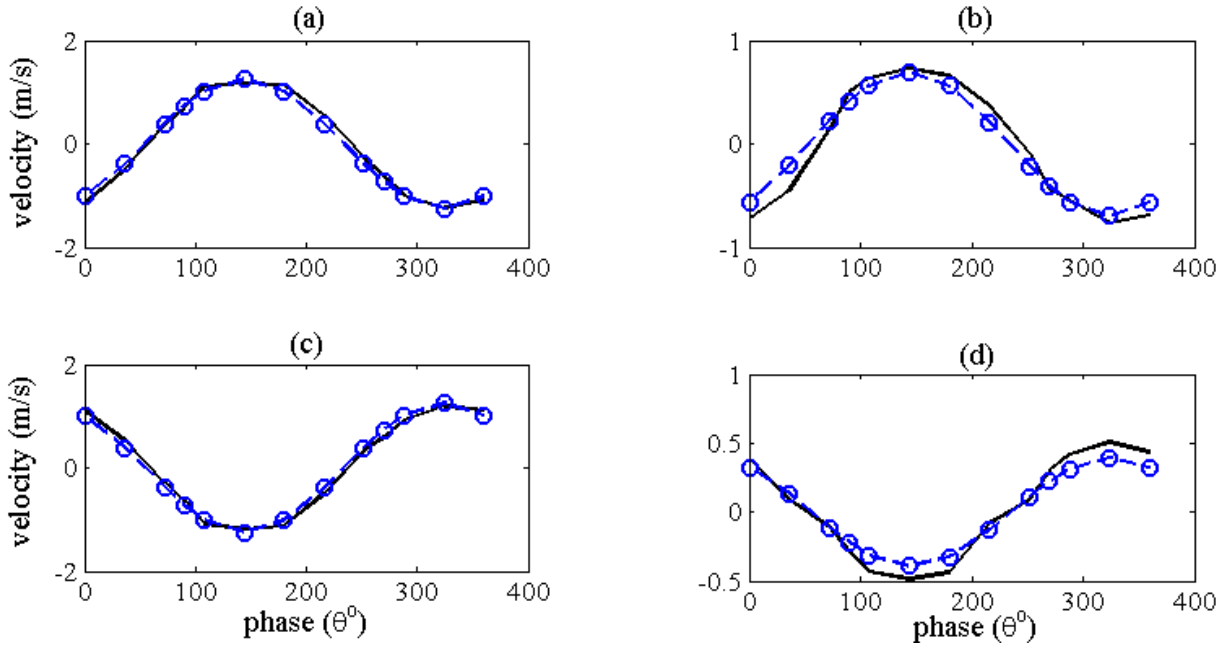

Figure 3.3 Time evolution of the axial component of the ensemble-averaged instantaneous acoustic velocity at different locations. (a) 0.45 m, (b) 0.49 m, (c) 0.6 m, (d) 0.64m. Predicted: blue -o-, and measured: ——. Locations are shown in Figure 3.2.

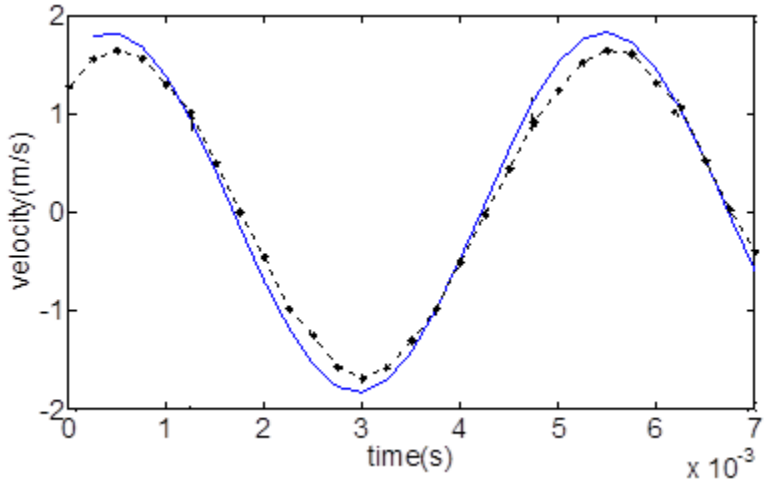

Figure 3.4 Axial component of the instantaneous acoustic velocity vs. time. Measured: -·-·-, and predicted: ——.

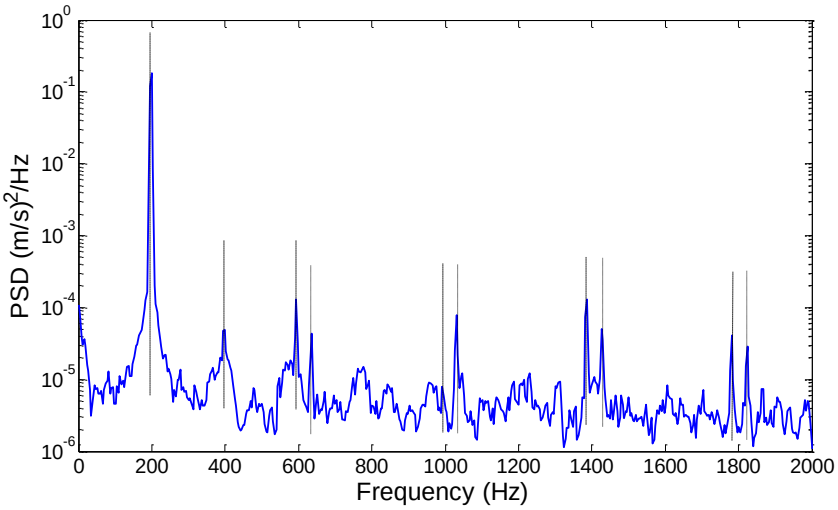

Figure 3.5 Power spectral density of the instantaneous acoustic velocity amplitude. The dotted lines represent the frequencies where non-harmonic peaks occur.

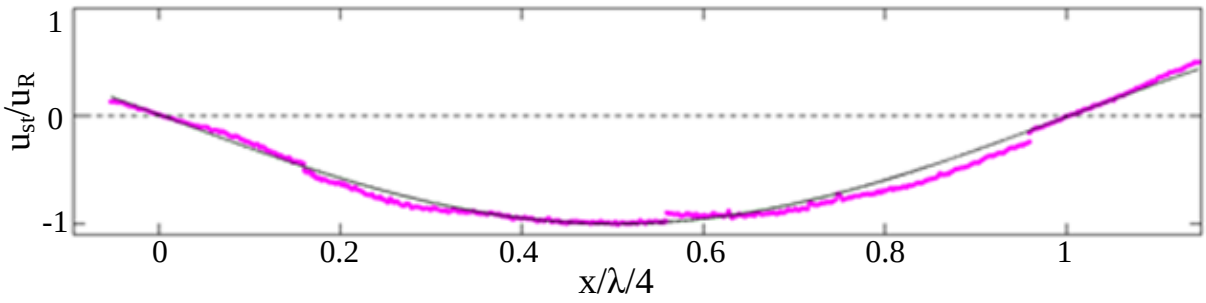

(a)

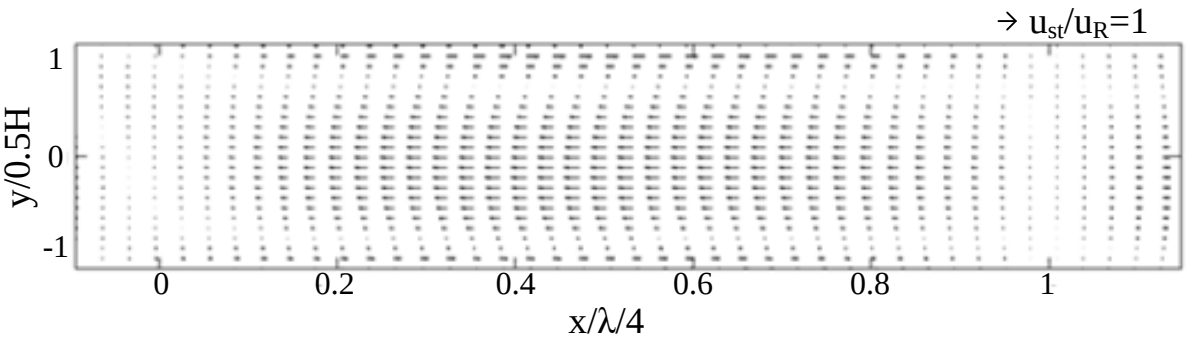

(b)

Figure 3.6 Rayleigh streaming velocity amplitude. (a) Axial component of the ensemble-averaged streaming velocity amplitude at waveguide centerline. (–predicted, pink dots ⋯ measured). (b) Rayleigh streaming velocity vectors at the symmetry plane.

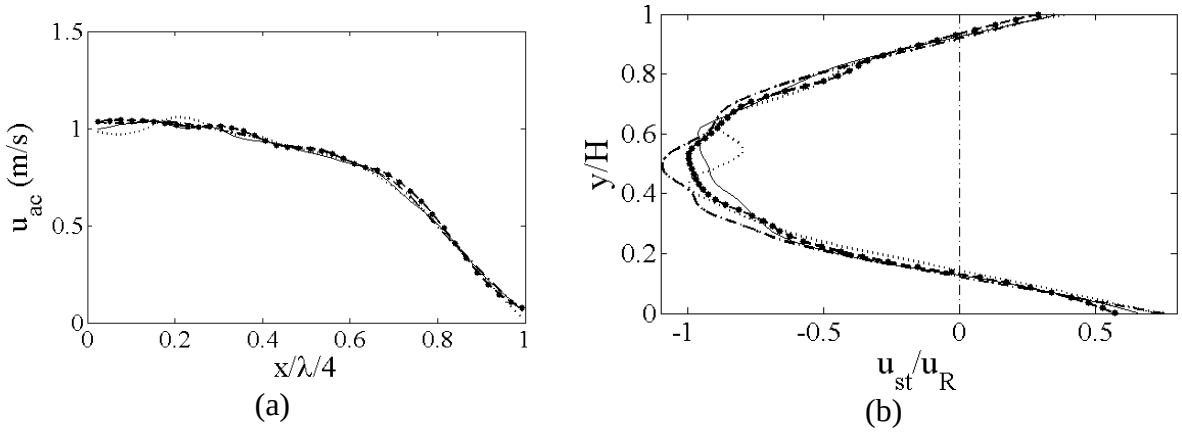

Figure 3.7 Time evolution of the axial component of the ensemble-averaged velocity. (a) Instantaneous acoustic velocity at the resonator centerline. (b) Rayleigh streaming velocity at $x = \lambda/8$. —— *T0*+3.0 min; —•— *T0*+4.7 min; ···*T0*+6.9 min; and ·—· *T0*+9.1 min.

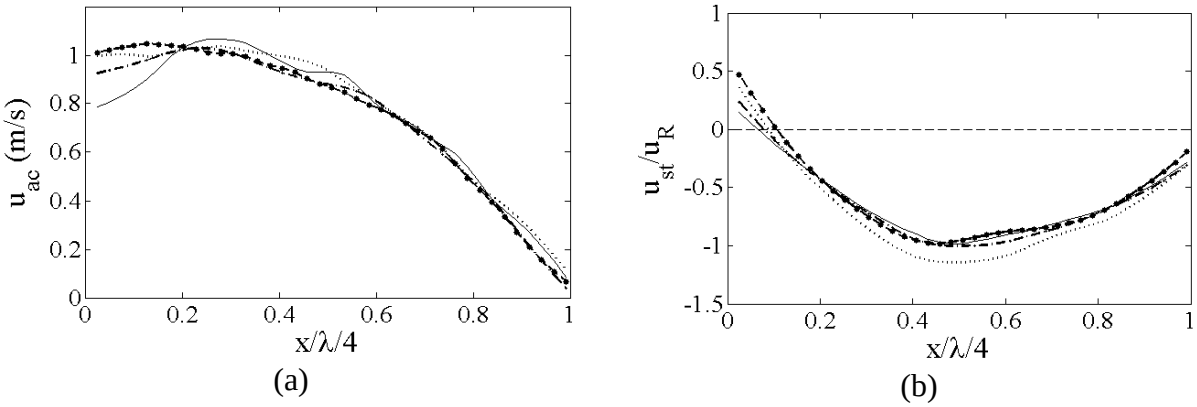

Figure 3.8 Axial variation of the ensemble-averaged axial component of (a) instantaneous acoustic velocity and (b) Rayleigh streaming velocity along the resonator centerline. —— Test 1; –·– Test 2; •—•Test 3; and ···Test 4.

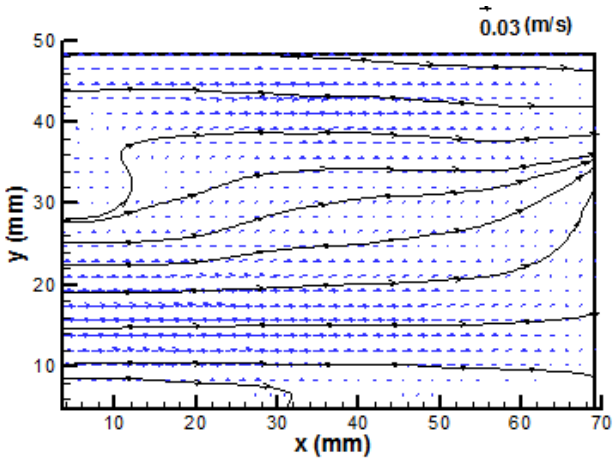

(a)

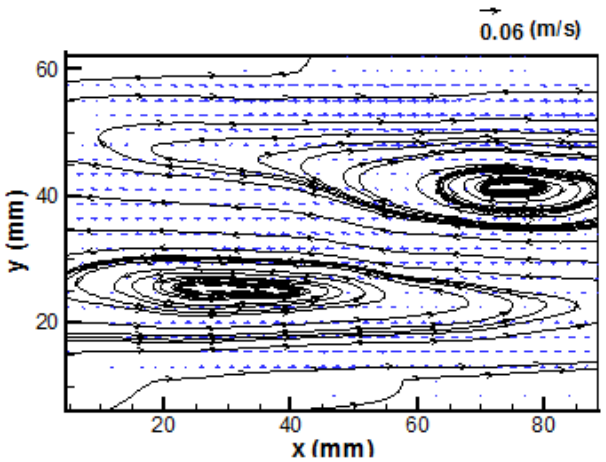

(b)

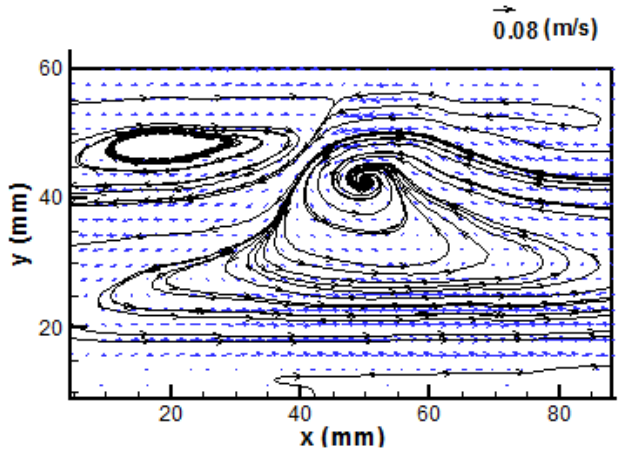

(c)

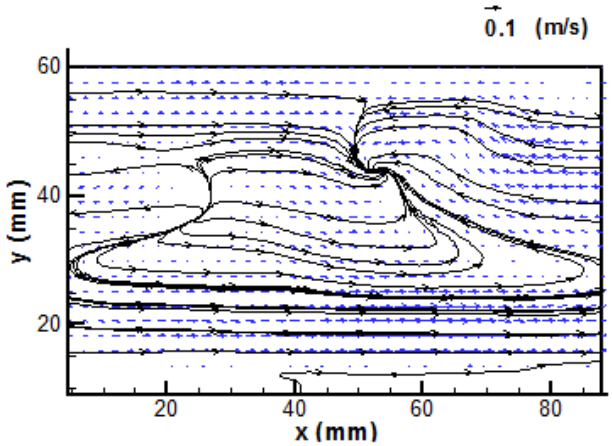

(d)

Figure 3.9 Evolution of the streaming cell shape at 818 Hz. The drive ratios (Ref: atmospheric pressure) were 0.3, 0.9, 1.3 and 1.6 %, respectively and the corresponding peak instantaneous acoustic velocities were 1.69, 2.87, 3.64 and 4.7 m/s respectively. Reference vectors are shown on top left of each figure.

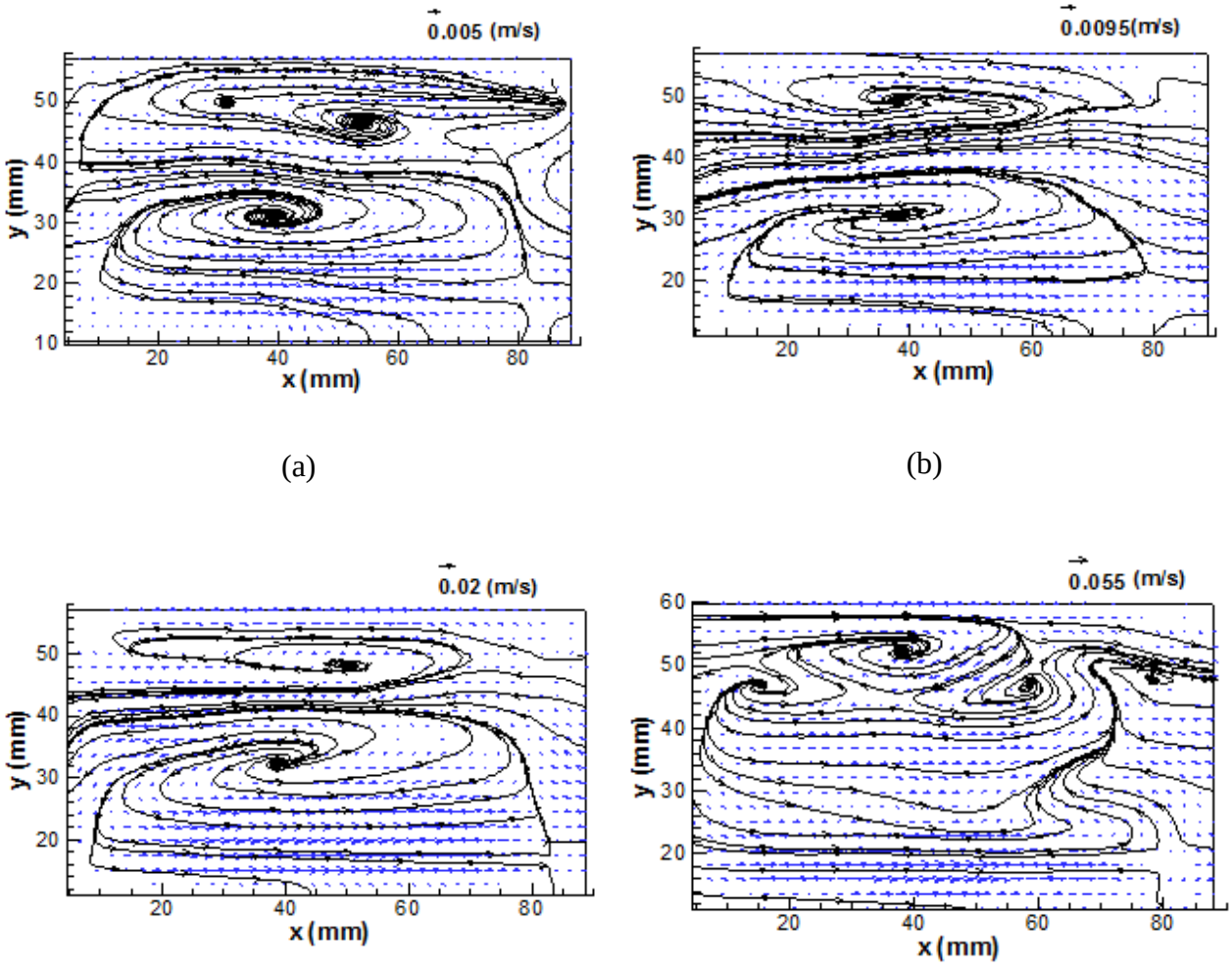

Figure 3.10 Evolution of the streaming cell shape at 1152 Hz. The drive ratios (Ref: atmospheric pressure) were 0.3, 0.4, 0.8 and 2.1%, respectively and the corresponding peak instantaneous acoustic velocities were 0.85, 1.1, 1.95 and 6.3 m/s respectively. Reference vectors are shown on top left of each figure.

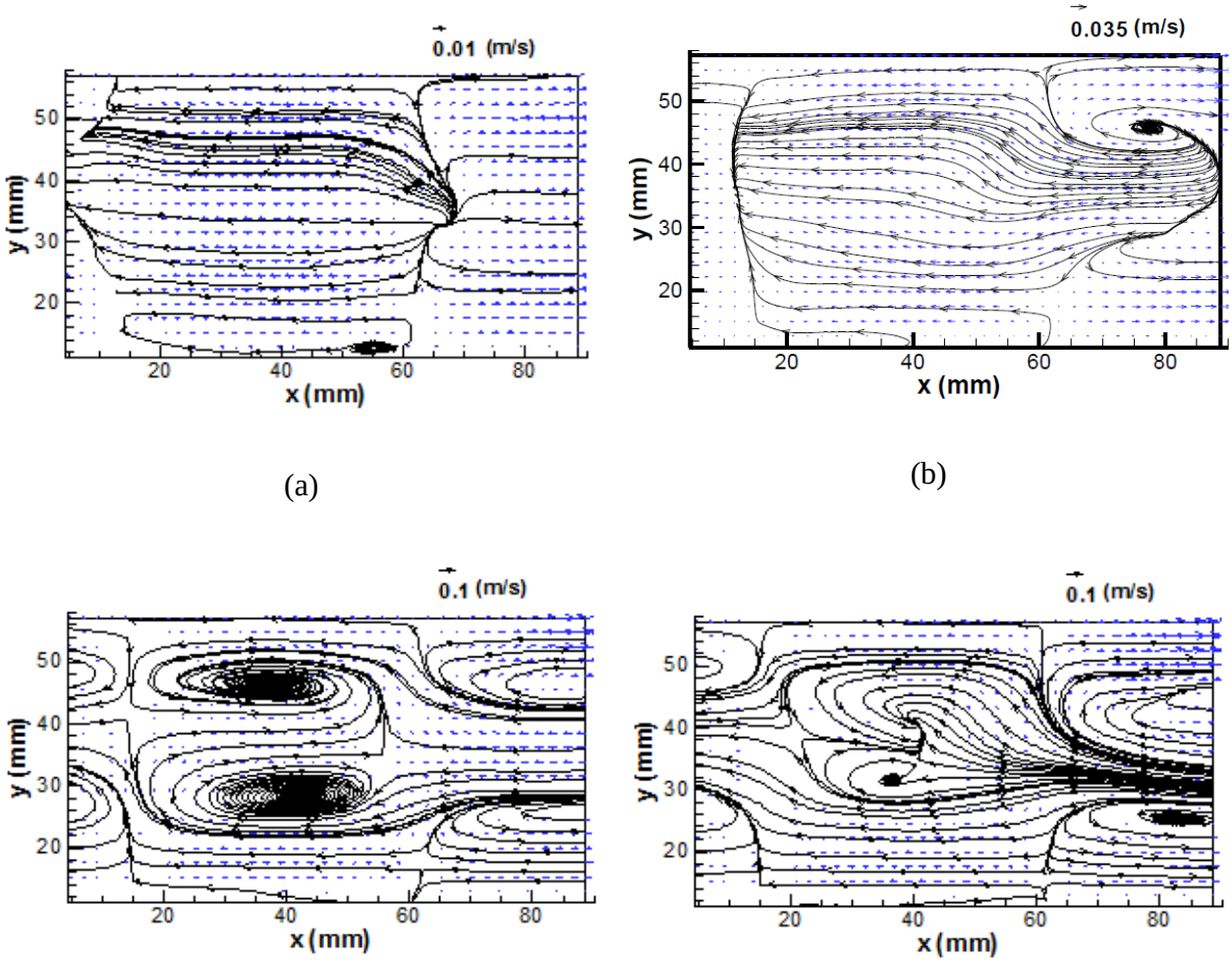

Figure 3.11 Evolution of the streaming cell shape at 1658 Hz. The drive ratios (Ref: atmospheric pressure) were 0.2, 0.5, 0.8 and 0.94%, respectively and the corresponding peak instantaneous acoustic velocities were 0.63, 1.42, 1.65 and 2.12 m/s respectively. Reference vectors are shown on top left of each figure.

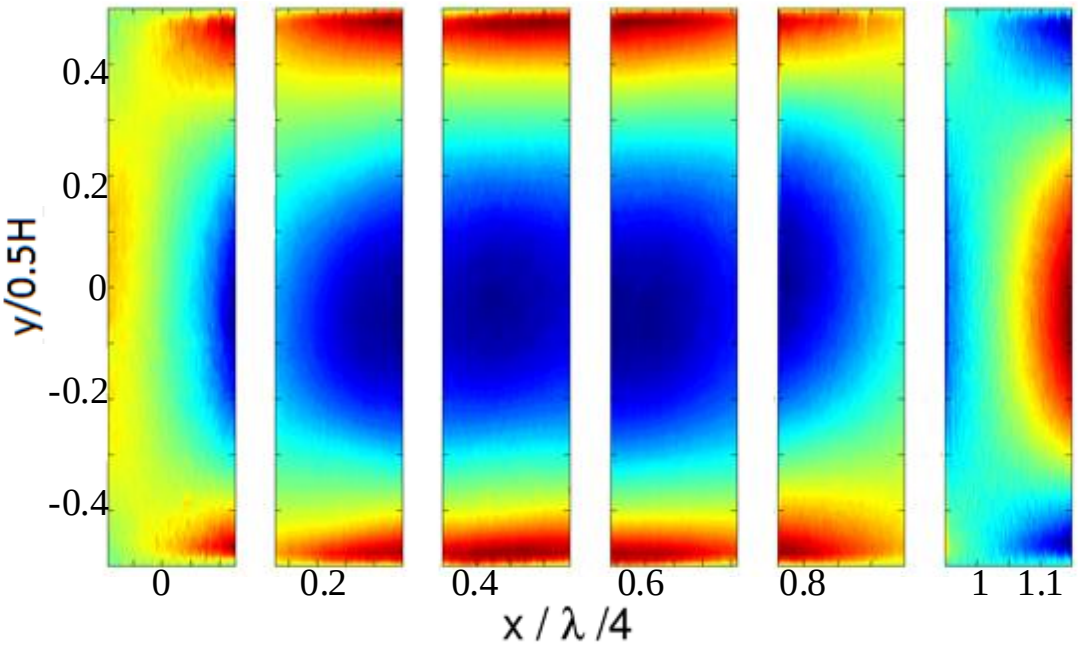

(a)

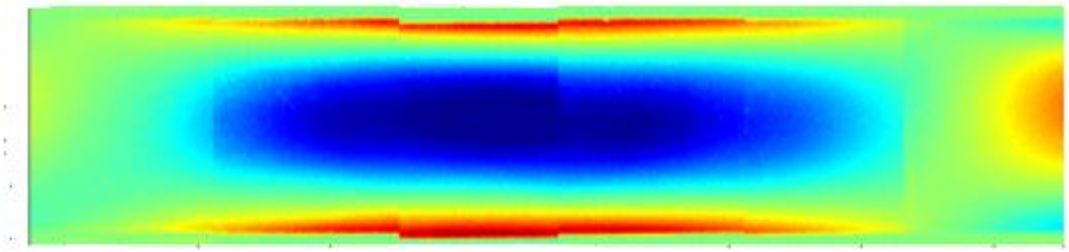

(b)

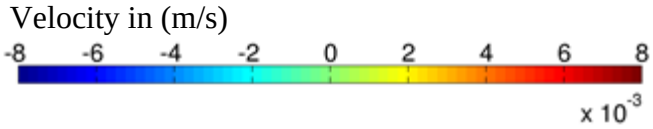

Figure 3.12 Planar view of the axial component of the ensemble-averaged streaming velocity amplitude at channel center. (a) Unstitched, at six camera locations, and (b) stitched. The six velocity fields shown in (a) were stitched using a MATLAB script.

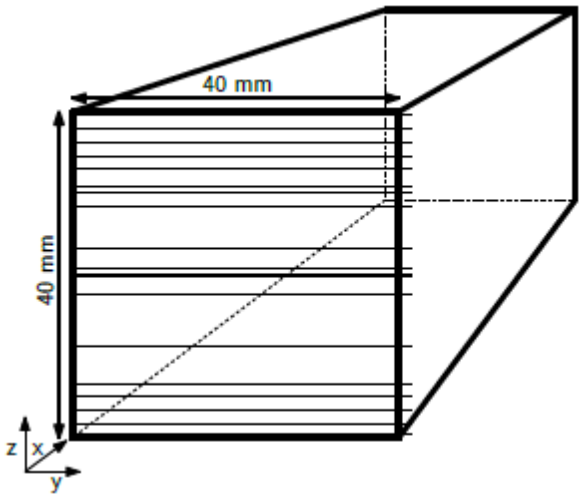

Figure 3.13 Schematic of the resonator. The lines on the front face represents the Z plane locations of the PIV scans.

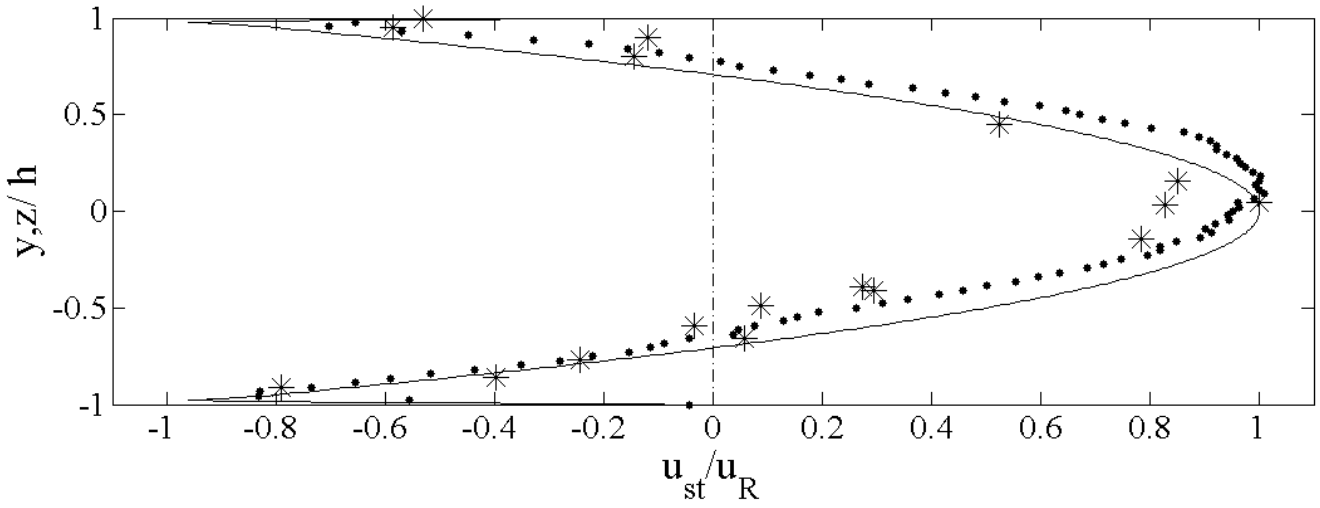

Figure 3.14 Axial component of the ensemble-averaged streaming velocity amplitude at the axial location where streaming velocity antinode occurs. $h = 0.5H$. ··· u_{st} along y at z=0; *** u_{st} along z at y=0; and – analytical solution.

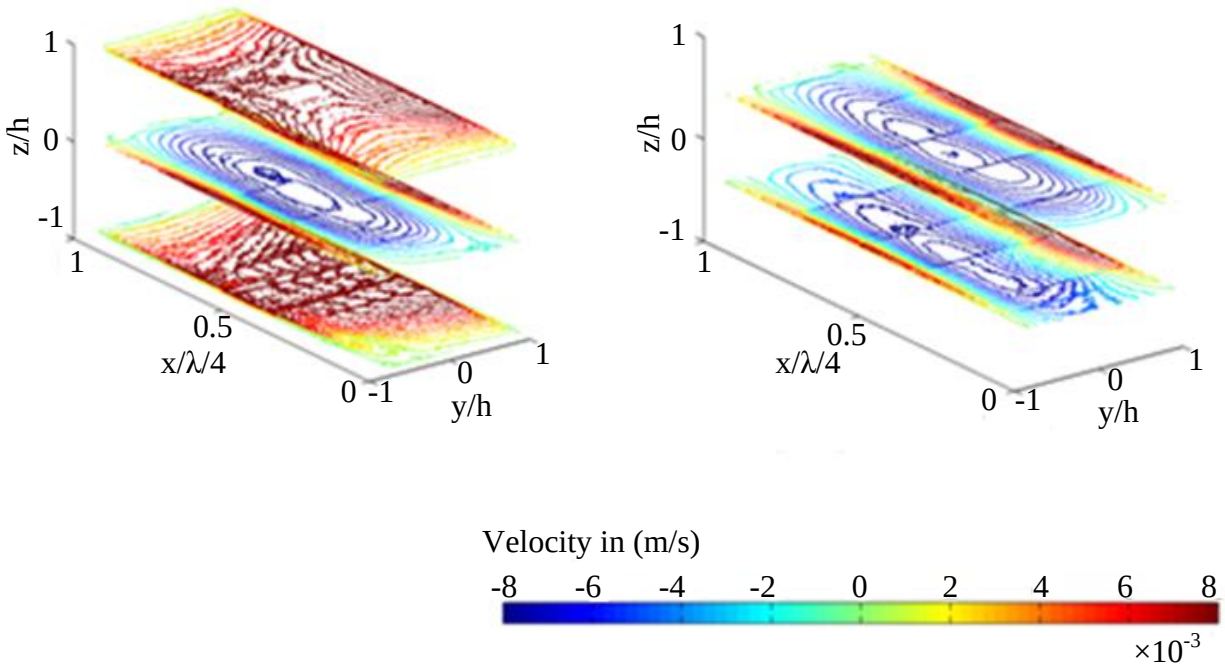

Figure 3.15 Two-dimensional axial component of the ensemble-averaged streaming velocity amplitude slices after being stitched and arranged in *z* axis. *h*=0.5*H*.

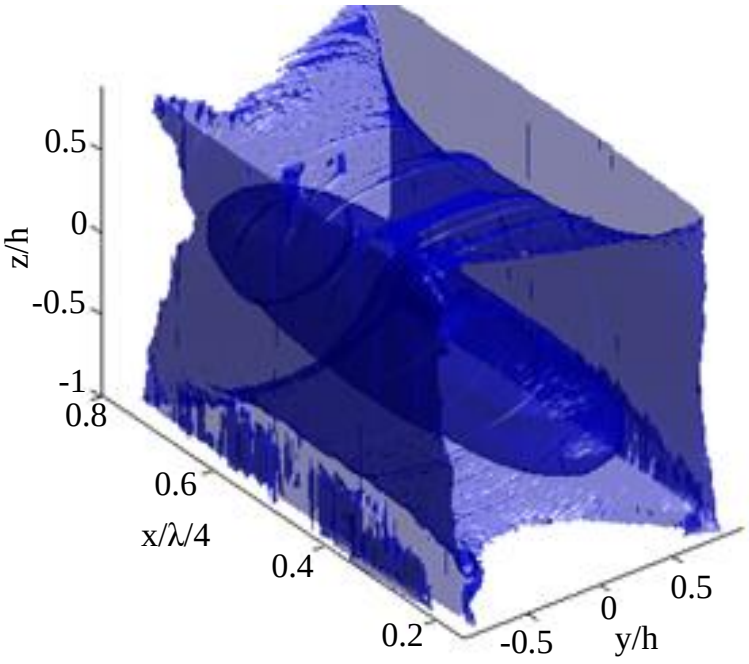

(a)

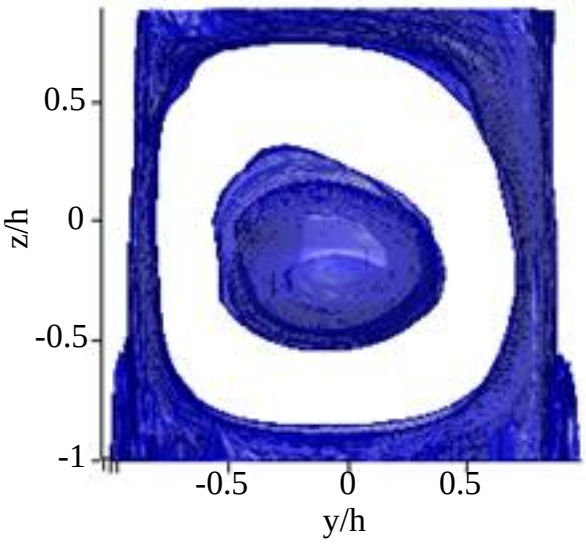

(b)

Figure 3.16 Three-dimensional iso-surface view of the axial component of the streaming velocity magnitude inside a square cross section resonator for $u_{st} = 0.0006\,\text{m/s}$ from different viewpoints: (a) isometric view; and (b) front view with +X axis coming out of the plane of paper.

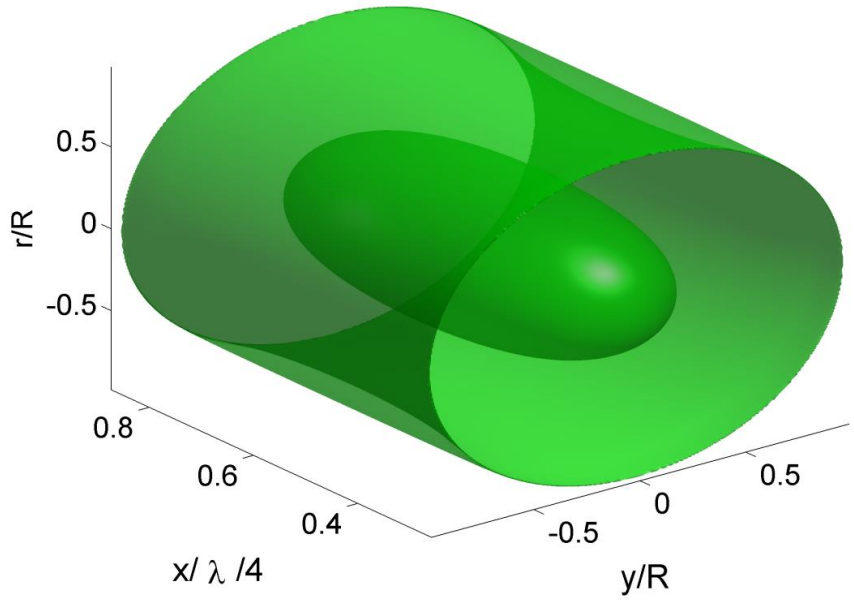

Figure 3.17 Three-dimensional iso-surface view of the axial component of streaming velocity magnitude inside a cylindrical resonator for $u_{st} = 0.0006\,\text{m/s}$.

4 Acoustic streaming due to the introduction of a stack in the resonator

4.1 Introduction

In a real thermoacoustic system, the acoustic streaming patterns are complex. These complex streaming flow structures originate from the interactions between the acoustic flow and the thermoacoustic core, namely the stack and the heat exchanger. Although, many experimental and numerical studies [30, 49, 82] have investigated acoustic streaming in an empty resonator, few studies are available on the acoustic streaming in a simplified thermoacoustic system. There is no literature on the characterisation of the acoustic steaming environment in a real thermoacoustic system. In this chapter, different configurations of simplified thermoacoustic core elements namely, stack and heat exchanger are introduced in the resonator and the resulting streaming environment is studied.

4.2 Methodology

Initially, the resonator was excited at an acoustic frequency of 1658 Hz which corresponded to a wavelength of 0.2 m. The camera field of view was $0.1\times0.08\,\mathrm{m}^2$. This selection of acoustic wavelength and camera field of view allowed for the capture of more than one complete streaming cell in the camera field of view. One complete streaming cell was captured in the center of the camera field of view and one-half streaming cell in the front and the back. The first stack configuration used is shown in Figure 4.1. It was made of ceramic with square pores of cross section 0.12×0.12 mm^2. The length of the stack was 1 cm. The second and the third stack configurations were similar with the only difference being the plate gap, g. The second stack, as shown in Figure 4.2.a had a plate gap of 1 mm and the third stack, shown in Figure 4.2.b had a

plate gap of 2 mm. These stacks were fabricated from glass plates used in microscope slides. Each plate had a dimension of $40\,\text{mm} \times 25.4\,\text{mm} \times 1\,\text{mm}$.

The first order instantaneous and the second order streaming velocities were simultaneously captured using the phase-locked ensemble averaging method described in chapter 2. Both the laser and the camera were synchronised with the pressure signal at the hard end of the resonator. The PIV system captured images at the phase corresponding to the peak instantaneous acoustic velocity. The sampling rate was same as the acoustic excitation frequency. Three hundred images were captured and the final velocity was found after ensemble averaging 300 velocity vector maps. All the vectors shown in the following sections are for the ensemble-averaged velocities.

4.3 Results and discussion

The instantaneous acoustic and the streaming velocity vector map of the acoustic flow at 1658 Hz are shown in Figure 4.3.a and Figure 4.3.b respectively. The instantaneous acoustic velocity node occurred at x=16 mm, as shown in Figure 4.3.a. The velocity antinode (peak instantaneous acoustic velocity) occurred one-quarter wavelength, $\lambda/4$, away from the velocity node. For wavelength, λ, of 0.2 m, the velocity antinode occurred at x=66 mm, as shown in Figure 4.3.a. The peak streaming velocity occurred at a distance of $\lambda/8$ from the instantaneous acoustic velocity node. As shown in Figure 4.3.b, $\lambda/8$ occurs at x=40 mm. The peak ensemble-averaged acoustic velocity magnitude was 1 m/s and the peak ensemble-averaged streaming velocity magnitude was 0.005 m/s. The streaming velocity vector map shows one complete streaming cell in the center and the portion of another streaming cell in the front and in the wake.

In order to study the effects of the stack on the Rayleigh streaming, the stack, shown in Figure 4.1 was located at one of the two locations. The first location was at x=66 mm, or $\lambda/4$, as shown in Figure 4.4. At this location, the instantaneous acoustic velocity is maximum and the Rayleigh streaming velocity is minimum, as shown in Figure 4.3. The resulting instantaneous acoustic and streaming velocity vector maps for the first stack location are shown in Figure 4.4.a and Figure 4.4.b, respectively. Previous experimental studies [38] have reported changes in the streaming velocity amplitude and in the shape of the Rayleigh streaming cell near the stack. Similar results were observed during the experiments reported here. The presence of the stack at the location of maximum instantaneous acoustic velocity caused the flow to become irregular, which can be seen when comparing the velocity vector maps for the acoustic velocity of Figure 4.3.a and Figure 4.4.a. A comparison between the streaming velocity vector maps of Figure 4.3.b and Figure 4.4.b revealed that the shape of the streaming cell was changed. In the absence of the stack, the horizontal dimension of the streaming cell was such that there were two streaming cells formed along the resonator width. In the presence of the stack, there was only one streaming cell along the transverse direction. The longitudinal dimension of the steaming cell was not affected in the presence of the stack.

The second location for the stack was at x=40 mm, or $\lambda/8$ from the acoustic velocity antinode, as shown in Figure 4.5. At this location, the streaming velocity amplitude was largest and the instantaneous acoustic velocity was less than one-half of the peak amplitude. The velocity vector map for the instantaneous acoustic velocity in Figure 4.5.a shows much less flow irregularity when compared with Figure 4.4.a. This was due to the fact that the acoustic velocity was considerably lower at this location than at the previous location. The velocity vector map for acoustic streaming in Figure 4.5.b shows different streaming cell shapes on either side of the

stack. As for the previous stack location, the streaming velocity amplitude on the right side of the stack, $45<x<80$, was larger than on the left side. This may be attributed to the fact that the instantaneous acoustic velocity amplitude is greater on the right side of the stack. The difference in the streaming velocity amplitude on either side of the stack was more pronounced at the second location, which again can be attributed to the larger difference in acoustic velocity amplitude on either side of the stack for the second stack location. Near the edges of the stack data could not be obtained due to flaring of the images. The flaring occurred due to reflection of the laser light from the stack wall. The presence of stack alters the Rayleigh streaming cell and introduces a different streaming pattern. It would therefore be necessary to characterise this form of streaming to better understand its effect on the heat transfer between the heat exchanger and the stack. For this, a detailed knowledge of the streaming flow near the stack edges and in between the stack plates is required, as described next.

Acoustic streaming near the stack end and in between the plates was observed for the two stacks, as shown in Figure 4.2. The flow was excited at 245.5 Hz, which corresponds to L=3λ/4. The peak instantaneous acoustic velocity amplitude was $u_a = 3.4$ m/s. The stack center was located at a distance of $3\lambda/8$ from the hard end. The stack shown in Figure 4.2.a had a gap, $g = 1$ mm or $7\delta_\nu$, in between the plates and the stack shown in Figure 4.2.b had a gap, $g = 2$ mm or $14\delta_\nu$. The streaming velocity for the stacks with a gap of 1 and 2 mm are shown in Figure 4.6 and Figure 4.7, respectively. In their analytical work, Hamilton *et al*. [16] studied the acoustic streaming in channels with arbitrary width. They concluded that, for channel widths smaller than $10\delta_\nu$, classical Rayleigh streaming was insignificant and only an inner streaming vortex was present. Even for a channel width of $20\delta_\nu$, the inner streaming vortex occupied 10% of the

channel width. In presence of a stack, a transition region is present near the stack ends. The transition region and the stack length determine the overall streaming environment inside and around the stack. The streaming velocity results for the stack with plate gap, $g = 7\delta_\nu$, are shown in Figure 4.6. One single streaming cell is present, as predicted by the analytical model. The magnitudes of the streaming velocity both inside the stack and near the stack ends were greater than the streaming velocity away from the stack. The streaming velocity results obtained for the stack with plate gap, $g = 14\delta_\nu$, indicate the presence of more than one streaming cell inside the stack near the edge. Since the plate gap was more than $7\delta_\nu$, a distinct outer streaming vortex was observed. The results presented here were in accordance with the analytical model predictions.

In a thermoacoustic core, heat exchangers are located on both side of the stack. A simple fin tube heat exchanger has parallel plates (as for the stack) with tubes running perpendicular to the axial flow direction. One single transparent glass cylinder was used in order to idealise the tubes in a fin tube heat exchanger. The cylinder was 1 mm in diameter and the length was equal to the resonator width. The flow was excited at 85 Hz and 100 Hz. The streaming velocity flow inside a resonator resulting from the interaction of the acoustic standing wave with the circular cylinder is shown in Figure 4.8 and Figure 4.9. At 85 Hz, the streaming flow was studied for various instantaneous acoustic velocity amplitudes at the location of the cylinder. For low acoustic amplitude, the streaming vortices were not fully developed as evident from Figure 4.8. Fully developed streaming cells were observed at higher velocity amplitudes, as shown in Figure 4.9 and Figure 4.10 respectively. In a fully developed streaming flow, four vortices were observed, one in each quadrant. The streaming behaviour observed in this study is similar to the analytical results presented by Nyborg [6].

4.4 Conclusions

Attempts were made to characterise the acoustic streaming flows present in an idealised thermoacoustic machines. It was found that presence of the stack significantly changes the streaming flow from the Rayleigh streaming observed in an empty resonator. Higher magnitudes of streaming velocities were observed near the stack end and inside the stack. Results were obtained for two stacks with different plate gaps. The results were consistent with analytical model predictions. The difference between the experimental results and the analytical results may also be due to absence of the effects of the transition region in the analytical model. The streaming flow structures resulting from the presence of a circular cylinder were completely different from either Rayleigh streaming or streaming due to stack. Four circulation regions were observed.

Idealised thermoacoustic core elements were introduced in the resonator and the resulting streaming flow structures were observed to be very different from Rayleigh streaming. A real thermoacoustic core would have both stack and heat exchangers and their interaction with each other would create a complex streaming environment. The main observation was that one simple Rayleigh streaming model is insufficient for characterising the overall streaming flow behaviour inside a standing wave thermoacoustic machine. Streaming could contribute significantly to heat transfer. The streaming flow patterns and the velocity amplitudes appear to depend strongly on the geometry of the stack and the heat exchangers.

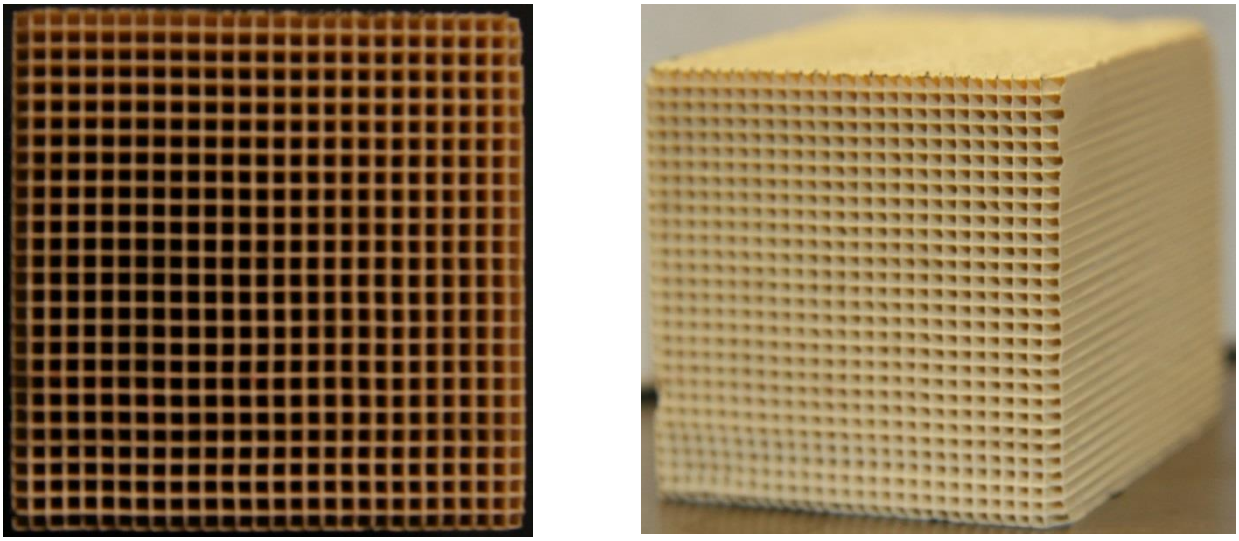

(a) (b)

Figure 4.1 Ceramic stack: (a) front view; and (b) perspective view.

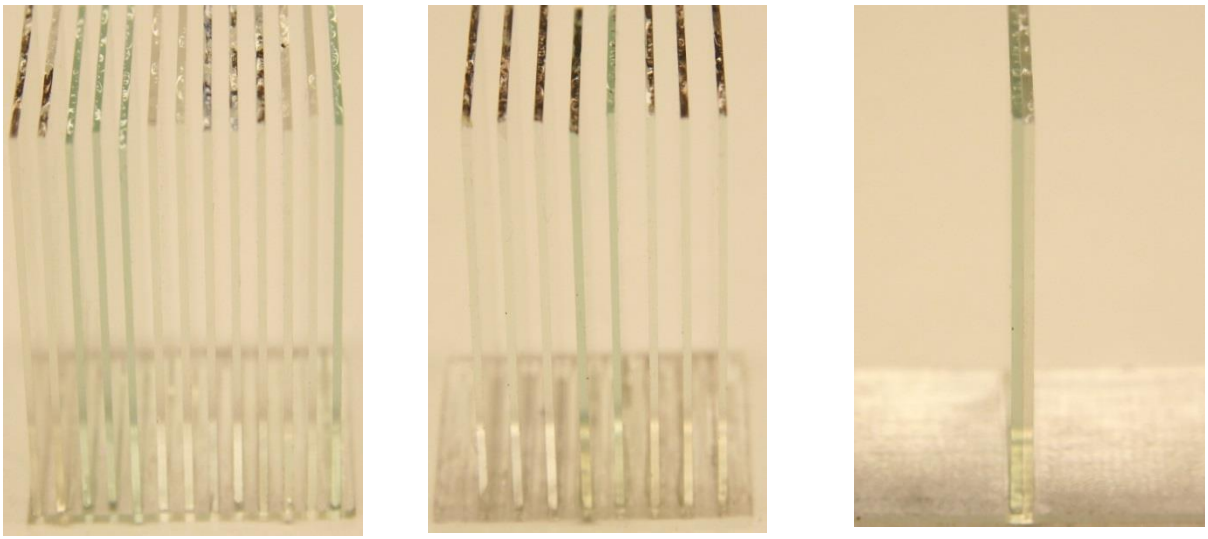

(a) (b) (c)

Figure 4.2 Glass stack: (a) plate gap of 1 mm; (b) plate gap of 2 mm; and (c) single plate.

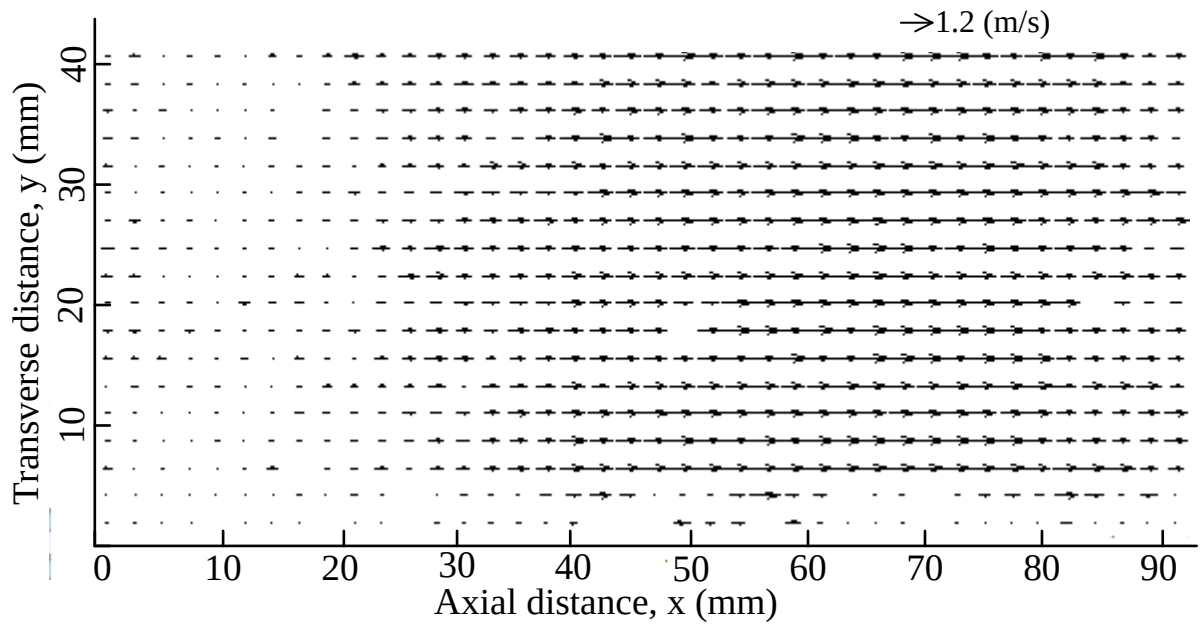

(a)

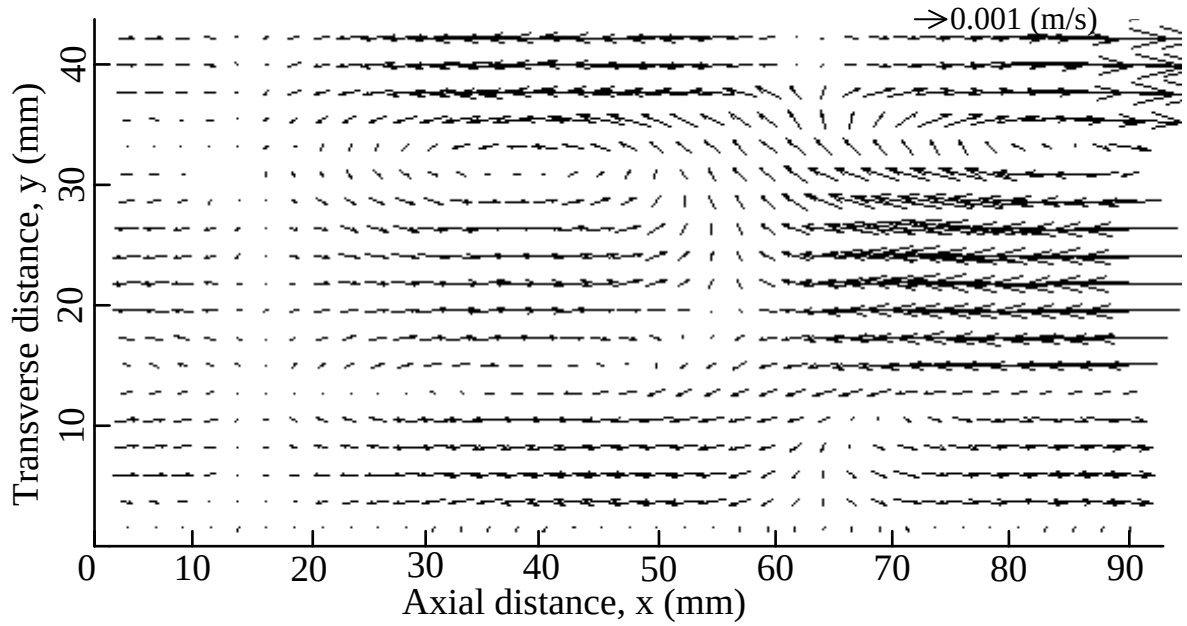

(b)

Figure 4.3 Velocity vector map at 1658 Hz without stack: (a) ensemble-averaged instantaneous acoustic velocity; and (b) ensemble-averaged streaming velocity.

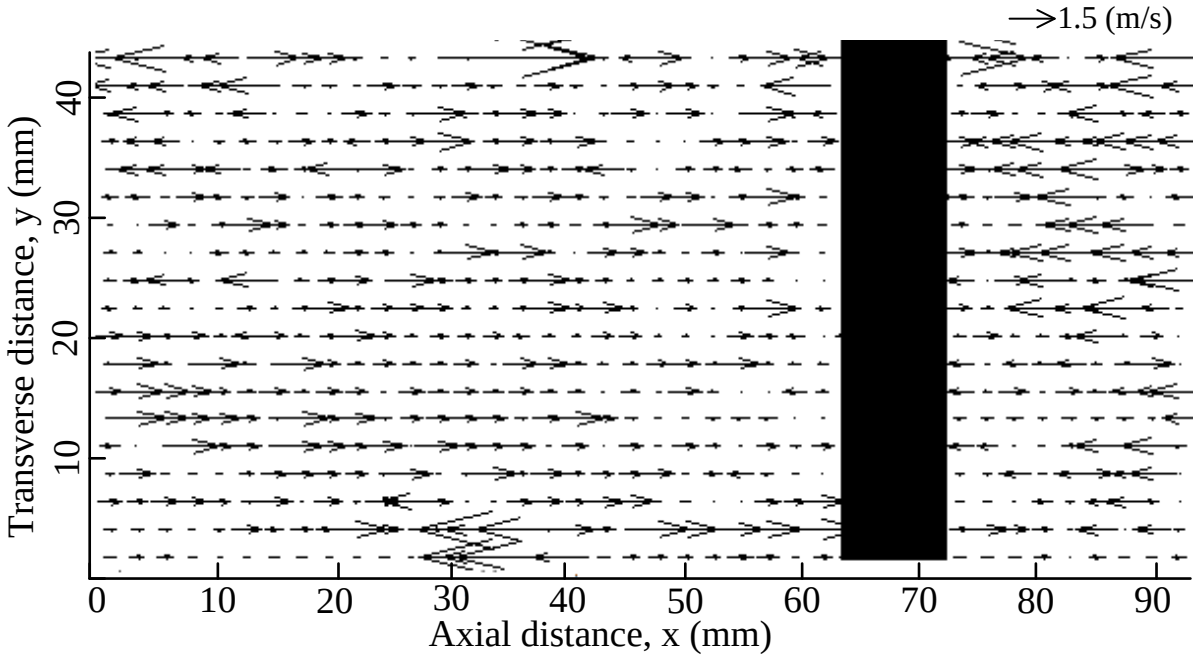

(a)

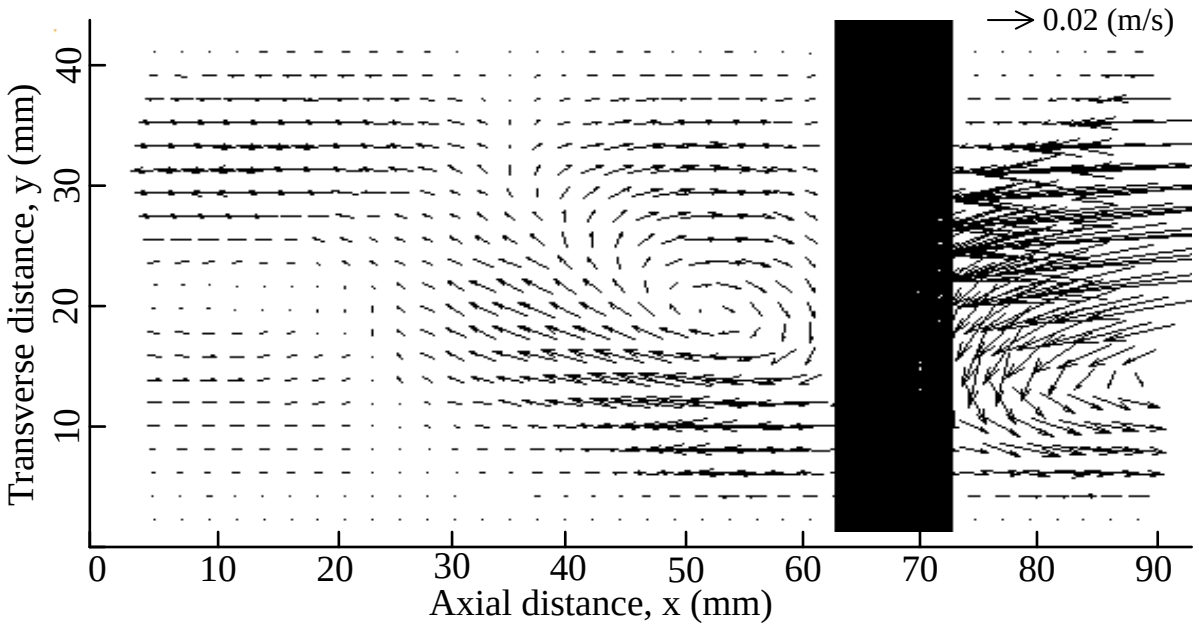

(b)

Figure 4.4 First stack location. Stack center located at x=66 mm. (a) Ensemble-averaged instantaneous acoustic velocity; and (b) ensemble-averaged streaming velocity.

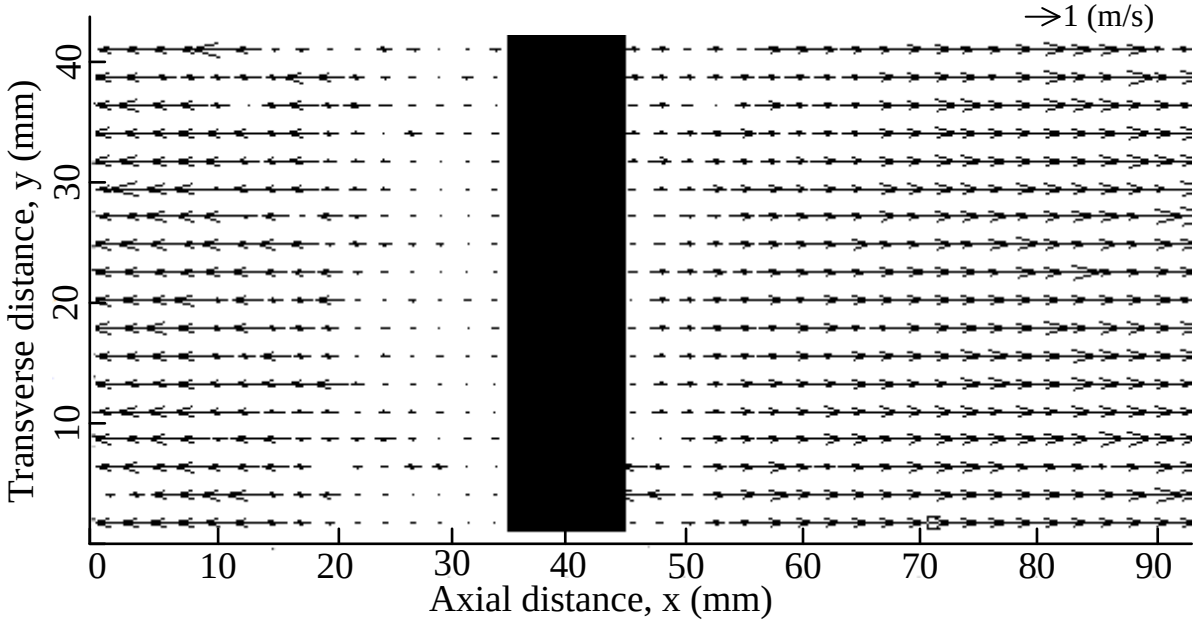

(a)

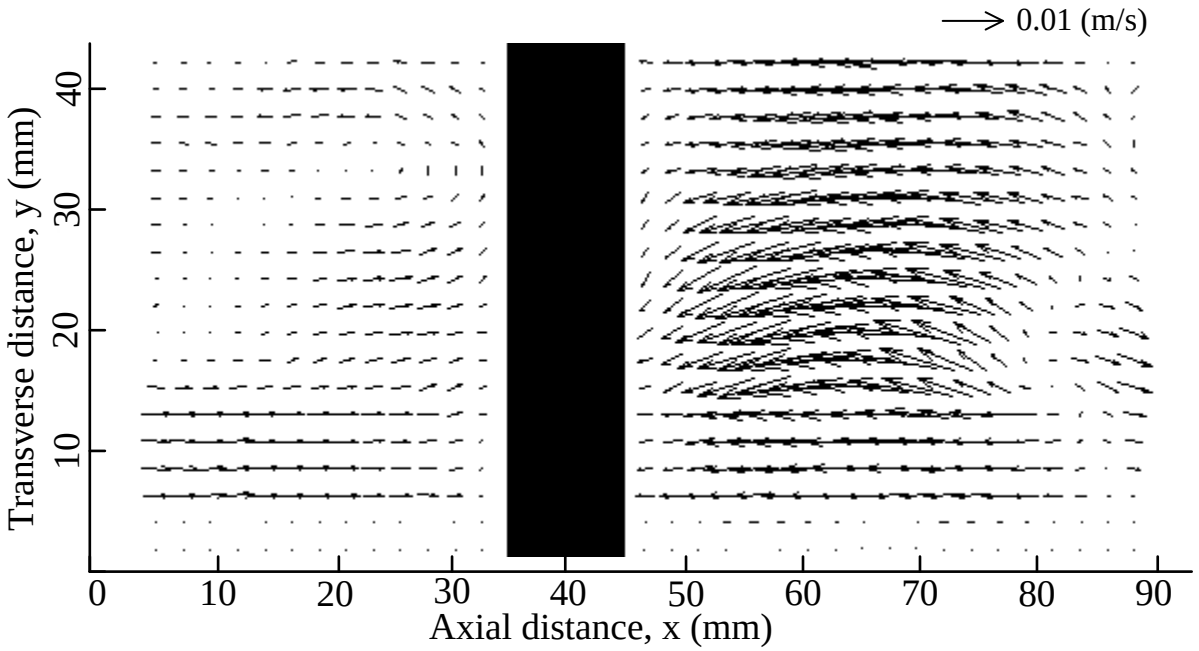

(b)

Figure 4.5 Second stack location. Stack center located at x=40 mm. (a) Ensemble-averaged instantaneous acoustic velocity; and (b) ensemble-averaged streaming velocity.

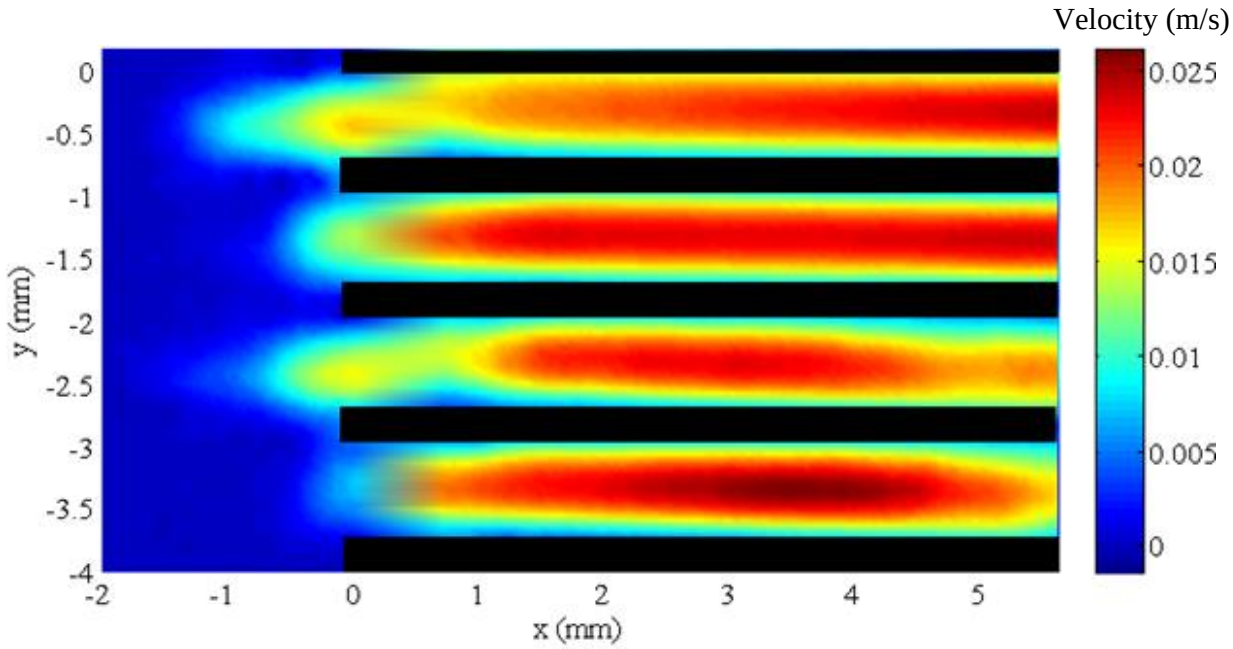

Figure 4.6 Ensemble-averaged streaming velocity for the glass stack with 1 mm gap between the plates. The flow was excited at 245.5 Hz and the peak instantaneous acoustic velocity amplitude was $u_a = 3.4$ m/s.

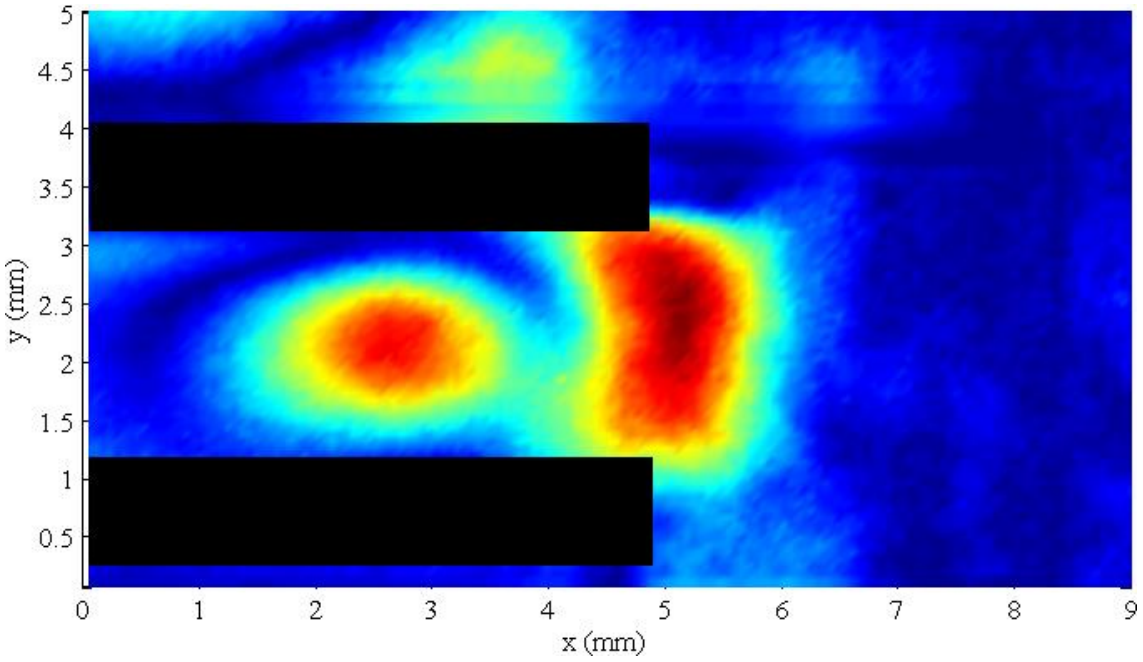

Figure 4.7 Ensemble-averaged streaming velocity magnitude for the glass stack with 2 mm gap between plates. The flow was excited at 245.5 Hz and the peak instantaneous acoustic velocity amplitude was $u_a = 3.4$ m/s. The color scheme of Figure 4.6 applies.

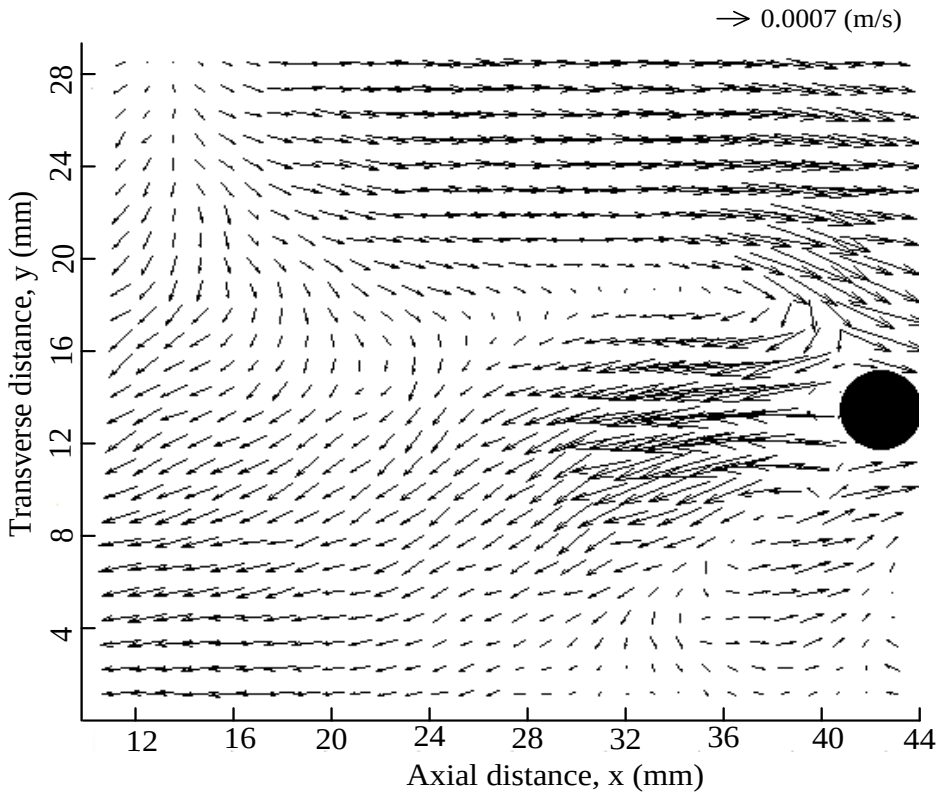

Figure 4.8 Ensemble-averaged streaming velocity around a cylinder at 85 Hz for a peak instantaneous acoustic velocity of u_a=0.34 m/s.

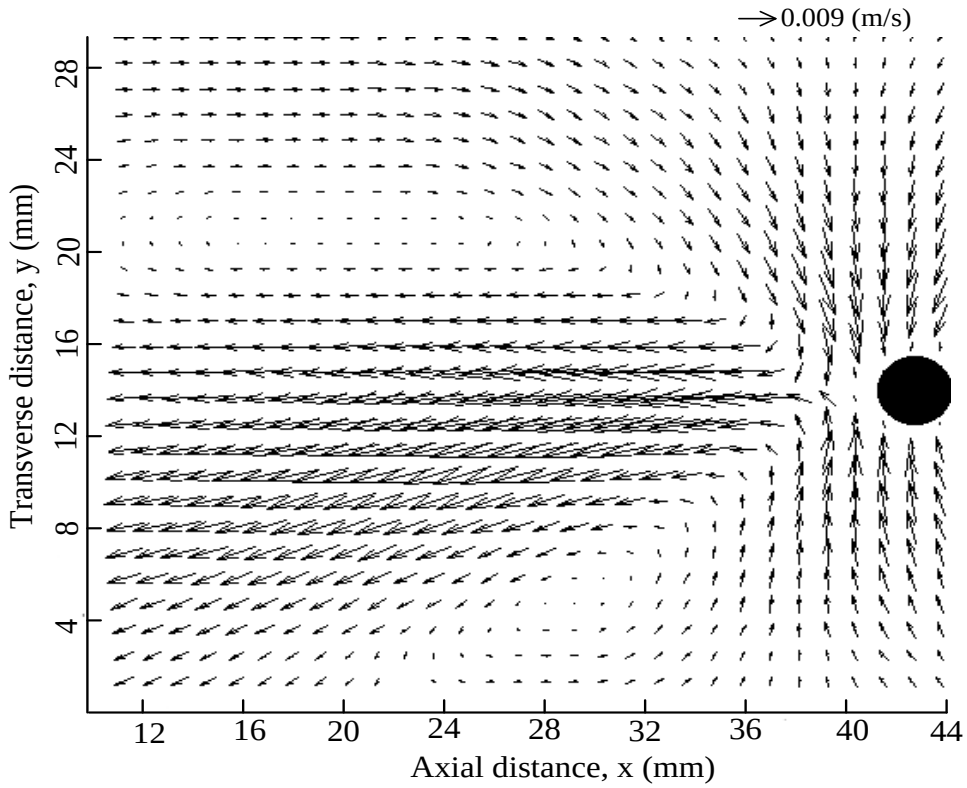

Figure 4.9 Ensemble-averaged streaming velocity around a cylinder at 85 Hz for a peak instantaneous acoustic velocity of u_a=0.76 m/s.

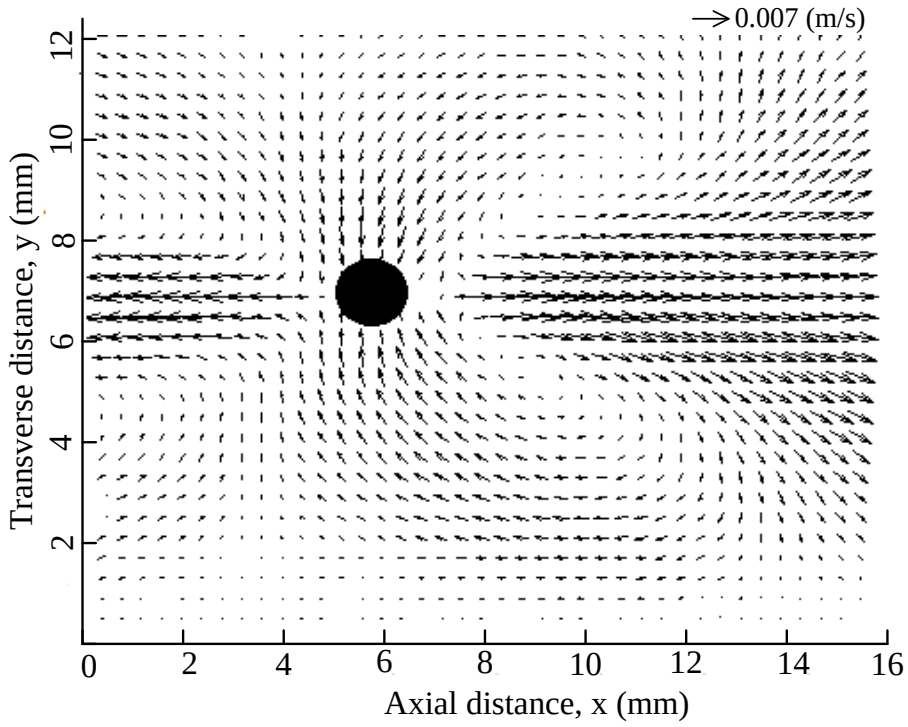

Figure 4.10 Ensemble-averaged streaming around a cylinder at 100 Hz. u_a =0.57 m/s

5 Numerical study of acoustic streaming in a standing wave resonator

5.1 Introduction

The Lattice Boltzmann Method, LBM is used to perform the numerical simulations of the acoustic standing waves flow in a resonator. The numerical results obtained from the LBM simulation are first validated for the acoustic and the streaming velocities through comparisons with the analytical results. Results for the Rayleigh streaming and the acoustic streaming in the region near the edges of a flat spoiler are then obtained. Finally, the flow and the spoiler geometry parameters are varied and their effect on the acoustic streaming is observed. The parameter studied are the peak instantaneous acoustic velocity, spoiler thickness, spoiler length and spoiler edge shape.

5.2 Validation

In order to verify the validity of the numerical results obtained from the LBM, comparisons were made with the analytical results available from the linear acoustic theory. The axial dimensions were non-dimensionalised by one-quarter wavelength, $\lambda/4$ and the transverse dimensions were non-dimensionalised by half the resonator width, $0.5H$. One-quarter wavelength was chosen as the characteristic axial dimension due to the fact that a Rayleigh streaming cell is one-quarter wavelength long. The numerical results presented are for the cases shown in Table 5-1. The analytical results were taken from the linear acoustic model developed by Nyborg [6].

5.2.1 Acoustic velocity

The axial component of the instantaneous acoustic velocity obtained from the analytical and the numerical results for case 2 of Table 5-1 is shown along axial and transverse directions in Figure 5.2.a and Figure 5.2.b respectively. The velocity profiles were obtained from the 2D numerical simulation results along the centerline of the resonator corresponding to Y=0 along the axial direction. The velocity profile in the transverse direction were obtained at the location of instantaneous acoustic velocity antinode, which corresponds to $X = \lambda/4$. The instantaneous axial acoustic velocity is plotted at two time instants corresponding to $\theta = \pi/2$ and $\theta = \pi/3$ rad. Very good agreement between the analytical and the numerical results was obtained. The axial component of the instantaneous acoustic velocity along the transverse direction is shown over the top half of the resonator in Figure 5.2.b. Three time instants corresponding to $\theta = \pi/2$, $\theta = \pi/3$ and $\theta = \pi/180$ rad were selected for comparison. As for the axial direction, the numerical results were in excellent agreement with the analytical results. The velocity overshoot, most pronounced for the time instant corresponding to $\theta = \pi/180$ rad, was well captured in the simulation. The numerical results appear to be accurate in the acoustic boundary layer and in regions away from the wall. The mean difference between the theoretical and the numerical results was found to be 1.4 % for the results shown in Figure 5.2.b.

5.2.2 Streaming velocity

The Rayleigh streaming results obtained from the LBM were compared with the analytical results. The axial (Figure 5.3.a) and the transverse (Figure 5.3.b) variations of the Rayleigh streaming velocity magnitude are shown in Figure 5.3. The velocity profiles were obtained from the 2D numerical simulation results along the centerline of the resonator corresponding to Y=0

along the axial direction. The velocity profile in the transverse direction was obtained at the location of the streaming velocity antinode, which occurred at $X = \lambda/8$. The numerical results presented here corresponds to cases 1, 2 and 3 of Table 5-1. The numerical results for the Rayleigh streaming velocity along the axial direction were in satisfactory agreement with the analytical results. The axial variation of the streaming velocities corresponding to Mach number, M=0.014 and M=0.031 were in very good agreement with analytical results. As the Mach number was increased, the deviations from linear acoustic theory became more significant, as expected. This can be attributed to the non-linear effects which were not taken into account by the linear acoustic theory. The drive ratio corresponding to case 3 was approximately 5.9%, near the limit of validity of the linear theory. Another deviation observed in the numerical results from the analytical results with increasing M was the axial dimension of a complete Rayleigh streaming cell. For M=0.043, the axial dimension of the streaming cell was smaller than the analytically predicted value of $\lambda/4$ by 3%.

The numerical and the analytical results for the transverse variation of the Rayleigh streaming velocity magnitude were in very good agreement at M=0.014 and M=0.031. Both the inner and the outer streaming cells were well resolved by the numerical scheme. As for the axial variation, the numerical results tend to deviate from the analytical results for large amplitude. The transverse dimension of the inner streaming cell tends to be smaller than the predicted cell dimensions for higher Mach numbers. The analytical results slightly under predicted the streaming velocity magnitudes in the inner streaming cell while they over predicted in the outer streaming cell when compared with the numerical results obtained at high drive ratios, as in case 3.

The simulation of the Rayleigh streaming in an empty resonator was challenging because the streaming velocity amplitude was very small in comparison with the amplitude of acoustic particle velocity. The verification results for the instantaneous acoustic and the streaming velocities confirmed the accuracy of the numerical method for the study of acoustic streaming in a standing wave resonator.

5.3 Streaming from a rectangular spoiler

A rectangular, uniform spoiler was added to the simulation domain, corresponding to case 2 of Table 5-1. The length, Lp of the flat spoiler was taken to be very small, 2% of the acoustic wavelength and the spoiler thickness, t_p was 10% of the resonator width, H. As the blockage ratio, t_p/H was $\leq$ 10% it was safely assumed that the wall effects due to resonator can be neglected. The center of the spoiler was located at $X = 3\lambda/8$ and $Y = 0$ according to the coordinate system shown in Figure 5.1. Two types of acoustic streaming were observed in the presence of a thin rectangular spoiler in the standing wave resonator. The first type of streaming was Rayleigh streaming, characterised by the streaming cells of length equal to $\lambda/4$. Both inner and outer streaming cells were observed. The peak streaming velocity amplitude for each case was two orders of magnitude smaller than the peak instantaneous acoustic velocity amplitude, as shown in Table 5-1.

A second type of streaming was observed near the edges of the spoiler. For convenience, it was referred to as edge streaming. The acoustic streaming due to the interaction between the standing wave and the spoiler is shown in Figure 5.4 . For convenience the origin was moved along the horizontal axis to coincide with the right side edge of the spoiler. In order to plot the axial and

the transverse variation of the edge streaming, velocity magnitude data was extracted along the red dashed lines depicted in Figure 5.1. The interaction between the spoiler and the acoustic flow in the standing wave resonator generated an acoustic streaming pattern which was distinct from the Rayleigh streaming produced due to acoustic standing wave interaction with the wall of a resonator without any obstruction in the flow path. The most important feature of the edge streaming was the peak streaming velocity magnitude. When comparing the edge streaming amplitude with the Rayleigh streaming of Figure 5.3 for M=0.031, it was observed that the peak edge streaming amplitudes were two orders of magnitudes greater than the peak Rayleigh streaming velocity amplitude. The second distinct feature of the edge streaming was presence of two streaming cells on either edges of the spoiler. The first streaming cell, which was adjacent to the spoiler end, was smaller in size and larger in peak velocity amplitude than the second streaming cell. The maximum streaming velocity of the second cell was approximately 25% smaller than the velocity amplitude of the first streaming cell. But it was still one order of magnitude greater than the Rayleigh streaming velocity amplitude. The third distinct feature of edge streaming was that its amplitude was proportional to the magnitude of the maximum instantaneous acoustic velocity at the edge. It can be inferred from Figure 5.5 that the streaming velocity amplitude for both the streaming cells on the left hand side, LHS edge of the spoiler was higher than the streaming amplitudes of the two cells on right hand side, RHS edge. The magnitude of the maximum instantaneous acoustic velocity at the edge also affects the dimension of the two streaming cells. The axial length of each streaming cell on the LHS of the flat spoiler was larger than its respective counterpart on the RHS of the spoiler. An important detail to consider here is the location of the spoiler. The spoiler center was located at a distance of $\lambda/8$ away from the location of the peak instantaneous acoustic velocity in the resonator which

occurred at X= $\lambda/4$. Neither edges of the spoiler were located at an instantaneous acoustic velocity antinode. For the simulation results presented in Figure 5.5, the maximum instantaneous acoustic velocity at the RHS of the spoiler was 8.24 m/s, while the peak instantaneous acoustic velocity in the resonator at the location of X= $\lambda/4$ was 10.57 m/s. If either edge of the spoiler was located at an instantaneous acoustic velocity antinode, it would experience higher streaming velocity magnitudes than for the present case. A schematic of different streaming vortices formed due to the rectangular spoiler is shown in Figure 5.6. The streaming cells are shown for the R.H.S only. The primary/first streaming cells are shown in red colour, the secondary/second streaming cells are shown in yellow and the Rayleigh streaming cells are shown in blue. The peak edge streaming amplitudes and the axial dimensions of the first and second edge streaming cells are also shown in the curve below the resonator schematic.

The edge streaming is an important type of acoustic streaming. It is distinct from the Rayleigh streaming. Due to its high velocity amplitude and localised nature, edge streaming seems to play a more significant role in heat transfer when compared to Rayleigh streaming. This would appear to have important applications in the design of thermoacoustic engines. In order to further understand edge streaming, a parametric study was performed. The flow and the spoiler geometry parameters were varied and their effects on edge streaming were investigated. Results of the parametric study are presented in the following subsections. Except for the results discussed in section 5.3.1, where effects of peak instantaneous acoustic velocity amplitude were studied, the peak instantaneous acoustic velocity was fixed at 10.57 m/s for rest of the cases.

5.3.1 Acoustic velocity amplitude

The effect of peak instantaneous acoustic velocity amplitude on edge streaming is shown in Figure 5.7 and Figure 5.8. The axial and the transverse variation of the streaming velocity magnitude are presented in both dimensional (Figure 5.7) and non-dimensional (Figure 5.8) forms. The axial axis was non-dimensionalised by $\lambda/4$, which corresponds to the length of one Rayleigh streaming cell. The transverse axis was non-dimensionalised by the half resonator width, $0.5H$. The flow parameters for the three cases along with some results considered are shown in Table 5-2.

The axial variation in Figure 5.7 shows an increase in the peak streaming velocity magnitude with increasing M. The length of the streaming cell adjacent to the spoiler edge does not change significantly with M. On the other hand, the length of the second streaming cell increases with increasing M. The transverse variation of the edge streaming was symmetric on either side of $y/0.5H = 0$, which coincides with the center line of the spoiler. As for the axial variation, the peak streaming velocity magnitude increases with M. The peak velocity magnitudes of the first and the second streaming cell were compared with the peak instantaneous acoustic velocity magnitude and the results are shown in Table 5-2. A comparison between these results with the results of Table 5-1 shows that for all cases, with the exception of case 4, the second streaming cell was present. Thus, for very low maximum instantaneous acoustic velocities, only one edge streaming cell occurs. Two streaming cells appear when the maximum instantaneous acoustic velocity at the edge was further increased.

The non-dimensional edge streaming velocity magnitude variation along the axial and the transverse directions is shown in Figure 5.8. The edge streaming velocity was non-

dimensionalised by the peak Rayleigh streaming velocity as given in Table 5-1. The non-dimensional results show a trend opposite to those of the dimensional results. In general, it was observed that the peak non-dimensional edge streaming velocity magnitude decreased with increasing M. This trend was reversed for the second streaming cell, as evident from the axial variation. Let $f(u)$ and $g(u)$ be the analytical functions of the maximum instantaneous acoustic velocity, u occurring at the spoiler edge, which governs the behaviour of the first and the second edge streaming cells, respectively. In Figure 5.8, the edge streaming velocity was non-dimensionalised by the Rayleigh streaming velocity which is a function of u^2. The trend shows that when u increases $f(u)/u^2$ decreases but $g(u)/u^2$ increases. It can be concluded that any power law dependence on the velocity in $f(u)$ must have a maximum power of two while there would be velocity terms in $g(u)$ with a power of three or more. This further demonstrates a distinct feature of the edge streaming when compared with the Rayleigh streaming.

5.3.2 Effects of spoiler thickness

The effects of the spoiler thickness, t_p on edge streaming are shown in Figure 5.9. The spoiler thickness was non-dimensionalised by the resonator width, H. Different streaming velocity amplitudes and streaming cell dimensions related to different spoiler thicknesses are given in Table 5-3. Three thicknesses of the spoiler were selected for this study. The three spoiler thicknesses corresponded to t_p/H = 0.05, 0.1 and 0.15. These three values of t_p/H were selected in order to eliminate or to minimise the effects of the resonator wall on the flow structures developed resulting from the interactions between the acoustic flow and the spoiler.

Another way of representing the spoiler thickness parameter was based on ratio of the spoiler thickness and the acoustic penetration depth, t_p/δ_v. This non-dimensional spoiler thickness parameter shows the effect of spoiler thickness relative to acoustic penetration depth. The three t_p/δ_v ratios considered were 2.3, 4.6 and 6.9. The axial and the transverse variations, shown in Figure 5.9 demonstrate similar trends. The edge streaming amplitude increased with increasing spoiler thickness. The results of Table 5-3, show that when the spoiler thickness was doubled from 0.05 to 0.1 or from 0.1 to 0.15 the peak edge streaming amplitudes corresponding to the first, V_{sp1} and the second, V_{sp2} edge streaming cells respectively were not increased in the same proportion. The shift in the peak amplitude of edge streaming away from spoiler centerline in the transverse direction and spoiler edge in axial direction was indicative of the spoiler thickness. Although a shift in the peak amplitude location was observed, the axial length of the primary streaming cell, Ls1 adjacent to the spoiler remains constant.

5.3.3 Effects of spoiler length

In thermoacoustic systems, much work has been done in order to optimise the gap between the stack and the heat exchangers. The acoustic displacement was considered to regulate the heat transfer [55]. In current study also, effects of the spoiler length on the edge streaming relative to the maximum acoustic displacement were studied. The results are shown in Table 5-4. The three spoiler length to peak acoustic displacement ratio, Lp/x_a considered were one-half, one and four, respectively. It was hypothesized that, for a spoiler length smaller than the acoustic displacement, the acoustic flows on either side of the spoiler would interact with each other. Conversely, for spoiler length four times the maximum acoustic displacement, flow on either ends would not be affected. Figure 5.10 illustrates the effect of the spoiler length on the edge

streaming. The axial variation shows that the peak streaming velocity and the length of the streaming cell for the streaming cell adjacent to the spoiler edge remains unaffected by spoiler length. A careful examination of the peak streaming velocity reveals a slight decrement due to increasing spoiler length. The secondary streaming cell in the axial direction experiences variations in both the peak streaming velocity magnitude and the cell length due to variation in the spoiler length. A decrease in the peak streaming velocity amplitude and the cell length with increasing spoiler length was observed. This trend is consistent with the hypothesis made earlier. For each case, the center of the spoiler was located at the velocity antinode of the resonator and for longer spoiler lengths the maximum instantaneous acoustic velocity at the edge of the spoiler decreases because the spoiler edge was further away from the instantaneous acoustic velocity antinode.

5.3.4 Influences of edge cross-sectional shape

The effects of different spoiler edge shapes on edge streaming were also investigated. Five different cross-sectional profiles were considered. These different configurations and their effects on edge streaming are summarised in Table 5-5. Two triangular end configurations with converging angle, α of 45^o and 26.6^o were investigated, along with a circular, an elliptical and a rectangular edge profile. The axial and the transverse variations of the edge streaming velocities for different edge configurations are illustrated in Figure 5.11. Both the primary and the secondary streaming cells were influenced by the edge shape. The primary streaming cell experienced changes in both the peak streaming amplitude and the cell length with different edge configurations. As expected, more streamlined edge configurations yielded smaller peak streaming amplitudes and streaming cell lengths. The triangular edge configuration (26.6^o) where the height, a, is equal to the width, b, of the spoiler, resulted in the smallest peak streaming

amplitude and cell length. The rectangular edge yielded the highest peak streaming magnitude and cell length for the first edge streaming cell. The elliptical configuration led to smaller magnitudes for both peak edge streaming velocity and streaming cell length when compared with the circular configuration. The primary or the first streaming cell for both the triangular (45^o) and the circular edges exhibited a similar peak streaming velocity magnitude but the length of streaming cell for the triangular configurations was smaller than the round configurations. The peak streaming velocity of the secondary streaming cell for the elliptical and the triangular (26.6^o) configuration was the same. The peak streaming velocity for the triangular (45^o) configuration was slightly greater than for the circular configuration. Overall, the extent of the secondary streaming cell along the axial direction, Ls2 was same for all the configurations except for the rectangular edge, which extends even further. The transverse variations illustrated some important artifacts which resulted from varying the edge configuration. As for the axial variation, transverse variation also showed similar trend for peak streaming amplitude. An outward shift of the peak from the center line of the spoiler was also observed which was a result of increasing spoiler tip thickness, from the streamline configuration ($\alpha=26.6^o$) towards the rectangular edge. Another interesting feature was that although the streaming velocity reaches an asymptotic value for $y/0.5H = \pm 0.4$, there were two distinct streaming cells for the triangular configuration ($\alpha=26.6^o$) on both side of the spoiler, and one single streaming cell for the rectangular configuration. In between these two configurations, this secondary streaming cell merged into the primary streaming cell, from streamlined to blunt configurations.

5.4 Three-dimensional simulation of acoustic streaming flow

All the numerical results reported thus far were from the 2D simulations, where depth of the resonator was considered negligible. In a real thermoacoustic system, interaction of acoustic standing wave with stack and heat exchangers would cause 3D streaming flow structures. The computational cost of the 3D simulations was very high. Therefore, only two cases corresponding to case 2 and 5 of Table 5-1 and Table 5-2 were simulated in 3D. The depth of the resonator was taken same as its width, H. For case 5, the span of the spoiler was same as the resonator depth. This was done to avoid tip vortices. The results for the 3D simulations of case 2 are shown in Figure 5.12. In Figure 5.12 the planar Rayleigh streaming velocities are shown corresponding to one streaming cell only i.e. for half the resonator length. In the top figure, the streaming velocity is shown over the center plane along the axial direction corresponding to $Z = 0$. The maximum streaming velocity occurs in the center plane. It was observed that away from this plane the velocity amplitude decreases over the outer streaming cell. This is clearly shown by the three velocity planes perpendicular to the axial direction. In Figure 5.12.b, an iso-surface is shown for a velocity magnitude equal to 0.02 m/s. The iso-surface is shown for half the depth of the resonator for positive Z direction. The inner streaming cell was affected by the resonator shape while the outer streaming cell was circular in cross section and thus remained unaffected by the resonator shape. Similar conclusions were obtained from experimental study of Rayleigh acoustic streaming inside a square cross section resonator in chapter 3. In thermoacoustic machines, the bulk of heat transfer between the stack and the heat exchangers occurs in the plane perpendicular to the axial direction. In order to assess the effects of Rayleigh streaming on heat transfer, the velocity in the plane perpendicular to axial direction needs to be studied. Figure 5.12 also shows that the streaming velocity magnitudes are high near the

resonator wall and also near the resonator corner. This constitutes inner streaming. Higher magnitudes of outer streaming occur near the resonator centerline. The perpendicular plane in which the largest streaming magnitudes were found was located in the center of the Rayleigh streaming cell. It was observed that away from the center of the Rayleigh streaming cell, the velocity magnitude and the area of the outer streaming cell along the perpendicular plane also decreased. At the resonator edges, velocity magnitudes were higher which may be attributed to circulation of the flow at the corners.

The results from the 3D simulations of the acoustic streaming in a square cross section resonator with a rectangular spoiler are shown in Figure 5.13 and Figure 5.14. As shown in Figure 5.6, with the introduction of a spoiler, different streaming structures appeared in the resonator. In Figure 5.13, the Rayleigh streaming structures are shown. Here also the Rayleigh streaming cells have a similar shape as for the empty resonator. These Rayleigh streaming cells appeared away from the spoiler on either side. Different iso-velocity surfaces for the edge streaming are shown in Figure 5.14. The results shown are for only one-half of the resonator in the positive Z direction. The 3D nature of the edge streaming was evident in the regions near the side walls of the resonator. For lower edge streaming velocity magnitudes, the streaming structure near the wall differs from that away from wall. But as the velocity magnitude increases, those near wall streaming structures disappear. Thus unlike the Rayleigh streaming where the velocity magnitudes are higher in the near wall and in the corner region, the edge streaming near the wall has smaller magnitudes.

5.5 Conclusions

The Lattice Boltzmann Method based numerical scheme was used to simulate acoustic streaming. Both the instantaneous acoustic and the Rayleigh steaming results were validated through comparisons with the linear acoustic theory. It was found that the LBM provided accurate numerical predictions for the acoustic standing wave flows inside a resonator. An idealised stack in the form of one single rectangular spoiler was introduced in the simulation domain and the resulting streaming environment was studied. Distinct salient features of the edge streaming were observed and compared with the Rayleigh streaming. It was concluded that the edge streaming would play a much more important role in heat transfer than the Rayleigh streaming, especially in the case of stack and heat exchangers. A parametric study of the edge streaming was performed and it was observed that a spoiler with greater thickness, rectangular end shape and shorter length would yield greater edge streaming amplitudes.

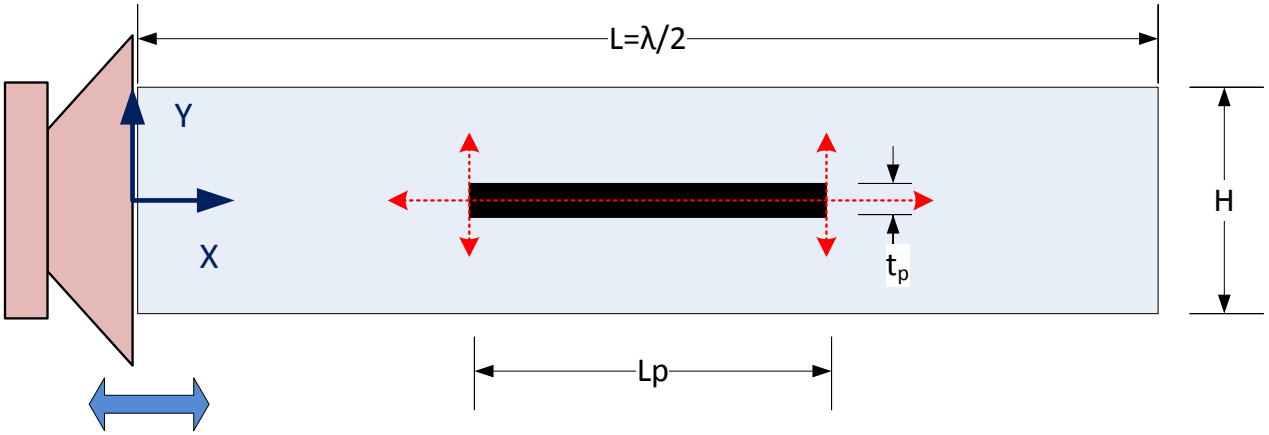

Figure 5.1 Schematic of the numerical setup of the resonator with a spoiler. The red dashed lines represent the lines along which velocity data was extracted for the results shown for edge streaming. The coordinate system is also shown with +Z axis coming out of the plane of paper.

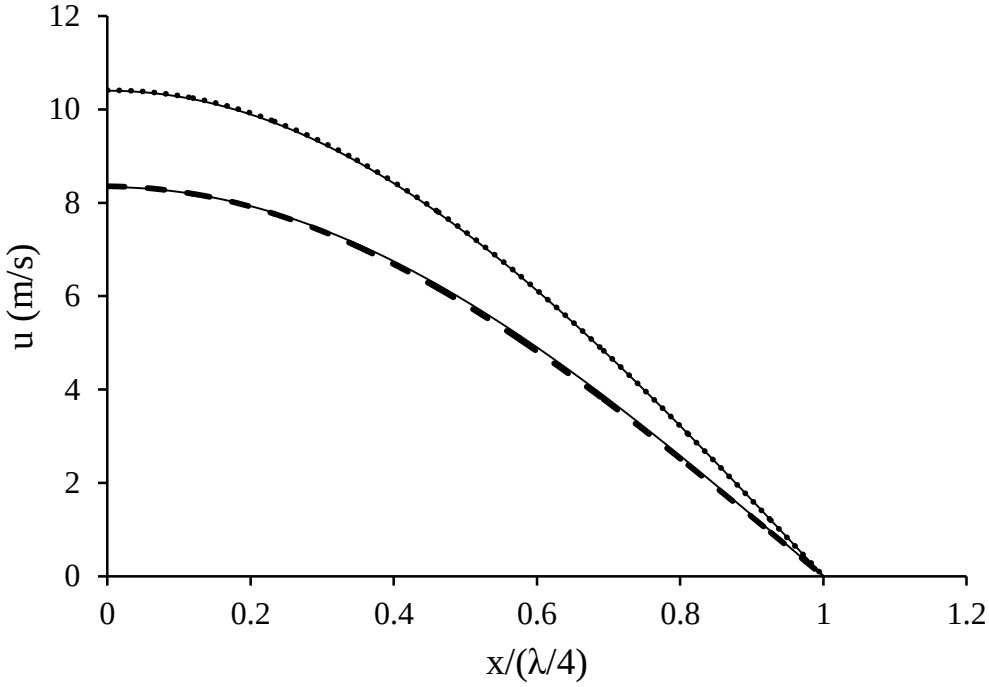

(a)

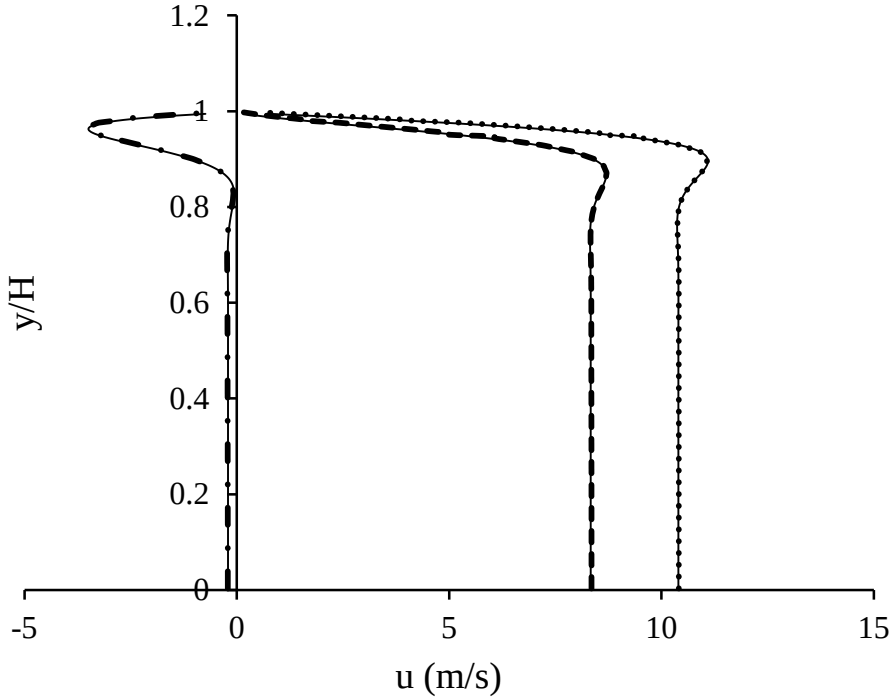

(b)

Figure 5.2 Theoretical and numerical axial component of the instantaneous acoustic velocity. (a) Axial direction, and (b) transverse direction. (··· $\theta = \pi/2$, -- $\theta = \pi/3$, -•- $\theta = \pi/180$ and solid line=analytical)

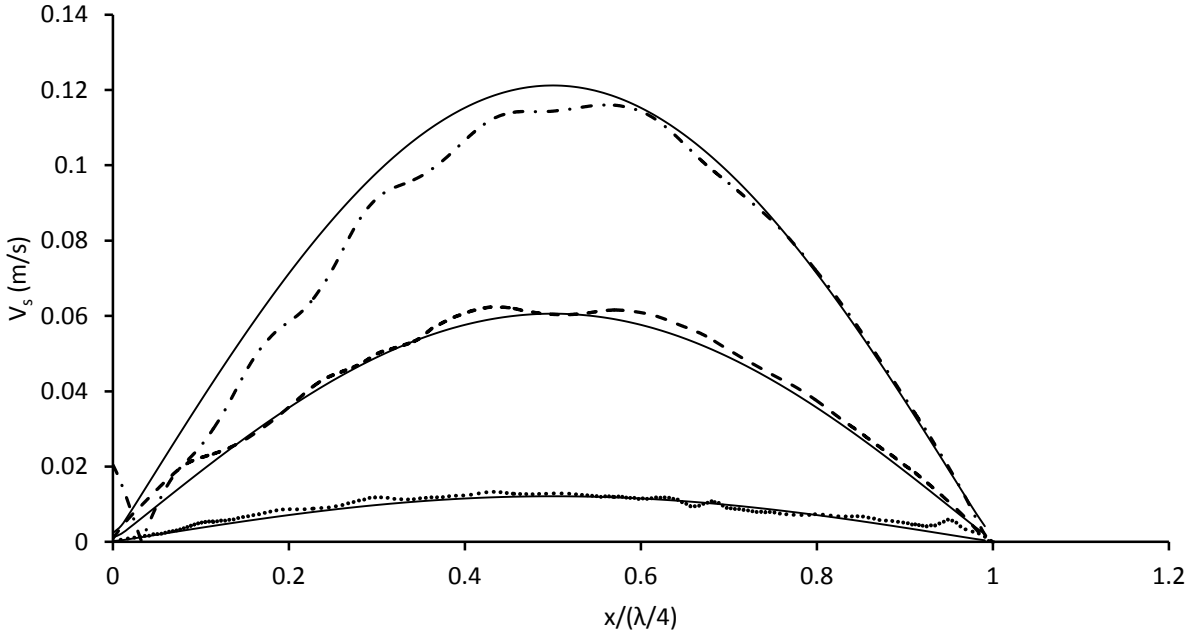

(a)

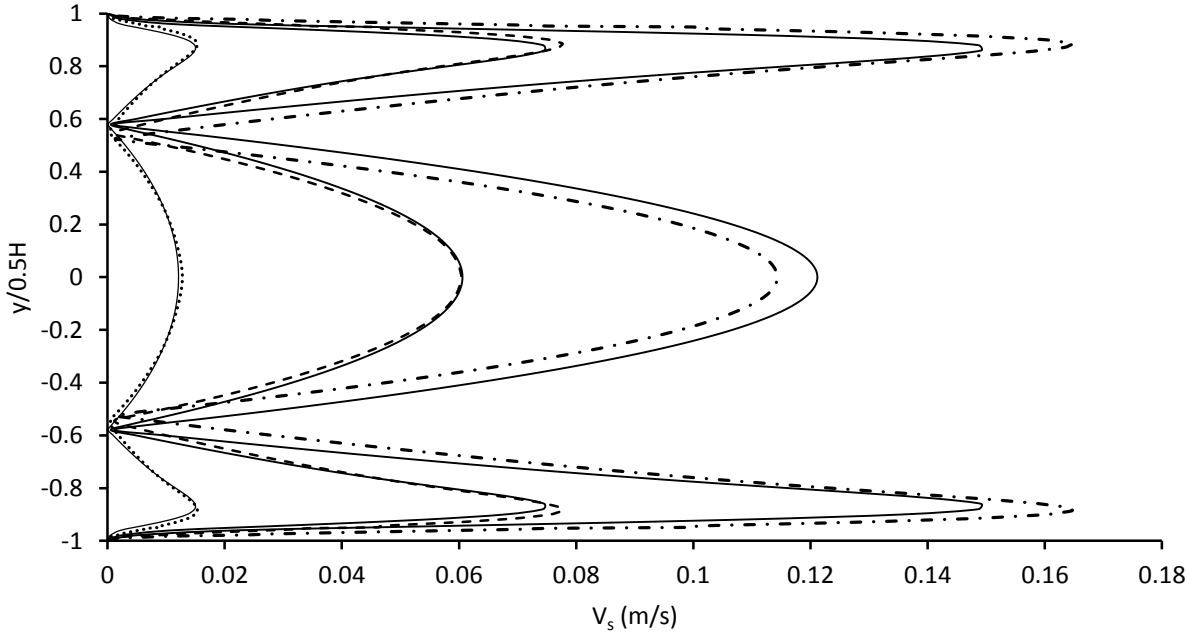

(b)

Figure 5.3 Theoretical and numerical streaming velocity magnitude for different Mach numbers. (a) Axial direction, and (b) transverse direction. (⋯ M=0.014, -- M=0.031, -•- M=0.043 and solid line=analytical)

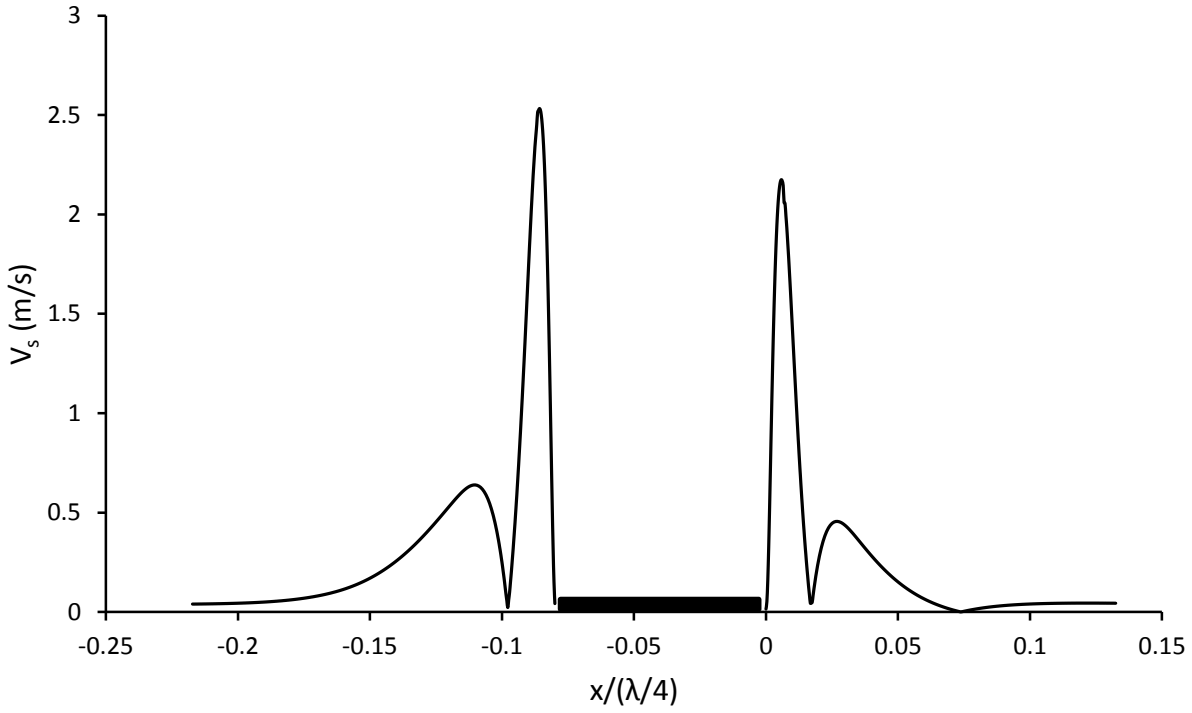

Figure 5.4 Axial variation of the streaming velocity magnitude due to asymmetric acoustic velocities at the two spoiler ends.

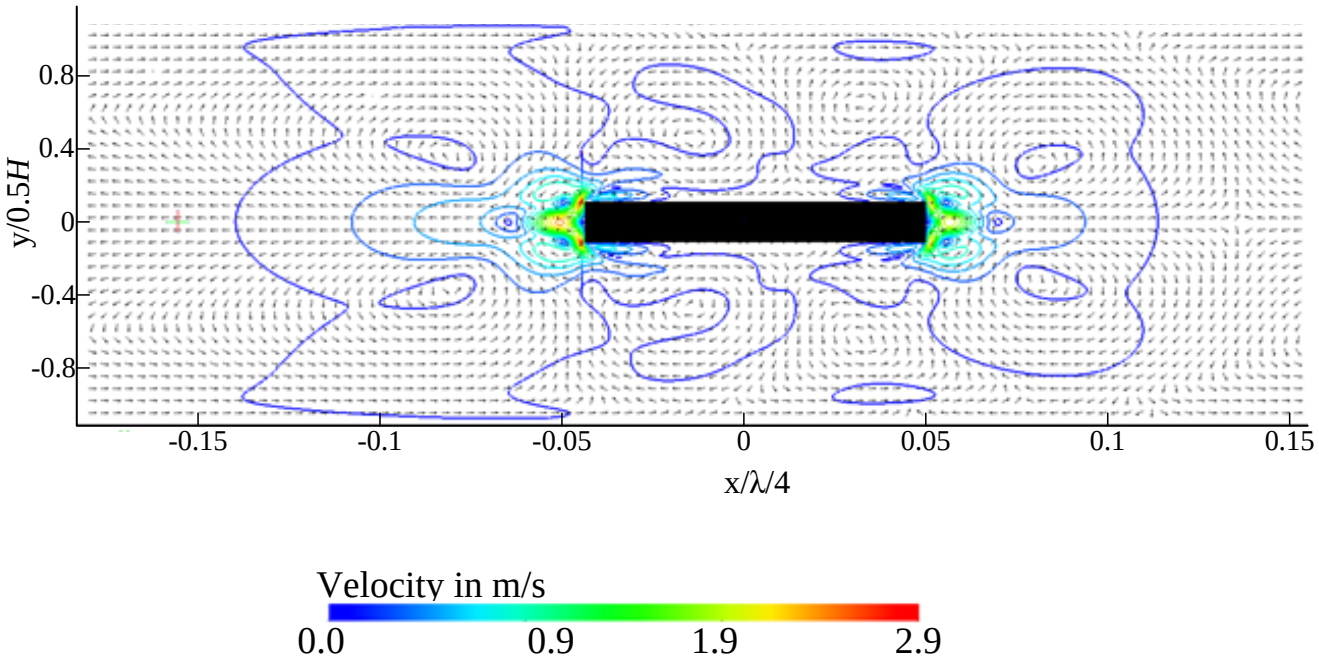

Figure 5.5 Two-dimensional vector plot of acoustic streaming velocity magnitude with superimposed velocity contours. All the velocity vectors were of same size. They are not representative of the velocity magnitude. The color of the velocity contours is representative of the velocity magnitude.

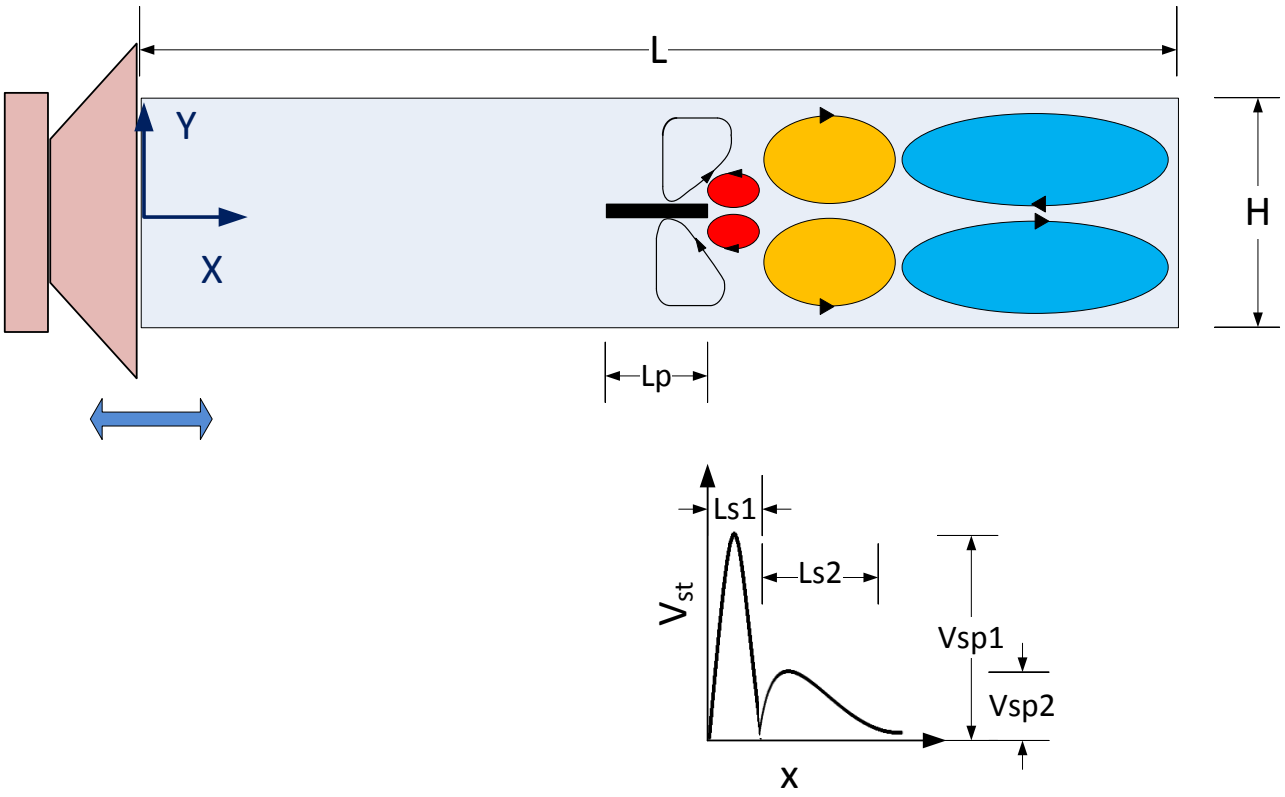

Figure 5.6 Schematic of the different streaming vortices (not to scale) in a resonator with a rectangular spoiler. Red and yellow vortices represent the primary and the secondary edge streaming cells respectively. Blue vortices represent the Rayleigh streaming cells. The curve below the resonator shows a qualitative variation of the overall edge streaming magnitude with respect to the axial distance away from the right edge. Ls1 and V_{sp1} represent the axial dimension and the velocity magnitude of the primary edge streaming cell. Ls2 and V_{sp2} represent the axial dimension and the velocity magnitude of the secondary edge streaming cell.

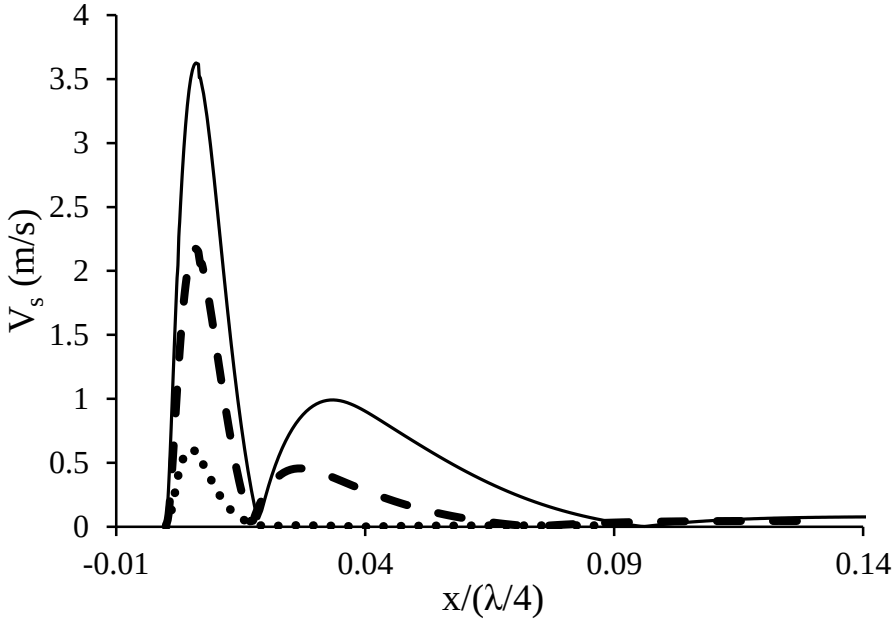

(a)

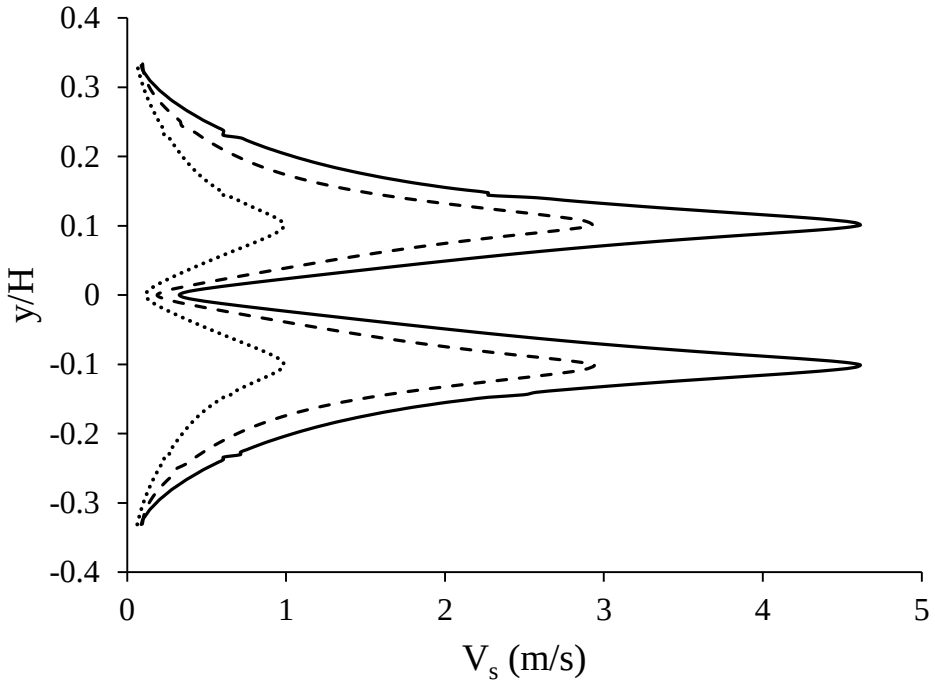

(b)

Figure 5.7 Effect of increasing peak instantaneous acoustic velocity amplitude on the edge streaming velocity magnitude. (a) Axial direction, and (b) transverse direction. (⋯ M=0.014, -- M=0.031, — M=0.043)

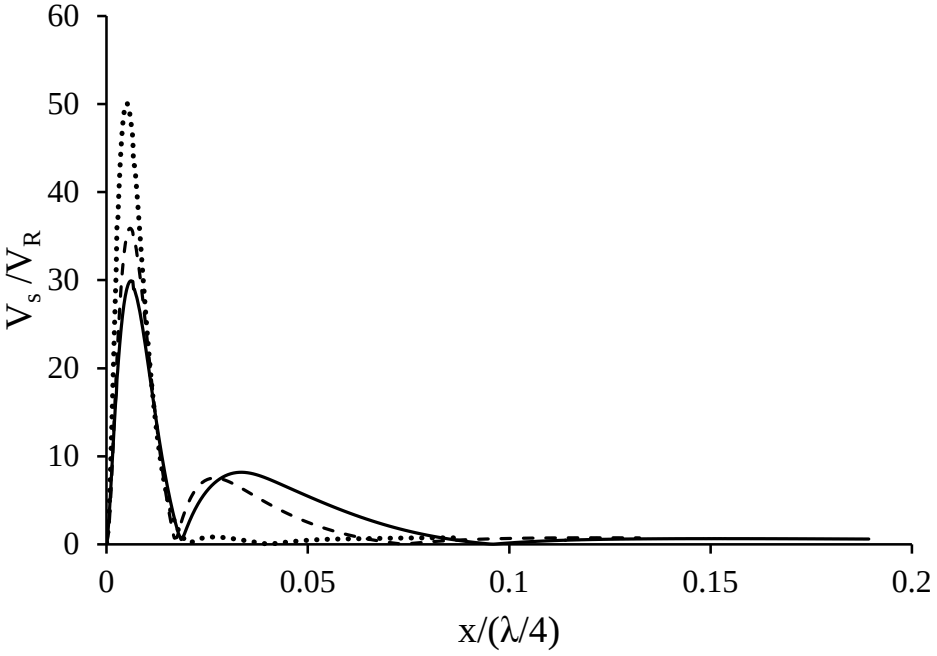

(a)

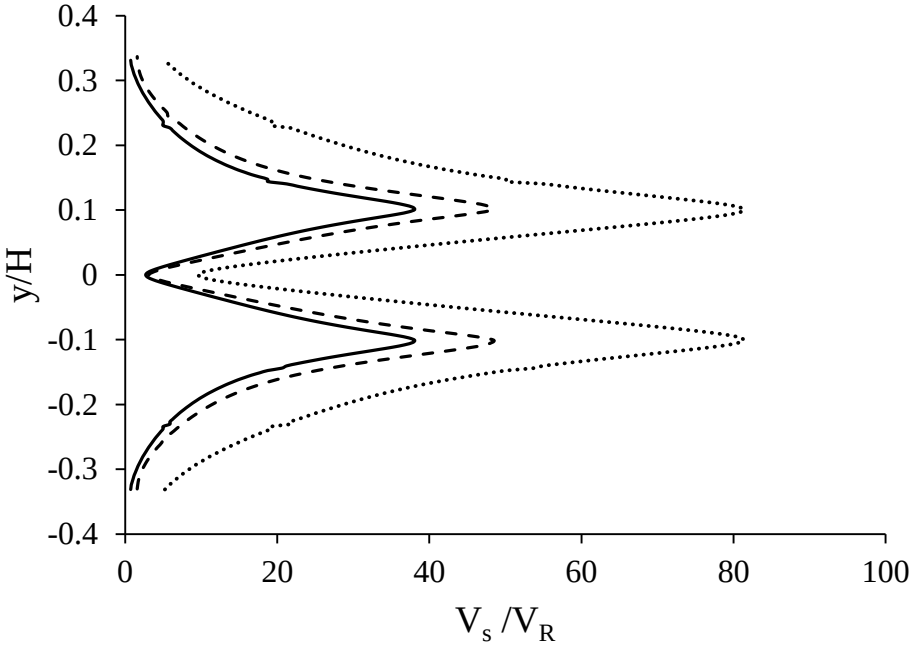

(b)

Figure 5.8 Effect of increasing peak instantaneous acoustic velocity amplitude on the non-dimensionalised edge streaming velocity magnitude. (a) Axial direction, and (b) transverse direction. (⋯ M=0.014, --M=0.031, — M=0.043)

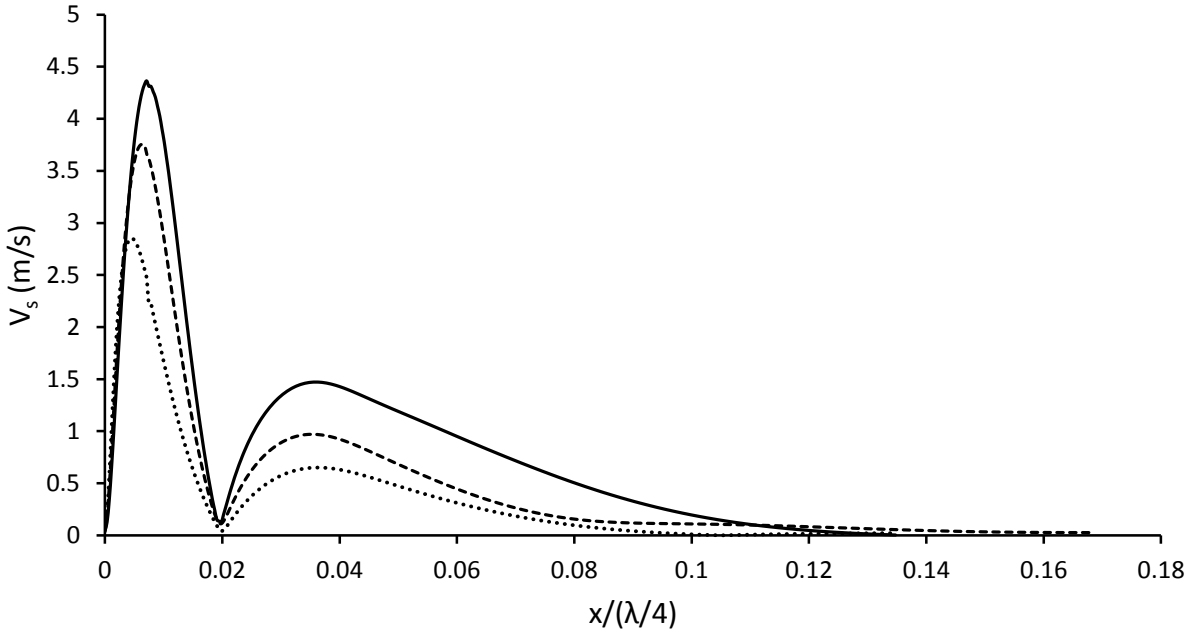

(a)

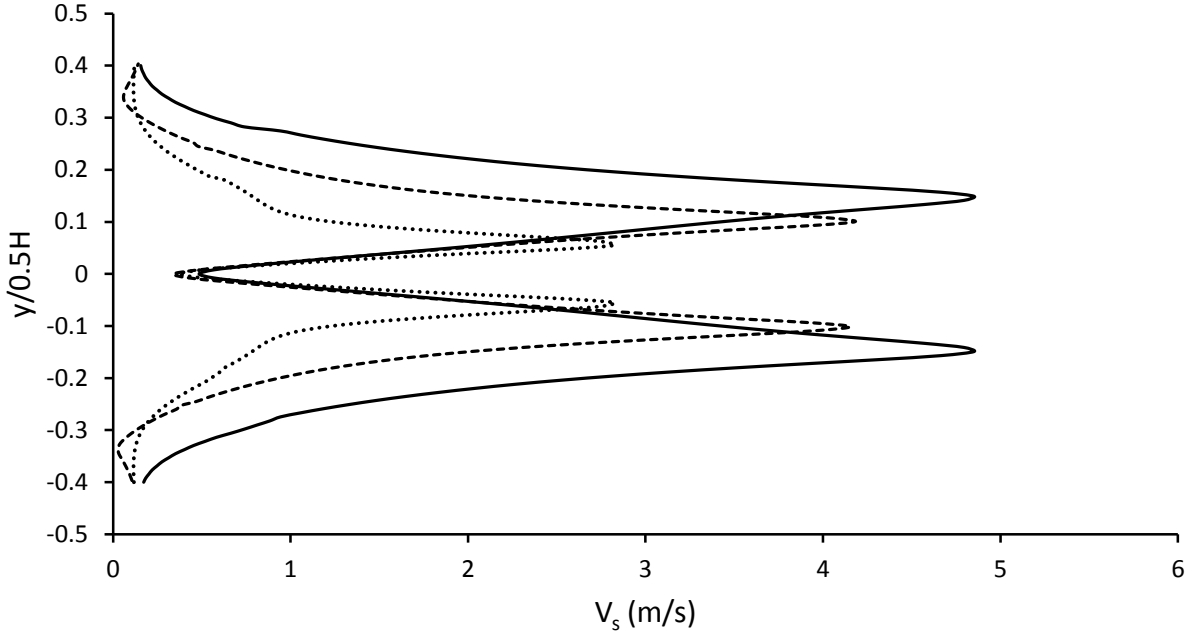

(b)

Figure 5.9 Effect of spoiler thickness on edge streaming velocity magnitude. (a) Axial direction, and (b) transverse direction. (⋯ t_p=0.05H, -- t_p=0.1H, — t_p=0.15H)

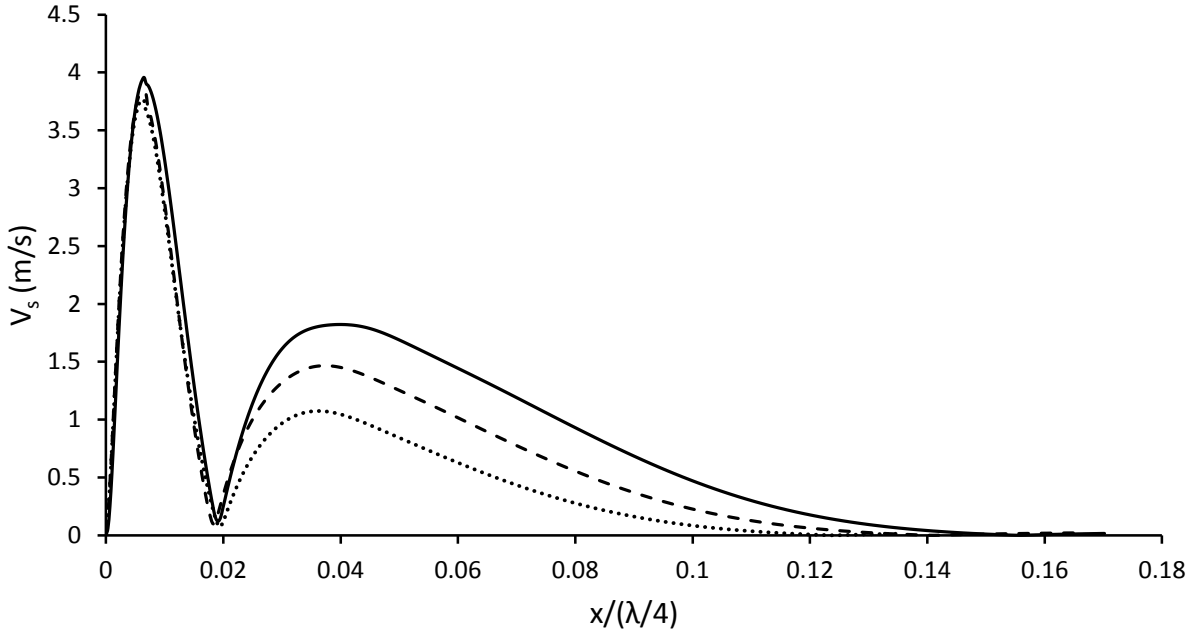

(a)

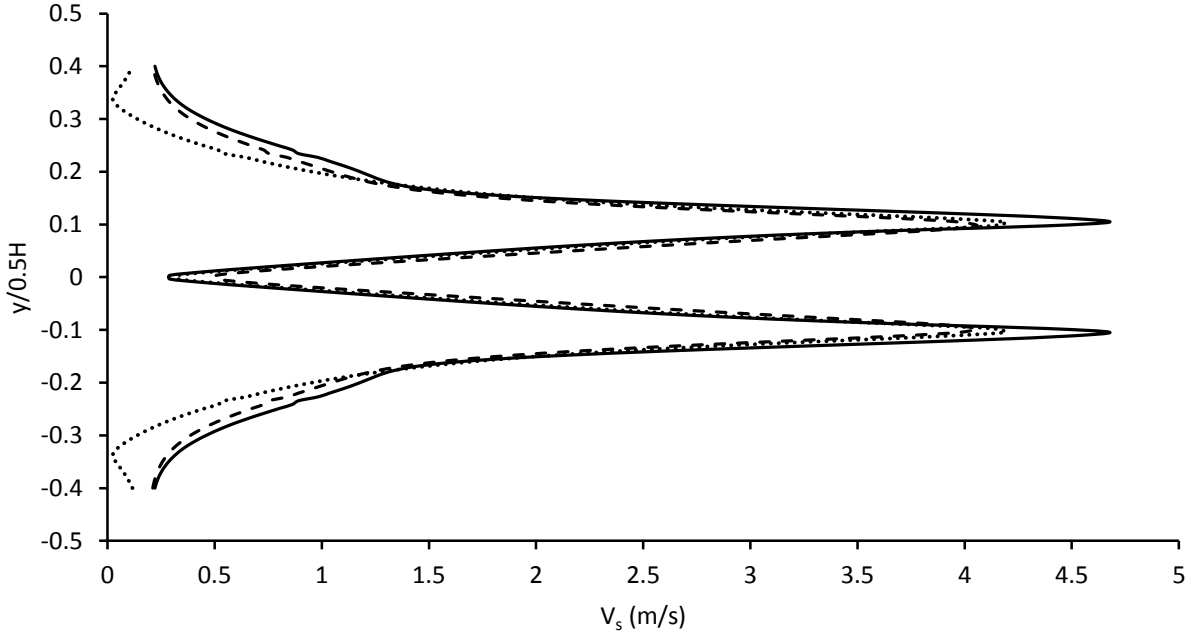

(b)

Figure 5.10 Effect of spoiler length on the edge streaming velocity magnitude. (a) Axial direction, and (b) transverse direction. (— $Lp/x_a = 0.5$, --- $Lp/x_a = 1$, ··· $Lp/x_a = 4$)

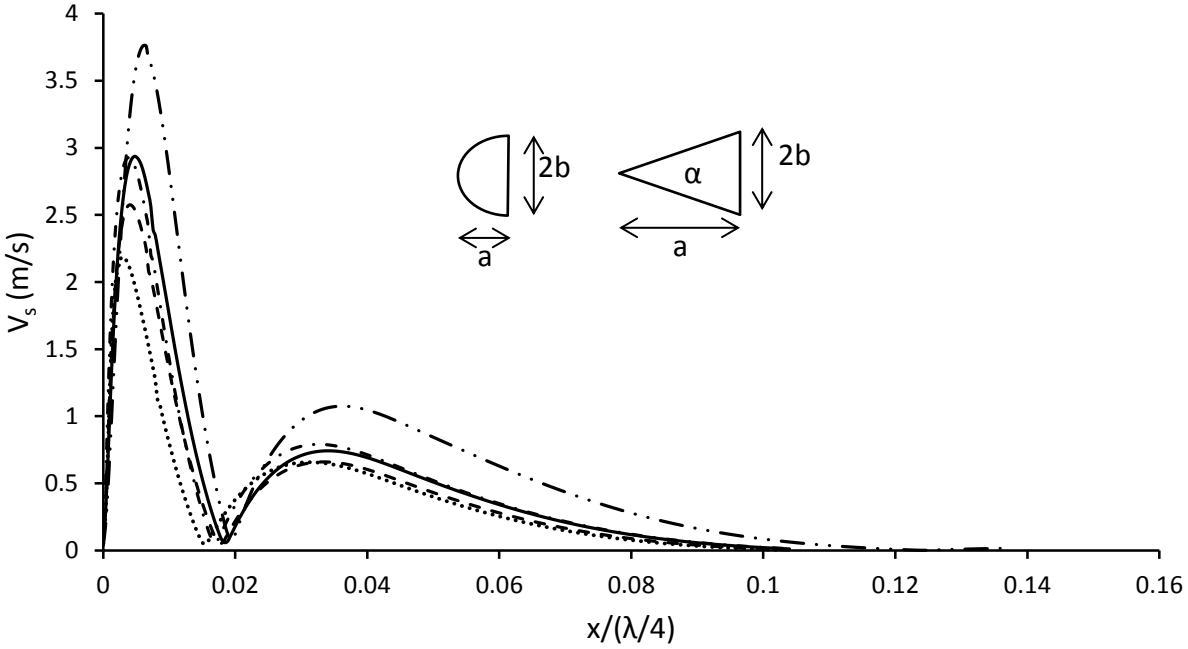

(a)

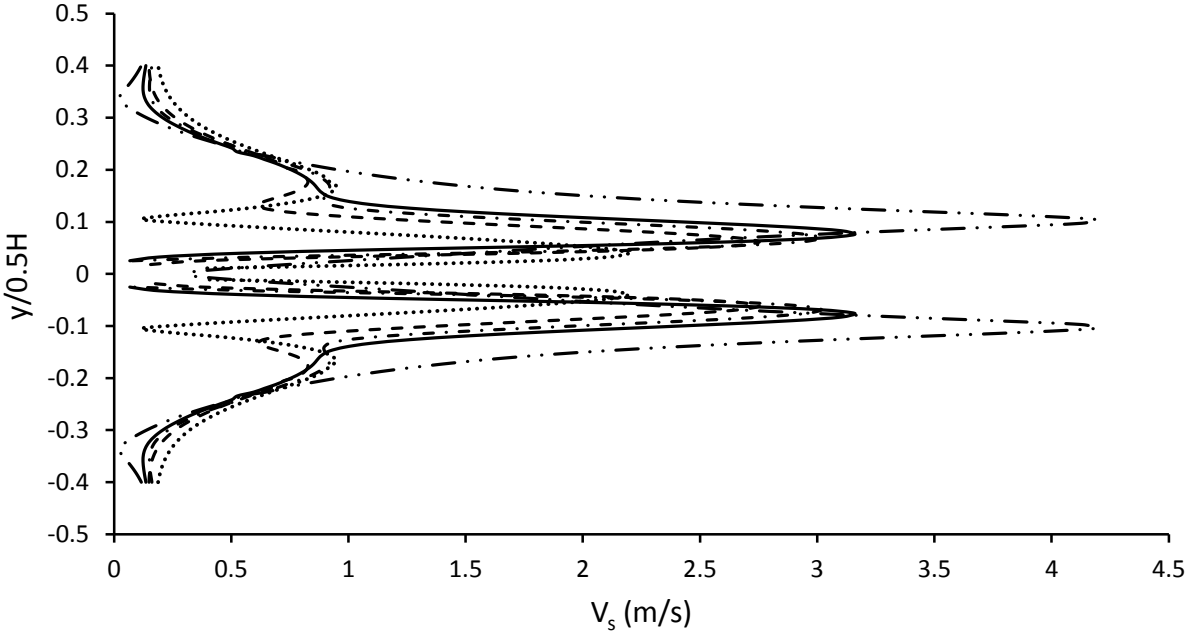

(b)

Figure 5.11 Effect of spoiler end shape on the edge streaming velocity magnitude. (a) Axial direction, and (b) transverse direction. (⋯ α=26.5o, -•- α=45o, —a=b, -- a=2b, -••- flat edge)

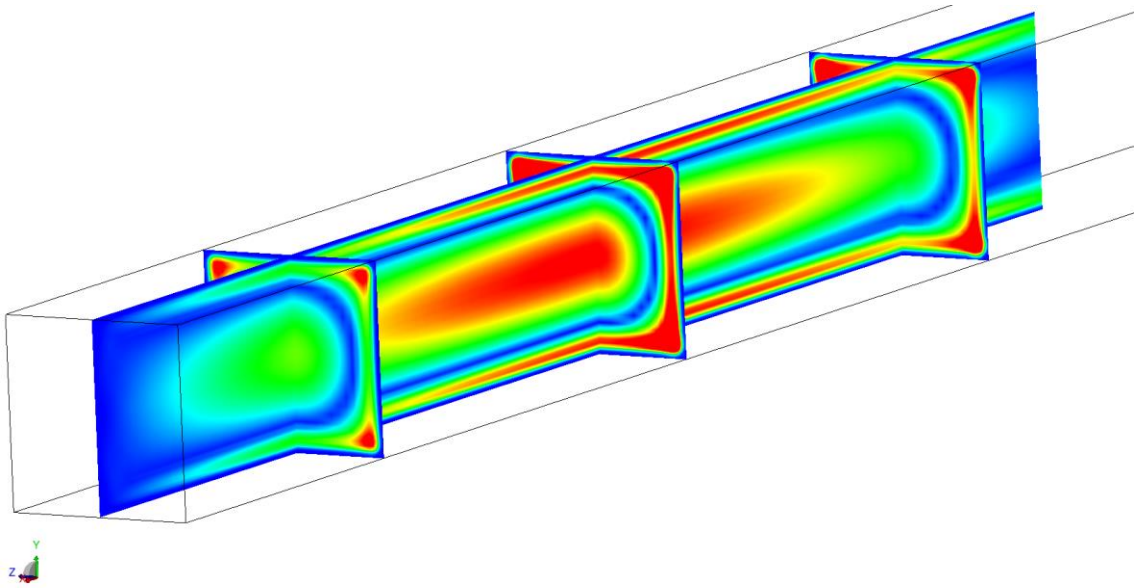

(a)

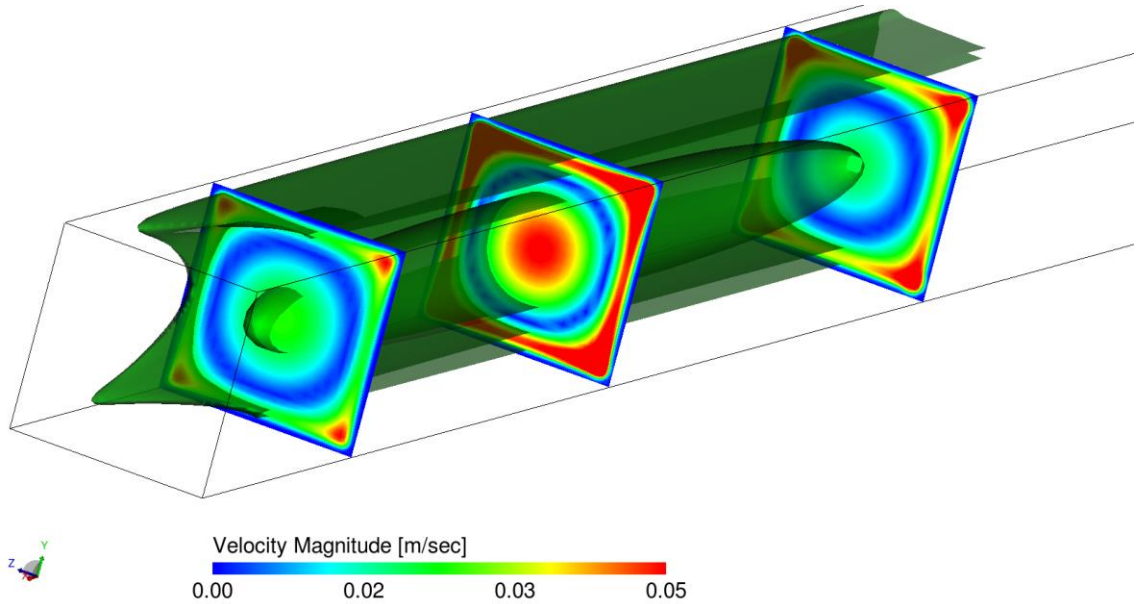

(b)

Figure 5.12 Three-dimensional Rayleigh streaming velocity in an empty resonator. (a) Contourslice at different location and planes. (b) Iso-velocity surface for V_s= 0.02 m/s.

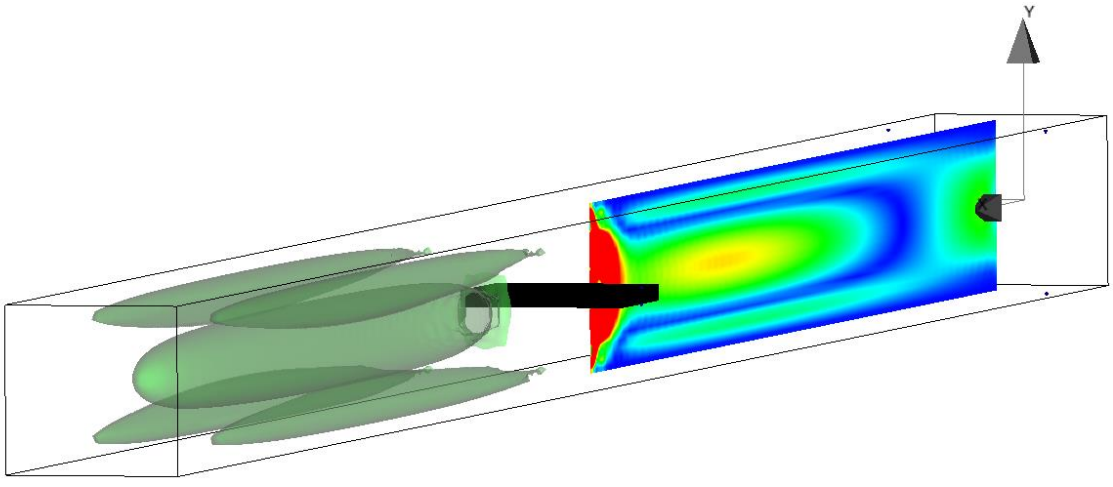

(a)

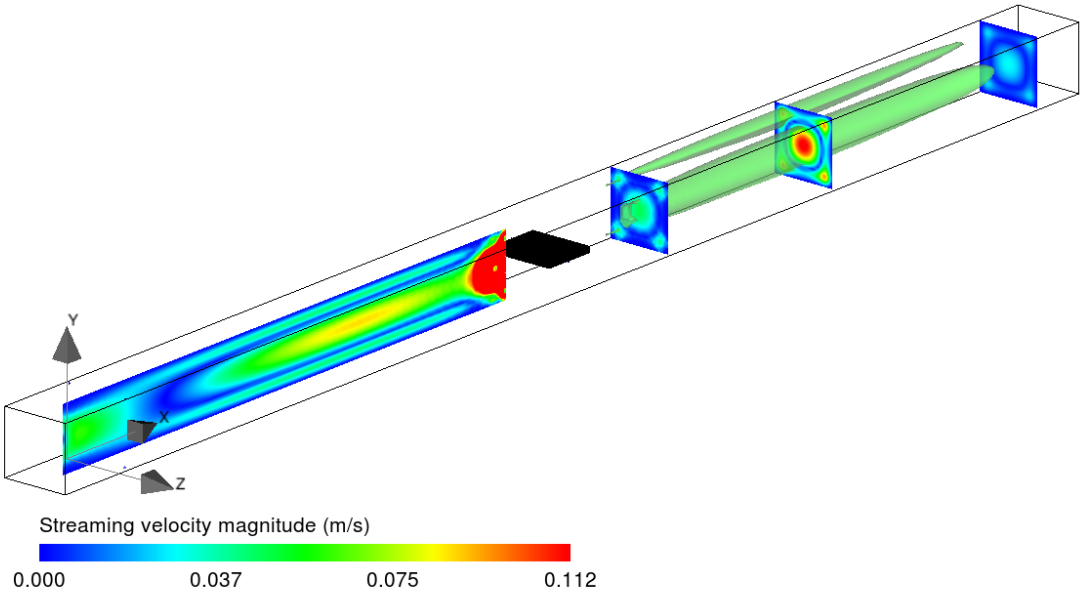

(b)

Figure 5.13 Three-dimensional Rayleigh streaming velocity with a spoiler. (a) 3D iso-surface for V_s=0.04 m/s, (b) streaming velocity along different 2D planes.

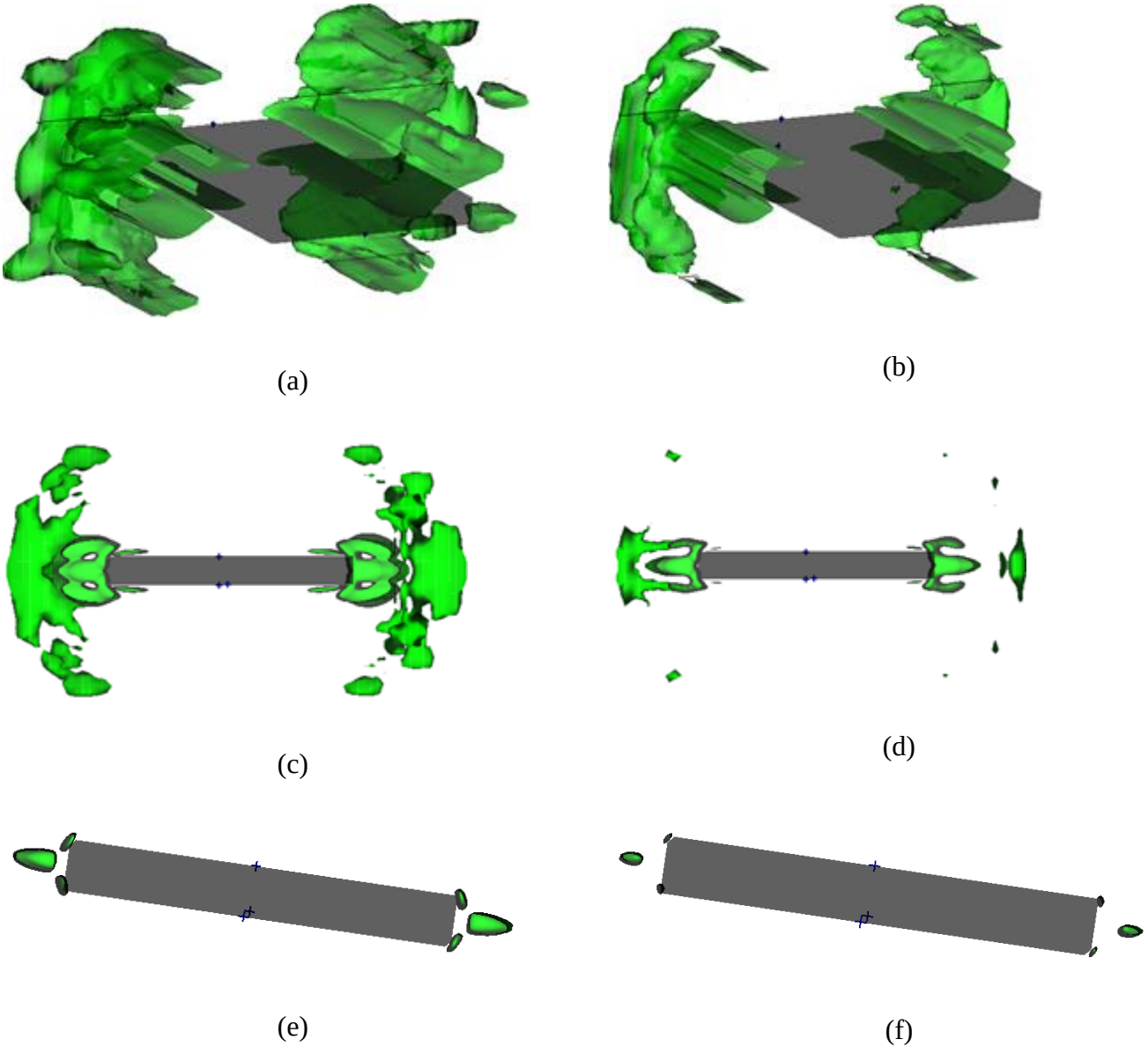

Figure 5.14 Iso-surface for the edge streaming velocity magnitude. (a) V_s= 0.4 m/s, (b) V_s= 0.8 m/s, (c) V_s= 1 m/s, (d) V_s=1.5 m/s, (e) V_s=3.5 m/s, and (f) V_s=4 m/s.

Table 5-1: Effect of Reynolds number on the Rayleigh acoustic streaming.

Case number→	1	2	3
Parameters ↓			
Peak acoustic velocity amplitude: u_a (m/s)	4.73	10.57	14.95
Inlet pressure amplitude (kPa)	1.88	4.20	5.94
Drive ratio (%)	1.86	4.16	5.88
Mach number, M	0.01	0.03	0.04
Reynolds number, Re= $u_a\delta_v/\nu$	8.45	18.90	26.73
Peak Rayleigh streaming velocity u_R (m/s)	0.01	0.06	0.12
u_R/u_a (%)	0.21	0.57	0.81

Table 5-2: Effect of Reynolds number on the edge streaming.

Case number→	4	5	6
Parameters ↓→		u_a (m/s)	
u_a (m/s)	4.73	10.57	14.95
Axial V_{sp1} (m/s)	0.61	2.17	3.63
Axial V_{sp2} (m/s)	0.01	0.46	0.99
Non-dim length of 1st streaming cell: Ls1	0.021	0.017	0.018
Non-dim location of 2nd streaming cell: Ls1+Ls2	0.026	0.074	0.096
Transverse V_{sp1} (m/s)	0.986	2.94	4.61
Non-dim height of 1st streaming cell: H_s1	0.101	0.101	0.101
V_{sp1}/u_a (%)	12.896	20.529	24.281
V_{sp2}/u_a (%)	0.21	4.352	6.622

Table 5-3: Effect of spoiler thickness to resonator width ratio on the edge streaming.

Case number→	7	8	9
Parameters ↓→	Spoiler thickness w.r.t resonator width		
t_p/H	0.050	0.100	0.150
Axial V_{sp1} (m/s)	2.852	3.752	4.364
Axial V_{sp2} (m/s)	0.651	0.971	1.472
Non-dim Length of 1st streaming cell: Ls1	0.020	0.020	0.020
Non-dim Location of 2nd streaming cell: Ls1+Ls2	0.105	0.168	0.135
Transverse V_{sp1} (m/s)	2.822	3.957	4.852
Non-dim location of transverse u_{sp1} : Hs1	0.055	0.093	0.149
V_{sp1}/u_a (%)	26.726	35.497	41.287
V_{sp2}/u_a (%)	6.159	9.186	13.926

Table 5-4: Effect of spoiler length to maximum acoustic displacement ratio on the edge streaming.

Case number→	10	11	12
Parameters ↓→	Spoiler length		
Lp/x_a	0.500	1.000	4.000
Axial V_{sp1} (m/s)	3.956	3.837	3.764
Axial V_{sp2} (m/s)	1.822	1.466	1.075
Non-dim Length of 1st streaming cell: Ls1	0.019	0.018	0.020
Non-dim Location of 2nd streaming cell: Ls1+Ls2	0.156	0.141	0.124
Transverse V_{sp1} (m/s)	4.677	4.058	4.189
Non-dim location of transverse usp1 : Hs1	0.105	0.097	0.105
V_{sp1}/u_a (%)	37.427	36.301	35.610
V_{sp2}/u_a (%)	17.237	13.869	10.170

Table 5-5: Effect of spoiler end shape on the edge streaming.

Case number→	13	14	15	16	17
Parameters ↓→	Spoiler end shape				
Spoiler end shape	triangle α=45	triangle α=26.56	circular	ellipse a=2b	flat
Axial V_{sp1} (m/s)	2.927	2.187	2.937	2.575	3.764
Axial V_{sp2} (m/s)	0.790	0.657	0.742	0.659	1.075
Non-dim Length of 1st streaming cell: Ls1	0.017	0.015	0.019	0.018	0.020
Non-dim Location of 2nd streaming cell: Ls1+Ls2	0.103	0.102	0.104	0.105	0.124
Transverse V_{sp1} (m/s)	3.018	2.195	3.160	2.753	4.189
Non-dim location of transverse u_{sp1} : Hs1	0.068	0.040	0.076	0.061	0.105
V_{sp1}/u_a (%)	27.692	20.691	27.786	24.361	35.610
V_{sp2}/u_a (%)	7.474	6.216	7.019	6.235	10.170

6 Transient flow characteristics in a channel with a spoiler

6.1 Introduction

The transient flow structures resulting from the interactions between the acoustic standing waves and the stack are investigated. The transient flow structures are captured at different stages within one acoustic cycle, in the vicinity of the spoiler. The flow and the spoiler geometry parameters are varied and their effects on the instantaneous flow structures are observed.

6.2 Acoustic flow at the stack plate ends

The interactions between the high amplitude acoustic waves and the stack-heat exchanger couple create complex flow structures which regulate convective heat transfer. The formation of vortices at the stack end, their interaction with the heat exchangers, and the acoustic streaming, need to be characterized to better quantify their effects on the performance of the thermoacoustic devices. Models based on the linear acoustic theory commonly neglect the production of vorticity at the stack boundaries. A better understanding of the interactions between the acoustic standing waves and the stack ends is needed in order to optimize and increase the efficiency of thermoacoustic engines. In the studies performed by Zhang *et al*. [44, 45], correlation was made between the instantaneous flow structures formed due to different geometrical and flow parameters with the heat transfer within the thermoacoustic core. In the results presented here similar correlations were made between the instantaneous flow structures and the heat transfer.

The flow structures near the end of a stack made of an array of identical parallel plates were studied using PIV. Figure 6.1 shows a schematic of the experimental setup, along with a nomenclature for discussing the results. The stack was made from glass microscope slides. The

dimensions of each stack plate were $4\text{cm}\times 2.5\text{cm}\times 1\text{cm}$. Two stacks with different plate gaps, g, were used as discussed in chapter 4. For both stacks, the plate thickness, t_p, was 1 mm and the gap between the plates was $g=1$ mm and $g=2$ mm, respectively. The experimental setup, the data acquisition method and the data processing methodology were essentially the same as described in chapter 2. The flow was excited at an excitation frequency of 245.5 Hz, which corresponded to $L=3\lambda/4$. The peak instantaneous acoustic velocity amplitude was $u_a=3.4$ m/s.

The effects of acoustic amplitude, excitation frequency and stack design parameters on the heat transfer process were investigated by making correlation between the transient vortical flow structures and the flow mixing. The vortices formed around the edge and between the stack plates were identified. The associated flow mixing could significantly enhance heat transfer, motivating their study. To characterise these vortical structures, phase locked ensemble-averaged velocity acquisition were performed. The velocity data were obtained at 20 phase values, θ, in an acoustic cycle as shown in Figure 6.2. The gap between two successive phases was $\pi/10$. The velocity data was collected for 150 consecutive acoustic cycles at each individual phase and then ensemble-averaged. Before each new set of velocity data acquisition, the acoustic driver was operated for five minutes such that the acoustic velocity reached a steady state. In other previous experimental studies employing PIV [56, 84] performed earlier, the flow around the stack was illuminated using a mirror placed inside the resonator. The introduction of a mirror in the resonator could disturb the streaming flow and may also affect the acoustic flow at the stack edges, depending on the resonator length. Here, the illumination was from the side wall of the resonator. The plates located further away from the wall received progressively less illumination

as the laser light was scattered by the stack plates. For this reason, the best results were obtained for the stack plates that were closest to the resonator wall.

The flow structures formed at the stack end for $g = 1$ and 2 mm are shown in Figure 6.3 and Figure 6.4, respectively. The results are shown in the form of vorticity plots with superimposed velocity vectors. From $\theta 1$ to $\theta 10$ the flow moves towards $x = L$ and out of the stack at $x = x_R$. In this so-called ejection stage, the flow moves out of the stack. The acceleration phase is the period between $1 \le \theta \le 5$ and the deceleration phase constitutes the period where $6 \le \theta \le 10$. Figure 6.3 shows one pair of symmetric counter rotating vortices building up over the period $1 \le \theta \le 3$. From $4 \le \theta \le 9$, the radius of the counter rotating vortex pair attached to the plate edge increases. Meanwhile, a second pair of vortices begins to develop at the edge and the primary vortex pair moves further away from the plate and starts to detach from the edge. From $\theta 11$, the ingestion stage of the acoustic cycle begins and the flow starts to move inside the stack at $x = x_R$. The vortex pair starts to collapse and by $\theta 13$, the vortex pairs have broken down into several smaller vortices, which involve additional flow mixing. In the deceleration phase of the ingestion stage, a shear layer starts to form at the plate end and extends inside the stack.

Figure 6.4 shows the results for $g = 2$ mm. The results show similar trend as for the stack with gap, $g = 1$ mm. The vortices formed in the ejection stage are more symmetric in shape with respect to the plate center line. Two pairs of counter-rotating vortices appear at the edge during the beginning of the ejection stage. These vortices are formed by the two shear layers of opposing vorticity signs inside the stack. The primary vortex pair, which is formed by the shear layer adjacent to the plate wall, has greater vorticity strength than the secondary pair of vortices which are farther from the plate wall. At $\theta 5$, the secondary vortex pair detaches from the shear

layer and the primary vortex core radius increases. By $\theta 9-10$, a third pair of vortices appears at the edge of the stack plate and the primary vortex pair detaches from the shear layer. From $\theta 11$, the ingestion stage starts and the vortex pairs start to move towards the stack and collapse. There were some differences between the flow structures of the two stack configurations. For the stack with $g = 2$ mm, more vortex pairs were being formed. During the ingestion stage, the primary vortex pair did not collapse completely but it was ingested into the stack. From $\theta 16$, the deceleration phase of the ingestion stage started, but there was enough time for the secondary vortex pair to reach the plate end. The third vortex pair which was formed during the deceleration phase of the ejection stage did not leave the plate edge and this vortex pair is assimilated into the shear layer when the suction stage starts. This assimilation causes a noticeable increase in the thickness of the shear layer at the plate end as compared to further inside the plate. The vortex formation enhances the heat transfer by causing mixing of cold and warm fluid. For the stack with larger gap, more vortices were formed at the stack end. Therefore it can be deduced qualitatively that the heat transfer from the end of the stack with $g = 2$ mm should be larger than that for the stack with $g = 1$ mm. These differences between the two stack configurations highlight the effects of the plate gap on the instantaneous acoustic fluid flow.

In the present experimental study, vortex shedding was not observed, in contrast to some other experimental studies [34, 40]. It was due to the comparatively small instantaneous acoustic velocity amplitude, and large excitation frequency. This meant that the vortex pairs being formed did not have sufficient time during the ejection stage to move farther away from plate end and form a vortex street.

6.3 Flow between the stack plates

The vorticity plots for the acoustic flow between the stack plates are shown in Figure 6.5 and Figure 6.6 for the two stacks with gaps, $g = 1$ and 2 mm, respectively. The viscous penetration depth, δ_ν for the experimental study was 1.4×10^{-4} m. The gap between the plates can also be expressed in terms of δ_ν as $7\delta_\nu$ and $14\delta_\nu$. The heat transfer in the stack plate takes place between the solid plate surface and the gas within the penetration depth. For both the stack configurations, thickness of the shear layer adjacent to the plate is on the order of one viscous penetration depth. Therefore, the volume of gas which participates in the thermoacoustic heat transfer process is within the shear layer adjacent to the plate. In order to enhance the heat transfer between the solid surface of the stack plate and the gas between the plates, a larger volume of gas needs to be involved in the thermoacoustic heat transfer process. This can be achieved by causing mixing of the gas in the shear layer with the outside gas. This mixing can be achieved if the vortices formed at the plate end can be convected inside the stack. From the vorticity plots of the stack with $g = 1$ mm, shown in Figure 6.5, it was observed that the thickness and the magnitude of the shear layer changes within the acoustic cycle. When the stack with a larger gap was used, the vortices formed at the stack end were subsequently convected inside the stack. In Figure 6.6 the stack end is located on the LHS at $\mathrm{x} = x_L$. In this case, $1 \le \theta \le 10$ corresponds to the ingestion stage, and $11 \le \theta \le 20$ to the ejection stage. The vortex core moves in and out of the stack during the ingestion and ejection stages of each acoustic cycle. The portion of the stack along the vortex path undergoes enhanced heat transfer between the gas and the plate as compared to rest of the stack. The displacement of the vortex core during the ingestion stage inside the stack was greater than the vortex core displacement during the

ejection stage from the plate end. This was due to the flow acceleration upon entering the stack because of the area contraction, and the flow deceleration upon leaving the stack because of the area expansion. The vortical flow behaviour at either end of the stack could be different, depending on the local instantaneous acoustic velocity at either end. Based on these observations; the stack geometry, its location inside the resonator and the gap between the stack and the heat exchanger at either end are all factors that could be optimised for enhanced heat transfer.

6.4 Parametric study

The introduction of a rectangular spoiler in a standing wave resonator changes the Rayleigh streaming structures. As discussed in the study of streaming due to spoiler in chapter 5, additional localised streaming structures were observed along the edges. These streaming flow structures were smaller in axial dimension but much larger in velocity amplitude when compared to Rayleigh streaming structures. A parametric study of the oscillating acoustic flow over a rectangular spoiler was performed in order to better understand edge streaming caused by the acoustic flow interactions with the rectangular spoilers.

The parametric study was performed numerically using a commercially available LBM solver, PowerFLOW. A simplified model of the parallel plate stack and heat exchanger was used. The elements of the thermoacoustic core, stack and heat exchanger were idealised as one single rectangular spoiler. The flow parameters considered were the peak acoustic amplitude and the excitation frequency. The geometrical parameters of the spoiler considered for the study were; the location of the spoiler in the resonator, the spoiler length, the spoiler width and the spoiler edge shape. The flow and the geometric parameters studied in this chapter were same as studied

in the numerical streaming study presented in chapter 5. One distinct feature of the numerical model used in this study when comparing with other previous numerical studies [54, 56] in this field was the computational domain. In previous studies, only the region of the resonator surrounding the stack plate was considered. The present numerical study included the entire resonator inside the computational domain. This allowed for the study of flow structures inside a complete resonator. The results presented in this chapter were obtained from 2D simulations.

All the results are presented in terms of vorticity plots. The vortex structures formed due to interaction of the spoiler with the acoustic standing wave can be related to mixing which in turn can be related to heat transfer. The vorticity is a better indicator of non-linearity, mixing and heat transfer characteristics than flow velocity.

6.4.1 Influence of peak instantaneous acoustic velocity amplitude

The effects of peak instantaneous acoustic velocity amplitude are shown in Figure 6.7-Figure 6.9. The three cases presented are for peak instantaneous acoustic velocities of 10.4, 14.9 and 40.5 m/s, respectively. Vorticity plots for four time instants within one acoustic cycle are shown namely, $\theta = \pi/2$, $\theta \to \pi$, $\theta = 3\pi/2$ and $\theta \to 2\pi$. The time instant represented by $\theta \to \pi$ is just before the flow changes direction from $\mathrm{x} = L$ to $\mathrm{x} = 0$ and the time instant represented by $\theta \to 2\pi$ is just before the flow changes its direction from $\mathrm{x} = 0$ to $\mathrm{x} = L$. Figure 6.7.a shows the flow vorticity at the time instant $\theta = \pi/2$, when the flow velocity is directed outwards towards $\mathrm{x} = L$. At this time instant, the instantaneous acoustic velocity amplitude, the vorticity of the shear layer, and the vortex pair at the stack end were largest. At the time instant, $\theta \to \pi$, shown in Figure 6.7.b, when the flow is still moving towards $\mathrm{x} = L$, the vortex pair was stretched and the center of the vortex core reached its maximum position. The flow behaviour shown in

Figure 6.7.c, where $\theta = 3\pi/2$ and Figure 6.7.d, where $\theta \to 2\pi$ are similar to Figure 6.7.a and Figure 6.7.b, respectively, except that the flow was reversed and moving towards $x = 0$.

When the peak instantaneous acoustic velocity increases, the behaviour of the vortices formed at the end also starts to change. A comparison between Figure 6.7.a, Figure 6.8.a, and Figure 6.9.a shows that the shape of the vortex pair at the spoiler end tends to elongate as the peak instantaneous acoustic velocity was increased, until vortex shedding starts and a von Karman vortex street appears. At low peak instantaneous acoustic velocity, the vortical flow structures formed during the ejection stage at $x = x_R$ were symmetric with those formed during the ejection stage at the left end, $x = x_L$. But comparison between Figure 6.9a,b and Figure 6.9.c,d shows that the flow is not symmetric at both ends for greater peak instantaneous acoustic velocity. The displacement of the vortices during the ingestion stage also increases with increasing peak instantaneous acoustic velocity, which was indicative of increasing acoustic displacement. Therefore, for a given spoiler length, increasing the instantaneous acoustic velocity amplitude caused the vortices formed at one end of the spoiler during ejection stage to interact with the other end of the spoiler when they were sucked in during the ingestion stage. In terms of heat transfer enhancement, at high amplitudes heat was transferred to larger distances along the axial direction from the spoiler end due to both larger acoustic displacement and larger mixing due to formation of the vortex street. The vortices also moved further in the transverse direction as the velocity amplitude was increased. Therefore the vortices shed from one plate of the stack interact with the neighboring plates and enhance heat transfer between the stack plates.

6.4.2 Effects of spoiler thickness

The effects of spoiler thickness on the flow structures resulting from its interaction with a standing wave are shown in Figure 6.10. Three values of the t_p/H ratio were investigated. The complete set of parameters is given in Table 5-3 of Chapter 5. Figure 6.10a,b shows results for $t_p/H = 0.05$ during the flow ejection stage, $\theta = \pi/2$ and during the flow ingestion stage, $\theta = 3\pi/2$, respectively. Similarly, Figure 6.10c,d and Figure 6.10e,f show the vorticity plots for $t_p/H = 0.1$ and $t_p/H = 0.15$, respectively. During the ejection stage, the radius of the vortex core decreased as the spoiler thicknesses was increased. For small spoiler thickness, the vortices were more elongated in shape. The center of the vortex core was located further away from the spoiler end for larger spoiler thicknesses. During the ingestion stage, greater shear layer thicknesses were observed at the spoiler end for spoilers with larger thicknesses. In terms of heat transfer, a thinner spoiler convected heat to longer axial directions but a thicker spoiler led to better heat transfer between the gas and the solid surface of the stack during the ingestion stage.

6.4.3 Effects of spoiler length

The effects of spoiler length on the instantaneous flow structures resulting from the interaction of the spoiler with the standing wave are shown in Figure 6.11. The time instants shown in the figure correspond to $\theta = \pi/2$. Three non-dimensionalised spoiler lengths were used, with $L_p/x_a = 0.5$, $L_p/x_a = 1$ and $L_p/x_a = 4$, respectively. At $L_p/x_a = 0.5$, the vortices created during ingestion stage at $x = x_L$ travelled farthest towards $x = L$. These vortices travelled as far towards $x = L$ as the vortex pair created during ejection stage. As the L_p/x_a ratio was increased, the displacement of vortices created at the left end of the spoiler towards the right end

of the spoiler decreased. For $L_p/x_a < 2$, the flow structures at one end of the spoiler were affected by those at the other end. In terms of the primary vortex pair formed at $x = x_R$, the effect of L_p/x_a ratio was not much. This may be the reason for the behaviour of edge streaming due to different spoiler lengths observed in chapter 5. For the streaming flow, it was found that the primary streaming cell remains almost unaffected by the L_p/x_a ratio, but the secondary streaming cell showed increasing peak velocity amplitude with decreasing L_p/x_a ratio. In terms of heat transfer in the thermoacoustic core, a sufficiently long stack length is needed in order to isolate the effects of one heat exchanger from another.

6.4.4 Influence of spoiler edge profile

The effects of different spoiler edge shapes on the vortical structures formed at the spoiler end are shown in Figure 6.12. The results are presented for two time instants. The results in the left column correspond to $\theta = \pi/2$ and in the right column correspond to $\theta = 3\pi/2$. The edge shape parameters were taken from Table 5-5 of chapter 5. The results shown in Figure 6.12 are presented in order of increasing edge shape smoothness. The edge shape influences the flow behaviour both in the wake of the spoiler during the ejection stage and towards the spoiler center in the ingestion stage. Among different edge shapes, shown in the right column, it was observed that the smoother edge shapes provided less resistance to the incoming flow during the ingestion stage. The rectangular edge result shown in Figure 6.12.b features the thickest shear layer and the largest vortical strength of the ingested vortex pair. The triangular edge result shown in Figure 6.12.j features the thinnest shear layer and no ingested vortices. Therefore, the stack with smooth edge shapes caused less dissipation of the acoustic energy. In terms of heat transfer enhancement, blunt end shapes would lead to larger volumes of gas to participate in the

thermoacoustic heat transfer process due to thicker shear layer and also due to ingestion of vortices during the ingestion stage. During the ejection stage, the center of the vortex core was displaced the farthest for the most blunt end shape. This caused additional circulation to develop near the end region as visible in Figure 6.12.a. The vortex core radius was larger for the rectangular edge, and it was reduced as the edge got smoother. This may be one of the reasons for the edge streaming behaviour observed for different edge shapes. It was observed that the peak amplitude of the edge streaming decreased as the edge shape got smoother, transitioning from rectangular to triangular. In terms of the heat transfer capabilities, the stack with a rectangular edge shape would transfer heat farther in the axial direction when compared with the stack with a triangular edge shape.

6.4.5 Effects of excitation frequency

The effects of different excitation frequencies on the instantaneous flow were also studied and the results are shown in Figure 6.13. Three excitations frequencies, 824, 412 and 206 Hz, respectively, were considered. The length of the resonator was one-half the acoustic wavelength for each case. The length of the spoiler was 2% of the resonator length. The peak instantaneous acoustic velocity amplitude was 10.5 m/s for all three cases. The peak acoustic displacement, u_a/ω, for smaller excitation frequencies is larger. As per the first principle, the $\rho du/dt$ term, for larger excitation frequency case would be larger due to constant peak instantaneous acoustic velocity amplitude of 10.5 m/s. This means that the force exerted by the fluid on the spoiler would be more for larger frequencies. The results for the ejection and ingestion stages are shown in the left and the right columns of Figure 6.13, respectively. Larger vorticity magnitudes were observed with increasing excitation frequency.

6.5 Conclusions

The flow structures formed from the interaction between the stack and the acoustic standing wave inside a resonator were studied both experimentally and numerically. Experimental results were presented for two stack configurations. Two flow stages were identified, namely the ejection stage and the suction stage. Different vortical structures in these flow stages were also identified. A parametric study was performed using the LBM based numerical scheme. The effects of different flow and geometrical parameters on the heat transfer enhancement were identified. It was observed that for a given peak acoustic amplitude and excitation frequency, the spoiler with a length ratio $L_p / x_a < 2$, larger thickness and rectangular edge would lead to greater heat transfer.

From the results and discussion, it was inferred that LBM can be successfully employed for the study of acoustic flow past stack. In the context of the present study, LBM provides certain advantages. A complete resonator was included in the computational domain. In the future, more complex models of stack and heat exchanger can be incorporated.

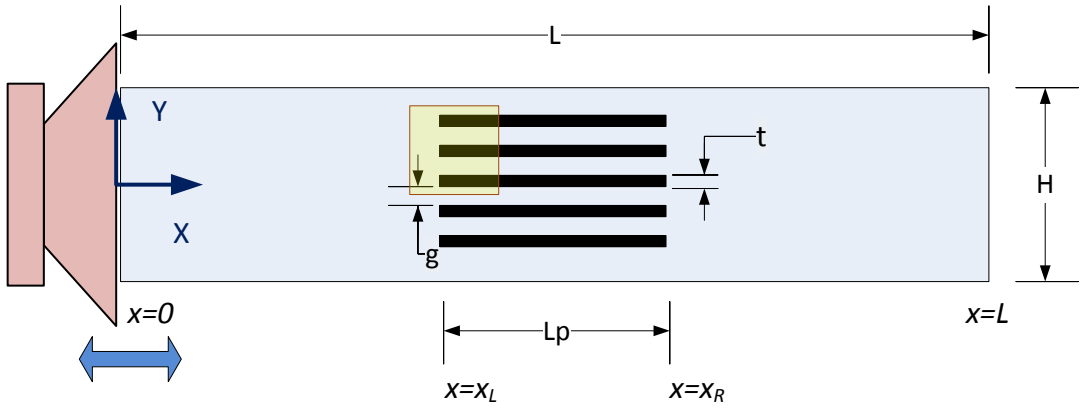

Figure 6.1 Schematic of the experimental setup. The velocity data was collected in the region shown by the yellow shaded box.

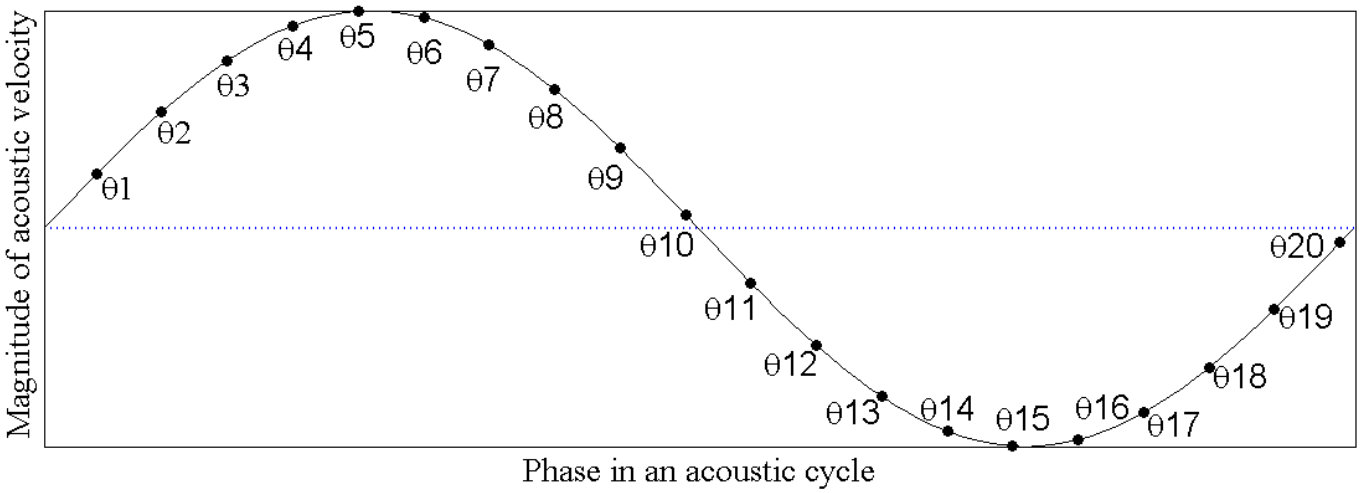

Figure 6.2 Illustration of the 20 phases at which phase-locked velocity data was acquired.

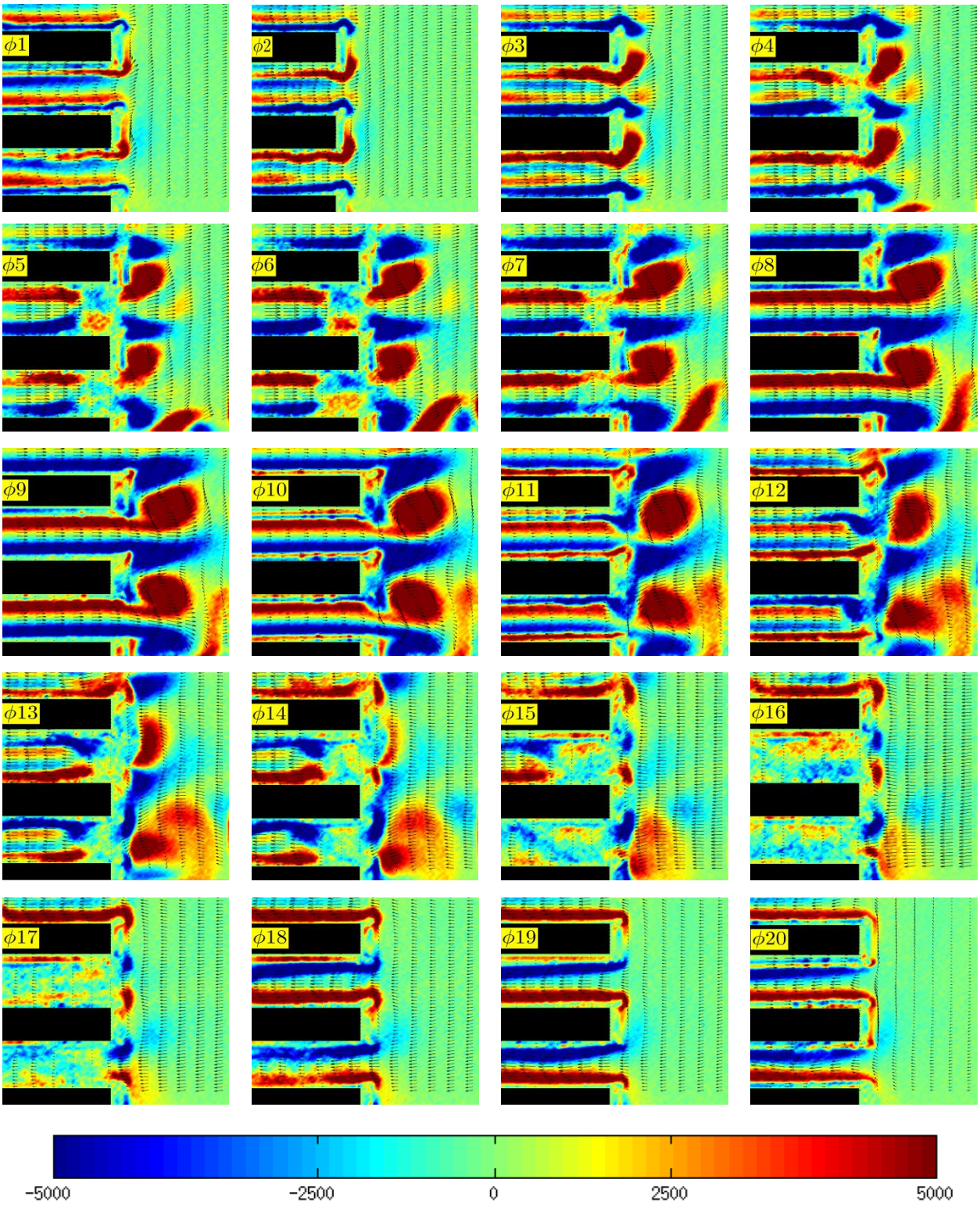

Figure 6.3 Vorticity contours near the stack end at different phases within an acoustic cycle as shown in Figure 6.2. The arrows in the plot represent the velocity vectors. The stack has a plate gap, $g = 1\,\text{mm}$. The color bar represents the vorticity amplitude with units of 1/s.

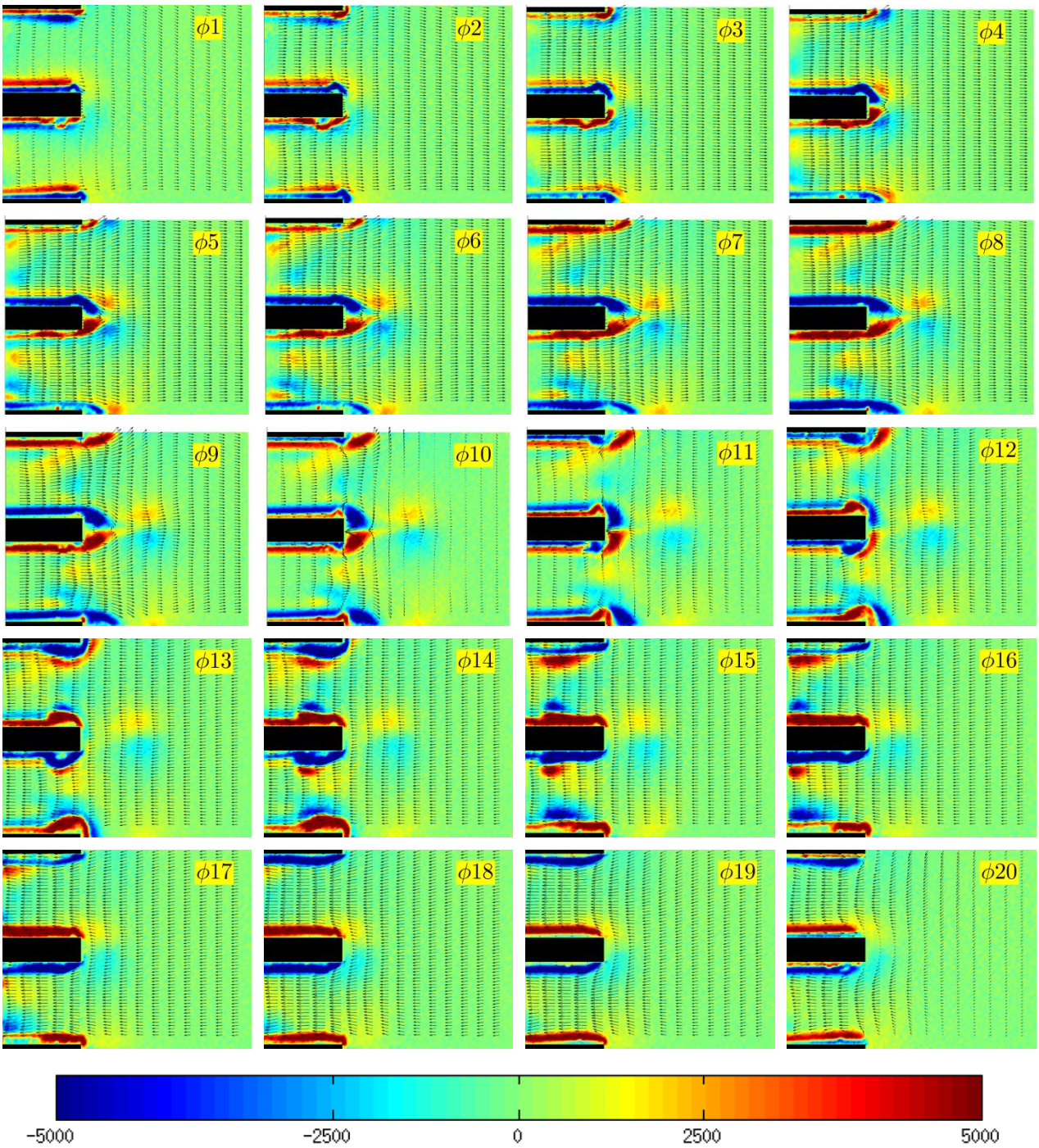

Figure 6.4 Vorticity contours near the stack end at different phases within an acoustic cycle as shown in Figure 6.2. The arrows in the plot represent the velocity vectors. The stack has a plate gap, $g = 2$ mm. The color bar represents the vorticity amplitude with units of 1/s.

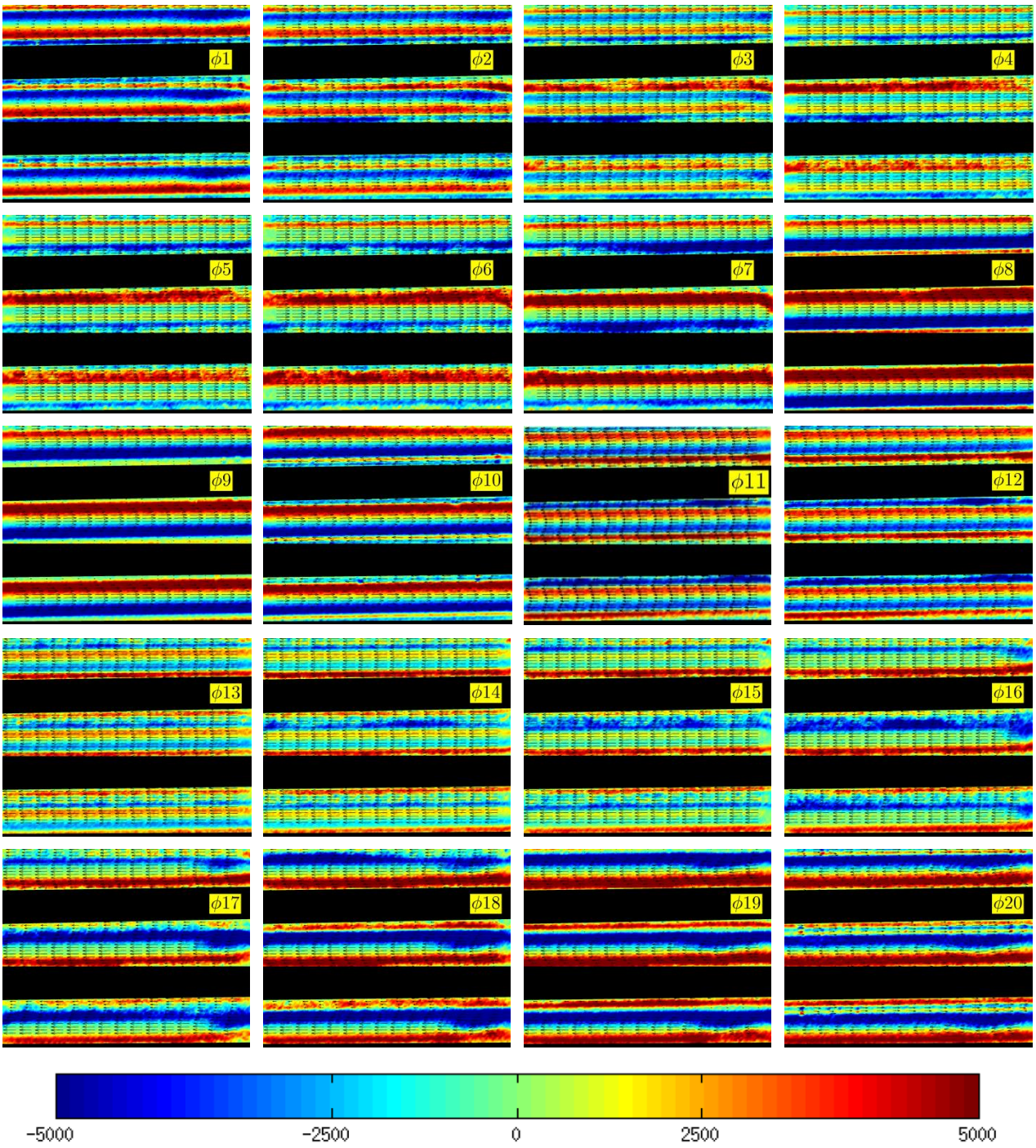

Figure 6.5 Vorticity contours in between the stack plates at different phases within an acoustic cycle as shown in Figure 6.2. The arrows in the plot represent the velocity vectors. The stack has a plate gap, $g = 1$ mm. The color bar represents the vorticity amplitude with units of 1/s.

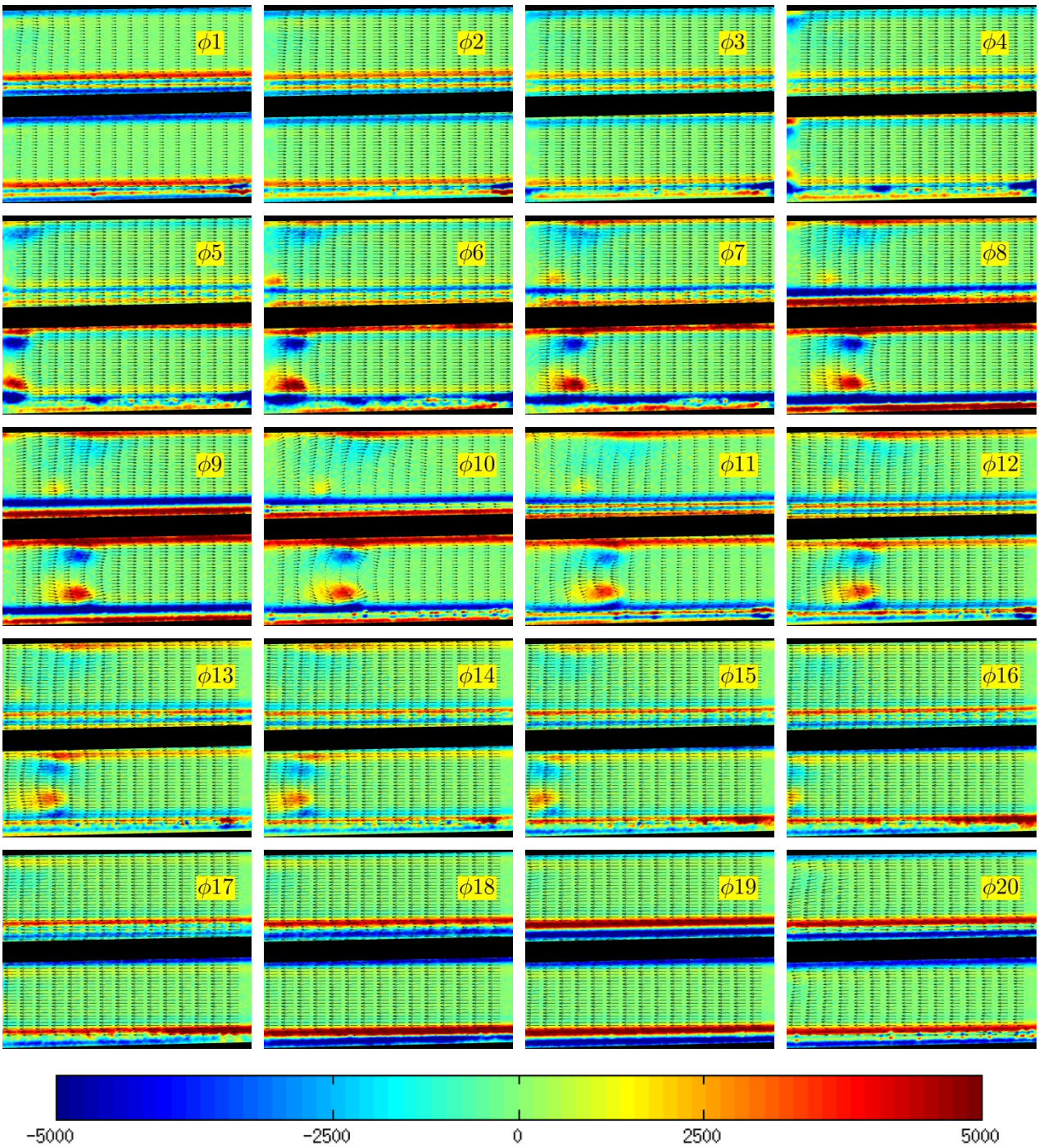

Figure 6.6 Vorticity contours in between the stack plates at different phases within an acoustic cycle as shown in Figure 6.2. The arrows in the plot represent the velocity vectors. The stack has a plate gap, $g = 2\,\text{mm}$. The color bar represents the vorticity amplitude with units of 1/s.

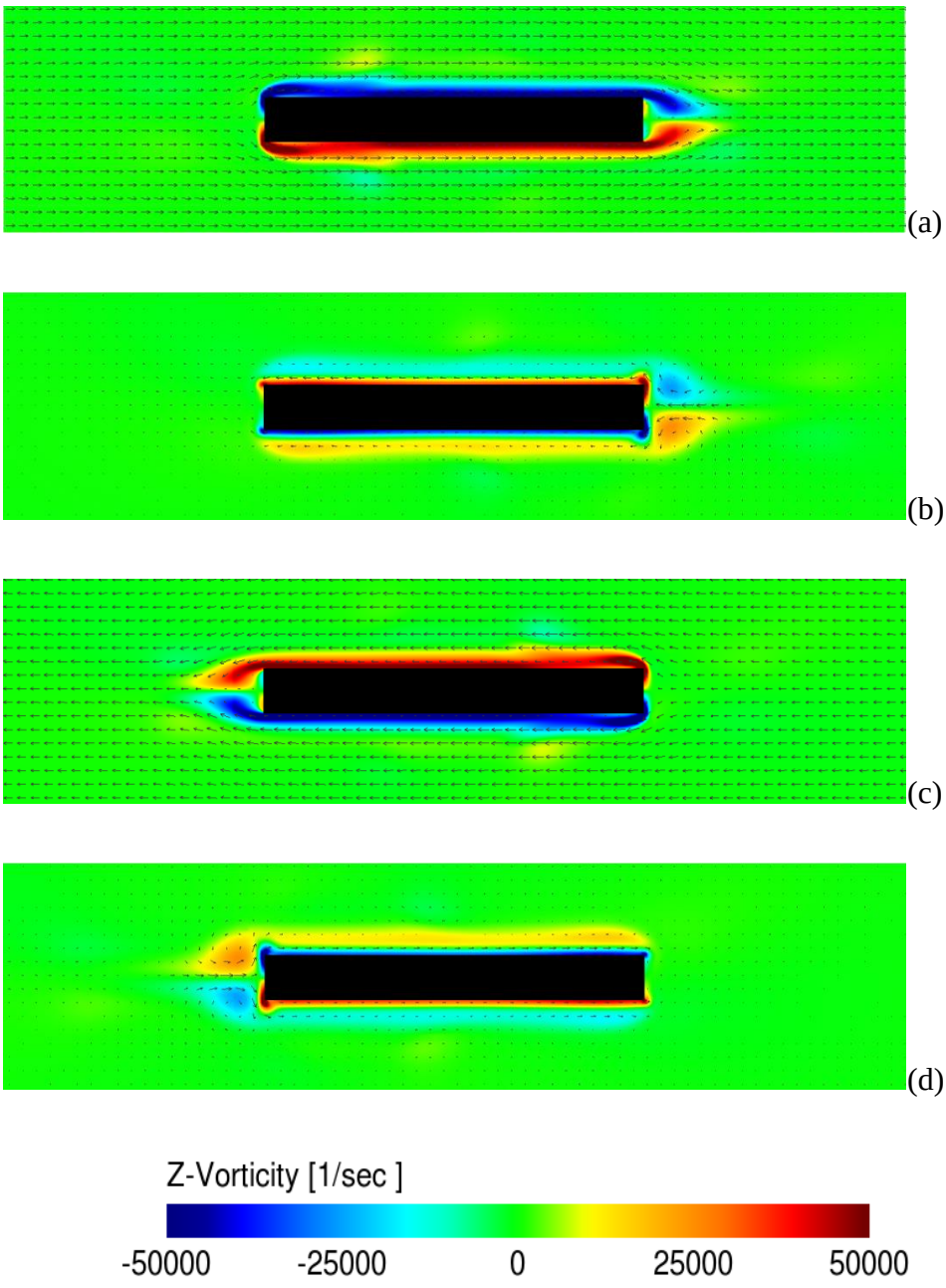

Figure 6.7 Effects of the peak instantaneous acoustic velocity (u_a=10.4 m/s) on the flow structures formed due to interaction of the standing wave and the spoiler. The effect is shown in terms of vorticity plots at four phases in an acoustic cycle: (a) $\theta = \pi/2$; (b) $\theta \to \pi$; (c) $\theta = 3\pi/2$; and (d) $\theta \to 2\pi$.

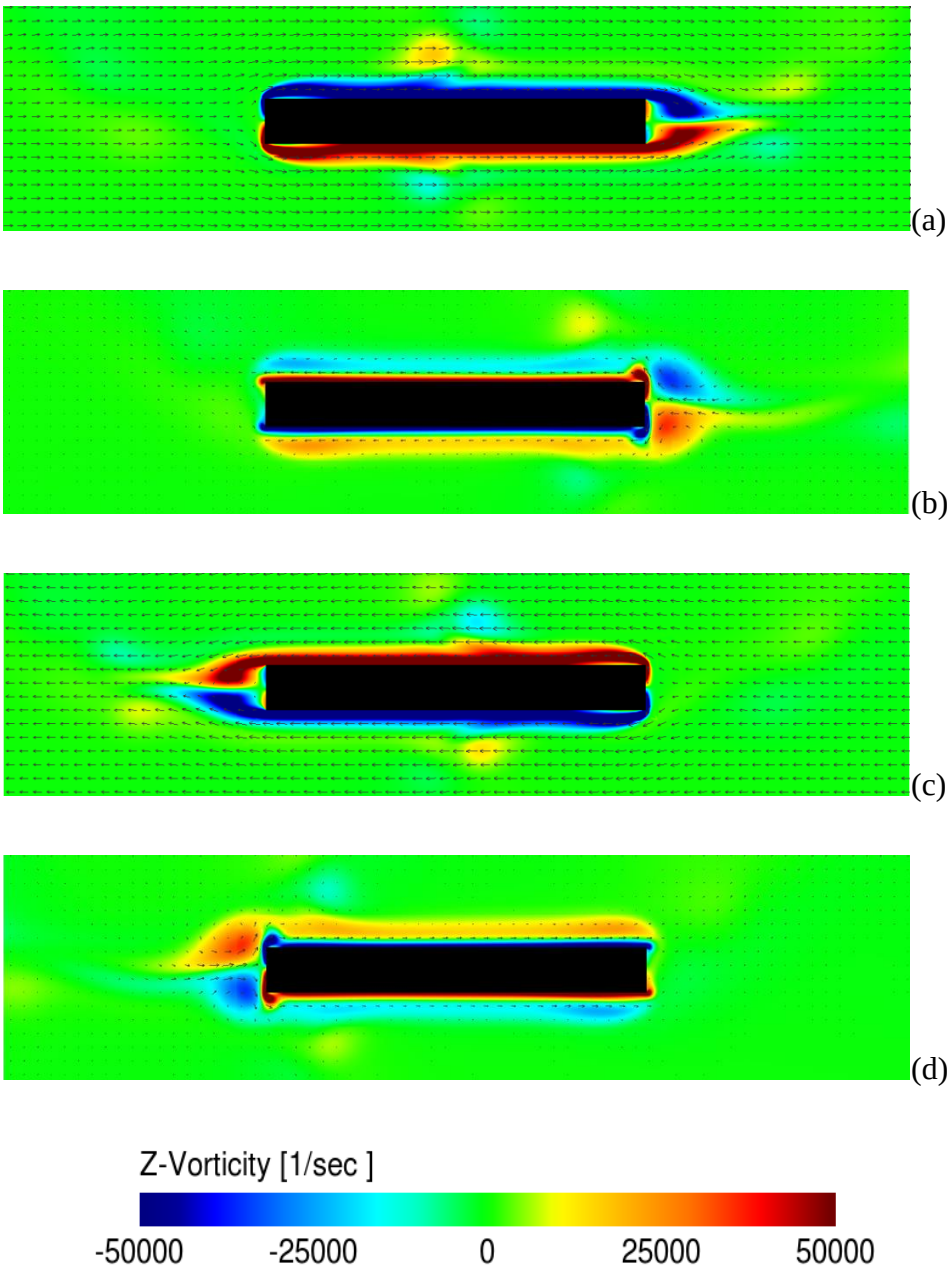

Figure 6.8 Effects of the peak instantaneous acoustic velocity (u_a = 14.9 m/s) on the flow structures formed due to interaction of the standing wave and the spoiler. The effect is shown in terms of vorticity plots at four phases in an acoustic cycle: (a) $\theta = \pi/2$; (b) $\theta \to \pi$; (c) $\theta = 3\pi/2$; and (d) $\theta \to 2\pi$.

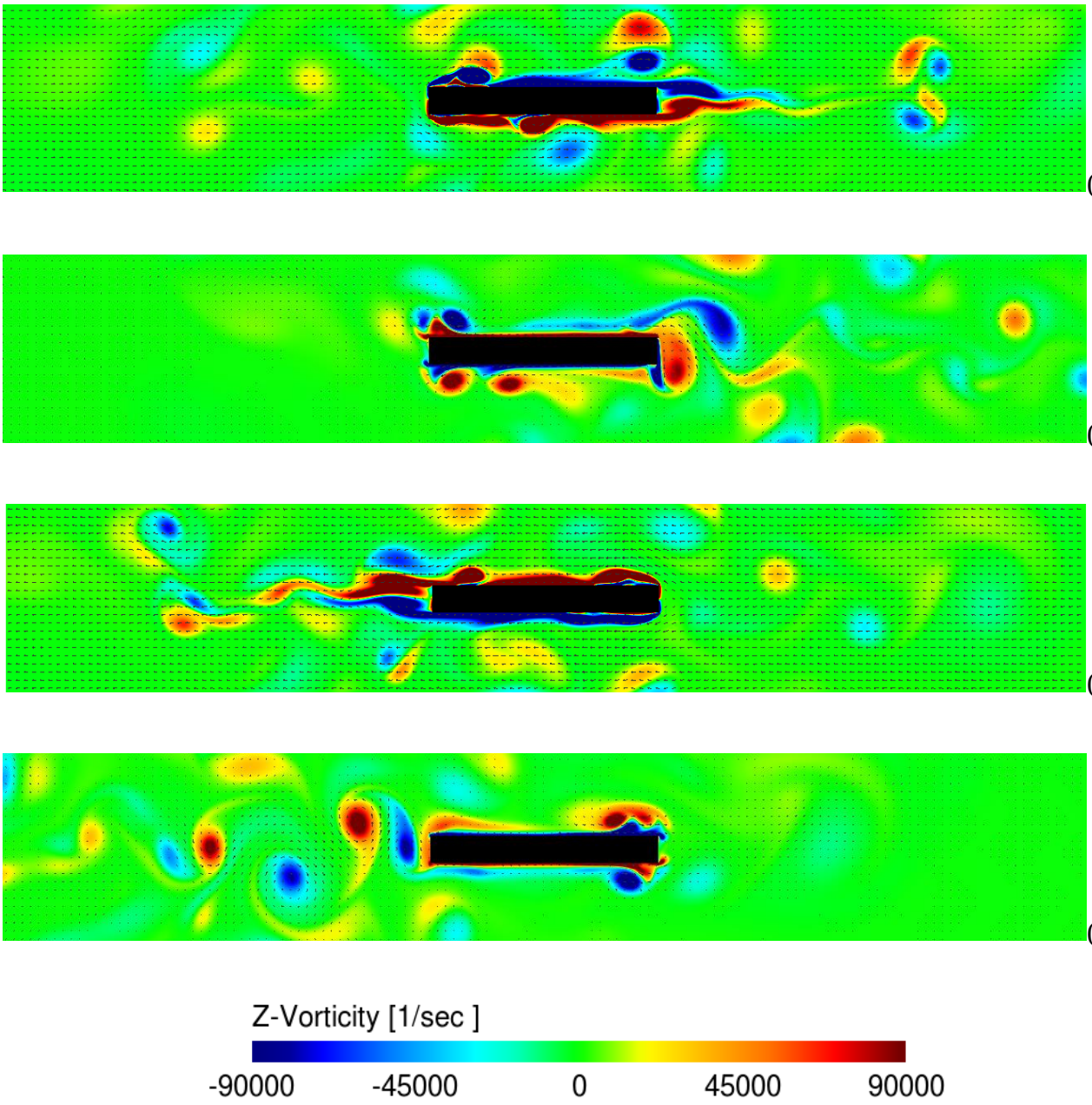

Figure 6.9 Effects of the peak instantaneous acoustic velocity (u_a = 40.5 m/s) on the flow structures formed due to the interaction of the standing wave and the spoiler. The effect is shown in terms of vorticity plots at four phases in an acoustic cycle: (a) $\theta = \pi/2$; (b) $\theta \to \pi$; (c) $\theta = 3\pi/2$; and (d) $\theta \to 2\pi$.

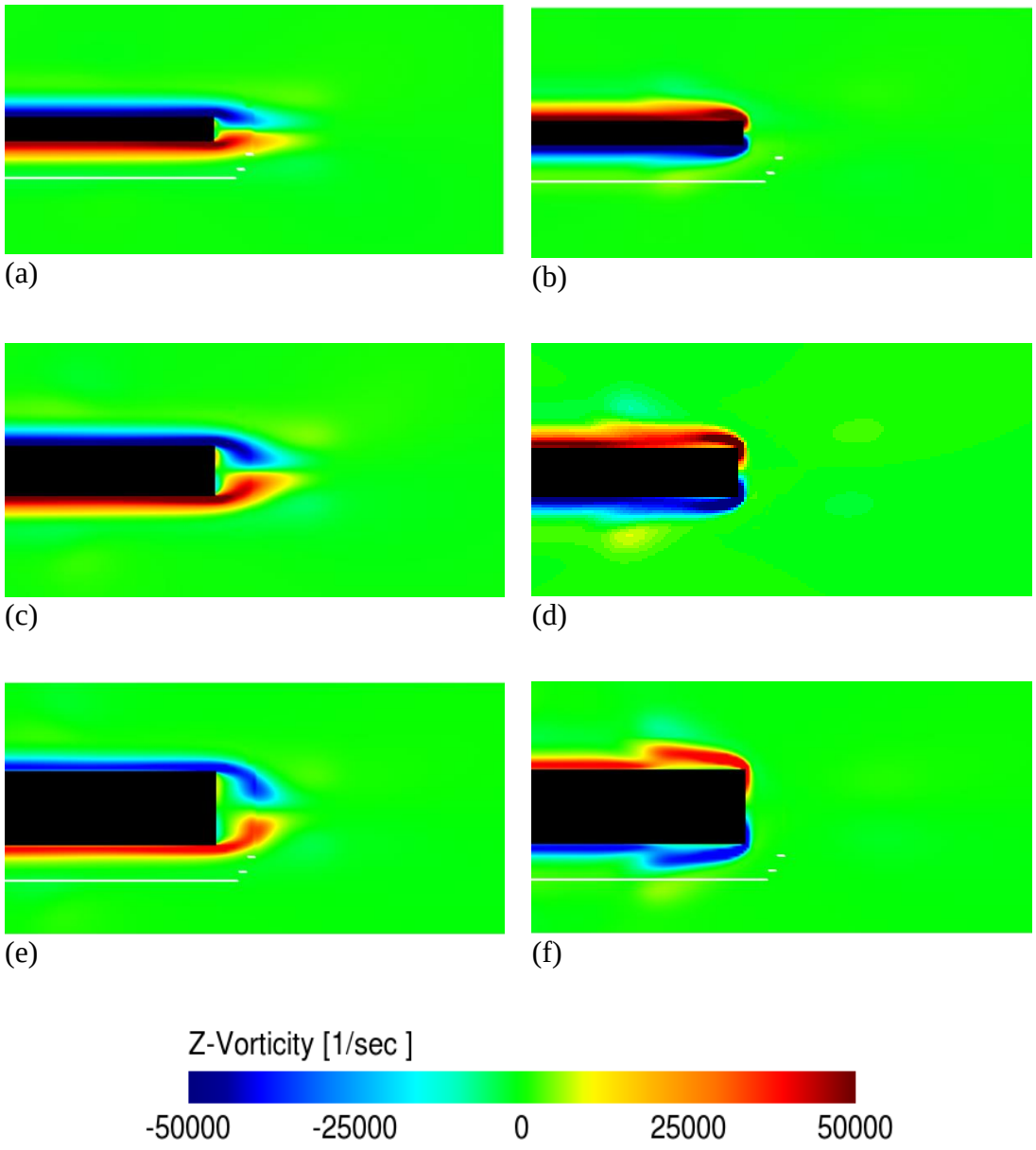

Figure 6.10 Effects of the spoiler thickness on the flow structures formed due to interaction of the standing wave and the spoiler. Three non-dimensional spoiler thicknesses were studied. The spoiler thickness was non-dimensionalised by the resonator width. First spoiler thickness (t_p=0.05H) is shown in figures (a,b), second spoiler thickness (t_p=0.1H) is shown in figures (c,d) and third spoiler thickness (t_p=0.15H) is shown in figures (e,f). Right Column shows the time instant in an acoustic cycle corresponding to $\theta = \pi/2$. Left Column shows the time instant in an acoustic cycle corresponding to $\theta = 3\pi/2$.

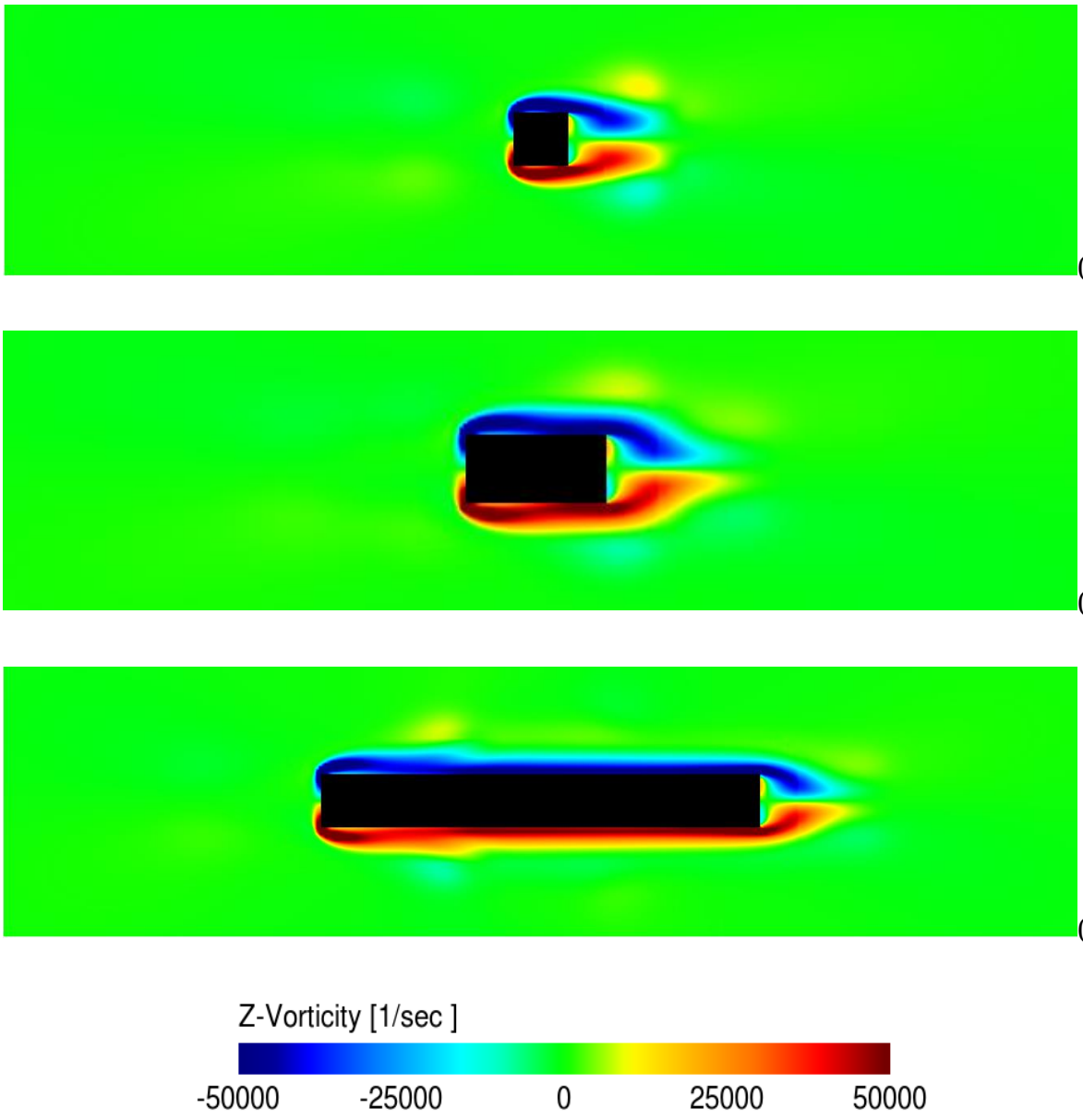

Figure 6.11 Effects of the spoiler length on the flow structures formed due to interaction of the standing wave and the spoiler. Three non-dimensional spoiler lengths were studied. The spoiler length was non-dimensionalised by the peak acoustic displacement. First spoiler length, $Lp/x_a = 0.5$, is shown in figures (a,b), second spoiler length, $Lp/x_a = 1$, is shown in figures (c,d) and third spoiler length, $Lp/x_a = 4$, is shown in figures (e,f).

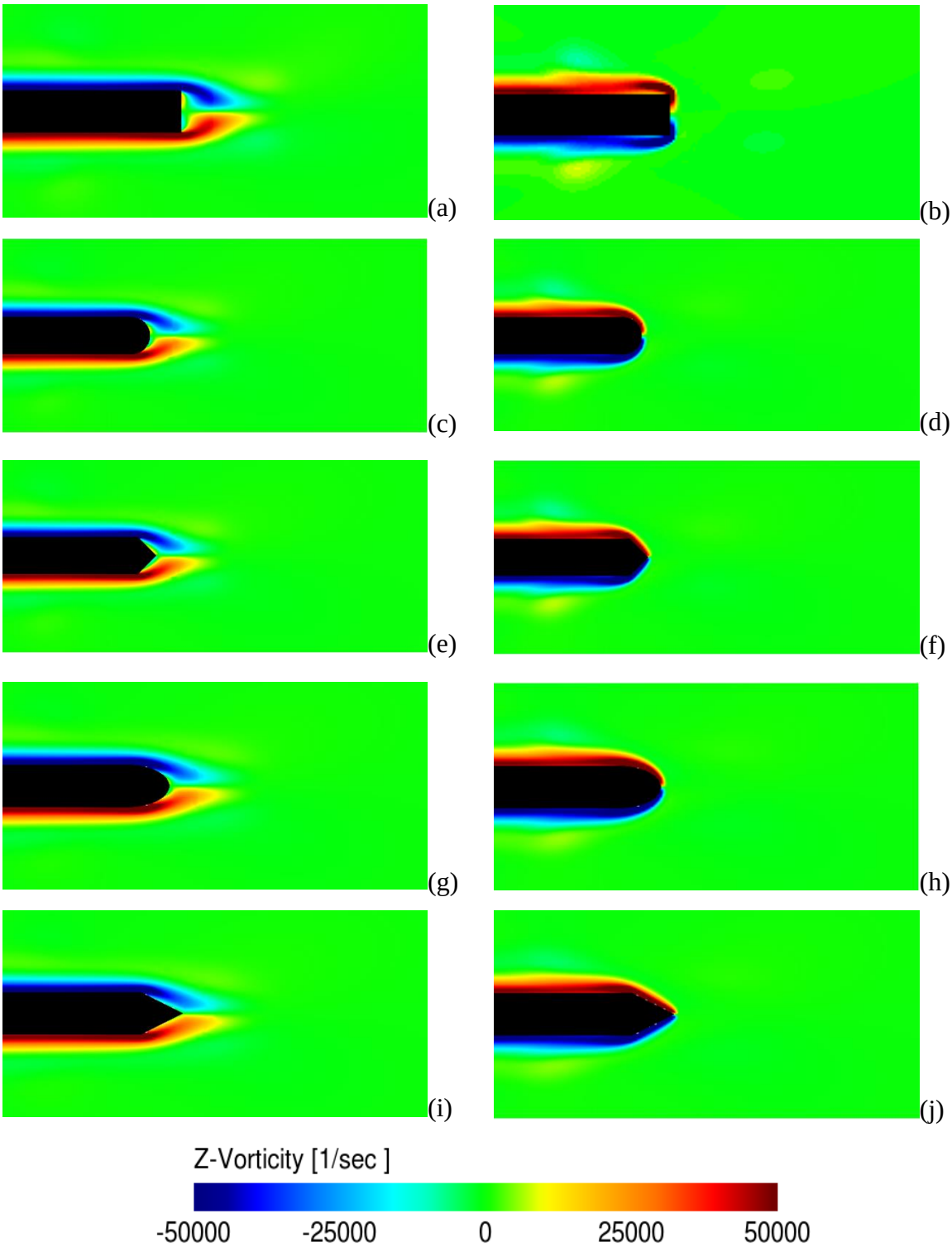

Figure 6.12 Effects of the spoiler edge shape on the flow structures formed due to interaction of the standing wave and the spoiler. Four spoiler edge shapes were studied: (a,b) rectangular edge, (c,d) circular edge, (e,f) triangular $\alpha=45^{o}$, (g,h) elliptical, and (i,j) triangular $\alpha=26.5^{o}$. Right

column shows the time instant in an acoustic cycle corresponding to $\theta = \pi/2$. Left Column shows the time instant in an acoustic cycle corresponding to $\theta = 3\pi/2$.

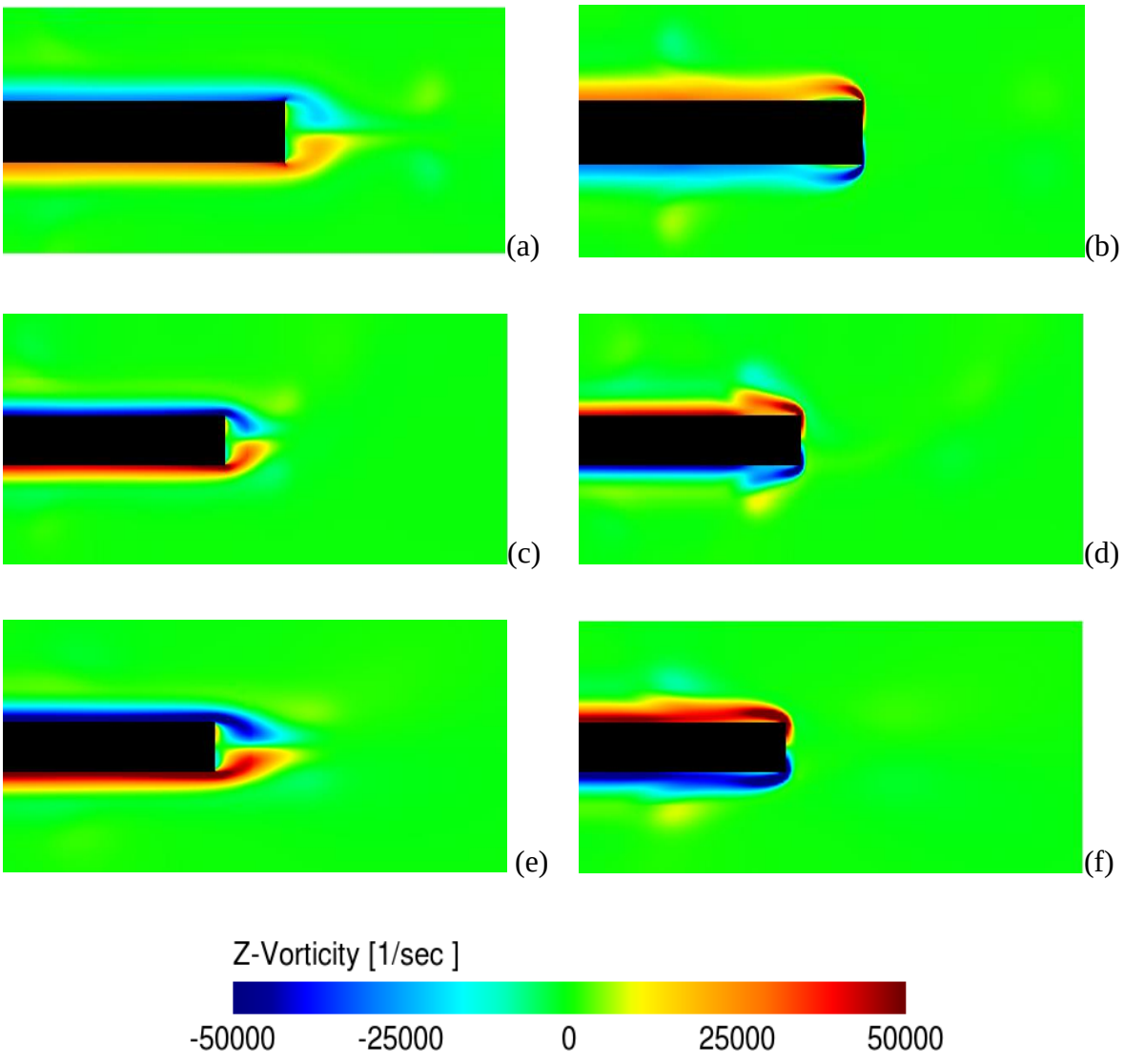

Figure 6.13 Effects of the excitation frequency on the flow structures formed due to interaction of the standing wave with the spoiler. Three different excitation frequencies were studied. The vorticity plots for f_a =206 Hz, are shown in figures (a,b), for f_a =412 Hz, are shown in figures (c,d), and for f_a =824 Hz, are shown in figures (e,f). Right Column shows the time instant in an acoustic cycle corresponding to $\theta = \pi/2$. Left Column shows the time instant in an acoustic cycle corresponding to $\theta = 3\pi/2$.

7 Conclusions and Future work

7.1 Summary

The phenomenon of acoustic streaming has niche applications in situations where enhancement of heat and mass transfer, enhancement of reaction rate and material removal is needed. Acoustic streaming has been extensively studied analytically, numerically and experimentally for different applications. In the case of standing wave thermoacoustic machines, much research has been focused on two-dimensional Rayleigh streaming in an empty resonator. Thermoacoustic machines, however, also include heat exchangers and a stack. The interaction of these components with the acoustic standing wave was found to produce different types of acoustic streaming flows with significantly greater velocity magnitudes than Rayleigh streaming. There is no systematic study available in the literature on the streaming recirculated flows resulting from the interactions between stack and heat exchangers and standing waves in thermoacoustic systems. The overall objective of the present study, as stated in chapter 1, was to identify and characterise different streaming flows existing in an idealised standing wave thermoacoustic machine. The originality of the research project was to use experiments and numerical simulations in order to characterise the streaming flows in a standing wave thermoacoustic refrigerator with idealised stack and heat exchanger. The resonator of a thermoacoustic machine was idealised by a square cross-section standing wave resonator. The stack was idealised as a rectangular spoiler for convenience in fabrication. More complex spoiler shapes were investigated using computer models. The overall objective was met by the identification and quantification of the Rayleigh streaming and the edge streaming in a standing wave resonator in

the presence of a spoiler. In order to characterise these different streaming flows, both qualitative and quantitative comparisons were made between the Rayleigh and the edge streaming. Three specific aims or objectives were defined for realising the overall objective of this study as stated in chapter 1. Specific contributions made from the experimental and the numerical studies are described in the following sections.

7.2 Conclusions from experimental studies

One of the specific objectives of this research was to characterise the Rayleigh streaming in an empty standing wave resonator and to analyse the effects of the resonator cross section on the outer and the inner streaming cells. In order to realise this objective, Rayleigh acoustic streaming inside a square cross section resonator was experimentally studied using PIV. Experimental results for the ensemble-averaged instantaneous acoustic and the streaming velocities were found to be in good agreement with the analytical predictions from the linear acoustic model. A time evolution study was performed to quantify the time needed for reaching steady state magnitudes of the instantaneous acoustic and the streaming velocity. It was found that the instantaneous acoustic and the streaming velocities reached steady state amplitude after around three and five minutes after the initial flow excitation, respectively. The effect of the streaming Reynolds number, Re_s, on the Rayleigh streaming cell shape was also studied. It was found that the streaming cell shape was irregular at low Re_s. As Re_s was increased, the streaming cell shape became regular. The cell shape was again irregular following a further increase of Re_s. Almost all the experimental studies on the Rayleigh streaming were performed within the symmetry plane of the resonator. In addition, a 3D Rayleigh acoustic streaming cell was reconstructed from

a collection of planar velocity data sets. This was done to better understand the 3D behaviour of Rayleigh streaming, and to study the effect of resonator shape on the streaming cell form. It was found that the outer streaming cell was not affected by the resonator shape. However, the inner streaming cell shape changed with the shape of the resonator. The 3D Rayleigh streaming cell further suggested that the enhancement of heat transfer due to Rayleigh streaming should be maximum in the symmetry plane, and should decrease sinusoidally away from the symmetry plane, up to the end of the outer streaming cell. Thus, in a standing wave thermoacoustic refrigerator the effect of Rayleigh streaming on heat transfer may not be equal over the entire stack or heat exchanger area normal to the principal direction of wave propagation. It was also found that the magnitudes of the inner streaming cells were larger than those of the outer streaming cells. The inner streaming cell would cause enhancement of heat transfer at the resonator wall and the outer streaming cell would cause heat transfer enhancement in the resonator core.

Actual thermoacoustic machines include stacks and heat exchangers. The interaction between these components and the acoustic standing waves significantly changes the streaming flow from the Rayleigh streaming which was observed in an empty resonator. The second aim of this research was to characterise the streaming flow borne from the interaction of standing waves with an obstacle inside a resonator. In order to study this type of streaming, simplified stack models were introduced in the resonator and the resulting streaming behaviour was observed using PIV. It was found that the presence of solid obstacles in the resonator changed the streaming flows completely. High amplitude acoustic streaming was observed near the extremities of the stack. The streaming flow arising from the interaction of standing wave with

solid objects was termed “edge streaming”. The edge streaming was found to be localised in nature, and to depend on the magnitude of the maximum instantaneous acoustic velocity at the stack edge. The heat exchanger was idealised by a single circular cylinder. This obstacle created four streaming cells, one in each quadrant. As for the edge acoustic streaming, the shape of the streaming cells formed by the cylinder was dependent on the maximum instantaneous acoustic amplitude at the location of the cylinder. From the results of simple stack and heat exchanger models it was concluded that streaming flows in an actual thermoacoustic system are complex and deviate from the Rayleigh streaming near spoilers and rigid elements within the thermoacoustic core.

7.3 Conclusions from numerical studies

A secondary objective of the study presented in this dissertation was to assess the applicability of the LBM based commercial code called PowerFLOW for simulations of the streaming flows in a standing wave resonator with and without rigid obstacles. In order to acquire further insight into the complex streaming environment caused by the interactions of the standing wave with an obstacle inside a resonator, numerical models were developed in a LBM based commercial software, PowerFLOW. The current research is among very studies of acoustic streaming using a LBM flow solver. An acoustic standing wave was first simulated in an empty rectangular resonator using a 2D model. The results obtained for the instantaneous acoustic and the Rayleigh streaming velocities were verified through comparisons with the analytical results. The Rayleigh streaming inside a 3D square cross-section resonator was simulated using a 3D LBM model. The numerical model also predicted similar behaviour as were found from the experimental study of

the 3D Rayleigh streaming cells. It was concluded that the LBM based numerical model could accurately quantify the acoustic and the streaming velocities in both 2D and 3D fluid domains.

There is little literature available for acoustic streaming flow due to a rectangular spoiler inside a standing wave resonator. As stated in chapter 1, one of the specific aims of this research was to quantify the acoustic streaming which results from interactions of the standing wave with the idealised thermoacoustic core elements. The stack and the plates of the plate fin heat exchanger were idealised as a rectangular spoiler. The introduction of a spoiler in the numerical domain resulted in the emergence of edge streaming cells in the vicinity of the spoiler edges. The edge streaming was found to be distinct from the Rayleigh streaming. Two edge streaming cells were observed at the spoiler end. A primary streaming cell was located near the spoiler end, and a secondary streaming cell was located next to the primary cell. Away from the spoiler, a Rayleigh streaming cell was also found to exist beyond the secondary edge streaming cell. The axial dimension of the primary edge streaming cell was around 2% of the axial dimension of the Rayleigh streaming cell. The size of the secondary cell was always larger than the primary cell, and depended on the maximum instantaneous acoustic velocity magnitude at the spoiler end. The velocity magnitude of the edge streaming was very large when compared with the Rayleigh streaming. This implies that the heat transfer caused by the edge streaming would be larger in comparison with the Rayleigh streaming. In the parametric study, the peak edge streaming velocity amplitude was found out to be 36 to 72 times greater than the peak Rayleigh streaming velocity amplitude. The peak Rayleigh streaming amplitude depended on the peak instantaneous acoustic velocity amplitude in the entire resonator while the peak magnitude of edge streaming depended on the value of maximum instantaneous acoustic velocity at the location of the spoiler

end. Earlier studies, as described in chapter 1, appeared to imply that Rayleigh streaming was the primary cause of heat transfer from the thermoacoustic core to the environment. The present study showed that the edge streaming was dominant in terms of velocity magnitude over the Rayleigh streaming. A parametric study was performed in which the flow and the spoiler geometric parameters were varied and their effects on the edge streaming were studied. It was observed that stacks made of spoilers which were thicker in width, shorter in length and had a rectangular edge shape resulted in higher magnitudes of edge streaming velocity and therefore would cause greater heat transfer.

The third objective of this study was to characterise the instantaneous vortical flow structures which were developed due to interactions of the standing wave with an idealised stack and heat exchanger. In order to realise this objective, numerical investigation of the instantaneous flow structures formed due to the interaction of the acoustic standing wave with the spoiler were performed. Two phases were identified within an acoustic cycle namely, the ejection phase, when the flow moves out of the stack end and the ingestion/suction phase, when the flow moves towards the stack end. Different flow and spoiler parameters were varied and their effects on the instantaneous vortical flow structures were identified. The flow parameters studied were maximum instantaneous acoustic velocity amplitude and excitation frequency and the spoiler parameters studied were thickness, length and edge shape. It was observed that, for a given spoiler geometry, greater peak acoustic velocity amplitude and greater excitation frequency caused larger flow mixing which would cause greater heat transfer rates. For a given excitation frequency and peak acoustic velocity amplitude, spoilers with larger thickness and edge shapes

which provided greater flow resistance during the ingestion stage of an acoustic cycle would cause higher heat transfer rates.

The present work is the first detailed numerical study of the acoustic flow in the environment surrounding the stack in a standing wave resonator. The entire resonator was included within the simulation domain, allowing for the identification of different types of streaming flows. The numerical results presented in this work suggest that LBM based numerical models accurately predict the instantaneous and the streaming flows in a standing wave resonator both with and without spoilers.

7.4 Proposed future work

In the study presented here, acoustic streaming arising from interactions between the standing wave and a single spoiler were observed. The LBM provides the advantage of easy incorporation of complex geometries in the simulation domain. Therefore, in future studies, more realistic geometries of stack, heat exchanger and their combination can be introduced in the simulation domain. This would give a better idea of the overall streaming environment in a realistic thermoacoustic machine.

It was generally believed that acoustic streaming hampers the efficiency of thermoacoustic machines [1]. The results presented here showed that acoustic streaming caused heat transfer enhancement. Acoustic streaming may lead to better heat transfer between the stack and the two heat exchangers, which would increase the efficiency of the thermoacoustic machine. Further work is needed in characterising the overall effect of the different types of acoustic streaming on

the thermoacoustic efficiency. This would help in designing more efficient thermoacoustic machines.

The experimental and the numerical results presented in this study were for the instantaneous and the cycle averaged, streaming velocity field in a standing wave resonator. Further studies can be performed where combined thermal and flow behaviour of the flow in an acoustic standing wave resonator can be studied. Experimentally, this can be achieved by performing combined PIV/PLIF investigation and numerically this can be achieved by simulating a coupled momentum-energy equation in LBM. This would help in better characterising the effect of different types of acoustic streaming on the heat transfer rates.

The main focus of the present study was to study the effect of acoustic streaming on heat transfer. There are other applications of acoustic streaming. Previous studies have shown that acoustic streaming can help in material removal, mass transfer and increasing chemical reaction rates [6]. In the field of dentistry, micro acoustic streaming is believed to help in the cleaning process where ultrasonic files are used [85]. There are very few studies available where the effectiveness of acoustic streaming was quantitatively studied and therefore experimental and numerical study of the effectiveness of acoustic streaming in material removal with applications in dentistry can be performed.

Appendix: Comparison between experimental and numerical results

In this appendix, comparison between the experimental and the numerical results is shown. The results and discussion presented here were published before [86] in a paper co-authored by the author of this dissertation.

INTRODUCTION

Thermoacoustic cooling systems use environmentally benign working gasses to convert acoustic energy into heat pumping. Within the stack, the interactions between high amplitude acoustic waves and the solid substrate, here a stack of thin parallel plates, leads to heat pumping through net time-averaged enthalpy flux within the boundary layer, where there is in-phase phasing between temperature and velocity. The interactions between the high amplitude acoustic waves and the stack-heat exchanger couple create complex flow structures which regulate convective heat transfer. The formation of vortices at the stack end, their interaction with the heat exchangers and acoustic streaming needs to be characterized to better quantify their effects on the performance of thermoacoustic devices. Models based on linear acoustic theory commonly neglect the production of vorticity at the stack boundaries. A better understanding of the interactions between the acoustic waves and the stack ends is needed in order to optimize and increase the efficiency of the thermoacoustic engines.

Flow measurement techniques like Hot Wire Anemometry or usage of pressure transducers can be intrusive. Non-intrusive techniques like Laser Doppler Anemometry and Particle Image Velocimetry (PIV) do not disturb the flow but due to close proximity of stack and heat

exchangers and also highly pressurized gases being used in realistic thermoacoustic refrigerators, optical access is limited and it is difficult to use these non-intrusive techniques. Recently, PIV has been used in idealized configurations to study the flow structures behind the stack.

A detailed study of the flow structures around the stack of a simplified thermoacoustic refrigerator operated in ambient air was performed by Berson *et al*. [33]. They measured the acoustic particle velocity inside the boundary layer between the stacks. Symmetric pairs of counter-rotating vortices were identified near the end of the stack at low pressure levels. Vortex shedding and loss of symmetry was observed for high acoustic pressures. Mao *et al*. [40] suggested the characterization of fluid motion around the stack using ensemble-averaged, phase-locked PIV. They stressed the need for a better understanding of the turbulence characteristics of oscillatory flows past a stack of parallel plates.

Due to limitations of experimental methods of the direct measurement of flow variables in real thermoacoustic refrigerators, numerical techniques can be employed to better capture the complex flow interactions present in stack-heat exchanger couples. Analytical and numerical studies of the effects of reciprocating flows on heat transfer in channels can be found in the literature. Siegel [87] studied the heat transfer in channels with periodically oscillating flow. A review of similar studies was given by Cooper *et al*. [88]. Zhao and Cheng [89] showed that oscillatory flows enhance heat transfer in ducts and enclosures. Sert and Beskok [90] studied the effects of frequency on flow and heat transfer in two-dimensional channels with reciprocating flow. Other mechanisms such as the addition of a porous layer have been shown to have a significant effect on the heat transfer in oscillatory flows in channels [91].

Few numerical studies of the flow over stacks inside thermoacoustic devices have been performed. A low-Mach-number compressible flow model of unsteady, thermally stratified flow in two-dimensional thermoacoustic stacks was developed by Worlikar *et al*. [92]. Both fluid flow and heat transfer between two ideal stack plates were modeled using the finite difference method. Marx and Blanc-Benon [93] investigated the two-dimensional flow in coupled heat exchanger-stack configurations by solving the Navier-Stokes equations coupled with energy equations including viscous dissipation terms. They performed simulations for high-amplitude acoustic waves. The formulation of Worlikar *et al.* was used in addition to the thin-plate stack the assumption Besnoin and Knio [94] to find the thermal efficiency of thermoacoustic heat exchangers and characteristics of cooling loads, using the finite-volume method.

In the present study, the lattice Boltzmann Method (LBM) was utilized to simulate the acoustic flow field around a single-plate stack with finite thickness and to capture the vortex formation phenomenon. The numerical setup was tailored to closely match an experimental setup used to visualize and quantify the flow field using PIV.

Lattice Boltzmann Method

Methodology and application

Numerical simulations of fluid dynamics based on solutions of the macroscopic Navier-Stokes equations involve the explicit calculation of macroscopic fluid properties by imposing conservation laws. An alternative approach, called the Lattice Boltzmann Method (LBM), is based on kinetic theory. In this method, a particle distribution function is considered in a discrete lattice domain. By imposing streaming and collision laws governed by the lattice-Boltzmann

equation (LBE), transient macroscopic fluid properties are obtained. Through the Chapman-Enskog expansion, [95] LBE recovers the compressible Navier-Stokes equation at the hydrodynamic limit [46]. The conserved variables such as density, momentum and internal energy are obtained by performing a local integration of the particle distribution function. The LBM has many potential advantages over Navier-Stokes based methods. The availability of particle-based models for solid-fluid boundaries, and the absence of Jacobians to compute grid metrics allow the treatment of solids with complex shapes to the computational domain without a considerable increase in computational cost. The method is intrinsically parallelizable. The convection operator in the lattice-Boltzmann equation is linear; however, nonlinear features are recovered by particle advection/collision relations together with multi-scale expansions. The main disadvantage of this method is known to be the Mach number limitation, according to the compressibility criterion [46], associated with one widely used simplified form of the collision operator. Benchmark problems such as flow over cylinders, airfoils [96], and rectangular cavities [97] have been shown to be accurately modeled using the LBM. In the area of aeroacoustics, Crouse *et a1*. [98] have studied series of canonical acoustic sound propagation problems and problems involving strong interactions between flow and sound.

The LBM recovers the compressible Navier-Stokes equations, including an ideal gas equation of state, and thus inherently captures acoustic phenomenon. Pressure waves are propagated at the so-called lattice sound speed, which is a function of the state-space of the particle distribution function. A commercially available code, PowerFLOW 4.3b, based on the LBM kernel was used for the simulations in the present study.

Basic Formulation

Considering, the lattice unit length Δx and the lattice unit time step Δt, the lattice-Boltzmann equation may be written in the following form.

$$f_i(\hat{x} + c_i\Delta x, t + \Delta t) - f_i(\hat{x}, t) = -\frac{\Delta t}{\tau}\left(f_i - f_i^{eq}\right) \quad , \tag{1}$$

where the distribution function $f_i(\hat{x}, t)$ can conveniently be considered as a typical histogram representing the frequency of occurrence of particles at position $\hat{x}$ with velocity $\boldsymbol{c_i}$ in the i direction at time t . The frequencies may be considered to be direction-specific fluid densities. The left hand side of (1) represents the propagation of particles in the discretized lattice domain, whereas the right hand side is the collision operator adopted from the Bhatnagar-Gross-Krook (BGK) approximation [46]. A relaxation time parameter, τ, used in this model is related to the kinematic viscosity, v, such that $\tau = \left(\nu + \Delta t\right)/T$. The equilibrium distribution function f_i^{eq} relates the lattice Boltzmann model to hydrodynamic properties and is essential for local conservation criteria to be satisfied. In this study, f_i^{eq} was obtained from the D3Q19 model [46]. The D3Q19 scheme represents discrete velocities towards neighboring cells as shown in Fig. 1. It has been shown that this model is second order accurate in both time and space [46]. The conservative fluid properties such as the density and momentum are obtained by summing the moments in velocity directions.

$$\rho = \sum_{i=1} f_i(\hat{x}, t), \qquad \rho\hat{u}(x, t) = \sum_{i=1} f_i(\hat{x}, t), \quad , \tag{2}$$

Experimental Setup

Instrumentation

A schematic of the experimental setup is shown in Fig. 2. The acoustic resonator (j) used in this experimental study had a square cross section, $4cm \times 4\ cm$ and a length of 98 cm. The walls of the resonator were 9 mm thick. A 200 W acoustic driver (e) with a DC coil resistance of 8 Ω excited the acoustic standing wave in the resonator. A function generator (a) produced a sinusoidal excitation signal which was fed to a 200 W RMS power amplifier (d). A power analyzer (b) was connected in parallel with the acoustic driver to monitor the instantaneous true RMS voltage, current and power fed to the acoustic driver. Two high-resolution ICP pressure transducers were mounted flush near the two extremities of the resonator for measuring the dynamic pressure. The particle image velocimetry (PIV) system was a dual-cavity, time-resolved (TR) Nd:YLF laser (g) with a maximum repetition rate of 10 kHz per cavity. A CCD-CMOS camera (f) with a frame rate of 2000 fps and a resolution of 1280×1024 pixels was used. The pixel pitch of the camera was 12 μm. The camera was mounted on a traversing mechanism (i) which allowed mapping of the velocity field over the entire length of the resonator. A controller unit (c) supplied by the PIV system manufacturer was employed in order to synchronize the camera and the laser. A Laskin nozzle seeding generator, using olive oil, produced 1μm particles which were used for flow seeding process.

Data acquisition and analysis

To obtain vortex patterns and acoustic velocity at different phases the phase-locked ensemble averaging method described by Nabavi *et al*. [30] was employed. To synchronize PIV

acquisition and acoustic waves, the signal from a pressure transducer mounted at the rigid end of the channel was used. The time duration between two laser pulses, Δt, was sufficient enough to allow the seeding particles to move quarter of the interrogation region. The size of interrogation region was 16×16 pixels. At each phase (Φ), 150 images were captured. The phase averaged data were acquired for 20 distinct phases per acoustic cycle.

Numerical Setup and Case study

A schematic representation of the computational domain is shown in Fig. 3. Experiments were performed for one acoustic amplitude and frequency, 245.5 *Hz*, which corresponds to one of the resonance frequencies of the channel. The acoustic amplitude was measured to be 2.5 m/s. Based on the channel dimensions, specified in section 3.1, the key dimensionless geometrical quantities were $a/\lambda = 0.03$, $t/\lambda = 7.13\times10^{-4}$ and $L/\lambda = 0.7$.

The computational domain was divided into structured lattice arrays with variable resolutions (VR). In the numerical setup, seven variable resolution zones were used. The process of partitioning the computational domain into variable resolution regions in LBM is similar to the grid refinement and stretching seen in finite-difference/volume numerical schemes. The lattice length always varies by a factor of two from one VR to another to ensure appropriate particle convection from one lattice to another based on allowed and pre-assigned discretized velocity directions. The fluid viscosity was matched with that of the experiment. The Reynolds number, based on stack thickness and acoustic particle velocity amplitude was set

to 453. A total of 24 grid points were placed inside the acoustic penetration depth. The flow characteristics of the simulation are summarized in table 1.

The fluid domain consisted of 1.6 million grid cells (voxels). The smallest voxel size was located inside the acoustic boundary layer around the stack. A schematic of the grid distribution near the stack plate is shown in Fig. 4. The excitation was provided by imposing a sinusoidal, constant amplitude and single frequency velocity at the inlet. A no-slip wall boundary condition (*V(L) = 0*) was imposed at the end of the tube.

$$V_{Inlet} = \Re(V(x=0)e^{i\omega t}) = V_0 \cos(\omega t) \quad , \tag{3}$$

Results and Discussion

The running time of the simulation was *18* hours using *32* cores. The time history was sufficient to capture *21* complete acoustic cycles. Data sampling started after the fourth cycle. The flow phase locked data (pressure, velocity and vorticity) were ensemble averaged over ten cycles.

The vorticity contours at time corresponding to different phases within an acoustic cycle are shown in Fig.5. The vorticity values obtained from the simulations are in good qualitative and quantitative agreement with the PIV measurements.

Vortex shedding may occur based on the local Reynolds number and the nominal Keulegan-Carpenter number. The spectral density of the velocity at a location *0.5t* along the lip line of the stack edge is shown in Fig. 6 while the spectrum is dominated by the periodic excitation

frequency and its harmonic, one can detect a frequency component close to the Strouhal number 0.209, which is compatible with the value obtained by tracking the snapshots of the vorticity field and from the time intervals between consecutive shedding.

The axial velocity profiles are plotted perpendicular to the stack surface at a distance of one stack thickness from the leading edge are shown in Fig. 7 at selected phases during an acoustic cycle. The middle two profiles (red circle and khaki squares) illustrate the flow reversal phenomenon. These two profiles correspond to the bottom two subfigures shown in Fig. 5. The velocity profile trends and magnitudes are in general agreement with experimental results. Some discrepancies in the region near the stack boundary can be due to the parallax effect which causes fictitious particle movement on the solid surface.

The drag coefficient quantifies the overall losses within the stack. The pressure losses across the stack affect the operating condition and performance of thermoacoustic devices. The total drag force, *D*, exerted by stack is defined as the sum of the pressure drag obtained from a surface integral of the normal stress tensor, $\tilde{P}$ projected in the x-direction and the friction drag (surface integral of the shear stress tensor, $\tilde{\tau}_w$ projected in x-direction). (Eqn.4). The total drag coefficient is calculated by normalizing the drag force with dynamic force based on the acoustic excitation velocity amplitude and the projected area ($A_P = t \times 1m$).

$$D = \int_A \tilde{P}.\vec{n}_x \, dA + \int_A \tilde{\tau}_w.\vec{n}_x \, dA \quad , \qquad (4)$$

$$C_D = \frac{D}{\frac{1}{2}\rho V_0^2 A_p} \quad , \qquad (5)$$

The drag coefficient based on Eqns. (4) and (5), is shown in Fig.8. The drag coefficient exhibits a transient oscillating behavior as the shear stress and the normal surface pressure change during flow reversal. The impact of previously convected vortices in consecutive cycles also adds to the chaotic nature of the flow. A comparison between the excitation velocity response, shown in Fig.9, and the drag history reveals a phase difference between the excitation velocity amplitude and the maximum drag. This difference in phase varies cycle to cycle with an average value around 0.43 *rad*.

CONCLUSIONS

Numerical simulation of an unsteady 2D reciprocating flow over a rectangular plate in a channel was performed using the Lattice Boltzmann method. The velocity field was obtained experimentally using particle image velocimetry (PIV). A comparison between the results indicates that the LBM accurately captures the physics of acoustic flows over solid bodies. The vortex shedding phenomena was visualized and quantified by processing the velocity signals near the edge of the stack. The transient behavior of the resultant drag force was studied by calculating the instantaneous total drag force imposed by the stack. The drag force variation was periodic but not sinusoidal. A phase lag was also detected between the maxima of drag force and the maximum excitation velocity, which is different from laminar steady flow over solid bodies where the change in drag force is in phase with change in flow velocity.

Acknowledgements

The authors would thank Exa corporation for providing PowerFLOW academic license and for their continuous support. We thank Calcul Quebec for the use of the high performance computational resources. The numerical simulations were performed on clusters supported by the Consortium Laval, Université du Québec, McGill and Eastern Quebec (CLUMEQ).

Table 1 Parameters used in the numerical setup.

Parameter	Magnitude
Acoustic viscous Penetration depth ($\delta_\upsilon = \sqrt{2\nu/\omega\rho}$)	$1.18\times10^{-4}\ m$
Nominal Reynolds Number ($Re = \frac{V_{x=0}t}{\nu}$)	453
Womersley number ($\alpha = t\sqrt{\frac{\omega}{\nu}}$)	10.1
Keulegan-Carpenter number ($KC = V(x=0)/\left(f_{exc}t\right)$)	8.31 m/s

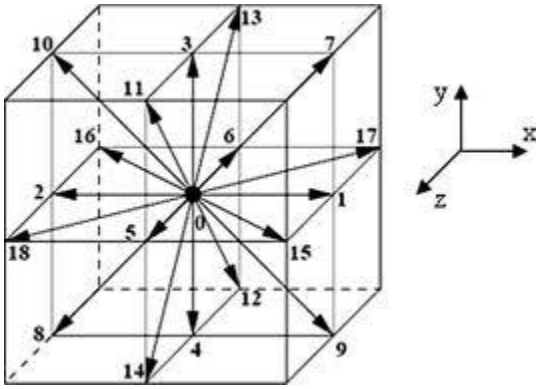

Fig. 1 - D3Q19 discretized phase-space configuration

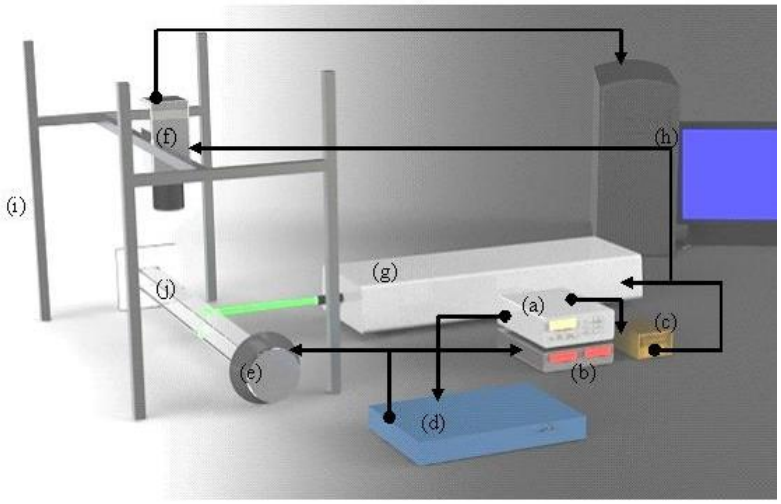

Fig. 2 - Schematic of the experimental setup. (a) Function generator; (b) Power analyzer; (c) Synchronization unit; (d) Power amplifier; (e) Acoustic driver; (f) CCD camera; (g) Laser; (h) Computer with frame grabber; (i) Traversing mechanism; (j) Resonator tube.

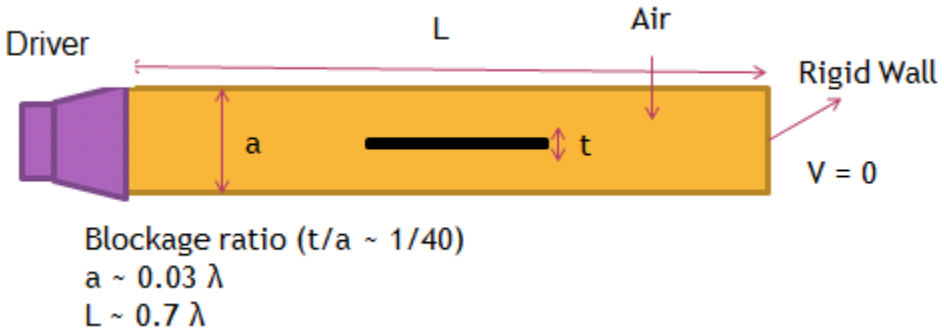

Fig.3 – Configuration of single stack plate inside the resonator

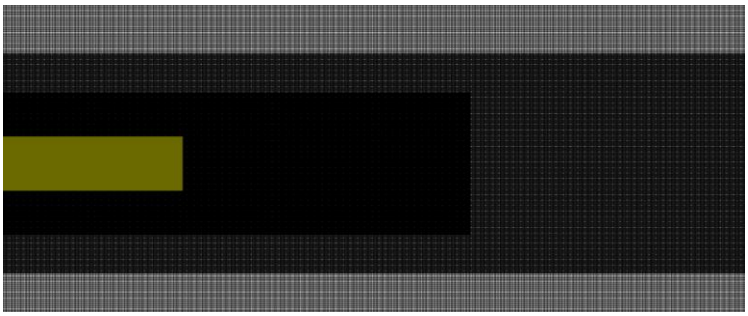

Fig. 4 – Voxel distribution near the Stack

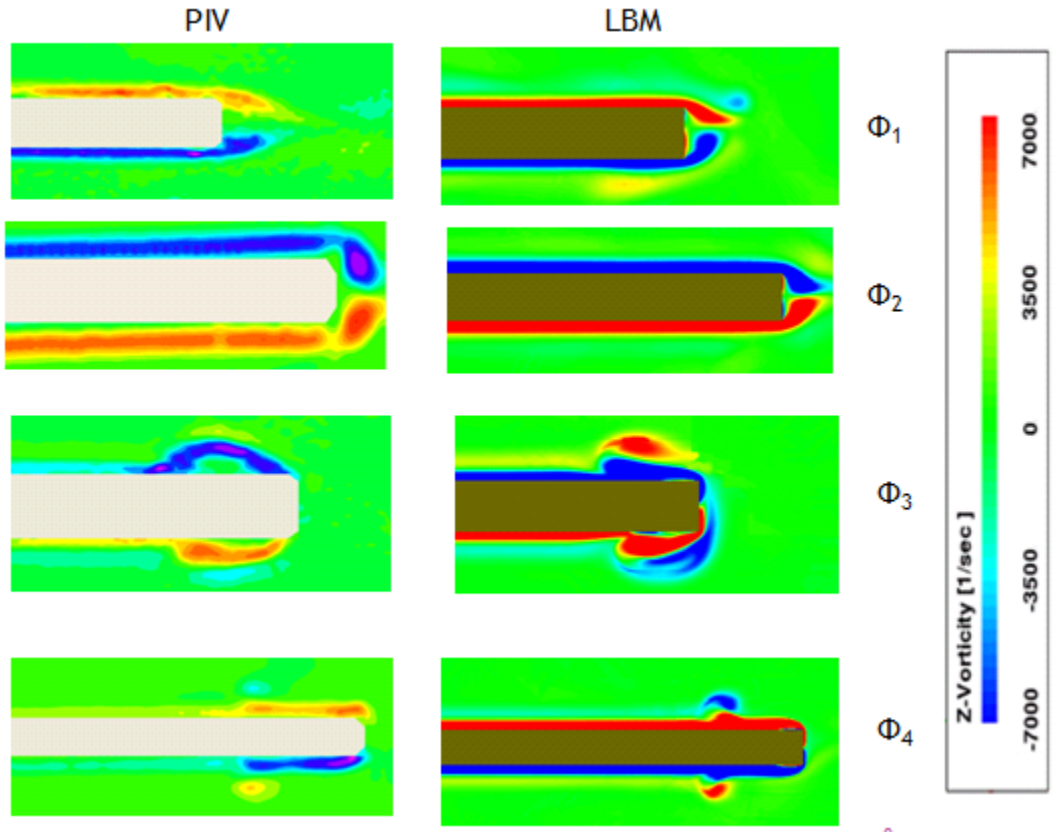

Fig. 5 – Vorticity contours near the edge of the stack

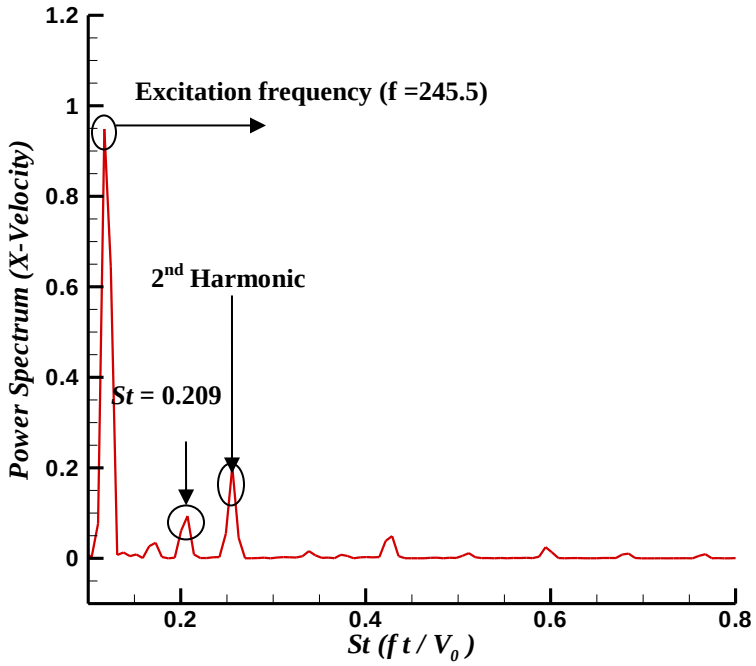

Fig.6 – Velocity powerspectrum at a probe located along the lip line of the stack (at x= 0.5 t from the bottom edge of the stack)

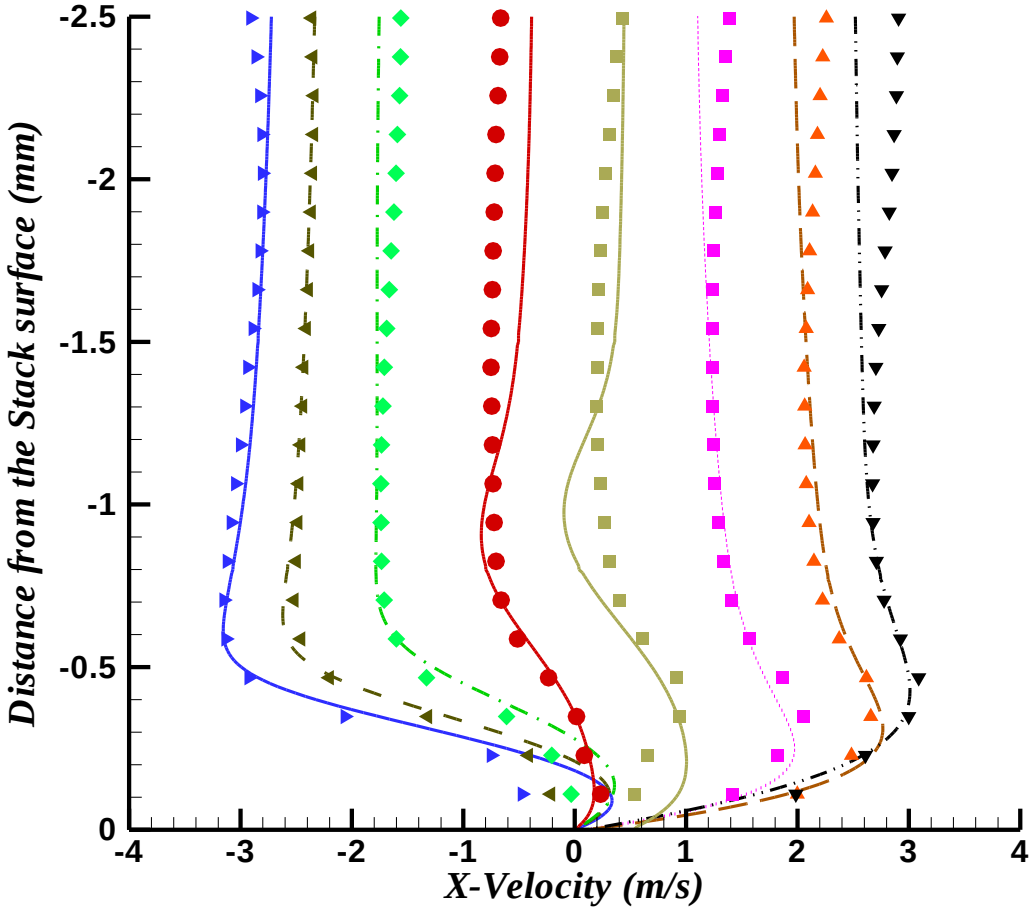

Fig. 7 –Velocity comparison profile for different phases. LBM results are presented by lines and symbols corresponds to the experimental data.

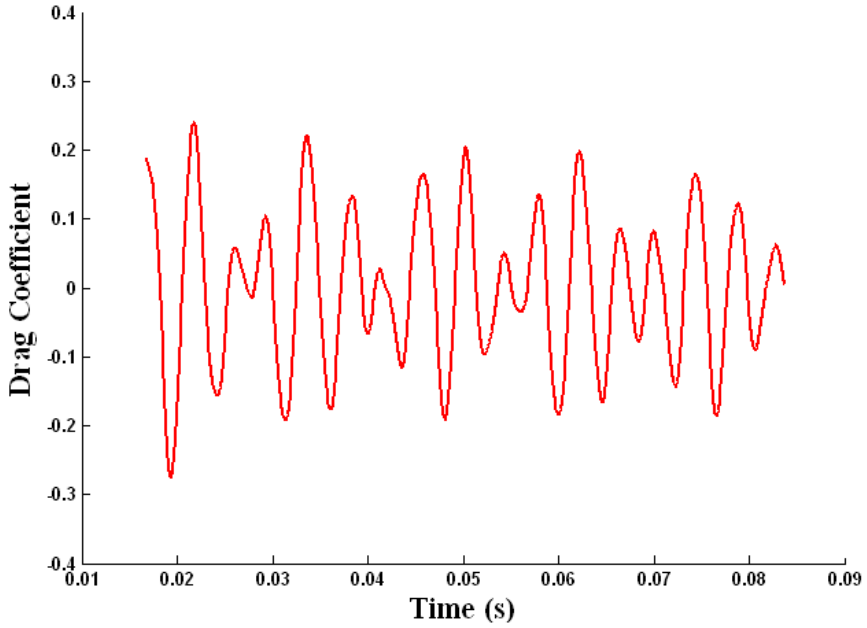

Fig. 8 – Time history of total drag coefficient of the stack

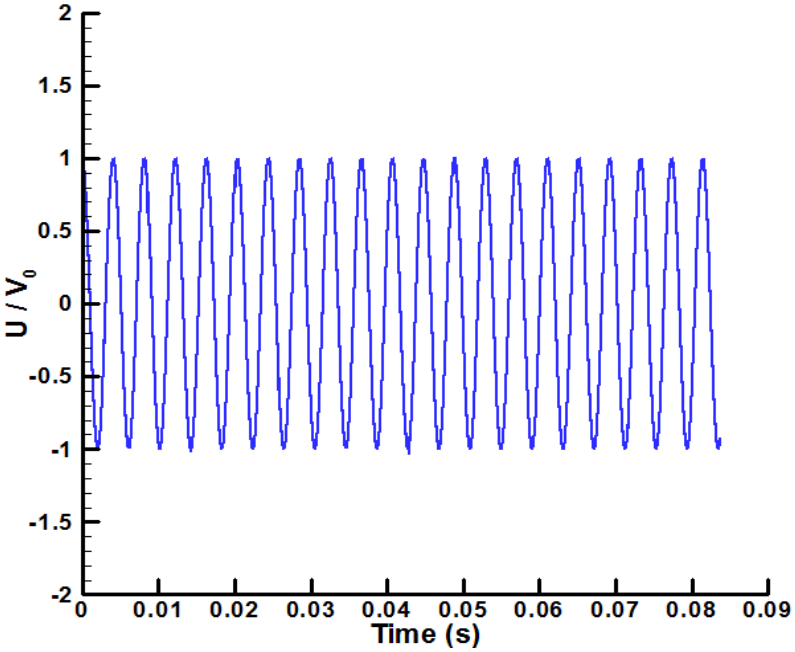

Fig. 9 – Velocity response of the resonator at a probe location near the driver

References

1. Swift, G.W., *Thermoacoustics: A unifying perspective for some engines and refrigerators*. 2002, Melville, NY: Acoustical Society of America through the American Institute of Physics.
2. Wuebbles, D.J., *The role of refrigerants in climate change.* International Journal of Refrigeration, 1994. **17**(1): p. 7-17.
3. Adeff, J.A. and Hofler, T.J., *Design and construction of a solar-powdered, thermoacoustically driven, thermoacoustic refrigerator.* The Journal of the Acoustical Society of America, 2000. **107**: p. L37.
4. Johnson, R., Garrett, S., and Keolian, R., *Thermoacoustic cooling for surface combatants.* Naval engineers journal, 2000. **112**(4): p. 335-345.
5. Swift, G.W., *Thermoacoustic engines.* The Journal of the Acoustical Society of America, 1988. **84**: p. 1145.
6. Nyborg, W.L., *Acoustic streaming*, in *Physical Acoustics Principles and Methods,* M.W. P., Editor. 1965, Academic Press: New York. p. 290-295.
7. Riley, N., *Acoustic streaming.* Theoretical and computational fluid dynamics, 1998. **10**(1-4): p. 349-356.
8. Boluriaan, S. and Morris, P.J., *Acoustic streaming: from Rayleigh to today.* International Journal of aeroacoustics, 2003. **2**(3): p. 255-292.
9. Faraday, M., *On a Peculiar Class of Acoustical Figures; and on Certain Forms Assumed by Groups of Particles upon Vibrating Elastic Surfaces.* Philosophical Transactions of the Royal Society of London 1831. **121**: p. 299-340.
10. Lighthill, S.J., *Acoustic streaming.* Journal of Sound and Vibration, 1978. **61**(3): p. 391-418.

11. Rayleigh, L., *On the Circulation of Air Observed in Kundt's Tubes, and on Some Allied Acoustical Problems.* Philosophical Transactions of the Royal Society of London, 1884. **175**: p. 1-21.

12. Rudenko and Soluyan, *Theoretical foundations of nonlinear acoustics*. 1997, New York: Consultants Bureau.

13. Qi, Q., *The effect of compressibility on acoustic streaming near a rigid boundary for a plane traveling wave.* Journal of the Acoustical Society of America, 1993. **94**(2 I): p. 1090-1098.

14. Waxler, R., *Stationary velocity and pressure gradients in a thermoacoustic stack.* Journal of the Acoustical Society of America, 2001. **109**(6): p. 2739-2750.

15. Bailliet, H., Gusev, V., Raspet, R., and Hiller, R.A., *Acoustic streaming in closed thermoacoustic devices.* Journal of the Acoustical Society of America, 2001. **110**(4): p. 1808-1821.

16. Hamilton, M.F., Ilinskii, Y.A., and Zabolotskaya, E.A., *Acoustic streaming generated by standing waves in two-dimensional channels of arbitrary width.* Journal of the Acoustical Society of America, 2003. **113**(1): p. 153-160.

17. Backhaus, S. and Swift, G.W., *A thermoacoustic-Stirling heat engine: Detailed study.* Journal of the Acoustical Society of America, 2000. **107**(6): p. 3148-3166.

18. Paek, I., Braun, J.E., and Mongeau, L., *Characterizing heat transfer coefficients for heat exchangers in standing wave thermoacoustic coolers.* Journal of the Acoustical Society of America, 2005. **118**(4): p. 2271-2280.

19. Menguy, L. and Gilbert, J., *Non-linear acoustic streaming accompanying a plane stationary wave in a guide.* Acustica, 2000. **86**(2): p. 249-259.

20. Campbell, M., Cosgrove, J.A., Greated, C.A., Jack, S., and Rockliff, D., *Review of LDA and PIV applied to the measurement of sound and acoustic streaming.* Optics and Laser Technology, 2000. **32**(7-8): p. 629-639.

21. Rafat, Y. and Mongeau, L. *Time-resolved Particle Image Velocimetry of the flow in an acoustic standing wave tube*. Proceedings of the *International Congress on Acoustics*. Australia.

22. Arroyo, M.P. and Greated, C.A., *Stereoscopic Particle Image Velocimetry.* Measurement Science & Technology, 1991. **2**(12): p. 1181-1186.

23. Hann, D.B. and Greated, C.A., *Particle image velocimetry for the measurement of mean and acoustic particle velocities.* Measurement Science & Technology, 1997. **8**(6): p. 656-660.

24. Hann, D.B. and Greated, C.A., *The measurement of flow velocity and acoustic particle velocity using particle-image velocimetry.* Measurement Science & Technology, 1997. **8**(12): p. 1517-1522.

25. Sharpe, J.P., Greated, C.A., Gray, C., and Campbell, D.M., *The Measurement of Acoustic Streaming Using Particle Image Velocimetry.* Acustica, 1989. **68**(2): p. 168-172.

26. Thompson, M.W. and Atchley, A.A., *Simultaneous measurement of acoustic and streaming velocities in a standing wave using laser Doppler anemometry.* Journal of the Acoustical Society of America, 2005. **117**(4): p. 1828-1838.

27. Thompson, M.W., Atchley, A.A., and Maccarone, M.J., *Influences of a temperature gradient and fluid inertia on acoustic streaming in a standing wave.* Journal of the Acoustical Society of America, 2005. **117**(4): p. 1839-1849.

28. Moreau, S., Bailliet, H., and Valiere, J.C., *Measurements of inner and outer streaming vortices in a standing wavegulide using laser doppler velocimetry.* Journal of the Acoustical Society of America, 2008. **123**(2): p. 640-647.

29. Reyt, I., Daru, V., Bailliet, H., Moreau, S., Valière, J.-C., Baltean-Carlès, D., and Weisman, C., *Fast acoustic streaming in standing waves: Generation of an additional outer streaming cell.* The Journal of the Acoustical Society of America, 2013. **134**: p. 1791.

30. Nabavi, M., Kamran Siddiqui, M.H., and Dargahi, J., *Simultaneous measurement of acoustic and streaming velocities using synchronized PIV technique.* Measurement Science and Technology, 2007. **18**(7): p. 1811-1817.

31. Nabavi, M., Siddiqui, K., and Dargahi, J., *Analysis of regular and irregular acoustic streaming patterns in a rectangular enclosure.* Wave Motion, 2009. **46**(5): p. 312-322.

32. Nabavi, M., Siddiqui, K., and Dargahi, J., *Influence of differentially heated horizontal walls on the streaming shape and velocity in a standing wave resonator.* International Communications in Heat and Mass Transfer, 2008. **35**(9): p. 1061-1064.

33. Berson, A., Michard, M., and Blanc-Benon, P., *Measurement of acoustic velocity in the stack of a thermoacoustic refrigerator using particle image velocimetry.* Heat and Mass Transfer/Waerme- und Stoffuebertragung, 2008. **44**(8): p. 1015-1023.

34. Mao, X. and Jaworski, A.J., *Application of particle image velocimetry measurement techniques to study turbulence characteristics of oscillatory flows around parallel-plate structures in thermoacoustic devices.* Measurement Science and Technology, 2010. **21**(3).

35. Aktas, M.K., Farouk, B., and YIQIANG, L., *Heat transfer enhancement by acoustic streaming in an enclosure.* Journal of heat transfer, 2005. **127**(12): p. 1313-1321.

36. Mozurkewich, G., *Heat transport by acoustic streaming within a cylindrical resonator.* Applied Acoustics, 2002. **63**(7): p. 713-735.

37. Wu, T. and Ro, P.I., *Heat transfer performance of a cooling system using vibrating piezoelectric beams.* Journal of Micromechanics and Microengineering, 2005. **15**(1): p. 213.

38. Moreau, S., Bailliet, H., and Valiere, J.C., *Effect of a stack on Rayleigh streaming cells investigated by laser Doppler velocimetry for application to thermoacoustic devices.* Journal of the Acoustical Society of America, 2009. **125**(6): p. 3514-3517.

39. Aben, P.C.H., Bloemen, P.R., and Zeegers, J.C.H., *2-D PIV measurements of oscillatory flow around parallel plates.* Experiments in Fluids, 2009. **46**(4): p. 631-641.

40. Mao, X., Yu, Z., Jaworski, A.J., and Marx, D., *PIV studies of coherent structures generated at the end of a stack of parallel plates in a standing wave acoustic field.* Experiments in Fluids, 2008. **45**(5): p. 833-846.

41. Rockliff, D., *Application of particle image velocimetry to the measurement of non-linear effects generated by high-intensity acoustic fields*. 2002, PhD Thesis, University of Edinburgh.

42. Shi, L., Yu, Z., and Jaworski, A.J., *Vortex shedding flow patterns and their transitions in oscillatory flows past parallel-plate thermoacoustic stacks.* Experimental Thermal and Fluid Science, 2010. **34**(7): p. 954-965.

43. Shi, L., Yu, Z., and Jaworski, A.J., *Investigation into the Strouhal numbers associated with vortex shedding from parallel-plate thermoacoustic stacks in oscillatory flow conditions.* European Journal of Mechanics, B/Fluids, 2011. **30**(2): p. 206-217.

44. Zhang, D.-W., He, Y.-L., Yang, W.-W., Wang, Y., and Tao, W.-Q., *Particle image velocimetry measurement on the oscillatory flow at the end of the thermoacoustic parallel stacks.* Applied Thermal Engineering, 2013. **51**(1–2): p. 325-333.

45. Zhang, D.-W., He, Y.-L., Yang, W.-W., Gu, X., Wang, Y., and Tao, W.-Q., *Experimental visualization and heat transfer analysis of the oscillatory flow in thermoacoustic stacks.* Experimental Thermal and Fluid Science, 2013. **46**(0): p. 221-231.

46. Chen, S. and Doolen, G.D., *Lattice Boltzmann method for fluid flows.* Annual review of fluid mechanics, 1998. **30**(1): p. 329-364.

47. Kawahashi, M. and Arakawa, M., *Nonlinear phenomena induced by finite-amplitude oscillation of air column in closed duct (Analysis of acoustic streaming).* JSME International Journal, Series B: Fluids and Thermal Engineering, 1996. **39**(2): p. 280-286.

48. Yano, T., *Turbulent acoustic streaming excited by resonant gas oscillation with periodic shock waves in a closed tube.* Journal of the Acoustical Society of America, 1999. **106**(1): p. L7-L12.

49. Aktas, M.K. and Farouk, B., *Numerical simulation of acoustic streaming generated by finite-amplitude resonant oscillations in an enclosure.* Journal of the Acoustical Society of America, 2004. **116**(5): p. 2822-2831.

50. Aktas, M.K. and Ozgumus, T., *The effects of acoustic streaming on thermal convection in an enclosure with differentially heated horizontal walls.* International Journal of Heat and Mass Transfer, 2010. **53**(23-24): p. 5289-5297.

51. Daru, V., Baltean-Carlès, D., Weisman, C., Debesse, P., and Gurunath Gandikota, V., *Two-dimensional numerical simulations of nonlinear acoustic streaming in standing waves.* Wave Motion, 2013.

52. Cao, N., Olson, J., Swift, G., and Chen, S., *Energy flux density in a thermoacoustic couple.* The Journal of the Acoustical Society of America, 1996. **99**: p. 3456.

53. Ishikawa, H. and Mee, D.J., *Numerical investigations of flow and energy fields near a thermoacoustic couple.* The Journal of the Acoustical Society of America, 2002. **111**: p. 831.

54. Blanc-Benon, P., Besnoin, E., and Knio, O., *Experimental and computational visualization of the flow field in a thermoacoustic stack.* Comptes Rendus - Mecanique, 2003. **331**(1): p. 17-24.

55. Besnoin, E. and Knio, O.M., *Numerical study of thermoacoustic heat exchangers.* Acta Acustica united with Acustica, 2004. **90**(3): p. 432-444.

56. Jaworski, A.J., Mao, X., and Yu, Z., *Entrance effects in the channels of the parallel plate stack in oscillatory flow conditions.* Experimental Thermal and Fluid Science, 2009. **33**(3): p. 495-502.

57. Patankar, S.V. and Spalding, D.B., *A calculation procedure for heat, mass and momentum transfer in three-dimensional parabolic flows.* International Journal of Heat and Mass Transfer, 1972. **15**(10): p. 1787-1806.

58. Cosgrove, J., Buick, J., Tonge, S., Munro, C., Greated, C., and Campbell, D., *Application of the lattice Boltzmann method to transition in oscillatory channel flow.* Journal of Physics A: Mathematical and General, 2003. **36**(10): p. 2609.

59. Wang, Y., He, Y.L., Li, Q., and Tang, G.H., *Numerical simulations of gas resonant oscillations in a closed tube using lattice Boltzmann method.* International Journal of Heat and Mass Transfer, 2008. **51**(11–12): p. 3082-3090.

60. Habibi, K., Lew, P.-T., and Mongeau, L., *Prediction of sound absorption characteristics of orifice plates with mean flow using the lattice Boltzmann method.* J. Acoust. Soc. Am., 2011. **129**(4): p. 1.

61. EXA Corp, *PowerFLOW user guide*, EXA Corp.

62. Stansell, P. and Greated, C.A., *Lattice gas automaton simulation of acoustic streaming in a two-dimensional pipe.* Physics of Fluids, 1997. **9**(11): p. 3288-3299.

63. Haydock, D. and Yeomans, J.M., *Lattice Boltzmann simulations of acoustic streaming.* Journal of Physics A: Mathematical and General, 2001. **34**(25): p. 5201-5213.

64. Haydock, D. and Yeomans, J.M., *Lattice Boltzmann simulations of attenuation-driven acoustic streaming.* Journal of Physics A: Mathematical and General, 2003. **36**(20): p. 5683-5694.

65. Meng, F., Wang, M., and Li, Z., *Lattice Boltzmann simulations of conjugate heat transfer in high-frequency oscillating flows.* International Journal of Heat and Fluid Flow, 2008. **29**(4): p. 1203-1210.

66. Gedeon, D., *DC gas flows in stirling and pulse tube cryocoolers.* Cryocoolers 9, 1997: p. 385-392.

67. Backhaus, S. and Swift, G.W., *An acoustic streaming instability in thermoacoustic devices utilizing jet pumps.* Journal of the Acoustical Society of America, 2003. **113**(3): p. 1317-1324.

68. Backhaus, S. and Swift, G.W., *A thermoacoustic Stirling heat engine.* Nature, 1999. **399**(6734): p. 335-338.

69. Dai, W., Luo, E.C., Hu, J.Y., and Ling, H., *A Heat-driven thermoacoustic cooler capable of reaching liquid nitrogen temperature.* Applied Physics Letters, 2005. **86**(22).

70. Dai, W., Luo, E.C., Zhang, Y., and Ling, H., *Detailed study of a traveling wave thermoacoustic refrigerator driven by a traveling wave thermoacoustic engine.* Journal of the Acoustical Society of America, 2006. **119**(5): p. 2686-2692.

71. Raffel, M., Willert, C.E., Wereley, S.T., and Kompenhans, J., *Particle Image Velocimetry: A Practical Guide*. 2007: Springer.

72. Lu, L. and Sick, V., *High-speed Particle Image Velocimetry Near Surfaces.* Journal of visualized experiments: JoVE, 2013(76).

73. Keane, R.D. and Adrian, R.J., *Optimization of particle image velocimeters. I. Double pulsed systems.* Measurement science and technology, 1990. **1**(11): p. 1202.

74. Kim, H.-B., Hertzberg, J., Lanning, C., and Shandas, R., *Noninvasive measurement of steady and pulsating velocity profiles and shear rates in arteries using echo PIV: in vitro validation studies.* Annals of biomedical engineering, 2004. **32**(8): p. 1067-1076.

75. Adrian, R., *Dynamic ranges of velocity and spatial resolution of particle image velocimetry.* Measurement Science and Technology, 1997. **8**(12): p. 1393.

76. Wernet, M.P., *A flow field investigation in the diffuser of a high-speed centrifugal compressor using digital particle imaging velocimetry.* Measurement Science and Technology, 2000. **11**(7): p. 1007.

77. Hirasawa, T., Sung, C., Joshi, A., Yang, Z., Wang, H., and Law, C., *Determination of laminar flame speeds using digital particle image velocimetry: Binary Fuel blends of ethylene,< i> n</i>-Butane, and toluene.* Proceedings of the Combustion Institute, 2002. **29**(2): p. 1427-1434.

78. He, X. and Luo, L.S., *Theory of the lattice Boltzmann method: From the Boltzmann equation to the lattice Boltzmann equation.* Physical Review E - Statistical Physics, Plasmas, Fluids, and Related Interdisciplinary Topics, 1997. **56**(6): p. 6811-6817.

79. Bhatnagar, P.L., Gross, E.P., and Krook, M., *A model for collision processes in gases. I. Small amplitude processes in charged and neutral one-component systems.* Physical Review, 1954. **94**(3): p. 511-525.

80. Ziegler, D.P., *Boundary conditions for lattice Boltzmann simulations.* Journal of Statistical Physics, 1993. **71**(5-6): p. 1171-1177.

81. Zou, Q. and He, X., *On pressure and velocity boundary conditions for the lattice Boltzmann BGK model.* Physics of Fluids, 1997. **9**(6): p. 1591-1596.

82. Nabavi, M., Siddiqui, M.H.K., and Dargahi, J., *Experimental investigation of the formation of acoustic streaming in a rectangular enclosure using a synchronized PIV technique.* Measurement Science and Technology, 2008. **19**(6).

83. Reyt, I., Rafat, Y., Mongeau, L., Taher, R., and Bailliet, H., *PIV measurements of 3-dimensional acoustic Rayleigh streaming in a square cross-section standing wave resonator.* Acoustics 2012 Nantes, 2012.

84. Berson, A. and Blanc-Benon, P., *Nonperiodicity of the flow within the gap of a thermoacoustic couple at high amplitudes.* Journal of the Acoustical Society of America, 2007. **122**(4): p. EL122-EL127.

85. Ahmad, M., Roy, R., and Kamarudin, A., *Observations of acoustic streaming fields around an oscillating ultrasonic file.* Dental Traumatology, 1992. **8**(5): p. 189-194.

86. Habibi, K., Rafat, Y., Mongeau, L., and Taher, R., *Numerical and experimental characterization of oscillatory flows over a flat spoiler in a duct.* INTER-NOISE and NOISE-CON Congress and Conference Proceedings, 2012. **2012**(9): p. 2702-2712.

87. Siegel, R., *Influence of oscillation-induced diffusion on heat transfer in a uniformly heated channel.* Journal of heat transfer, 1987. **109**(1): p. 244-247.

88. Cooper, W., Nee, V., and Yang, K., *An experimental investigation of convective heat transfer from the heated floor of a rectangular duct to a low frequency, large tidal displacement oscillatory flow.* International journal of heat and mass transfer, 1994. **37**(4): p. 581-592.

89. Zhao, T. and Cheng, P., *A numerical solution of laminar forced convection in a heated pipe subjected to a reciprocating flow.* International journal of heat and mass transfer, 1995. **38**(16): p. 3011-3022.

90. Sert, C. and Beskok, A., *Numerical simulation of reciprocating flow forced convection in two-dimensional channels.* Journal of Heat Transfer, 2003. **125**(3): p. 403-412.

91. Habibi, K., Mosahebi, A., and Shokouhmand, H., *Heat transfer characteristics of reciprocating flows in channels partially filled with porous medium.* Transport in porous media, 2011. **89**(2): p. 139-153.

92. Worlikar, A.S., Knio, O.M., and Klein, R., *Numerical Simulation of a Thermoacoustic Refrigerator: II. Stratified Flow Around the Stack.* Journal of Computational Physics, 1998. **144**(2): p. 299-324.

93. Marx, D. and Blanc-Benon, P., *Numerical simulation of stack-heat exchangers coupling in a thermoacoustic refrigerator.* AIAA journal, 2004. **42**(7): p. 1338-1347.

94. Knio, E.B., Omar M, *Numerical study of thermoacoustic heat exchangers in the thin plate limit.* Numerical Heat Transfer: Part A: Applications, 2001. **40**(5): p. 445-471.

95. Chapman, S. and Cowling, T.G., *The mathematical theory of non-uniform gases: an account of the kinetic theory of viscosity, thermal conduction and diffusion in gases*. 1970: Cambridge university press.

96. Shock, R.A., Mallick, S., Chen, H., Yakhot, V., and Zhang, R., *Recent results on two-dimensional airfoils using a lattice Boltzmann-based algorithm.* Journal of aircraft, 2002. **39**(3): p. 434-439.

97. Crouse, B., Senthooran, S., Freed, D., Balasubramanian, G., Gleason, M., Puskarz, M., Lew, P., and Mongeau, L., *Experimental and numerical investigation of a flow-induced cavity resonance with application to automobile buffeting.* AIAA Paper, 2006(2006-2494).

98. Crouse, B., Freed, D., Balasubramanian, G., Senthooran, S., Lew, P.-T., and Mongeau, L., *Fundamental aeroacoustic capabilities of the lattice-Boltzmann method.* AIAA paper, 2006. **2571**.